

Diss. ETH No. 16210

# Water and Salt Management in the Yanqi Basin, China

A dissertation submitted to the  
SWISS FEDERAL INSTITUTE OF TECHNOLOGY,  
ZURICH

for the degree of  
Doctor of Science

presented by

Philip Andreas Brunner

Dipl. Ing. ETH

born on July, 24 1975

citizen of Valendas, Switzerland

accepted on the recommendation of

Prof. Dr. Wolfgang Kinzelbach, examiner

Prof. Dr. Hannes Flühler, co-examiner

2005



## Acknowledgements

First of all, I would like to thank my supervisor, Professor Wolfgang Kinzelbach. Working on a project in China was not only a great opportunity from a scientific point of view. By encouraging me to learn Chinese Professor Kinzelbach has opened the door to a different culture and a different way of thinking to me. During this project, many friendships have developed which definitely will last even after this work has been completed. Doing fieldwork in China was adventurous and the trips I was able to take in this country were full of new experiences. Many thanks go to the staff of the IHW, especially Ines Röser, Stephanie Zimmermann, Haijing Wang, Fritz Stauffer, Hannes Bühler, Harrie-Jan Hendricks Franssen, Tobias Siegfried, Peter Bauer, Lesego Kgotlhang, Amsicora Onnis and Markus Holzner. Finally, I wish to thank Thomy Keller for supporting me with the preparation of fieldwork. My thanks also go to the Institute of Geophysics, ETH Zurich, for providing some of the equipment used. The Institute of Geodesy and Photogrammetry, ETH Zurich, provided the differential GPS equipment. Stephano Bernasconi, Geological Institute of ETH Zurich was involved in the measurements of stable isotopes and kindly provided support whenever required. Daniel Braun and Fabienne Steiner from the D-BAUG were of great help in the analysis of the field soil samples.

I am grateful for all the support and help given by Dr. Li Wenpeng, our partner in China at the Beijing Institute of Geo-Environmental Monitoring. It was Dr. Li who initially had the idea to carry out a project in the Yanqi basin. Moreover, without his continuously cutting red tape, my fieldwork would not have been possible. His student, Li Haitao, accompanied me three times to the Yanqi basin, helping me to carry out the measurement campaigns. Without Li Haitao's support in dealing with the local authorities in the project area, and without the good contacts of Li Wenpeng, field work would not have been possible in this remote area of Xinjiang. I also wish to thank the following members of staff of Li Wenpeng's institute: Dr. Hao Aibing and Li Xiaomei supported me during fieldwork and were always quick in providing me with any kind of required information. Our partner in Xinjiang, Prof. Dong Xinguang has not only made all his unpublished data about the Yanqi basin available. His knowledge of this region has greatly contributed to my work. Dr. Fang Chunsheng of Jilin university in China was involved in this project for one year. During that period he programmed the first version of a GIS-based, user friendly interface for the model developed in this thesis. A very special thank you goes to Jemmet Krmabula, our Uygur driver in China. He was the only person in this project to speak the local Uygur language, which was of great help. I also thank the Department of Water Resources in Korla. Only with their kind support, did we have access to many, normally not freely accessible locations in the Yanqi basin.

Professor Shahbaz Khan from the CSIRO Land and Water Griffith Laboratory, Griffith, Australia was involved in parts of the project- I have learnt a lot from him. I also want to mention the two master students from the IGP, Michael Frick and Oliver Heller. I hope they will keep good memories of the relatively rough time they

---

spent in the project area.

Finally, I would like to thank everyone who has, in whatever way, supported me during this project. This, in the first place, includes my parents and my sister for their ongoing and unconditional support during all these years. Rahel Spring, Anna Fehlmann, Tan Xiaoqi, Beat Schäffer, Oliver Herz, Martin Eugster and my old flat mates Alexandra Karrer, Jürg Rauser and Sascha Marchetto have also contributed to this project by being great and reliable friends.

# Contents

---

<b>Acknowledgement</b>	<b>I</b>
<b>Abstract</b>	<b>XIII</b>
<b>German Abstract</b>	<b>XIV</b>
<b>1 Introduction</b>	<b>1</b>
1.1 Food supply in China . . . . .	1
1.2 Soil salinization and irrigation- General aspects . . . . .	2
1.2.1 Irrigation techniques . . . . .	2
1.2.2 Impact of soil salinization on crop production . . . . .	3
1.3 Goal and content of this thesis . . . . .	4
1.3.1 Strategies for action in the Yanqi basin . . . . .	5
1.3.2 Modelling approaches . . . . .	6
1.3.3 Contents of this thesis . . . . .	7
<b>2 Introduction to the Project Area</b>	<b>9</b>
2.1 Geology . . . . .	9
2.2 Surface hydrology . . . . .	10
2.2.1 The Kaidu river and the rivers in the north . . . . .	12
2.2.2 Bostan lake and Kongque He . . . . .	13
2.3 Agriculture and irrigation . . . . .	15
<b>3 Comparing Different Basins with Secondary Salinization</b>	<b>23</b>
3.1 General Overview . . . . .	23
3.1.1 Brief description of the project areas . . . . .	24
3.1.2 Some general thoughts on salinity . . . . .	26
3.1.3 Limitations and conclusions of the box approach . . . . .	31
3.2 System boundaries in relation to water and salt balances . . . . .	33
3.3 Towards sustainable agriculture . . . . .	34
3.4 Some suggestions for the areas considered . . . . .	35
<b>4 Salinity Mapping</b>	<b>37</b>
4.1 Introduction . . . . .	37
4.1.1 Overview . . . . .	38
4.1.2 Field data . . . . .	39
4.1.3 Remote sensing . . . . .	48
4.2 Combining remote sensing and field data . . . . .	53
4.2.1 Comparing measurements on the ground with satellite images from different dates . . . . .	54

4.2.2	Inaccuracies of the location of measurement sites on the ground	55
4.3	Results	56
4.3.1	Combining field data with uncalibrated salinity maps	56
4.3.2	Field data vs. spectral similarity	57
4.3.3	Field data vs. NDVI	58
4.3.4	Summary of obtained relations between field data and uncalibrated salinity maps	59
4.4	Conclusions	59
<b>5</b>	<b>Digital Terrain Modelling</b>	<b>63</b>
5.1	Generation of the DEM by using radar images, measurements on the ground and SRTM data	63
5.1.1	Preprocessed DEMs	63
5.1.2	A brief introduction to SAR interferometry	64
5.1.3	Calculating relative DEMs for the Yanqi basin by using SAR interferometry	67
5.2	Postprocessing	68
5.2.1	Obtaining ground control points	68
5.2.2	Coordinate systems and geoid correction	70
5.2.3	Merging the single DEMs into one	71
5.2.4	Patching wet areas	71
5.2.5	Verification and resampling of the elevation model	73
<b>6</b>	<b>Evapotranspiration and Infiltration</b>	<b>75</b>
6.1	Potential evapotranspiration and crop transpiration	75
6.2	Calculating evapotranspiration by using remote sensing techniques	77
6.3	Calculating phreatic evaporation on the basis of isotope profiles	79
6.3.1	Theoretical background	79
6.3.2	Soil sampling and extraction of soil water	80
6.3.3	Results	81
6.4	Splitting up NOAA-ET into evaporation and transpiration	82
6.5	Combining saltmaps with phreatic evaporation	84
6.6	Estimating infiltration rates	86
6.7	Estimating potential, phreatic evaporation considering vegetation	90
<b>7</b>	<b>Construction and Calibration of the Distributed Flow Model</b>	<b>93</b>
7.1	Introduction	93
7.2	Modflow	94
7.3	Flow packages and input data	96
7.3.1	Layer properties, units and geometric set-up	96
7.3.2	Hydraulic conductivities	97
7.3.3	Recharge and Pumps	98
7.3.4	Rivers and drains	98

---

7.3.5	Bostan lake . . . . .	101
7.3.6	Evaporation . . . . .	102
7.4	Steady state calibration and results . . . . .	103
7.5	Numerical considerations . . . . .	108
7.6	Additional data required for transient simulations . . . . .	108
<b>8</b>	<b>Modelling Results</b>	<b>111</b>
8.1	Calibrated steady state model . . . . .	111
8.1.1	Water balance of the aquifer . . . . .	111
8.1.2	Hydraulic heads . . . . .	112
8.1.3	Phreatic evaporation . . . . .	116
8.1.4	Surface water fluxes . . . . .	116
8.1.5	Bostan lake . . . . .	119
8.1.6	Comparison between the box model and the distributed steady state model . . . . .	119
8.2	Scenarios . . . . .	120
8.2.1	Zero-irrigation scenario . . . . .	120
8.2.2	Pumping groundwater scenario . . . . .	122
8.3	Transient model . . . . .	125
8.3.1	Initial conditions . . . . .	126
8.3.2	Transient simulation for the period from 1976 to 2000 . . . . .	126
8.3.3	Transient simulation of groundwater abstraction . . . . .	129
8.4	Evaluation of the long-term sustainability of groundwater abstraction	129
8.5	Conclusions . . . . .	135
8.5.1	Model development and verification . . . . .	135
8.5.2	Model results . . . . .	136
<b>9</b>	<b>Conclusions, recommendations and open questions</b>	<b>139</b>
9.1	Conclusions and recommendations . . . . .	139
9.2	Open questions and recommended further studies . . . . .	140
	<b>Bibliography</b>	<b>143</b>
	<b>Curriculum vitae</b>	<b>149</b>





# List of Figures

---

1.1	Population development and the increase of the irrigated area in China. . . . .	2
1.2	Location of the Yanqi basin and the main rivers. . . . .	5
2.1	Rough overview of the geological structure in the Yanqi basin. The thick black line separates the confined aquifer area from the unconfined system. . . . .	10
2.2	Average water balance [ $\text{m}^3 \cdot \text{s}^{-1}$ ] for the period 1990-1999. The amount of water drawn from the rivers for irrigation purposes is defined as diversion. The water flux evaporating from the groundwater into the atmosphere is defined as phreatic evaporation. The evaporation rate over Bostan Lake is $57 \text{ m}^3 \cdot \text{s}^{-1}$ . $1 \text{ m}^3 \cdot \text{s}^{-1}$ of groundwater is infiltrating into the lake. . . . .	11
2.3	Kaidu river discharge [ $\text{m}^3 \cdot \text{s}^{-1}$ ] at Dashan Kou and Yanqi City. . . . .	12
2.4	Main surface water features in the Yanqi basin. The dam separating the two lakes is plotted in green. The dam along the western shore of the lake is plotted in red. . . . .	13
2.5	Lake area plotted as a function of the lake level. . . . .	14
2.6	The upper image was taken close to the pumping station at the dam (July 2003). The dunes directly behind the lake are clearly visible. The photo below was taken within in the little lake system. . . . .	17
2.7	View of Bostan lake from south to north. The inflow of the Kaidu river as well as the dam separating the little lake from the open water surface is clearly visible (image produced by using the software Worldwind 1.3 by NASA). . . . .	18
2.8	Total of the in- and outgoing salt fluxes [ $10^4 \text{ t} \cdot \text{a}^{-1}$ ] in the Yanqi basin. . . . .	19
2.9	Average water level of Bostan lake- the annual variations are plotted as error bars. . . . .	19
2.10	Impression of the irrigated area in the Yanqi basin. In this specific area, trees are planted for protection against wind erosion. . . . .	20
2.11	Example of a field that was given up as a consequence of the high salinity. . . . .	21
2.12	Total amount of irrigated area and annual amount of irrigation water drawn from the Kaidu, Wulasitai, Qingshui He and Huangshui Gou. . . . .	22
3.1	Locations of the three irrigation areas considered in the box modelling approach. . . . .	23
3.2	Annual, average water balance [ $\text{m}^3 \cdot \text{s}^{-1}$ ] for the LIS (period 1981-2001). . . . .	25
3.3	Crude water balance (1993-2000) of the upper (right part of the image) and lower zones of Rechna Doab [ $\text{m}^3 \cdot \text{s}^{-1}$ ]. dS is the residual between incoming and outgoing water fluxes. . . . .	25

3.4	Schematic concept of irrigation area with the most basic processes considered. . . . .	26
3.5	Steady state (SS) groundwater table $h_{ss}$ [m] and steady state salt concentration $c_{ss}$ [ $\text{kg}\cdot\text{m}^{-3}$ ] as functions of the irrigation amount in the Yanqi basin [ $\text{m}^3\cdot\text{a}^{-1}$ ]. Furthermore, the time $t$ [a] to reach 99% of steady state for both the groundwater table and the salt concentration is also plotted as a function of the irrigation amount. . . . .	30
3.6	Steady state groundwater table $h_{ss}$ [m] and steady state salt concentration $c_{ss}$ [ $\text{kg}\cdot\text{m}^{-3}$ ] as functions of time in the LIS. . . . .	32
3.7	Suggestion for developing a sustainable water and salt management in irrigated areas. . . . .	35
4.1	Overview of the major steps and scales for mapping soil salinity. . . .	38
4.2	Measurement sites in the Yanqi basin. . . . .	41
4.3	Measurement layout of a EM38 station. It consists of 25 single EM38 measurement points (indicated by the circles). If soil samples were taken or a Schlumberger sounding was performed, it was always in the center of this measurement layout (indicated by the red circle) The contour lines were obtained by interpolation of the horizontal EM38 reading [ $\text{dS}\cdot\text{m}^{-1}$ ]. . . . .	42
4.4	Soil moisture and electrical conductivity profiles for the non-irrigated station 16 and the irrigated station 3. The x-axis indicates the depth from which the samples were taken. . . . .	43
4.5	Schlumberger sounding at station 17 ( $42^\circ 16.016\text{N}$ , $86^\circ 49.261\text{E}$ ); after point 11 a different spacing between the potential electrodes was used, 11, 12 and 13 were measured in both configurations. AB is the distance between the current electrodes, $r$ the measured apparent resistivity, $k$ is the geometrical constant. . . . .	45
4.6	Inversion of a resistivity sounding. The x-axis [m] represents both the spacing between the source electrodes as well as the depth of modelled resistivity at Stn. 17. Logarithmic apparent resistivity is represented by the y-axis: the red curve indicates the relationship between apparent resistivity $\rho$ and the spacing between the source electrodes for a soil having a resistivity profile as indicated with the blue curve. The green points are the measured, apparent resistivities at this station. . . . .	46
4.7	Relationship between saturated paste conductivities (y-axis, [ $\text{dS}\cdot\text{m}^{-1}$ ]) and the EM38 values (x-axis, [ $\text{dS}\cdot\text{m}^{-1}$ ]) for the three model layers (left: 0-30 cm, middle: 30-60 cm, right: 60-90 cm). The pink points are outliers. . . . .	47
4.8	Relationship between saturated paste conductivities (y-axis, [ $\text{dS}\cdot\text{m}^{-1}$ ]) and the reciprocal values of the apparent resistivities. The pink points are the outliers (stations 38 and 11). . . . .	48

---

4.9	Temporal distribution of ASTER- images over the Yanqi basin- the green colour indicates an insufficient coverage of the area of interest, the red colour indicates a high cloud cover, the blue colour indicates both sufficient image quality and sufficient area coverage. . . . .	49
4.10	Two examples of an image-derived spectrum from an ASTER image over the project area on November 11 <sup>th</sup> , 2002. The reflectance values in each channel of two pixels (see right image) are plotted as a function of wavelength (left). The station plotted in red (station 11) could be used as image derived reference spectrum, as electrical conductivity values observed at this location were very high. . . . .	50
4.11	The plot shows the spectral responses of the same, salinized pixel on four different images. . . . .	51
4.12	Map of spectral similarity calculated with the SCM (November 11 <sup>th</sup> , 2002). White areas indicate a high spectral similarity to the reference spectrum. . . . .	52
4.13	Uncalibrated salinity map calculated with the Spectral Correlation Mapper. The images (mosaic of two ASTER images) were recorded on September 3 <sup>rd</sup> , 2003. . . . .	53
4.14	Ratio between two maps calculated with a different reference spectrum (left) and their pixelwise comparison (right). The image was recorded on November 11 <sup>th</sup> , 2002. The white areas have a spectral similarity of zero. . . . .	54
4.15	Detail of the pixels surrounding station 36 (41° 52.028N, 86° 38.517E). The center of the measurement layout is very close to the center of the pixels 5,6,8,9. The contribution of each of these pixels is therefore around 25%. . . . .	56
4.16	Field data (y-axis) vs. pixel similarity (x-axis) for November 11 <sup>th</sup> , 2002 (left) and March 28 <sup>th</sup> , 2001 (right). Green points are from irrigated areas, blue points from non-irrigated sites. . . . .	58
4.17	Field data vs. spectral similarity and NDVI (September 3 <sup>rd</sup> 2003). . .	59
4.18	Field data vs. spectral similarity and NDVI (August 12 <sup>th</sup> , 2001). . . .	60
5.1	Schematic sketch of the geometric model used for SAR interferometry.	65
5.2	Continuous and wrapped phase function. . . . .	67
5.3	Collection geometry of the interferometric model. The parameters are explained in the text. . . . .	68
5.4	The black and the red box show the coverage of the two tandem pairs. The crosses indicate the locations where ground truth was measured. The different colours of the crosses indicate in which DEM their location has been predefined. . . . .	69
5.5	Examples of easily identifiable points in both the draft DEM and a panchromatic image (Landsat). . . . .	70
5.6	3-dimensional, vertically exaggerated view of the Yanqi basin (NW to SE), overlaid with a Landsat colour composition. . . . .	72

5.7	The raster map represents the digital elevation model [m.a.m.s.l.]. The crosses indicate measurement stations of DGPS, with an error smaller than 2 m. Only residuals larger than 2 m are plotted. . . . .	73
5.8	Difference between the minimum and the maximum value of the fine resolution DEM within a coarse pixel as a function of spatial resolution. Moreover, the average residuals are plotted. . . . .	74
6.1	Example feature space plot for a NOAA-AVHRR image (27. Feb 2000). Pixels in the plot with surface temperatures below 275 °K and high reflectances are covered with snow. These pixels are located on the high peaks of the Tian Shan mountains. . . . .	78
6.2	Evapotranspiration $ET_{NOAA}$ [ $mm \cdot a^{-1}$ ] over the project area for the year 2000. The white pixels were covered with clouds in at least one image and therefore cannot be calculated. . . . .	79
6.3	Two examples (station 11 and station 16) of $\delta^{18}O$ profiles. . . . .	81
6.4	Phreatic water evaporation vs. depth to groundwater. . . . .	82
6.5	$T_{VEG,NOAA}$ and $ET_{NOAA}$ versus the NDVI. . . . .	83
6.6	Phreatic evaporation for the year 2000 [ $mm \cdot a^{-1}$ ] and the soil salinity map, presented as spectral similarity. Both maps are overlaid by the drainage system of the basin. . . . .	85
6.7	Irrigation zones and irrigated areas (2001) - the background of the map is the NDVI [-] distribution (2001). . . . .	86
6.8	Relevant fluxes over an irrigated plot. Only the phreatic evaporation $E_P$ is dependent on the depth to groundwater. . . . .	87
6.9	Detail of the binary irrigation map (upper left), portion of irrigated area within a low resolution map (upper right) and the final infiltration map [ $mm \cdot a^{-1}$ ]. . . . .	89
6.10	Map of potential evaporation [ $mm \cdot a^{-1}$ ] for the model area. . . . .	91
7.1	Schematic overview of the required input data sets for the model as well as the model outputs. $E(h)$ is the relation between evaporation rate and the depth to groundwater. . . . .	94
7.2	Boundary conditions, rivers, drains and rough conductivity zonation for the first model layer. The Gobi-formation is shown in green, the Q3-4 formation in blue. Rivers are plotted with a thick, black line. Drainage channels are plotted in red. The red circles indicate the presence of measurement stations. . . . .	96
7.3	Layer thicknesses for the first three layers [m]. The crosses indicate where borehole data were available. These boreholes do not necessarily correspond to the observation boreholes presented in the flow model. . . . .	97
7.4	Schematic plot of the calibration process. Verification data are printed in italics, the most important parameters for every calibration step are printed bold. . . . .	105

---

7.5	Overview of the zonation of hydraulic conductivities used for the steady state model. . . . .	106
7.6	Two examples of calculated phreatic evaporation maps [ $\text{m}^3 \cdot \text{d}^{-1}$ ] obtained during the calibration. The first map was calculated by using a vertical hydraulic conductivity of $0.01 \text{ m} \cdot \text{d}^{-1}$ , the map below a value of $0.5 \text{ m} \cdot \text{d}^{-1}$ . If a small value of vertical hydraulic conductivity is applied, phreatic evaporation in the irrigation area is significantly increased. Along the lake shore, however, phreatic evaporation is reduced.	107
8.1	The irrigated area (shown in light green colour, also called area of interest) is of interest as phreatic evaporation and soil salinization occur mainly in this region. The lake is plotted in dark blue, the lake shore in light blue. . . . .	112
8.2	Comparison between observed and calculated groundwater tables for 3 layers. Data for the first layer are plotted in black (crosses), the second layer in blue and the third layer in red. . . . .	114
8.3	Comparison between observed (x-axis) and calculated depth to groundwater. The calculated heads in the lower left quadrant are above the soil surface. . . . .	115
8.4	Calculated groundwater tables [m] of the first layer- the numbers are the residuals between the measured and the observed groundwater tables. . . . .	115
8.5	Phreatic evaporation [ $\text{m}^3 \cdot \text{d}^{-1}$ ] from NOAA-AVHRR images and phreatic evaporation calculated by the calibrated model. . . . .	117
8.6	Quotient of the class map from the model output and the class map from remote sensing. 1 indicates an agreement, while 0.3 and 3 indicate the poorest agreement between the classifications. . . . .	118
8.7	Infiltration [ $\text{m}^3 \cdot \text{d}^{-1}$ ] into aquifer layer 1 (left) and layer 2 (right). . .	120
8.8	Phreatic evaporation [ $\text{m}^3 \cdot \text{d}^{-1}$ ] without irrigation. The area embraced between Wulasitai and the Kaidu river is a swamp and is periodically flooded. . . . .	121
8.9	Distribution of phreatic evaporation [ $\text{m}^3 \cdot \text{d}^{-1}$ ] for the pumping scenario. Crosses indicate that a pump is abstracting water from the second layer. . . . .	125
8.10	Integral of phreatic evaporation in time (years). The saltmap (plotted as spectral similarity) is representing the conditions for the year 2002.	128
8.11	Phreatic evaporation flux as a function of time for the three scenarios described. In scenario 1 and 2 the total abstraction rate is $12.6 \text{ m}^3 \cdot \text{s}^{-1}$ . In scenario 3, $15.2 \text{ m}^3 \cdot \text{s}^{-1}$ are abstracted. . . . .	130

8.12	Vertical exchange [ $\text{m}^3 \cdot \text{d}^{-1}$ ] between the second and the first aquifer layer for the confined area in the steady state pumping scenario. Positive numbers indicate a water flux from the second to the first layer. Crosses indicate that a pump is abstracting water. In the areas where no pumps have been installed, the drainage net is still active and an upward flux into the first layer is observed. . . . .	132
8.13	Salt fluxes for the confined area between first and second model layer. The system boundary to calculate the salt balance is plotted dark gray (see second layer). . . . .	133
8.14	Development in time of the salt concentration of the irrigation water and of the first and second aquifer layer. . . . .	135

---

## Abstract

In this thesis a hydrologic model of an agriculturally used basin in China is constructed. The project area, the Yanqi basin, is located in the Northwestern Chinese province of Xinjiang. The climate is continental and very dry. The annual amount of precipitation of around  $20 \text{ mm}\cdot\text{a}^{-1}$  is negligible compared to the potential evapotranspiration of  $1400 \text{ mm}\cdot\text{a}^{-1}$ . Nevertheless, the Yanqi basin has been one of the most productive agricultural areas in western China ever since irrigation was introduced in the second half of the 20th century. Irrigated water is drawn from the rivers flowing through the basin. At present, the irrigated area covers about  $1.2\cdot 10^5$  ha. As a consequence of this intensive agriculture, the productivity of the downstream systems is negatively affected.

The intensive irrigation has led to a series of environmental problems, the most important one being soil salinization. An excessive application of stream water without adequate drainage has raised the groundwater table during the last years, causing significantly increased groundwater evaporation. Salt stored for decades in the subsoil is dissolved as the groundwater table rises and accumulates at the soil surface as groundwater evaporates. Soil salinization leads to vegetation degradation as well as to a loss of arable farmland. In 2002, 60% of the entire irrigation area exhibited a groundwater table of less than 2 m below the surface and therefore is at risk of becoming saline. However, alternatives to today's practices exist. If a part of the irrigation water directly drawn from the rivers is substituted by river water pumped indirectly from the aquifer, the groundwater table will drop and the process of salinization will be slowed down. If the groundwater table drops sufficiently low, the process will be reversed by flushing down the salt.

The key parameter determining the long term sustainability is the ratio between river water and groundwater applied to irrigation. It is determined with a coupled model of groundwater and surface water flow. Such a model has been constructed and verified by using spatially distributed input data derived from remote sensing. Examples for spatially distributed parameters are a digital elevation model and the distribution of infiltration rates under the irrigated fields. The verification data consisted of observations of the groundwater table, the spatial distribution of phreatic evaporation and the distribution of salt in the project area as well as observed infiltration rates along the rivers. The model can reproduce the verification data satisfactorily. With this model, two scenarios have been developed and their influence on the water balance has been studied. The model predicts that the substitution of every  $\text{m}^3$  of river water by pumped groundwater will increase the available downstream resources at least by  $0.75 \text{ m}^3$ . The scenarios show that without lowering agricultural production sustainable solutions for the water allocation in the Yanqi basin and its downstream exist.



---

## Zusammenfassung

In diesem Projekt wurde ein hydrologisches Modell für ein landwirtschaftlich genutztes Becken in China erstellt. Das Projektgebiet liegt in der Provinz Xinjiang. Das Klima ist kontinental und die Niederschläge sind gering. Die jährlichen Niederschläge belaufen sich auf nur  $20 \text{ mm}\cdot\text{a}^{-1}$  - eine vernachlässigbare Menge im Vergleich zu den  $1400 \text{ mm}\cdot\text{a}^{-1}$  potentieller Verdunstung. Trotz des geringen Niederschlags gehört das Yanqi Becken zu den produktivsten landwirtschaftlich genutzten Flächen in Xinjiang. Dies wurde durch die Einführung der Bewässerung in den fünfziger Jahren möglich. Heute werden rund  $1.2 \cdot 10^5$  ha Land bewässert. Das Bewässerungswasser stammt von den Flüssen. Der verschwenderische Umgang mit den vorhandenen Wasserressourcen im Yanqi Becken führte zu einer Verringerung der verfügbaren Wasserressourcen im Flussunterlauf bei gleichzeitiger Erhöhung der Salzkonzentration.

Im Yanqi Becken selbst hat die intensive Bewässerung zu mehreren Umweltproblemen geführt, unter anderem auch zu einer Versalzung des Bodens. Die intensive Bewässerung ohne ein effizientes Drainage-Netz führte zu einer Anhebung des Grundwasserspiegels. Salz, das schon immer in der ungesättigten Zone gespeichert war, wurde durch den aufsteigenden Grundwasserspiegel gelöst und durch die direkte Verdunstung an die Bodenoberfläche transportiert. Die Bodenversalzung führt zu einer Verringerung der landwirtschaftlichen Produktivität und zu einer Reduktion der vorhandenen Bodenressourcen. Im Jahr 2002 war der Flurabstand auf 60% der landwirtschaftlich genutzten Flächen kleiner als 2 Meter. Diese Gebiete sind versalzungsgefährdet. Es existieren jedoch Alternativen zu der heutigen Bewässerungsstrategie. Falls ein Teil des Bewässerungswassers nicht direkt aus dem Fluss, sondern über der Aquifer indirekt aus dem Fluss entnommen wird, vergrößert sich der Flurabstand und die Versalzung wird verlangsamt. Wird der Grundwasserspiegel tief genug abgesenkt, kann die Versalzung der Wurzelzone durch das Auswaschen von Salz in den Grundwasserleiter sogar rückgängig gemacht werden.

Der entscheidende Parameter für eine langfristig nachhaltige Bewirtschaftung ist der Anteil des Grundwassers am Bewässerungswasser. Er wird mit einem gekoppelten hydrologischen Modell evaluiert, das sowohl das Grundwasser als auch die Oberflächengewässer simuliert. Das Modell wurde aufgrund räumlich verteilter Daten erstellt und verifiziert. Beispiele für räumlich verteilte Input-Daten sind ein digitales Geländemodell und die Versickerungsraten unter den bewässerten Flächen. Das Modell wurde mittels Bohrloch-Daten, der räumlichen Verteilung der direkten Verdunstung aus dem Grundwasserleiter, der Verteilung von Salz an der Erdoberfläche und den Infiltrationsraten entlang der Flüsse verifiziert. Es wurden zwei Szenarien entwickelt und ihre Einflüsse auf die Wasserbilanz der Region simuliert. Das Modell zeigt, dass die Substitution von jedem  $\text{m}^3$  Bewässerungswasser aus dem



Fluss durch Grundwasser die verfügbaren Ressourcen im Unterstrom um mindestens  $0.75 \text{ m}^3$  erhöht. Die Szenarien zeigen, dass eine nachhaltige Bewirtschaftung des Yanqi Beckens und seines Unterstroms ohne Produktionseinbussen möglich ist.



# Chapter 1

---

## Introduction

### 1.1 Food supply in China

Until recent years, China officially managed to supply itself sufficiently with food. But the pressure on the available land per person has been increasing every year for two reasons: The increasing population and the ongoing transformation of China from an agricultural society to an industrialized nation (Brown, 1995). Due to the one child policy the demographic growth is expected to slow down, but not until around the year 2017 (UN, 2003). The estimated peak of approximately 1.66 billion Chinese is expected around the year 2050, see figure 1.1. In order to increase the agricultural production and to reduce the pressure on the remaining arable land, the irrigated area has been increased continuously.

Irrigation techniques have been designed to permit crop production in areas where rainfall is either not sufficient or poorly distributed over the year (Hillel, 1987). Irrigation therefore helps to ensure a stable production compared to an agricultural system which is completely dependent on the weather. Worldwide, about 17% of the agricultural area is irrigated, but its production amounts to over 40% of the global agricultural outputs and to 60% of grain production. In a global ranking, China has with 50% of the total cultivated area the largest portion of irrigated farmland (FAO, 2004). The expansion of the irrigated areas has significantly influenced the local supply and demand balance of water. In eastern China (e.g. in Hebei province), the gap between the limited, renewable water sources and the continuously increasing water demand is, to a large extent, compensated by groundwater pumped and applied for irrigation. If the abstraction rate of an aquifer is above the recharge rate, the groundwater table inevitably drops. If the drawdown cones become too deep, the remaining water resources are difficult to access. It is clear that in areas where more water is used than recharged, agricultural production will decrease as the available resources get scarce. Ironically, abundant water resources do not guarantee sustainable production. In the semi-arid regions in western China such as Xinjiang or Inner Mongolia, irrigation water is not pumped from aquifers, but mostly drawn from rivers. The intensive irrigation has led to several negative impacts for crop production. Besides water logging, soil salinization is the most important one.

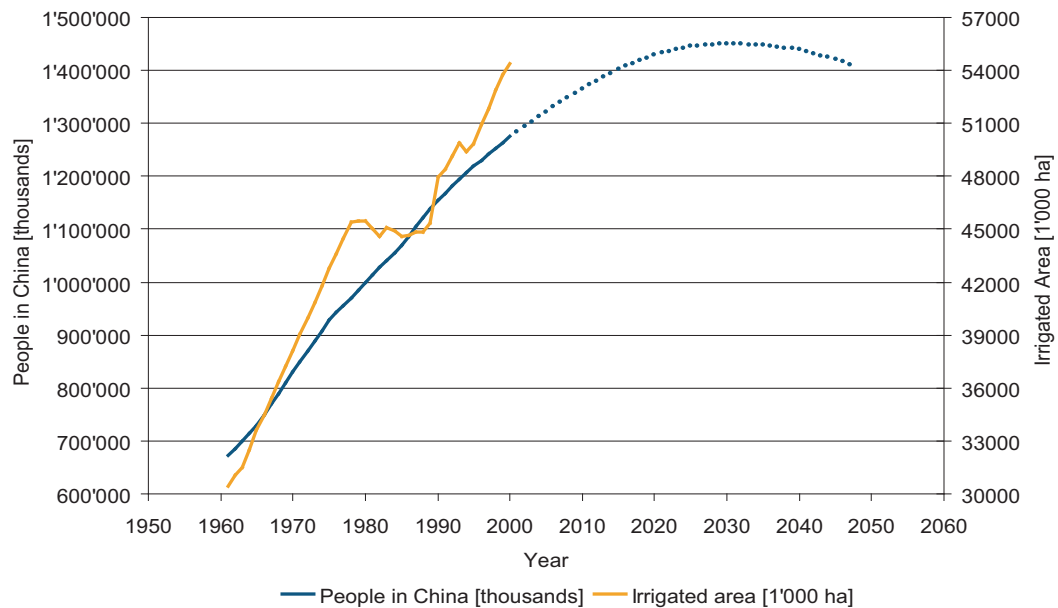


Figure 1.1: Population development and the increase of the irrigated area in China.

## 1.2 Soil salinization and irrigation- General aspects

Salinization occurs naturally (primary salinization) or due to human activities (secondary salinization). Besides deforestation, irrigation is one of the most common causes of secondary salinization. Comprehensive overviews covering most of the causes, consequences and possibilities to tackle the problem of salinization can be found in Hillel (2000); Jakeman *et al.* (1995); Richards (1954), to mention but a few examples. According to Oldeman *et al.* (1991), 76.6 Mha of farmland, which is about 30% of the total, worldwide irrigated area, is in one way or the other affected by human induced salinization. The consequences of soil salinity have accompanied societies that rely on irrigated agriculture through history. Various historic and present examples are described by Hillel (1990). Different forms of irrigation and their influence on salinization have widely been studied (e.g. Hillel (1987); Rhoades *et al.* (1992)) and are briefly described in the following section.

### 1.2.1 Irrigation techniques

A widely applied method of irrigation is to flood a field and simply let the water infiltrate. Various levels of development of this flood irrigation exist. The effectiveness of flood irrigation is, to a large extent, dependent on how even the field's surface is. Laser leveling of a field allows uniform irrigation by using only a small amount of water. If the field is uneven, however, a larger amount of water has to be applied to irrigate the planted area. The efficiency of flood irrigation over uneven plots can be

as low as 40%. Sprinkle irrigation allows to irrigate a field more uniformly even if the surface has not been made flat. Sprinkle irrigation sprays up water and allows it to fall on the plants and soil just as rain does. The most efficient technique in terms of water usage is the so called drip irrigation. Drip irrigation systems apply the irrigation water directly to the root zone. This is the most demanding method in terms of installation costs and maintenance but with a good "crop per drop" efficiency.

Irrigation water requirement is dependent on many factors such as the crop mix, the extent of soil salinity or climatic conditions. If exactly the amount required by vegetation is applied, the salts accumulating in the root zone decrease the crop productivity. The salt therefore has to be removed continuously. This is done by flushing down the salt, using additional water (over-irrigation). This may trigger a vicious circle. By flushing down the accumulated salts, the groundwater table rises if no adequate drainage has been installed. As a consequence of the increased phreatic evaporation and therefore increased transport of salt into the root zone, more water will be required during the next irrigation cycle. Without an adequate drainage, such a system is doomed to fail. The leaching requirement is crop specific and can easily be calculated. Assuming steady state conditions, the amount of salt imported by irrigation must equal the amount of salt in the drainage water:

$$V_d \cdot c_d = V_i \cdot c_i \quad (1.1)$$

with  $V_i$  being the volume of irrigation water and  $c_i$  its salt concentration and  $V_d$  the amount of drainage water with  $c_d$  the salt concentration in the drainage water. Because the volume drained is the difference between the volume of irrigation water and the volume of water removed by evapotranspiration ( $V_{ET}$ ), equation 1.1 can be written as:

$$V_i = \frac{c_d}{(c_d - c_i)} V_{ET} \quad (1.2)$$

To calculate the leaching requirements for a specific crop, the concentration of the drainage water is set to the salt concentration where this specific crop has its optimal conditions. The effectiveness of leaching is also dependent on the method of irrigation and the soil type. Under drip irrigation, the application of water is not distributed uniformly over the field. Even if the soil volume directly under the point of water release is leached sufficiently, long term drip irrigation may result in salt accumulation and consequently influence crop yield negatively. For both sprinkler irrigation as well as flood irrigation, the rate of leaching water applied should not exceed the highest infiltration of the soil, otherwise water logging and flooding of the field ensues.

### 1.2.2 Impact of soil salinization on crop production

Soil salinization changes the structure of the soil. These effects are mainly related to changes of the surface electrical properties of minerals (Hillel & Warrick, 1998).

A high salt concentration has also an adverse effect on crop production. The concentration of salt in the soil solution is related to the osmotic potential of the water (Hillel, 1987). An increased salt concentration lowers the energy potential and the plant therefore has to compensate the additional energy. This additional energy is provided by osmotic adjustment in the plant. Salt tolerant plants, also called halophytes, absorb salts and accumulate them in the vacuoles. Organic solutes (osmolytes) maintain the osmotic pressure in the cytoplasm. Most agriculturally used crops are salt sensitive and do not accumulate sodium and chloride in the leaves. Compared to halophytes, more osmolytes have to be produced in order to maintain the osmotic pressure. In the case of extreme salinization, the external potential of water may be below the osmotic pressure in the cells resulting in a net outflow of water from the plant. Several approaches have been suggested to describe the influence of salt on the crop. The standard approach suggested by Maas (1990) relates the crop yield  $Y_r$  linearly to salinity, see equation 1.3:

$$Y_r = 100 - b \cdot (EC_e - a) \quad (1.3)$$

$a$  is a salinity threshold [ $\text{dS}\cdot\text{m}^{-1}$ ],  $b$  a slope expressed in % of change in the crop yield and  $EC_e$  is the mean measured electrical conductivity of the root zone. Based on this relation crops are classified according to their sensitivity. Salt sensitive crops require an increased amount of excess irrigation water to leach the salt out of the root zone. An excellent database based on data presented by Maas (1990) and summarizing the impact of salinity on crop growth is provided by the US-Salinity Laboratory.

### 1.3 Goal and content of this thesis

The project area is the Yanqi basin, located in the far west of China (see figure 1.2). The goal of this thesis is to improve the utilization of water and soil resources in the Yanqi basin and, by doing so, increase the available water resources for areas downstream. The so called Green Corridor is dependent on the available freshwater resources flowing out of the Yanqi basin. The intensive agriculture has led to several environmental problems in the Yanqi basin, especially soil salinization. In the basin itself, agricultural production can still be maintained at a profitable level. This is only possible as surface water resources are sufficient and salinization can be controlled by over-irrigation. But the impact for downstream riparians, consisting both of agricultural and natural systems, is high: Surface water resources are not available to the required extent and the salt concentration has increased due to the high evaporation losses upstream, limiting the productivity of the affected systems. However, several options to manage the Yanqi basin in a more sustainable way exist.

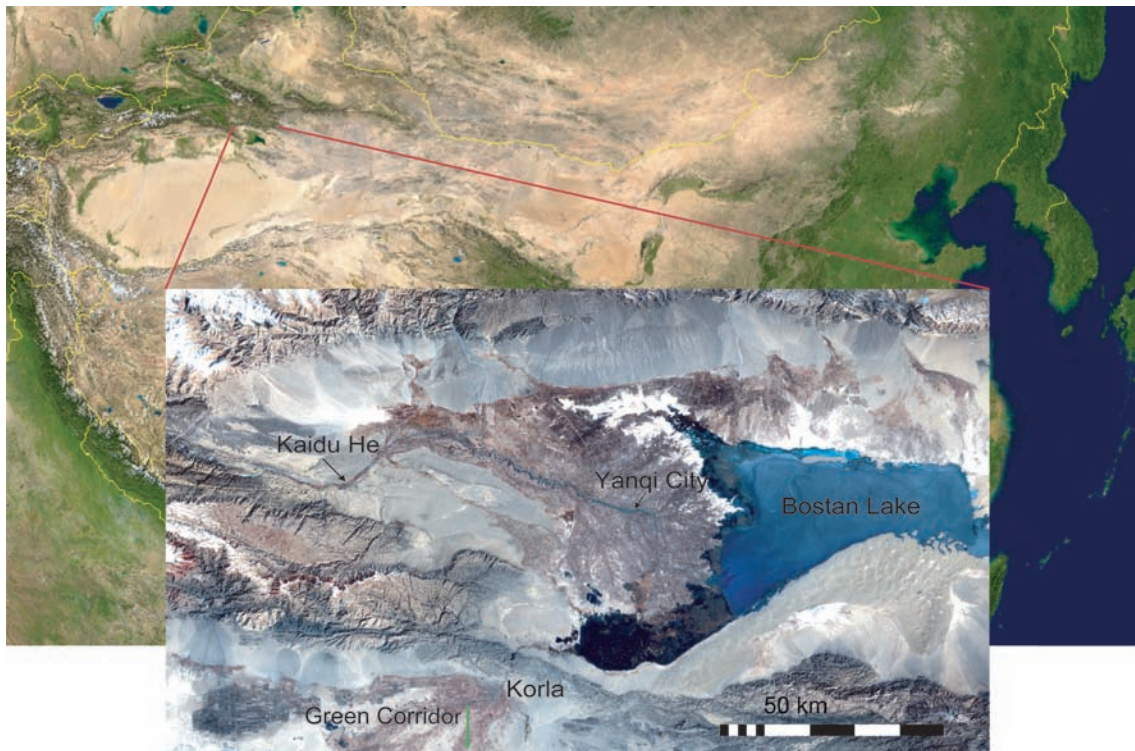


Figure 1.2: Location of the Yanqi basin and the main rivers.

### 1.3.1 Strategies for action in the Yanqi basin

Reducing the irrigated area, improving the efficiency of the irrigation system or planting salt tolerant crops would help to save water and to increase the depth to groundwater. However, the major decision variable to steer the system into a desirable state without reducing the irrigated area is the ratio of irrigation water drawn directly from the river to the water drawn indirectly from the river by pumping groundwater. Pumping groundwater lowers the groundwater table, reduces phreatic evaporation and therefore slows down the salinization of the topsoil. The conjunctive use of surface and groundwater was first studied in Australia by Evans & Nolan (1989) and has already been successfully applied in Pakistan and other countries. In the Yanqi basin, groundwater is hardly used today, as due to energy requirements groundwater is more expensive than surface water. However, if the water table can be kept low by pumping groundwater, the conservation of soil for continued agricultural use along the Kaidu river might strike the balance with a higher price of water. Furthermore, by substituting river water by groundwater every cubic meter of water not wasted for evaporation in the Yanqi basin could be used to irrigate the Green Corridor.

As shown in figure 2.2, Bostan lake evaporates over 42% of the total inflow into the basin (this equals 50% of the Kaidu discharge). An increase of the water resources could be reached if the surface of the lake was reduced. Although this

option was proposed several years ago by the water department in charge, further feasibility studies were cancelled as the consequences for the lake ecosystem and the local fishermen would have been dramatic. Another measure to reduce the salt flux transported downstream is to evaporate highly saline drainage water in the basin itself or to flush down the salt to the aquifer. As easily shown with a simple salt balance model, depositing salt within the area where the water has been evaporated prevents an increasing salt concentration in the downstream systems. Basically, this is a very attractive option. Several natural systems only survive over a long period of time using exactly this principle. In order to understand and reproduce the process of salinization on a regional basis and to simulate alternative strategies of water management, the relevant processes and fluxes determining salinization have to be quantified in a high spatial and temporal resolution.

### 1.3.2 Modelling approaches

All modelling approaches are a simplification of nature. Although models can be set up in a very complex manner including many possible processes, the predictive power cannot be raised indefinitely. The limiting factor is always the lack of accurate input data. In this modelling approach, the amount of processes taken into account is given by the amount of available data. For example, the unsaturated zone will not be included in this modelling approach, although models that provide the possibility to link the unsaturated zone between surface- and groundwater have been developed. Modelling the unsaturated zone requires a huge amount of additional, spatially distributed input data such as porosity, saturation-tension functions or the depth of plant roots as a function of time. The irrigated area in the Yanqi basin covers 1200 km<sup>2</sup>. For a large area such as the Yanqi basin, it has up to now been impossible to obtain such data with the required spatial resolution and accuracy. For the same reasons, the transport of salt has not been modelled explicitly. However, the salt balance in the Yanqi basin is strongly dominated by the water balance. This allows the results of the flow model to be compared with measures of salinization (e.g. the spatial distribution of salt in the project area).

The process of salinization is dependent on various factors and can be studied with the help of several techniques, involving the fields of geodesy, GIS, remote sensing, hydrology and soil science. Salinity can be modelled on different scales. Several approaches have been developed to model salinity in the unsaturated zone on a local scale, e.g. Hydrus 2d (Simunek *et al.*, 2000). An approach integrating both the unsaturated flow as well as ground and surface water on a regional scale is the WASIM package (Schulla, 1997). The WASIM code allows the user to model the unsaturated zone, surface water hydrology and the groundwater flow. Numerous tools have been developed to model groundwater. The core of the hydrological model used in this project is the Modflow code developed by McDonald & Harbaugh (1988). The flow of groundwater is described by the Darcy equation. Modflow is a standard tool to solve the Darcy equation for a finite difference grid.



---

### 1.3.3 Contents of this thesis

Chapter 2 provides an overview of the agriculture, the geology and the surface hydrology in the Yanqi basin. Most of the information provided in this chapter is based on unpublished reports in Chinese. The main data sources were the Institute of Geoenvironmental Monitoring in Beijing, Xinjiang Agricultural University in Urumqi and the Water Management Department in Korla.

Chapter 3 compares the water and salt fluxes by using a simple 1-box model for three regions suffering from salinization: Rechna Doab in Pakistan, the Liu Yuan Kou irrigation system (LIS) in Henan province of China, and the Yanqi basin. It is observed that the space and time boundaries of the system for which an acceptable level of sustainability should be achieved are crucial in this definition. Furthermore, the history of the water resources development in these areas is examined in order to understand the dynamics of salinization as well as the possible steady state solutions.

Considering the severe economic and ecological consequences of soil salinization, quantifying the distribution and extent of soil salinization is important for the management of affected areas. Several methods have been proposed to map soil salinity and alkalinity with remote sensing. In chapter 4, a new method is described which allows to map soil salinity in terms of electrical conductivity over large areas. This method consists of a combination of field measurements and uncalibrated salinity maps calculated from multispectral satellite images. Field measurements are based on both geophysical methods as well as the saturated paste conductivities of soil samples obtained.

The spatial distribution of salt at the soil surface is strongly determined by the evaporation flux from the aquifer to the atmosphere. This quantity depends, besides the hydraulic properties of the soil, on the depth to groundwater. A precise digital elevation model (DEM) as well as the distribution of its errors are therefore required. How such a DEM has been constructed is described in chapter 5. Both the water and salt balance of the Yanqi basin are influenced by evapotranspiration (ET). The quantification of evapotranspiration is described in chapter 6. The influence of vegetation on the basin's water balance is also discussed in this chapter. The hydrological model for the Yanqi basin consists of the aquifer system, rivers, drainage channels and the lake. All these elements are coupled and interacting. The model set-up and the governing equations are described in chapter 7. The model results, which include different scenarios, are presented in chapter 8. The final chapter describes the major conclusions and findings of this thesis.



## Chapter 2

---

### Introduction to the Project Area

Most of the information presented in this chapter is based on internal reports and has been made available through Prof. Dong Xinguang. Such data have not been cited explicitly. Surface hydrology data are documented by the Water Management Authorities in Korla.

#### 2.1 Geology

Figure 2.1 shows an overview of the relevant geological structures. The basement of the Yanqi basin consists mainly of pre-Mesozoic rocks such as gneisses, schists, granitoid and Mesozoic sediments, including sandstone, coal and conglomerates. The cenozoic strata are composed of siltstone, mudstone, weakly consolidated conglomerates, aeolian sand and salt. Chen (1994) divided the cenozoic strata into Holocene (indicated as Q4 on Chinese geological maps), upper Pleistocene (Q3), middle Pleistocene (Q2) as well as lower Pleistocene (Q1). Q4 consists of unconsolidated alluvial and glacial deposits, salts, loam and gravel, as well as aeolian deposits. Q3 consists of alluvial deposits, such as well rounded gravel, silt and sand. Q2 mainly consists of weakly consolidated lacustrine, glacial and alluvial deposits, such as clay and sand-loam interbeds. Q1 is mainly composed of moraine and glaciofluvial deposits, such as loam and gravel. The Q3 sediments feature a high hydraulic permeability. Between the surrounding mountains of the Yanqi basin and the area where Q3 is the predominant formation, the sediments form a weakly heterogeneous aquifer until the bedrock is reached. This structure is also called Gobi-formation.

The stratigraphy in the central area of the Yanqi basin is more complex. The first layer consists mainly of Q3-Q4 deposits. This is the only area where soil could develop and agriculture is possible. Below the first, fertile layer, silt lenses and loam are present and unevenly distributed. This central area of the Yanqi basin can be divided into four layers separated by relatively thin but nearly impermeable silt layers. The hydraulic conductivity of the second aquifer layer is over a magnitude larger than the hydraulic conductivities of the other layers. The high hydraulic conductivity of the second layer allows to abstract groundwater. The confined layers are all connected to the aquifer system following the mountain range surrounding the basin. Fresh water from the Kaidu river as well as the smaller rivers entering the Yanqi basin from the northern boundary infiltrates into the highly permeable Q3 sediments. The water of the confined layers is therefore of good quality and can be used for irrigation purposes. The large amount of salt deposited over time in the first layer, however, significantly reduces its water quality. The salt deposited in this layer is the main source which causes soil salinization.

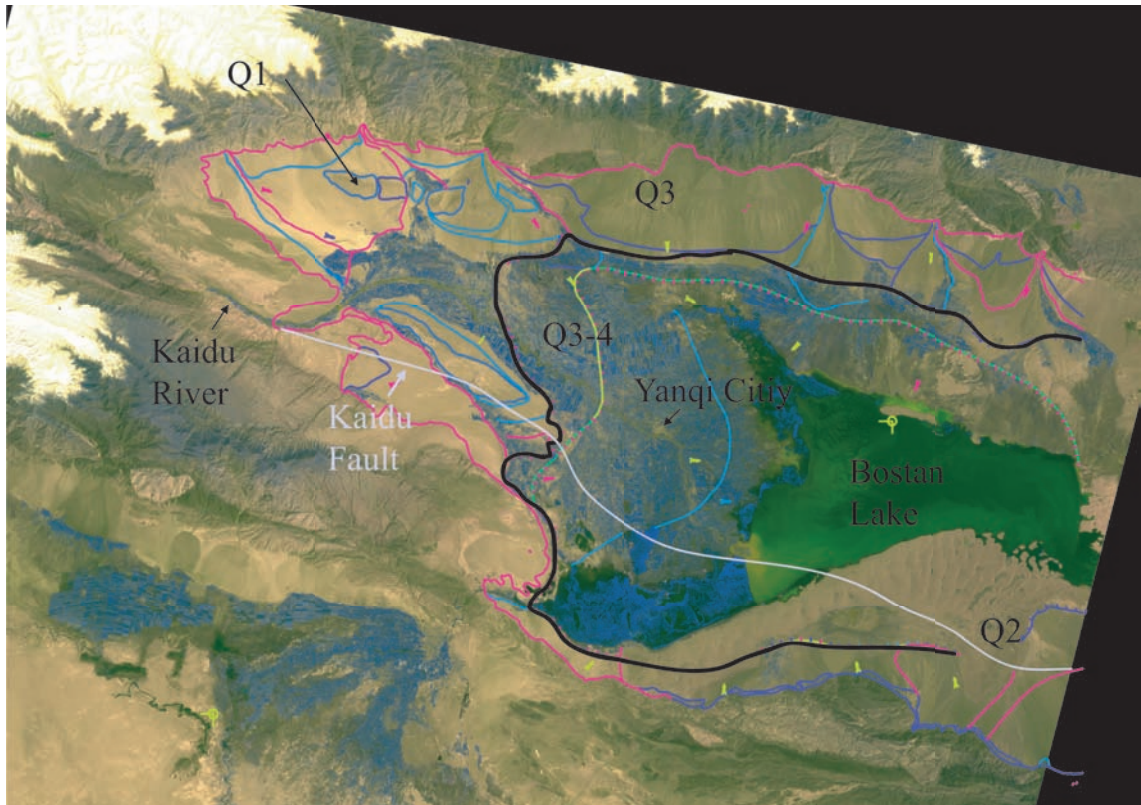


Figure 2.1: Rough overview of the geological structure in the Yanqi basin. The thick black line separates the confined aquifer area from the unconfined system.

Several fault systems have been identified in the Yanqi basin, the most predominant one being the Kaidu fault system. According to Lin *et al.* (2002), the Kaidu fault system is still active and extends WNW-ESE for over 300 km from the southwestern margin of the Yanqi basin through Bostan lake to the southernmost margins of the basin. According to this study, the vertical displacement rate along the Kaidu fault system is  $1 \text{ mm} \cdot \text{a}^{-1}$ . The last major earthquake in this area was in 1927. According to Lin, the seismic movement results in an horizontal offset of the natural drainage network along the Kaidu fault system: Individual upstream channels have up to five dried-up downstream channels immediately after the rivers are flowing across the Kaidu fault.

## 2.2 Surface hydrology

In the Yanqi basin, several control points along the rivers have been installed, regulating the surface water balance: The amount of water conducted to the irrigation areas, the direct discharge into Bostan lake and the outflow into the Kongque river are all regulated. The lowest point of the basin is Bostan lake. The Kaidu river flows into Bostan lake and leaves it as Kongque river. The Kongque river supplies

the so-called Green Corridor between Korla and the now dried out Lop Nor with water. Due to the water consumption in the Yanqi basin, the lake level has been dropping continuously. Before irrigation in the Yanqi basin and along the Kongque river took place, Lop Nor was the final salt sink of the Kaidu-Kongque system (Dong *et al.*, 2001). Nowadays, the salt transported by the Kaidu and Kongque rivers is distributed over irrigated areas, with the final sink moving upstream towards the water consumers. A crude average annual water balance of the Yanqi basin for the period 1990-1999 is presented in figure 2.2. The amount of water applied to

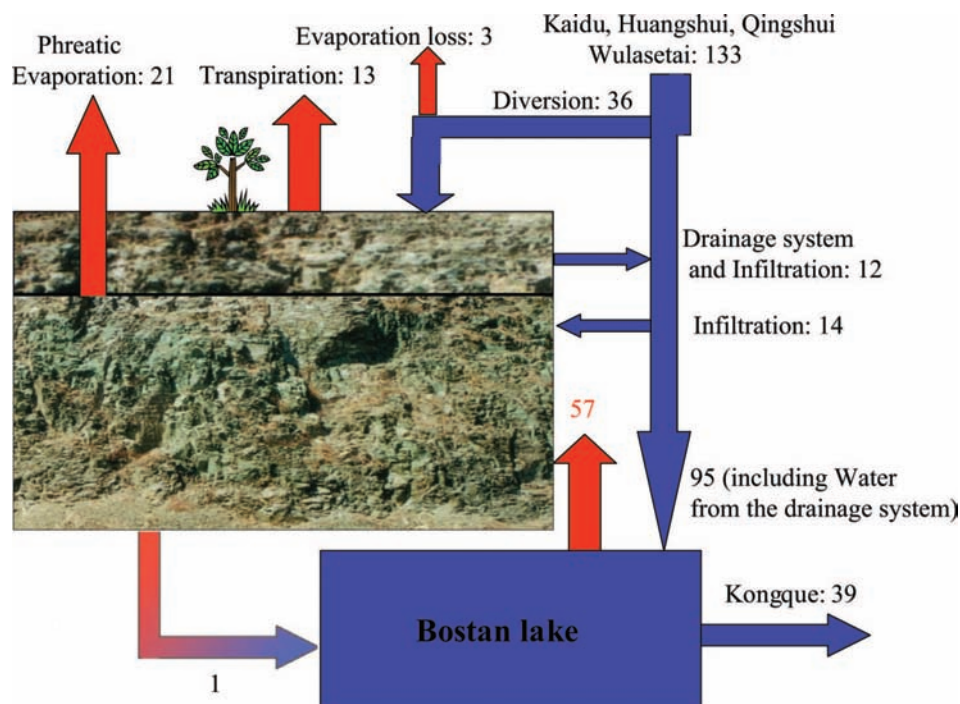


Figure 2.2: Average water balance [ $\text{m}^3 \cdot \text{s}^{-1}$ ] for the period 1990-1999. The amount of water drawn from the rivers for irrigation purposes is defined as diversion. The water flux evaporating from the groundwater into the atmosphere is defined as phreatic evaporation. The evaporation rate over Bostan Lake is  $57 \text{ m}^3 \cdot \text{s}^{-1}$ .  $1 \text{ m}^3 \cdot \text{s}^{-1}$  of groundwater is infiltrating into the lake.

irrigation, the inflow of the Kaidu river and the discharge of the Kongque river are measured quantities. The total amount of drainage water leaving the system as well as phreatic evaporation and river infiltration have been calculated with a simple boxmodel approach (see chapter 3). The evaporation loss is the amount of diverted water that evaporated in the channels or during irrigation. This quantity is estimated.

### 2.2.1 The Kaidu river and the rivers in the north

The locations of the rivers are presented in figure 2.4. Water is drawn from the rivers for irrigation purposes. The relatively high diversion rates reduce the water flow to Bostan lake by about 30%. The Kaidu river is the main source of water in the Yanqi basin. The degree of mineralization is very low. It drains the Yugar basin in the north and is fed through a mix of snow and glacier melt as well as rainwater. The documented discharge of the Kaidu river for two stations is presented in figure 2.3. Several measurement stations are installed along the Kaidu river. The first one

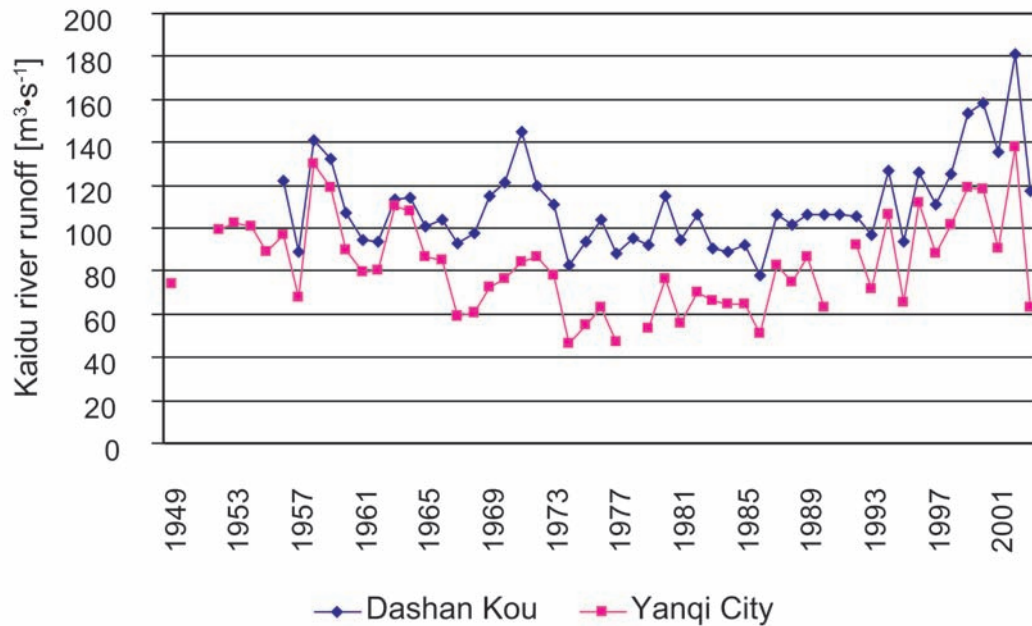


Figure 2.3: Kaidu river discharge [ $m^3 \cdot s^{-1}$ ] at Dashan Kou and Yanqi City.

is located at Dashan Kou, a small power plant in the western part of the area. The next measurement station is installed at the so called first diversion point. From this point, irrigation water is diverted and conducted to the irrigation channels. Between Dashan Kou and the first diversion point, the river water infiltrates into the underlying aquifer. For the year 1998, the infiltration rate between Dashan Kou and the first diversion point was around  $2 m^3 \cdot s^{-1}$ . After the Kaidu flows further through the Yanqi basin, the river no longer continuously infiltrates into the aquifer. As soon as the river flows over the Q3-4 formation, it alternatively drains and infiltrates the aquifer system. The net water flow is very difficult to quantify. Based on a water balance method, Li Wenpeng (oral communication) concluded that from the first diversion point to Bostan lake the Kaidu river drains the aquifer system, but with a very small rate of about  $1 m^3 \cdot s^{-1}$ .

The total discharge of the rivers in the north, Huangshui Gou, Wulasitai and Qingshui He contributes only with 10% of the Kaidu's discharge to the inflow of



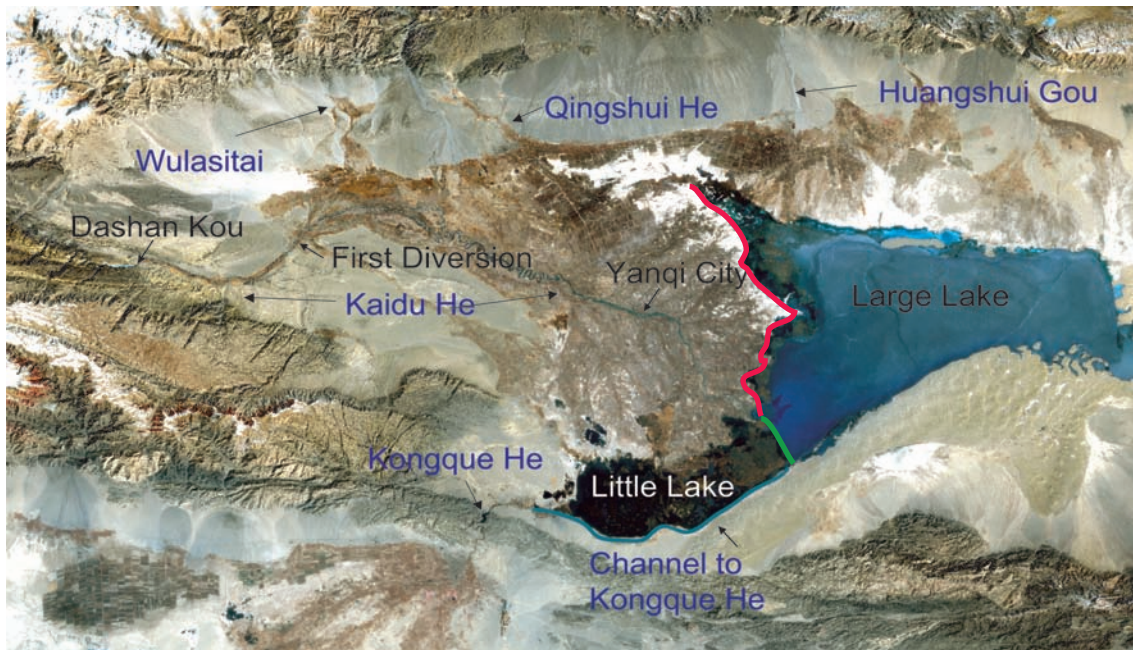


Figure 2.4: Main surface water features in the Yanqi basin. The dam separating the two lakes is plotted in green. The dam along the western shore of the lake is plotted in red.

the basin. Huangshui Gou and Qingshui He originate in the northern Tianshan mountains and contribute with  $13 \text{ m}^3 \cdot \text{s}^{-1}$  and  $5 \text{ m}^3 \cdot \text{s}^{-1}$  respectively to the inflow into the Yanqi basin (average value 1990- 1999). Wulasitai is a spring. The spring water also originates from the northern Tianshan mountains. All rivers infiltrate into the aquifer system as long as they flow above the Gobi-formation in the north.

## 2.2.2 Bostan lake and Kongque He

Bostan lake is with over  $1000 \text{ km}^2$  of open water surface the largest fresh water lake in Xinjiang. The deepest point is only 17 m below the water surface. The area covered by water as a function of the surface water level is presented in figure 2.5. Bostan lake is divided into the "large lake" and the "little lake", see figure 2.4. The "little lake" is a complex channel network, overgrown by thick reeds. The lakes have always been separated by a natural dam. In the late seventies, this natural dam was extended. Today, no water is flowing directly from the large to the little lake. Figure 2.6 shows a photo of the large lake as well as a photo taken within the little lake's channel system.

The two lakes are separated by a dam built in the seventies. The natural course of the Kaidu river was changed during the construction of the dam. Before the construction of the dam, over 80% of the water brought by the Kaidu flowed into the little lake system. With the damming, the natural outflow of the little lake system was replaced by a channel leading from the dam to the natural outflow

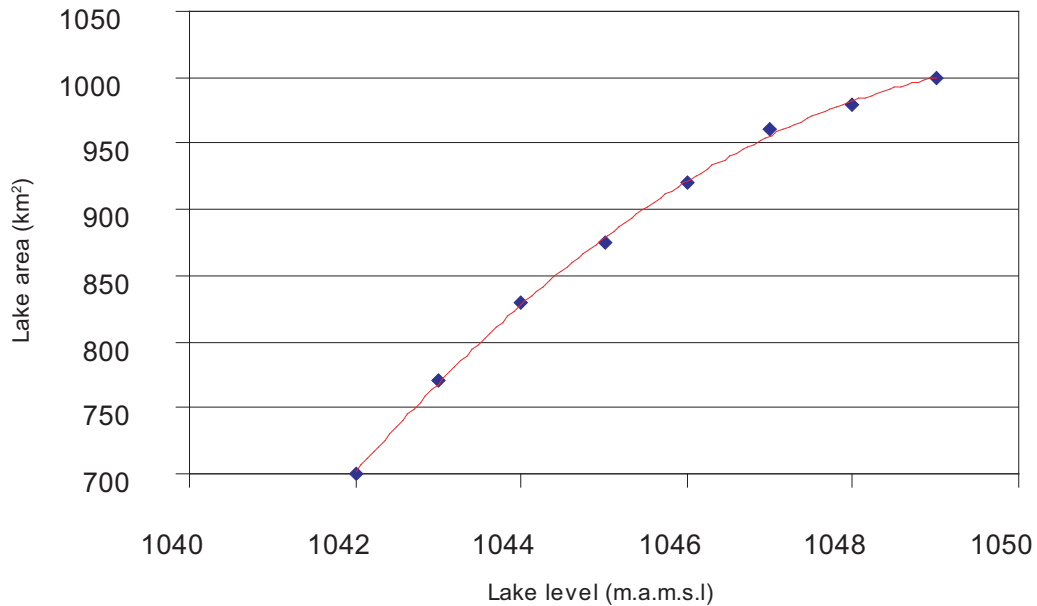


Figure 2.5: Lake area plotted as a function of the lake level.

of the little lake, the Kongque river. The water level of Bostan lake is regulated by pumping water into this channel. The pumping station is located close to the dam. The inflow of the Kaidu river is very close to this pumping station, causing a freshwater shortcut, clearly visible in figure 2.7.

A second dam around the western lake shore was also constructed in the late seventies. The elevation of the dam is 1048 m. Before the construction of this dam, the lake used to flood larger areas in years with a high inflow from the Kaidu river. The terrain elevation in the direct vicinity of the lake is below the present lake level. The water from the drainage channels has therefore to be pumped into the lake. The exchange of water between the lake and the aquifer is very difficult to quantify. However, there is a thick layer of sediment with a very low hydraulic conductivity, which covers the bottom of the lake. The exchange rate is very small compared to other fluxes such as evaporation over the lake area.

The construction of the dam, the increased inflow as well as the increased discharge of the lake have significantly reduced the average salt concentration in the large lake. Before the water balance of the lake system was put under human control, only the areas close to the border of the little lake had a sufficient freshwater inflow that diluted the high salt concentration in the large lake. Even after the construction of the dam, electrical conductivity in the eastern and northern parts of the large lake is still up to a factor of 2 higher than in the area around the dam. Before the construction of the dam, Bostan lake should not have been considered as a freshwater lake, except for the areas close to the border of the little lake. The



construction of the dam had a significant influence on the overall salt balance in the Yanqi basin. In figure 2.8 the inflow of salt into the Yanqi basin and the outflow through the Kongque river are plotted.

The natural resources of Bostan lake are an important economic and ecological factor for the region. The reed zones around Bostan lake are a habitat for various bird species. As one of the fishery bases of Xinjiang, Bostan lake is rich in fish. The fish catch in 1998 was over 2500 tons. As many as 24 different species including grass carp and silver carp can be found. The little lake is a major production area for reed in China. 60,000 tons of dry reed were harvested in the year 2000, mainly used for paper production. In 1950, the amount of harvested reed was documented with 250 tons. Tourism, including motorboat tours through the channels of the little lake, is getting more and more important, but the damage to the delicate ecosystem is severe.

Between 1950 and 1988, the surface level of the lake dropped from 1049 m to 1045 m, the lake's surface area was reduced by over 20% (see figure 2.9). The decreasing water level of the lake led to a considerable loss of reed zones, endangering the habitat of various bird species. Today, the level of Bostan lake is kept stable at around 1047 m.

Most of the drainage channels of the Yanqi basin discharge into Bostan lake. In terms of water quantities this is a negligible amount, but the high concentration of salt strongly influences the salt balance of the lake. Compared to the concentration of the Kaidu river, the electrical conductivities of the drainage water are up to a factor of 20 higher. In addition to pollutants such as pesticides and salt originating from agricultural production, the waste water of Yanqi city is still discharged into the little lake without treatment.

### 2.3 Agriculture and irrigation

The agriculture in the Yanqi basin started in the fifties with the construction of irrigation channels. Nowadays, the irrigated area covers about  $1.2 \cdot 10^5$  ha and the irrigation channels having reached a length of over 480 km. Agricultural products include grapes, cotton and chili. A picture taken within the irrigated areas is presented in figure 2.10. Agriculture is entirely based on the water drawn from the Kaidu river. The distribution system of irrigation water is inefficient; a large amount of water is wasted through inadequate supply systems and owing to irrigation practices. Intensive irrigation and the absence of an efficient drainage system have caused a considerable rise of the groundwater table. In the lower regions of the basin, the groundwater table has reached a steady state at a level as close as 1 m below surface. Consequently, the degree of soil salinization is very high. An example of an abandoned field is shown in figure 2.11.

Figure 2.12 plots the development of the irrigated area as well as the water diverted. The development of the irrigated area mirrors some major political movements in China. During Mao's so called "Great Leap Forward" from 1957-1960,

which finally resulted in mass starvation, the existing irrigation area was expanded rapidly. The next unfortunate political movement, the "Cultural Revolution", which started in 1966, lasted for 10 years. Millions of people were sent for re-education through labour to the countryside, and the population of the Yanqi basin doubled within 2 years. During this period, the irrigation- and drainage net was expanded and production in the existing areas was intensified. The amount of arable land, however, did not increase significantly. Since the cultural revolution, the irrigated area has increased continuously. The efficiency of the irrigation has significantly improved. For the period between 1957 and 1967, an annual average of 2 m<sup>3</sup> water per square meter soil was used. In the period between 1995 until present, only 1 m<sup>3</sup> water per square meter soil and year has been applied.

In the Yanqi basin, flood irrigation is the most common practice. Its mechanical simplicity and low energy costs (compared to pressurized systems) are the big advantages compared to more sophisticated systems. Despite its simplicity, flood irrigation causes a lot of problems. Leaching water is applied excessively. In most of the area, the infiltration rate of the soil is small and the applied excess irrigation water collects at the surface. The efficiency of flood irrigation over uneven fields is low and a lot of water is wasted. Dong Xinguang estimated that around 20% of the irrigation water is evaporated during irrigation. Some drip irrigation systems have been installed in the Yanqi basin, and their results have been promising so far. However, compared to the area irrigated by flood irrigation, the area equipped with drip irrigation is small.



*Figure 2.6: The upper image was taken close to the pumping station at the dam (July 2003). The dunes directly behind the lake are clearly visible. The photo below was taken within in the little lake system.*



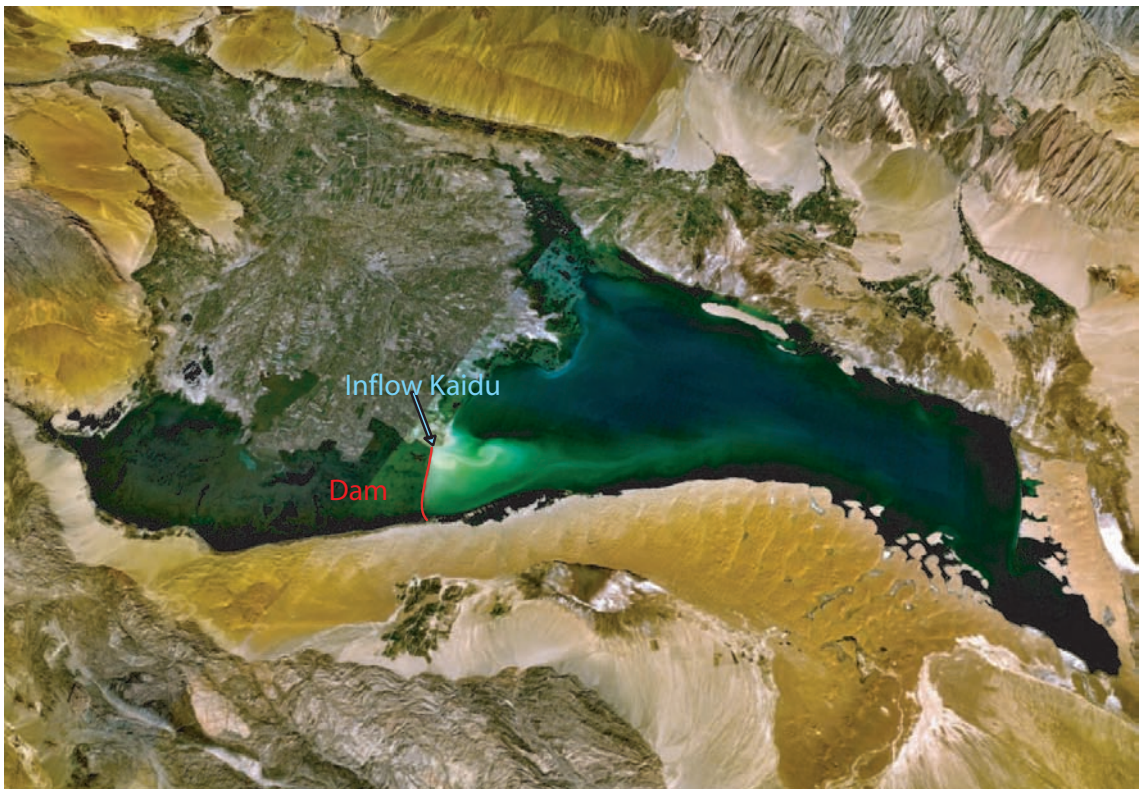


*Figure 2.7: View of Bostan lake from south to north. The inflow of the Kaidu river as well as the dam separating the little lake from the open water surface is clearly visible (image produced by using the software Worldwind 1.3 by NASA).*

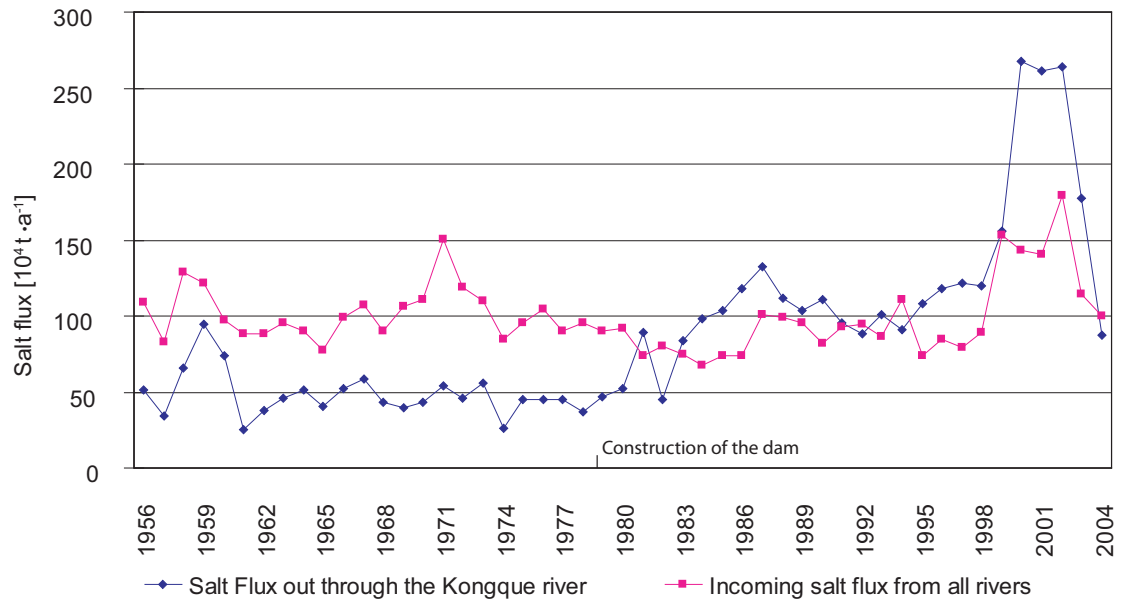


Figure 2.8: Total of the in- and outgoing salt fluxes [ $10^4 t \cdot a^{-1}$ ] in the Yanqi basin.

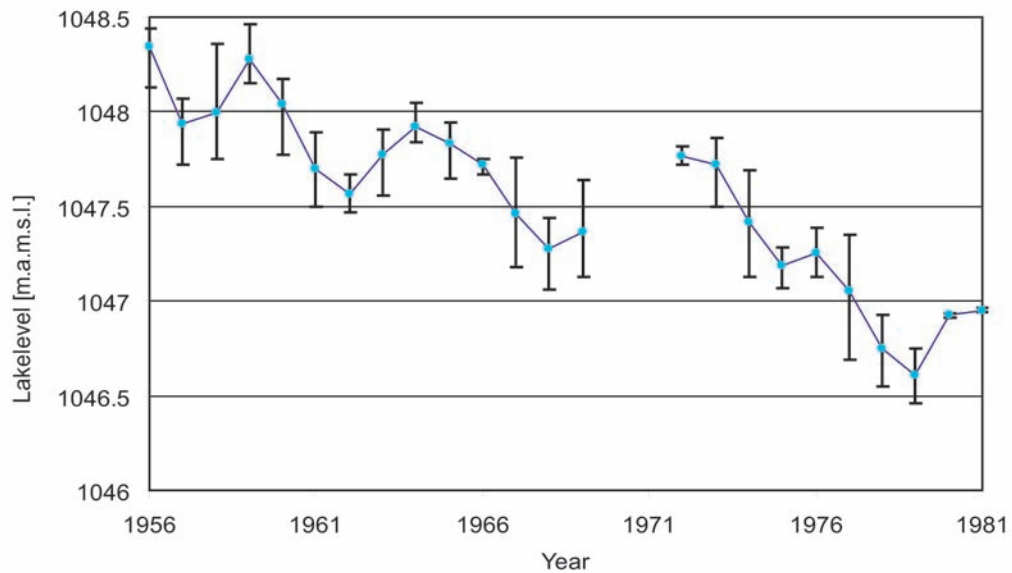
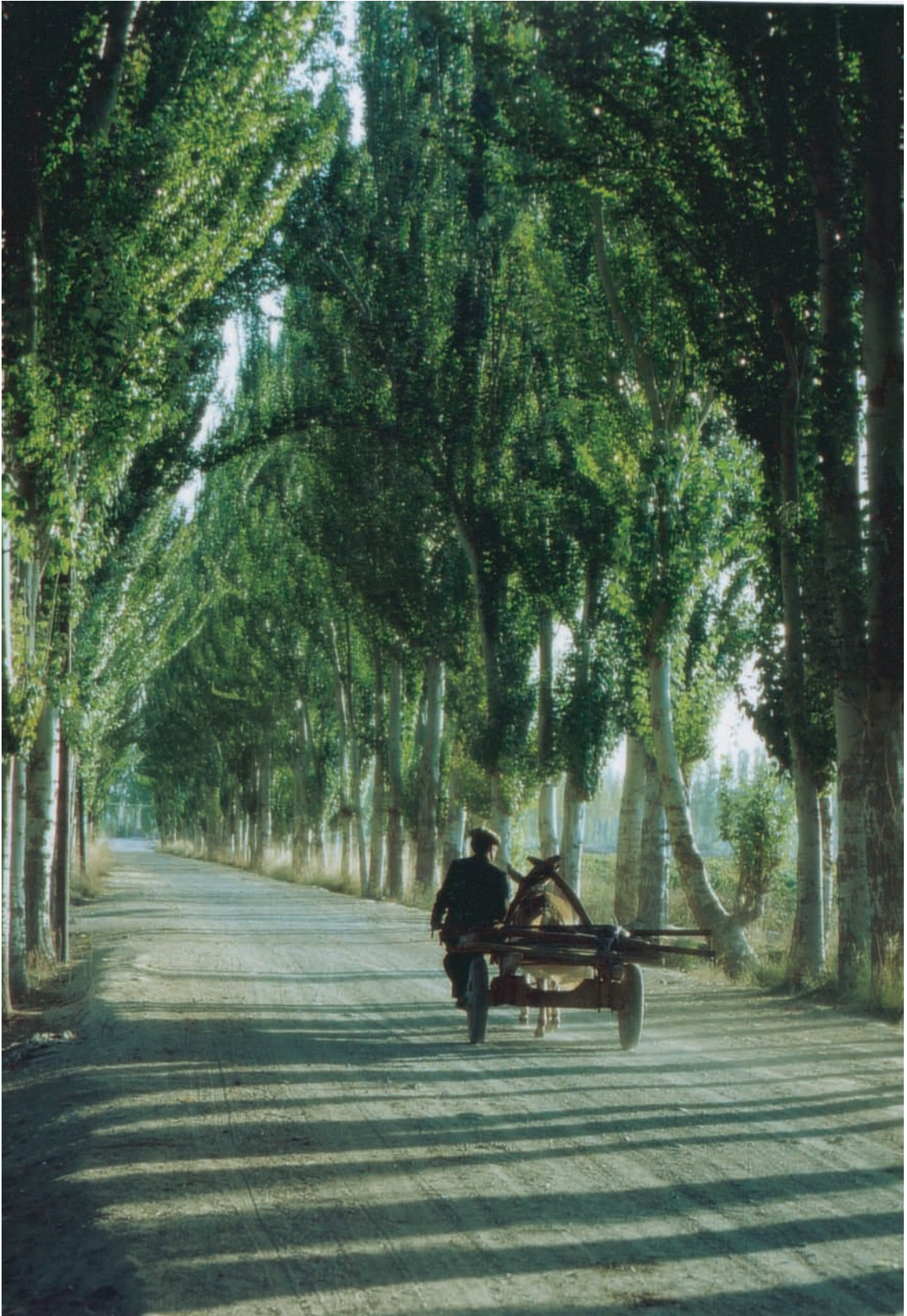


Figure 2.9: Average water level of Bostan lake- the annual variations are plotted as error bars.





*Figure 2.10: Impression of the irrigated area in the Yanqi basin. In this specific area, trees are planted for protection against wind erosion.*





*Figure 2.11: Example of a field that was given up as a consequence of the high salinity.*

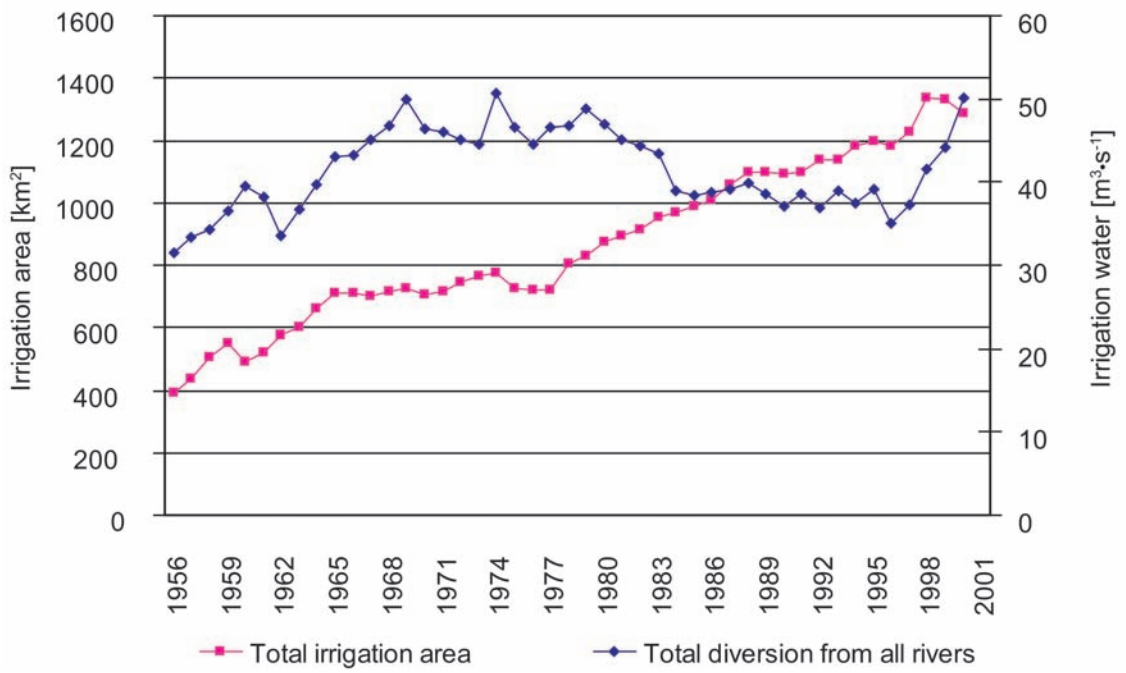


Figure 2.12: Total amount of irrigated area and annual amount of irrigation water drawn from the Kaidu, Wulasitai, Qingshui He and Huangshui Gou.



## Chapter 3

### Comparing Different Basins with Secondary Salinization

On the basis of the key data the water and salt balances are established for three different regions. All regions suffer from irrigation induced salinization. Based on the comparison of these three different basins, a unified conceptual framework to define and deal with the sustainability issue is formulated. The areas compared are Rechna Doab in Pakistan, the Liuyuan Kou irrigation system (LIS) in Henan province of China and the Yanqi basin. The locations of these areas are presented in figure 3.1.

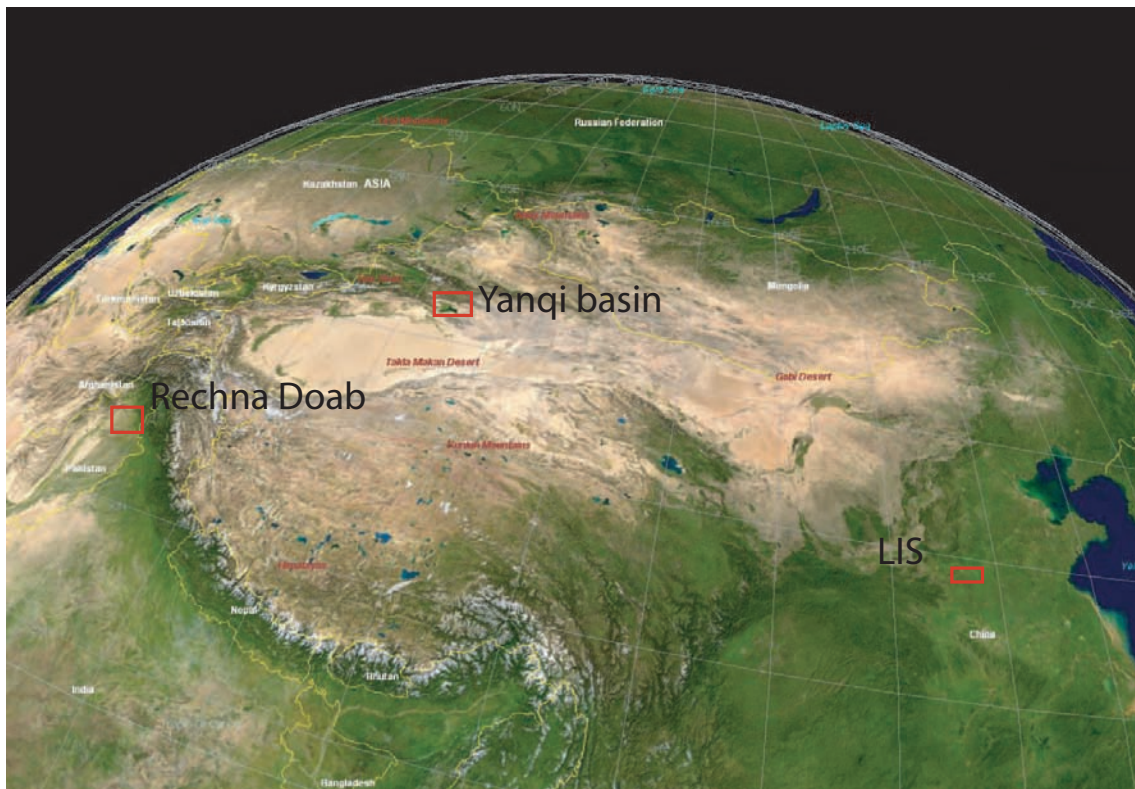


Figure 3.1: Locations of the three irrigation areas considered in the box modelling approach.

### 3.1 General Overview

Sustainable agriculture can be viewed from several perspectives (e.g. El Bassam (1998)). Farmers, for example, worry about the sustainability of their income and the quality of their soil and local resources, politicians view sustainable agriculture

as the ability to maintain food security and self sufficiency. Biologists may emphasize that sustainable agriculture takes the diversity of the genetic resources into account. A common, overall concept of sustainability was defined by Brundtland: "Meeting the needs of the present generation without compromising the ability of future generations to meet their needs" (World Commission on Environment and Development, 1987). General definitions such as the Brundtland definition can be useful as a framework for sustainable practices, but if management decisions have to be made concerning specific problems, such a general formulation doesn't actually help. The Brundtland definition does not include a spatial system boundary. A spatial boundary is crucial: A small, irrigated area can be managed indefinitely in a sustainable way, given sufficient water. Flushing all accumulated salt out of the root zone by over-irrigation will allow to maintain production within this irrigation area, but the downstream water quality and quantity for both agriculture and ecology will be reduced.

### 3.1.1 Brief description of the project areas

The three areas under consideration are located in semi-arid regions. The Yanqi basin has been described in chapter 1.1. The LIS receives a considerable amount of rain, but it is clearly below potential evapotranspiration. The major crops are maize, rice and cotton. The LIS has been operational since 1967. Eight branch channels were constructed between 1984-1988. During recent years, irrigation conditions have become more efficient, due to the improvement and maintenance of the hydraulic structures. Supplementary irrigation demand for crop production is met by water drawn from the channels as well as by groundwater pumping. Although a drainage system exists, the groundwater table has risen remarkably. In the northern part of the LIS the groundwater tables are very shallow (within 1 m from the land surface). The lateral outflow of the aquifer is very small compared to the total inflow of water (within the considered spatial boundaries of the system). A significant amount of the irrigation water leaves the LIS through phreatic evaporation and crop transpiration. An overview of the average annual water fluxes for the shallow aquifer is given in figure 3.2. The data was made available in 2002 by Shahbaz Khan, CSIRO Land & Water Griffith Laboratory, Australia (unpublished data).

Rechna Doab ("Land between two rivers") is the interfluvial sedimentary basin of the Chenab and Ravi rivers in Pakistan. It is one of the oldest, agriculturally richest and most densely populated irrigated areas of Punjab province. Irrigation water is pumped from the aquifer and drawn from the rivers. The gross area of Rechna Doab is 2.97 million ha, with a longitudinal extent of 403 km and a maximum width of 113 km. Around 2.3 million ha are prime cultivated land. The area is located in the rice-wheat and sugar cane-wheat agro climatic zones of Punjab province, with rice, cotton and forage crops dominating in summer, wheat and forage in winter. In some parts, sugar cane is also cultivated as an annual crop. In the upper part of Rechna Doab a significant amount of surface water is used for irrigation.

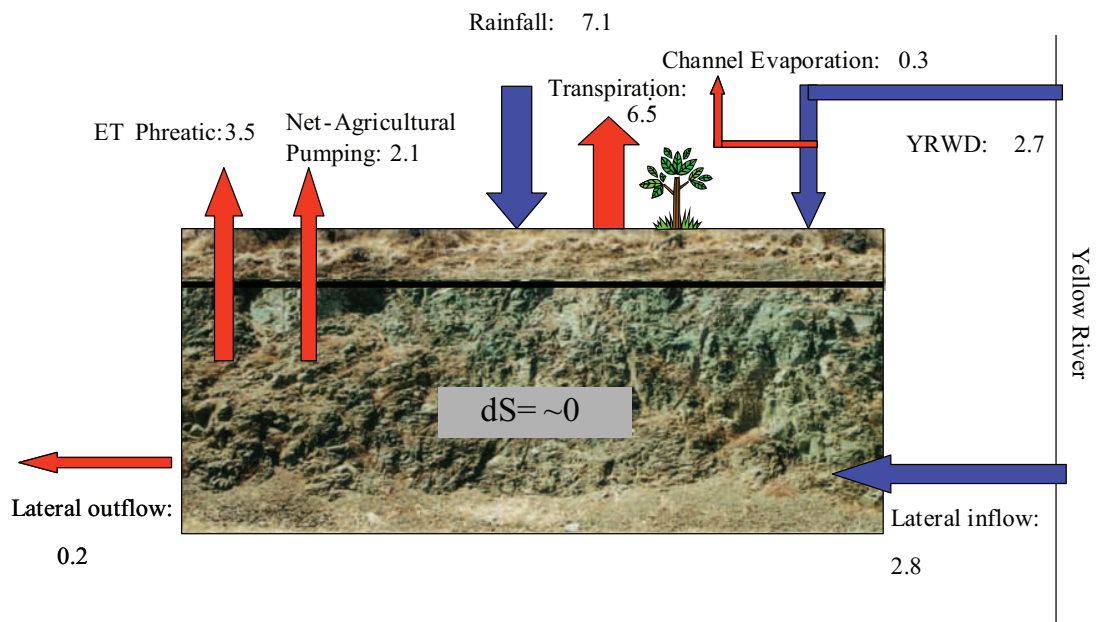


Figure 3.2: Annual, average water balance  $[m^3 \cdot s^{-1}]$  for the LIS (period 1981-2001).

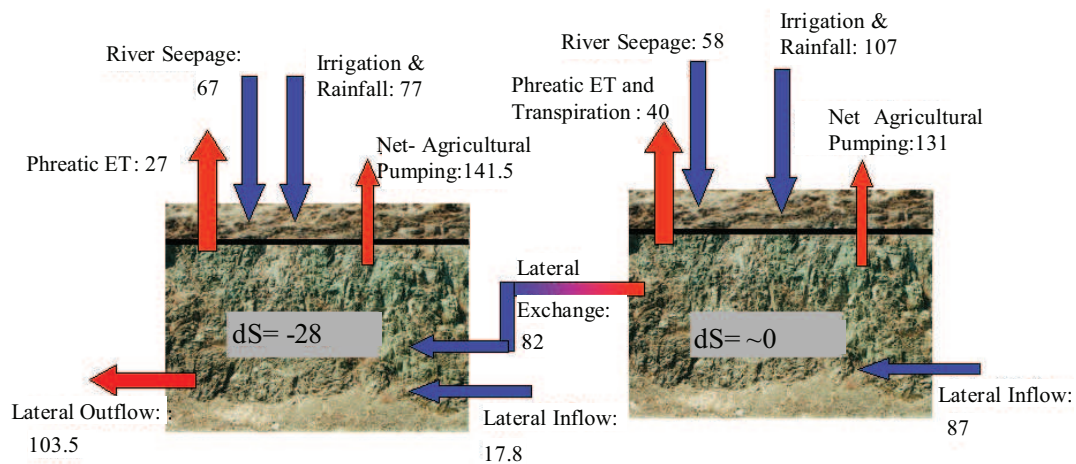


Figure 3.3: Crude water balance (1993-2000) of the upper (right part of the image) and lower zones of Rechna Doab  $[m^3 \cdot s^{-1}]$ .  $dS$  is the residual between incoming and outgoing water fluxes.

Relatively low volumes of surface water supplies are available in the lower part of Rechna Doab, therefore the crop demand is met to a larger extent by groundwater pumping. The declining groundwater tables in the lower part of Rechna Doab cause reduced economic gains, as the pumping costs for groundwater increase with falling groundwater levels. In contrast to the upper Rechna Doab, there is no phreatic evapotranspiration downstream. However, salinity becomes a bigger problem in the lower Rechna Doab, due to lower quality of the groundwater used for irrigation and

## Comparing Different Basins with Secondary Salinization

increased salt concentration of leached water below the root zone of crops. Larger scale drawdown in the lower part of Rechna Doab also promotes lateral flow of saline groundwater from the central part of Rechna Doab. The annual average water balance for Rechna Doab is presented in figure 3.3. The data as well as other relevant information have again been provided by Shahbaz Khan.

The water balance demonstrates that in the upper zones of Rechna Doab the groundwater table is stable, whereas in the lower part the water table is declining.

### 3.1.2 Some general thoughts on salinity

To understand the mechanism of salinization of soil and water resources, it can be helpful to apply the concept of a simple one-box model to an irrigation area. Consider an irrigation area simplified by the following parameters and processes summarized in a box model, compare figure 3.4:

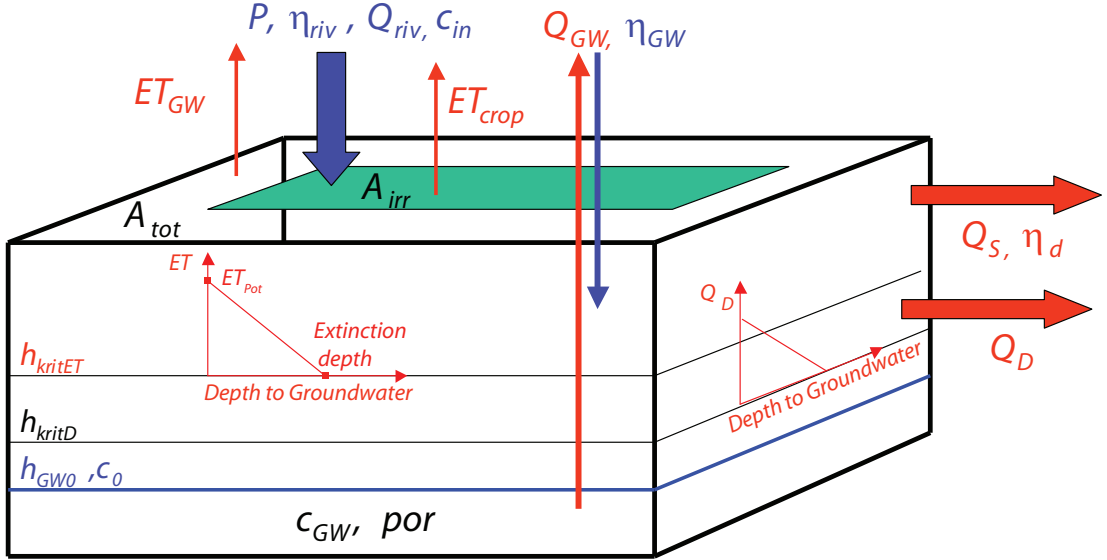


Figure 3.4: Schematic concept of irrigation area with the most basic processes considered.

The extent of the area considered is defined as ( $A_{tot}$ ). It consists both of irrigated sites ( $A_{irr}$ ) and non-irrigated areas. The aquifer is assumed to be homogeneous. The porosity of the material is defined as  $por$ . Before irrigation takes place, the groundwater table is at  $h_{GW0}$ . The concentration of dissolved salts is  $c_0$ . The amount of river water drawn for irrigation purposes and diverted through a channel system to the fields is defined as  $Q_{riv}$ . The amount of precipitation is defined as  $P$ .  $c_{in}$  is the concentration of salt in the irrigation water applied. No other sources of salt are taken into account.  $\eta_{riv}$  is, in this context, defined as the efficiency of the irrigation system:

$$\eta_{riv} = \frac{Q_{riv} - Q_{loss}}{Q_{riv}} \quad (3.1)$$

$Q_{loss}$  equals the amount of water evaporated per time unit on its way from the river to the fields, as well as unproductive evaporation on the field after irrigation.  $\eta_{riv}$  should not be confused with the efficiency of an irrigation system indicating e.g. the ratio of water lost through percolation in the channels and the amount of water reaching the field. Another source of irrigation water is groundwater pumped from the aquifer.  $Q_{GW}$  and  $\eta_{GW}$  are defined in the same way as  $Q_{riv}$  and  $\eta_{riv}$ .  $Q_{GW}$  is the amount of water pumped and applied to irrigation.  $\eta_{GW}$  is the portion of  $Q_{GW}$  that does not evaporate directly after irrigation on the fields. Evapotranspiration is the sum of evaporation  $ET_{GW}$  and transpiration  $ET_{crop}$ . Independent of the depth to groundwater, the cultivated crop transpires water at the rate  $ET_{crop}$ . Direct evaporation from the aquifer  $ET_{GW}$  occurs whenever the groundwater table is above the extinction depth  $h_{kritET}$ . Between this extinction depth and the soil surface a linear rate of phreatic evaporation is assumed, as indicated in figure 3.4. Alternatively, an exponential function or a stepwise linear function between the terrain elevation and the critical height  $h_{kritET}$  can be applied. If no vegetation is present, the highest possible phreatic evaporation rate equals the potential evapotranspiration. This potential rate is reached as soon as the depth to groundwater is zero. If a portion of the energy available has been consumed by crops, the potential phreatic evaporation is reduced by the transpiration rate of the crops. The surface drainage, e.g. an installed system of drainage channels or pipes, reduces infiltration underneath the irrigated area by the factor  $(1-\eta_d)$ .  $\eta_d$  is the efficiency of the drainage system. If  $\eta_d$  is 1, all infiltrating water is removed from the system and recharge in the irrigated areas is therefore 0. The infiltration rate  $Q_{inf}$  into the aquifer is given by:

$$Q_{inf} = (1-\eta_d) \cdot (P \cdot A_{irr} + \eta_{GW} \cdot Q_{GW} + \eta_{riv} \cdot Q_{riv} - ET_{crop} \cdot A_{irr}) + P \cdot (A_{tot} - A_{irr}) \quad (3.2)$$

The amount of water removed by the surface drainage  $Q_S$  is given by

$$Q_S = \eta_d \cdot (P \cdot A_{irr} + \eta_{GW} \cdot Q_{GW} + \eta_{riv} \cdot Q_{riv} - ET_{crop} \cdot A_{irr}) \quad (3.3)$$

The infiltrating water will raise the groundwater table. This change can be calculated and is described in paragraph (1). If the groundwater table is above the elevation of the downstream system  $h_{kritD}$ , a portion of water will flow to this system. As soon as the groundwater table is above  $h_{kritD}$ , this additional sink term has to be taken into account, see paragraph (2). As long as the system has not reached steady state, the groundwater table will continue to rise. If the groundwater table is above a critical elevation  $h_{kritET}$ , phreatic evaporation must be considered. In paragraph (3), the change of the groundwater table as a function of time is calculated by taking this additional flux into account. In the following, it is assumed that  $h_{kritD}$  is larger than  $h_{kritET}$ . If this assumption is not fulfilled, the equations discussed in the next paragraph need to be slightly modified: groundwater evaporation has to be taken into account before exfiltration starts.

- (1)  $h < h_{kritD}$ : Mathematically, the change of height of the groundwater table  $h$  is described by the following equation:



## Comparing Different Basins with Secondary Salinization

---

$$\frac{dh}{dt} = \frac{(1 - \eta_d)(P \cdot A_{irr} + \eta_{GW} \cdot Q_{GW} + \eta_{riv} \cdot Q_{riv} - ET_{crop} \cdot A_{irr})}{A_{tot} \cdot por} + \frac{P \cdot (A_{tot} - A_{irr}) - Q_{GW}}{A_{tot} \cdot por} \quad (3.4)$$

with  $h(0) = h_0$

The straightforward solution to equation 3.4 is:

$$h(t) = h_0 + t \cdot \left( \frac{P \cdot (A_{tot} - \eta_d \cdot A_{irr}) + Q_{GW} \cdot (\eta_{GW} - \eta_{GW} \cdot \eta_d - 1)}{A_{tot} \cdot por} + \frac{Q_{riv} \cdot (\eta_{riv} - \eta_{riv} \cdot \eta_d) + ET_{crop} \cdot (A_{irr} \cdot \eta_d - A_{irr})}{A_{tot} \cdot por} \right) \quad (3.5)$$

- (2)  $h_{kritD} < h < h_{kritET}$ : The second drainage process is a direct exfiltration  $Q_D$  from groundwater into a downstream system. If the groundwater table is above the critical height  $h_{kritD}$ , exfiltration into a downstream system starts with a flux calculated as the difference between the groundwater table and the critical depth  $h_{kritD}$ , and simply multiplied by a factor  $\alpha$ :

$$Q_D = \alpha \cdot (h(t) - h_{kritD}) \quad (3.6)$$

Until  $h_{kritET}$  is reached, equation 3.4 must be expanded by a subsurface drainage rate:

$$\frac{dh}{dt} = \frac{(1 - \eta_d) \cdot (P \cdot A_{irr} + \eta_{GW} \cdot Q_{GW} + \eta_{riv} \cdot Q_{riv} - ET_{crop} \cdot A_{irr})}{A_{tot} \cdot por} + \frac{P \cdot (A_{tot} - A_{irr}) - Q_{GW} - \alpha \cdot (h(t) - h_{kritD})}{A_{tot} \cdot por} \quad (3.7)$$

with  $h(0) = h_{kritD}$

The solution has the following structure:

$$h(t) = h_{kritD} + C_1 \cdot \left( 1 - e^{-\frac{t \cdot \alpha}{A_{tot} \cdot por}} \right)$$

$$C_1 = \frac{P \cdot (A_{tot} - \eta_d \cdot A_{irr}) + Q_{GW} \cdot (\eta_{GW} - \eta_{GW} \cdot \eta_d - 1)}{\alpha} + \frac{Q_{riv} \cdot (\eta_{riv} - \eta_{riv} \cdot \eta_d) + ET_{crop} \cdot (A_{irr} \cdot \eta_d - A_{irr})}{\alpha} \quad (3.8)$$

$C_1$  is the difference between the steady state head  $h$  and  $h_{kritD}$ .

- (3)  $h_{kritD} < h_{kritET} < h$ : If  $h_{kritET}$  is reached, or, expressed in mathematical terms  $h_{kritD} + C_1 > h_{kritET}$ , equation 3.7 must be expanded by adding phreatic evaporation.  $E_{pot}$  defines the maximum evapotranspiration. Hence the maximum phreatic evaporation is reduced by  $ET_{crop}$  over the irrigated area. Consequently, equation 3.7 must be expanded by two terms, one relating to irrigated areas and one to non-irrigated areas:

$$\begin{aligned} \frac{dh}{dt} = & \frac{(1 - \eta_D)(P \cdot A_{irr} + \eta_{GW} \cdot Q_{GW} + \eta_{riv} \cdot Q_{riv} - ET_{crop}) - \alpha \cdot (h(t) - h_{kritD})}{A_{tot} \cdot por} \\ & + \frac{-(A_{tot} - A_{irr}) \cdot (E_{pot} - \frac{h(t) \cdot E_{pot}}{h_{kritET}}) + A_{irr} \cdot (E_{pot} - ET_{crop} - \frac{h(t) \cdot (E_{pot} - ET_{crop})}{h_{kritET}})}{A_{tot} \cdot por} \\ & - \frac{P \cdot (A_{tot} - A_{irr}) - Q_{GW}}{A_{tot} \cdot por} \end{aligned} \quad (3.9)$$

with  $h(0) = h_{kritET}$  The solution of equation 3.9 is as follows:

$$\begin{aligned} h(t) = & \left( e^{\frac{t \cdot (-\alpha \cdot h_{kritET} + E_{pot} \cdot A_{tot} - ET_{crop} \cdot A_{irr})}{por \cdot A_{tot} \cdot h_{kritET}}} \cdot \frac{C_2 + \alpha \cdot h_{kritET} + ET_{crop} \cdot A_{irr}}{-E_{pot} \cdot A_{tot} + \alpha \cdot h_{kritET} + ET_{crop} \cdot A_{irr}} \right. \\ & \left. + \frac{-C_2 - A_{tot} \cdot E_{pot}}{ET_{crop} \cdot A_{irr} - E_{pot} \cdot A_{tot} + \alpha \cdot h_{kritET}} \right) \cdot h_{kritET}, \\ C_2 = & P \cdot (\eta_D \cdot A_{irr} - A_{tot}) + Q_{riv} \cdot (\eta_{riv} \cdot \eta_D - \eta_{riv}) - ET_{crop} \cdot A_{irr} \cdot \eta_D - \alpha \cdot h_{kritD} \\ & + Q_{GW} \cdot (1 - \eta_{GW} + \eta_{GW} \cdot \eta_D) \end{aligned} \quad (3.10)$$

In equation 3.9, it is assumed that the evaporation function is linear between the depth to groundwater and the phreatic evaporation. For the Yanqi basin, this relationship has been quantified by using stable isotopes. The function applied for the Yanqi basin is described in chapter 6, section 6.3.

Similarly to the water balance, a salt balance can be set up in order to calculate the development of the concentration of salt in the groundwater. It is assumed that the box is well mixed, so the concentration of salt in the outgoing fluxes equals the concentration in the box:

$$\frac{dM}{dt} = \eta_D \cdot (Q_{inf} \cdot c_{in}(M)) - \alpha \cdot (h(t) - h_{kritd}) \cdot \frac{M}{h(t) \cdot A_{tot} \cdot por} \quad (3.11)$$

The concentration of the infiltrating water is dependent on the salt concentration in the groundwater, as a portion of groundwater is applied for irrigation. Several systems exist in which the major source of salt is the aquifer itself. In the Yanqi basin as well as in the LIS, geogenic salt is present. The infiltrating water dissolves these salts. This can be taken into account by increasing the initial concentration in equation 3.11.

## Comparing Different Basins with Secondary Salinization

Equation 3.11 is complicated, and as no analytical solution exists it has to be solved numerically. Still, the steady-state concentration can easily be calculated. The constraint for a steady state salt concentration in the aquifer is, that the input salt flux equals the output flux while a steady state of groundwater flow is also reached.

$$c_{ss} = \frac{(1 - \eta_D) \cdot Q_{inf} \cdot c_{inf}}{\alpha \cdot (h_{SS} - h_{kritD}) + Q_{GW}} \quad (3.12)$$

Equation 3.12 is valid for both  $h_{ss} > h_{kritD}$  and for  $h_{ss} > h_{kritD}, h_{kritET}$ . For every steady state of groundwater flow a corresponding steady state in the salt concentration is reached (if the outflow is larger than 0). Together with equation 3.10 ( $t = \infty$ ) and equation 3.12, the steady state salt concentration can be calculated for  $h > h_{kritET}$ . Figure 3.5 demonstrates the steady state groundwater table and the steady state salt concentration as functions of  $Q$  for the Yanqi basin.  $Q$  is the amount of irrigation water applied.

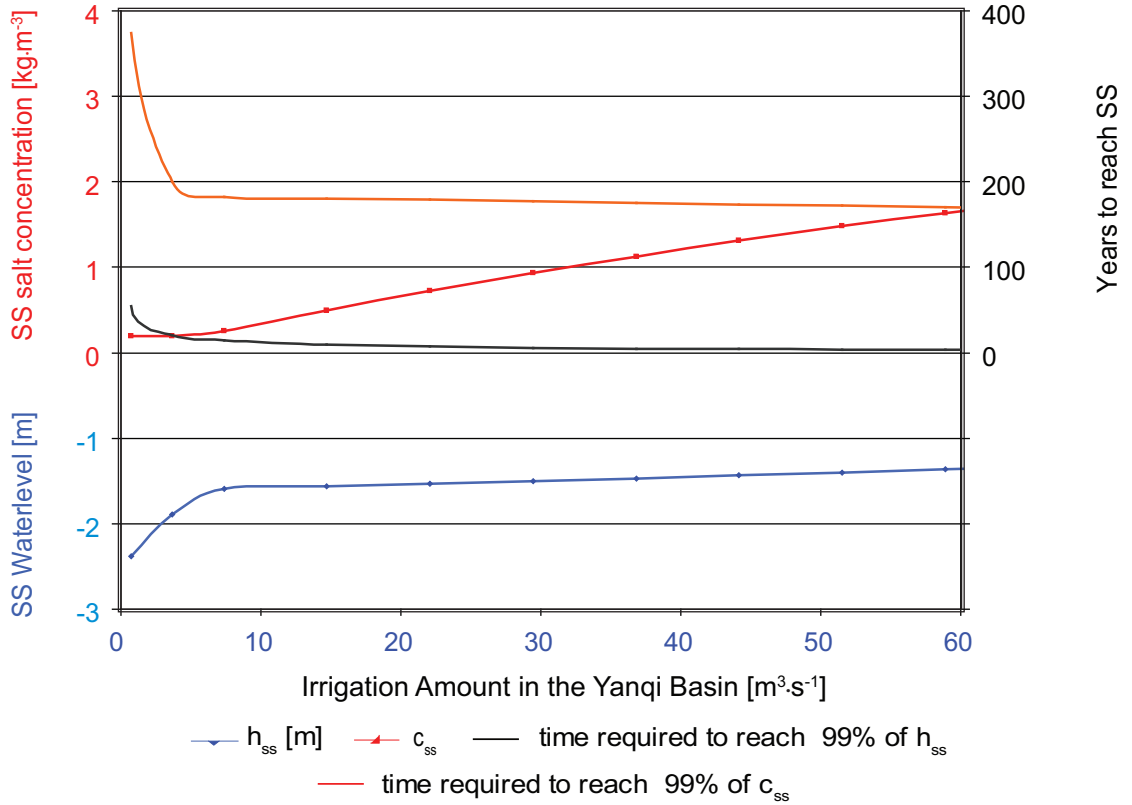


Figure 3.5: Steady state (SS) groundwater table  $h_{ss}$  [m] and steady state salt concentration  $c_{ss}$  [ $kg \cdot m^{-3}$ ] as functions of the irrigation amount in the Yanqi basin [ $m^3 \cdot a^{-1}$ ]. Furthermore, the time  $t$  [a] to reach 99% of steady state for both the groundwater table and the salt concentration is also plotted as a function of the irrigation amount.

Until  $h_{kritET}$  is reached, there is no change in the steady state concentration.



The reason for this is that the irrigation intensity has been held constant for the calculation of figure 3.5. The increasing values of  $Q$  are due to the increase of the irrigated area.

A different relation between  $h_{ss}$  and  $c_{ss}$  is found if the varying steady state groundwater tables in figure 3.4 are calculated by changing the intensity of irrigation instead of the irrigated area: until  $h_{kritET}$  is reached,  $c_{ss}$  declines. No matter whether the irrigated area or the intensity is changed, as soon as  $h_{kritET}$  is exceeded, phreatic evaporation increases to a much larger extent than the subsurface drainage. In the following, a system with  $h_{ss} > h_{kritET}$  is termed evaporation controlled system. In steady state a system will be evaporation controlled if the following constraint is fulfilled:

$$\alpha \cdot (h_{kritET} - h_{kritD}) - Q_{inf} < 0 \quad (3.13)$$

Independent of the amount of irrigation water applied, the groundwater table reaches its steady state much faster than the salt concentration. After  $h_{kritET}$  in the Yanqi basin is exceeded, the time required to reach 99% of the steady state salt concentration is around 300 years, the groundwater steady state is already reached after 20 years. If the outflow of a system is very small, as in the LIS, it can take a much longer time until a steady state of salt is reached. The resulting steady state concentration will be extremely high. This is demonstrated in figure 3.6 with data from the LIS. A steady groundwater table is reached very quickly after  $h_{kritET}$  is exceeded. Even though a portion of the irrigation water requirement is substituted by pumped groundwater and the distribution of irrigation water is efficient and augmented by a significant amount of rainfall, the salt concentration in the aquifer water will reach a higher level.

Systems with a very small  $\alpha$  will be evaporation controlled shortly after major irrigation takes place, unless the infiltration rate ( $Q_{inf}$ ) is kept small.  $Q_{inf}$  can only be kept small if the efficiency of the irrigation system and the installed drainage system are extremely high. These constraints can only be satisfied with major investments into the hydraulic structures. Irrigated areas similar to the LIS, which have a steady state salt concentration far beyond the critical concentration which allows plant growth, can only stay productive if the groundwater table is below  $h_{kritET}$ .

### 3.1.3 Limitations and conclusions of the box approach

Major simplifying assumptions have been made for describing an irrigation area with only one box. If management decisions have to be made, a more sophisticated technique such as a spatially distributed groundwater model should be applied. The box models for the Yanqi basin and the LIS have been set up in order to examine the water and the salt balances, and to put their behavior qualitatively into the context of sustainability. The most important simplifications and assumptions of the single box model are mentioned below. In reality, the depth to groundwater will not be evenly distributed over the project area. Depending on the topography, land

## Comparing Different Basins with Secondary Salinization

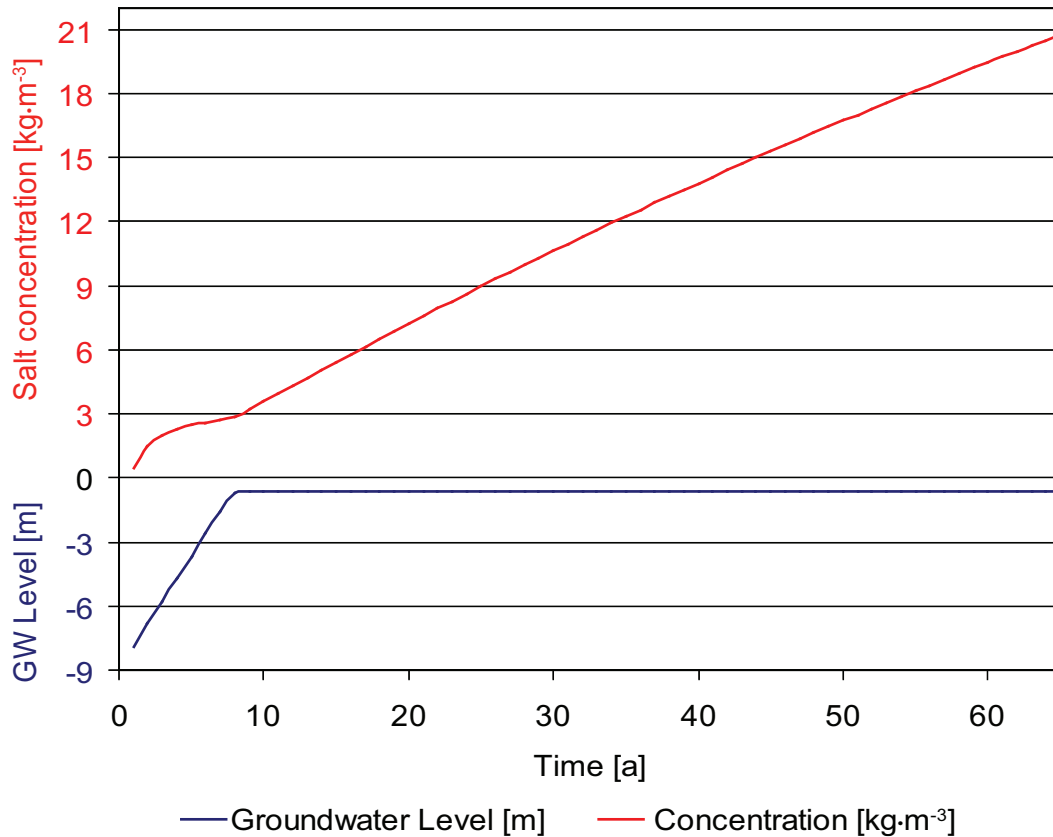


Figure 3.6: Steady state groundwater table  $h_{ss}$  [m] and steady state salt concentration  $c_{ss}$  [ $\text{kg}\cdot\text{m}^{-3}$ ] as functions of time in the LIS.

use and the hydrological parameters such as porosity or transmissivity, the depth to groundwater will be above or below  $h_{kritET}$ . Furthermore, some temporal effects have not been taken into account. It is assumed that the transition from irrigation water to groundwater recharge happens without any retardation. Moreover, seasonal variation of the irrigation intensity has not been taken into account. Neglecting this temporal effect leads to an underestimation of the highest possible concentration of salt in the unsaturated zone: while the soil is drying out between irrigation cycles, the salt concentration increases. The assumption of the well-mixed box is another simplification. In reality, there is no uniform distribution of the concentration in the aquifer and the unsaturated zone. Despite the simplifications made in the box model approach, it demonstrates that steady states for groundwater flow as well as salt concentration exist. Depending on how water in steady state is exported from the system, reaching a steady state salt concentration can take a very long time compared to reaching a steady state groundwater flow. The input salt concentration, together with the ratio of lateral outflow to groundwater recharge, directly determine the steady state concentration. Furthermore, the box approach shows that, due to

direct evaporation from the water table, the rate of accumulation of salts increases rapidly as soon as  $h_{kritET}$  is reached. If irrigation water is drawn from a river, the downstream system only receives a reduced salt freight until the steady state is reached. As a last conclusion, the amount of water available downstream is evidently reduced by the difference between the water used for irrigation and the lateral outflow.

### 3.2 System boundaries in relation to water and salt balances

A system such as the Yanqi basin with sufficient surface water availability can stay productive, even if irrigation water is wasted and the groundwater table has already reached a critical level. One could argue that the applied irrigation techniques and efficiencies in the Yanqi basin are sustainable because production has stabilized on a level which is still profitable. This of course cannot be called sustainable, because only the needs of the farmers in this particular irrigation system are satisfied. The reduced amount of available surface water as well as the increased salt concentration endanger the downstream ecosystems and worsen the economic situation for the Green Corridor.

A different situation is found in the LIS. The lateral outflow of the system is so small that for a very long time the system will accumulate salt without reaching steady state. All the salt imported by river irrigation is accumulating in the LIS. After a few years of irrigation, long before steady state conditions are reached, the concentration of dissolved salts in the groundwater will have risen to a level that no longer allows a productive agriculture. The salt concentration will not increase in the downstream of the Yellow river, but the downstream irrigation systems receive a reduced amount of water. For a reasonable system analysis the system boundary should, as in the Yanqi basin, exceed the LIS.

In Rechna Doab, two different conditions are present. In the upper part a situation similar to the Yanqi basin is found: high groundwater tables, an inefficient water distribution system and inefficient surface drainage. Production is still profitable as sufficient surface water is available. Agriculture in the lower part is getting more and more unprofitable as the pumping costs for groundwater have to be covered. With salt intrusion from the saline aquifer nearby, productivity is at risk even though the available resources are used in an economical way. For both the Yanqi basin and the upper part of Rechna Doab, the system boundary has to be expanded beyond the actual irrigation district. Before irrigation took place, the river transported the major portion of its salt freight to a final sink downstream. In the case of the Yanqi basin, the final sink was Lop Nor, in Rechna Doab the river discharges into the sea. Irrigation moves the final deposit of salt towards the irrigated areas upstream. Hence only a system boundary from the first irrigated plot to the final sink of the river is appropriate for a holistic approach to sustainability. The same conclusion is drawn for the LIS. Although the downstream situation is not worsened by an increased mineralization, the reduced flow will limit downstream production.

As important as the spatial boundary is the temporal one. Sustainable agriculture should guarantee that the system considered will remain productive "forever". This of course means that the system should reach a steady state at a level still allowing productive agriculture. Instead of fixing the temporal boundary to a certain time, it is more appropriate to consider the final state of the system.

### 3.3 Towards sustainable agriculture

A unified definition of sustainability must be applicable to all kinds of irrigation areas. As there are fundamentally different types of systems, we present our idea of sustainable agriculture in relation to salinity in the form of a flowchart rather than in the form of a "one sentence definition". The flowchart in figure 3.7 will be presented briefly and discussed in relation to the three areas considered.

The first step is to define an overall spatial system boundary. As emphasized above, the boundary should not be limited to the specific irrigation area considered. Basically, for irrigation systems based on river water we suggest to set the system boundary from the first irrigated plot to the next major tributary, or, if no tributary is present, to the final sink of the river. If irrigation water is pumped exclusively from an aquifer, the boundary should cover the catchment area of the pumping stations, as well as the discharge area of the drainage water. Within this large-scale boundary, subsystems should be defined. A classification into areas with a large and areas with a small lateral outflow is necessary. Systems with a small lateral outflow are at a high risk of becoming evaporation controlled, therefore different management options have to be considered. As a possible management option, the sacrifice of a subsystem with small lateral outflow should also be taken into account: concentrating accumulated salt by evaporating saline drainage water in this subsystem to prevent the diffusive distribution of salt over the irrigated areas may result in an overall higher productivity. Areas with different sources of irrigation water such as Rechna Doab should not be covered by one subsystem only. The available water resources for the downstream systems as well as their salt concentration are the result of the water management strategy applied.

The second step therefore consists in defining the minimum amount of water  $Q_{out,min}$  required for the downstream systems as well as the highest allowed concentration  $c_{out,max}$  of salt in this water. As soon as the available water resources for the downstream systems are below  $Q_{out,min}$ , or the concentration of salt above  $c_{out,max}$ , the management strategies for the subsystem should be reconsidered. The relations between irrigation intensity, irrigation water source, infiltration, steady state groundwater table and salt concentrations have to be investigated and quantified for the subsystem considered.

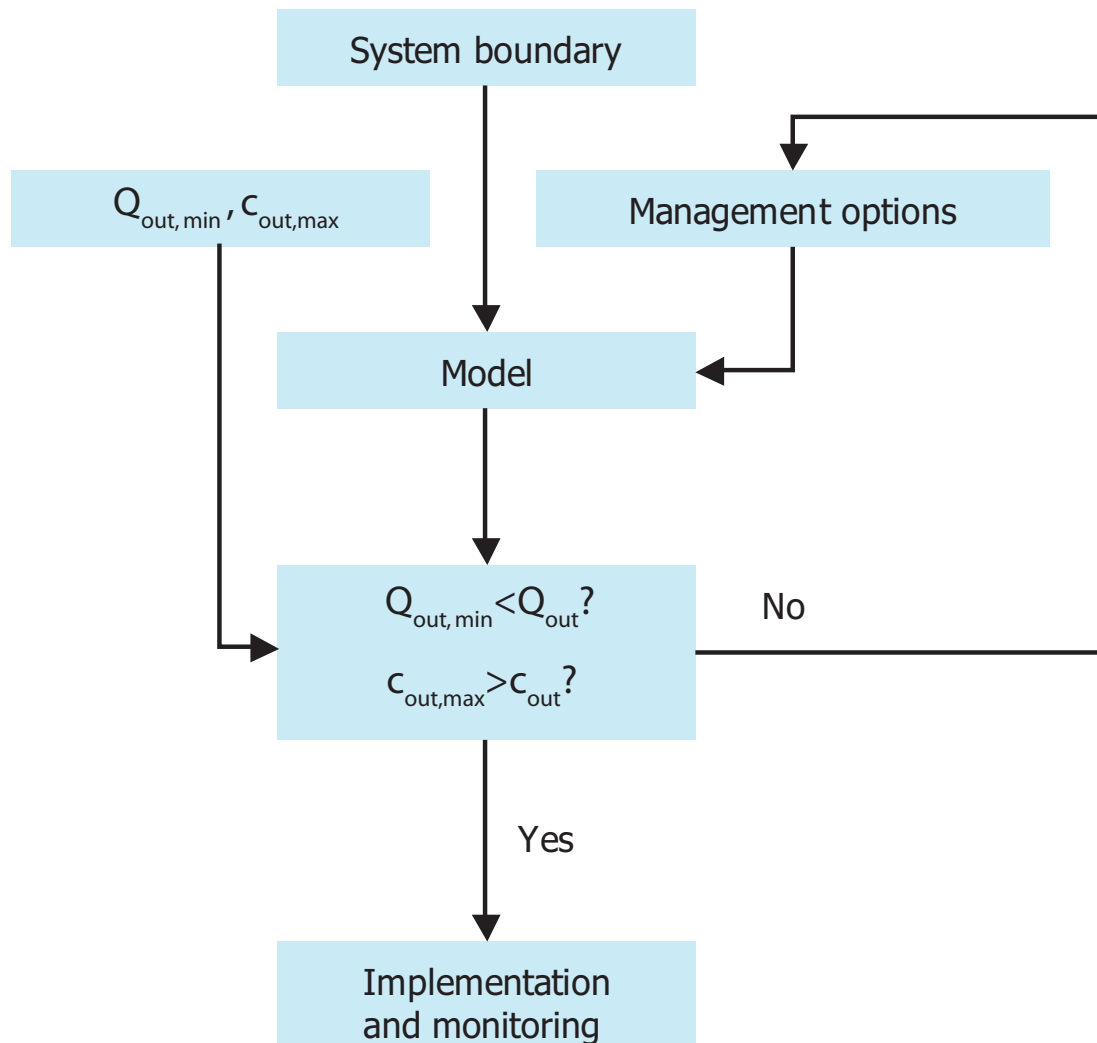


Figure 3.7: Suggestion for developing a sustainable water and salt management in irrigated areas.

### 3.4 Some suggestions for the areas considered

The large-scale system boundary of the Yanqi basin must include Bostan lake as well as the Green Corridor. The key to sustainable agriculture in the Yanqi basin and the downstream systems is keeping the groundwater table below  $h_{kritET}$ . If the irrigated area is not reduced, increasing the efficiency of irrigation techniques as well as substituting river water by groundwater can help to reduce phreatic evaporation. Pumping groundwater for irrigation lowers the groundwater table. An increase of the efficiency of the drainage net also has a positive influence on the groundwater table. However, the drainage water removed contains highly saline aquifer water and decreases the quality of the remaining water downstream. This problem does

## Comparing Different Basins with Secondary Salinization

---

not occur if the phreatic evaporation is reduced by pumping groundwater. In this case, the final sink of the salt is the aquifer itself.

Sustainable agriculture in an area with a small lateral outflow as in the LIS is challenging. The increasing salt concentration observed during the last years demonstrates that, although the hydraulic structures have been improved, their efficiency is not high enough. As long as the groundwater table is not lowered and the salt left behind from water evaporated by crops is flushed into the aquifer, the salt concentration will be increasing. Several selective measures must be applied: River water for irrigation purposes should be used as economically as possible. Reducing the amount of drawn river water will not only help to keep the groundwater table at a low level in the LIS itself, the downstream systems will profit from a higher surface water availability. Increased groundwater pumping can help in these tasks.

The conclusions for Rechna Doab are similar. The limited surface water availability downstream is a direct consequence of the wasteful use of water upstream. The upstream itself has got serious soil salinity problems, due to the high groundwater tables. The only way to address this problem is by lowering the groundwater table. As in the LIS and the Yanqi basin, this can only be achieved by the conjunctive and efficient use of ground- and surface water resources. Downstream irrigation systems can only profit from this measure, as reducing the wasting of water upstream provides more surface water for the downstream system.

The box model has shown that irrigation in the Yanqi basin can be carried out by using less surface water, reducing the danger of salinization and thereby increasing the available resources for the downstream systems. The analysis of the three areas compared in this chapter has shown that the definition of the system boundary is one of the most important parameters when it comes to analyzing a specific region. The system boundary has to include the downstream systems. Therefore, the availability of water resources for Bostan lake and the downstream systems have been considered together with the irrigation water requirements in the Yanqi basin throughout the project.

## Chapter 4

---

# Salinity Mapping

In this chapter, the use of multispectral remote sensing images to regionalize point values (field data) is described. Field data consist of measurements of electrical conductivity and are obtained by the combination of geophysical methods and the analysis of field soil samples. Uncalibrated salinity maps were calculated with spectral correlation mapping, using image based reference spectra of saline areas. As an alternative indicator for soil salinity, the NDVI was used. The method was verified in the Yanqi basin. Correlations between field data and the uncalibrated salinity maps were found over non-irrigated sites for all images. Good correlations ( $R^2$  up to 0.85) resulted for images collected during the winter months. The high correlation coefficients allow to scale the uncalibrated salinity maps to electrical conductivity maps.

### 4.1 Introduction

A recent review article (Metternicht & Zinck, 2003) discusses several salinity mapping methods and their possible constraints. As possible processing procedures of the raw remote sensing data, Metternicht and Zinck mention the Optimum Index Factor (Dwivedi & Rao, 1992), image transformations such as the principle component analysis and band ratios such as the NDVI (Wiegand *et al.*, 1994), intensity hue saturation transformations and unmixing of surface features. Moreover, a fuzzy classification based on JERS-1 SAR data is described. Including information such as geomorphic positions or different soil types into the spectral analysis may improve the results, as shown by Metternicht & Zinck (1997). Besides the processing procedures, several image data sources for mapping soil salinity are discussed: Various airborne and space borne sensors can be used, including sensors covering the visible to middle infrared (Csillag *et al.*, 1993; Rao *et al.*, 1995; Kalra & Joshi, 1996), thermal infrared (Mulders, 1987) and microwave sensors (Singh *et al.*, 1990; Taylor *et al.*, 1996). Airborne hyperspectral data are listed as one of the most promising sources of data to discriminate between different kinds of salt and soils. Examples of the use of hyperspectral imagery can be found in (Ben-Dor *et al.*, 2002; Taylor & Dehaan, 2000; Howari, 2003b; Howari *et al.*, 2002).

Despite all the potential factors that limit the precise and direct estimation of salt quantities from satellite remote sensing, Metternicht and Zinck conclude that good monitoring results can be obtained by integrating remote sensing data with field and laboratory data. In this chapter, a new method is described which allows to map soil salinity in terms of electrical conductivity over large areas. This method, in full agreement with the final conclusion of Metternicht and Zinck, consists of a combination of field data and uncalibrated salinity maps calculated from

space borne multispectral images. Field data consist of measurements of electrical conductivity. They were obtained by the combination of geophysical methods and the measurement of the saturated paste conductivities of soil samples.

### 4.1.1 Overview

The chapter consists of three major parts: Obtaining field data in terms of electrical conductivity of the soil (see section 4.1.2), calculating uncalibrated salinity maps (see section 4.1.3) and finally combining these two data sets (see section 4.2).

The three major steps required to calculate electrical conductivity maps are characterized by different spatial scales. Field data are obtained at point scale (single electrical conductivity measurements) and transformed to a pixel scale by averaging several measurements. The second step is on the scale of raster maps from satellite images. It consists of calculating uncalibrated salinity maps. Combining this raster map with field data on a pixel scale is the final step. A diagram illustrating these different scales and their combination is shown in figure 4.1. The single steps are discussed in detail in the following sections.

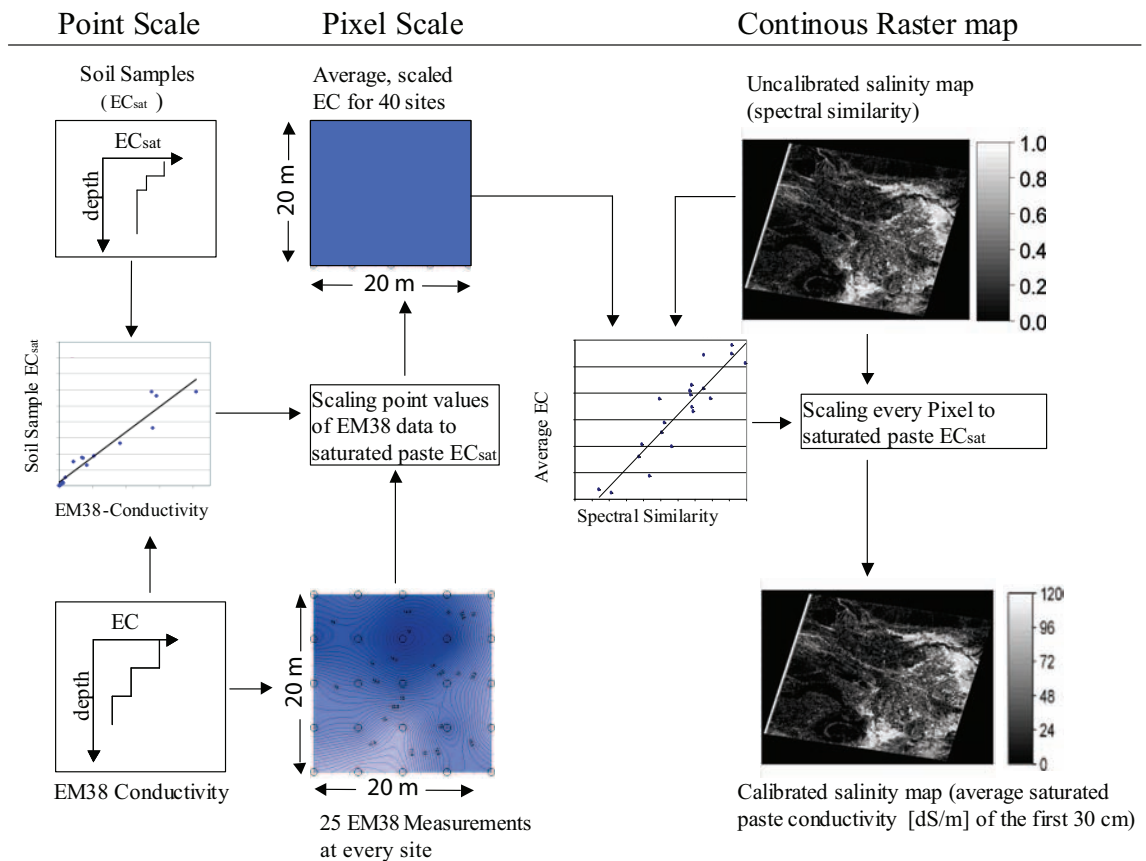


Figure 4.1: Overview of the major steps and scales for mapping soil salinity.



### 4.1.2 Field data

A wide range of methods exists to measure electrical conductivity of soils. Summaries covering most of these procedures can be found in Rhoades *et al.* (1999). Several standardized procedures have been suggested to measure soil salinity from soil samples, a selection of different methods to analyze soil samples was presented by Richards (1954). Besides the classical procedures of analyzing soil samples, indirect methods to quantify soil salinity have been developed.

One indirect method is based on Faraday's law. A transmitter coil induces circular eddy loops in the soil. Each loop induces a secondary electromagnetic field; a fraction of the secondary field is intercepted by the receiver coil, producing a voltage output. This voltage is directly proportional to a depth weighted electrical conductivity. A wide range of instruments based on the induction law has been developed. Details about the principle and a description of some sensors are discussed in McNeill (1992).

Another, classical method to indirectly quantify electrical conductivity of the soil are resistivity soundings. Geoelectric methods feed a current into the soil via current electrodes. The induced potential is measured with two other electrodes, called potential electrodes. A 1-dimensional electrical conductivity profile can be obtained by inverting the relationship between the electrode spacing and the measured resistivity (Telford *et al.*, 1990; Rhoades & Miyamoto, 1990).

All methods have their specific advantages and limitations. One common constraint of resistivity and induction methods is the requirement of a minimal amount of water. Rhoades *et al.* (1992) stated that measurements on soils with less than 10% of water per weight are not a reliable indicator of the extent of salinity.

Although taking soil samples is expensive and time consuming, a measure of electrical conductivity independent of the field conditions can be derived from them. Moreover, data such as the water content, the amount of salt in the sample and the chemical composition of the salts present can be determined.

Electromagnetic induction using the EM38 (manufactured by Geonics: <http://geonics.com/html/em38.html>) allows to quickly map the extent of soil salinity to a depth of around 2 m (see section 4.1.2). A EM38 measurement is performed within seconds by one single person. Although a measure for electrical conductivity can be obtained quickly, the measurements must be interpreted to obtain an electrical conductivity profile. The results of such an interpretation are maps showing the pattern of soil electrical conductivity. The absolute values of conductivities obtained are not directly comparable to values obtained with other methods.

The big advantage of resistivity measurements is that they are not restricted to a certain depth. The effective depth of exploration is about one-third of the distance between the current electrodes (Halvorson & Rhoades, 1976). In contrast to EM38 measurements, resistivity soundings can take over an hour and are best performed by several people.

All three methods were used in combination. Only the EM38 allows to map

large areas within a reasonable time period. Soil samples, on the other hand yield absolute values of electrical conductivity. It is therefore straightforward to combine these two methods: If EM38 data can be correlated with electrical conductivity data obtained through the analysis of soil samples, the found relation can be used to scale the interpreted EM38 data. To quantify electrical conductivity values in the areas with a large depth to groundwater, 4-pole resistivity measurements in the Schlumberger-array were performed.

### Measurement sites and layout

Field data were obtained in two field campaigns in the Yanqi basin (September to October 2002 and September 2003). In the first campaign, measurements were mainly performed over non-irrigated sites. The second campaign consisted of some additional Schlumberger measurements (see section 4.1.2) along the northern boundaries, as well as several EM38 measurements over irrigated areas. It was not possible to perform all 3 methods at every station. For example, EM38 measurements do not make sense along the northern boundaries of the basin as the depth of interest is much larger than the exploration depth of the EM38. Therefore only Schlumberger soundings were performed in these areas. Figure 4.2 summarizes the locations of the stations and indicates what kind of measurements were carried out. At 17 locations, soil samples were taken and Schlumberger soundings as well as EM38 measurements were performed. At 6 locations, only EM38 measurements were carried out and soil samples were taken. At 9 stations, only Schlumberger measurements were carried out. 7 locations were documented by Schlumberger measurements as well as EM38 measurements (in figure 4.2, these 7 points are not distinguished explicitly from the Schlumberger sites). At 21 locations, only EM38 measurements were carried out. At 3 sites, only soil samples were taken (not plotted in figure 4.2).

All the methods described yield 1-dimensional vertical profiles of electrical conductivity at a point. With regard to the goal, to correlate measurements on the ground with remote sensing data, point values are not sufficient. A pixel recorded by a multi-spectral sensor represents the spectral properties of the combination of the materials present over the whole pixel area. Salts tend to accumulate in patches. Point measurements of electrical conductivity may therefore not be representative for the average electrical conductivity covered by one pixel of the satellite. Thus, it is necessary to perform several measurements over an area with a spatial extent comparable to the resolution of the sensor used and then to relate an average of several measurements at specific locations on the ground with the raster data. At every EM38 station, 25 EM38 measurements distributed regularly over a square with 20 m by 20 m were performed (see figure 4.3). The spatial resolution of the raster data used was also 20 m by 20 m.

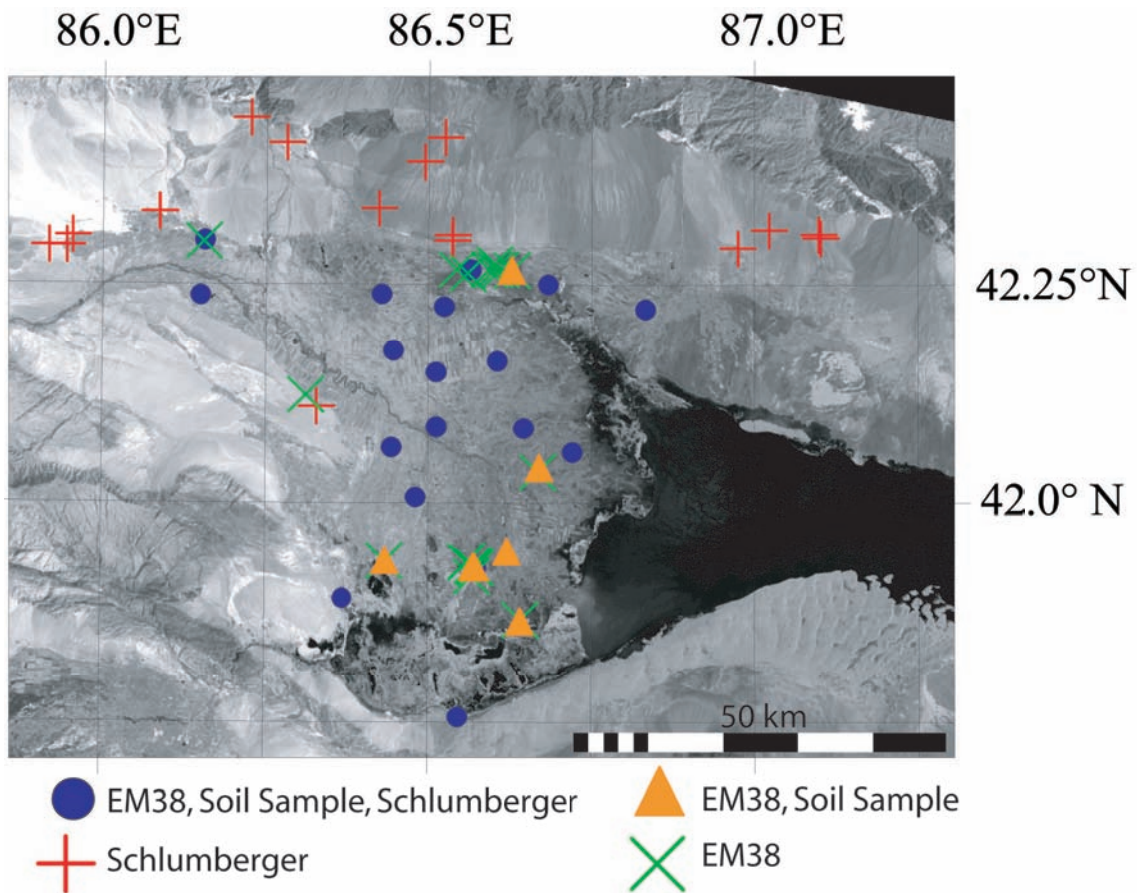


Figure 4.2: Measurement sites in the Yanqi basin.

### Soil samples

In total, 142 soil samples were taken from different depths at 26 sites. Soil samples were obtained with a hand Auger after the EM38 measurements and Schlumberger soundings were completed. The sampled soil was sealed in PET-containers to prevent evaporative loss. The case length of sub-samples was varying from 20 cm to 35 cm. At 5 stations, soil samples were obtained every 10 cm. The most common way to describe electrical conductivity independent of the soil water content is the saturated paste conductivity, discussed and described by several authors, e.g. Rhoades (1996).

This approach was used in this study: In a first step, the soil samples are dried. Distilled water is then added until the soil is saturated. The saturated paste conductivity is the electrical conductivity of the saturation extract. To correct the influence temperature, electrical conductivity was scaled to the standard temperature (25 °C). Besides electrical conductivity, the main chemical components of the saturated paste solution as well as the water content of the samples were determined. Measured saturated paste conductivities covered a range from 0.29  $\text{dS}\cdot\text{m}^{-1}$  up to 167  $\text{dS}\cdot\text{m}^{-1}$ .

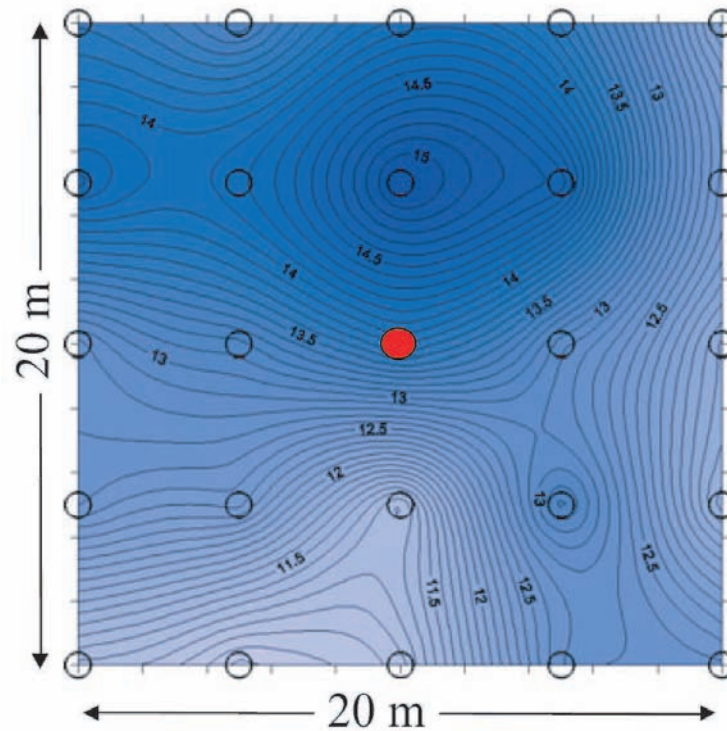


Figure 4.3: Measurement layout of a EM38 station. It consists of 25 single EM38 measurement points (indicated by the circles). If soil samples were taken or a Schlumberger sounding was performed, it was always in the center of this measurement layout (indicated by the red circle). The contour lines were obtained by interpolation of the horizontal EM38 reading [ $dS \cdot m^{-1}$ ].

The difference between irrigated and non-irrigated locations is very clear. Saturated paste conductivities of soil sample obtained over non-irrigated sites are up to a factor of 50 higher compared to the results obtained over irrigated sites. Typical electrical conductivity and soil moisture profiles of a non-irrigated and a recently irrigated site are plotted in figure 4.4. Electrical conductivity and water content of the non-irrigated station 16 ( $41^{\circ}55.642'N$ ,  $86^{\circ}34.402'E$ ) show a pronounced evaporative profile built up through the continuous evaporation of groundwater. The depth to groundwater at station 16 is only about 2 m, which explains the very high water contents at this site. The irrigated plot at station 3 ( $42^{\circ}15.549'N$ ,  $86^{\circ}29.989'E$ ) shows no pronounced profile both in the water content and in electrical conductivity.

The amount of water required to saturate the soil samples as well as the principal chemical components, are more or less the same for all irrigated and non-irrigated sites.

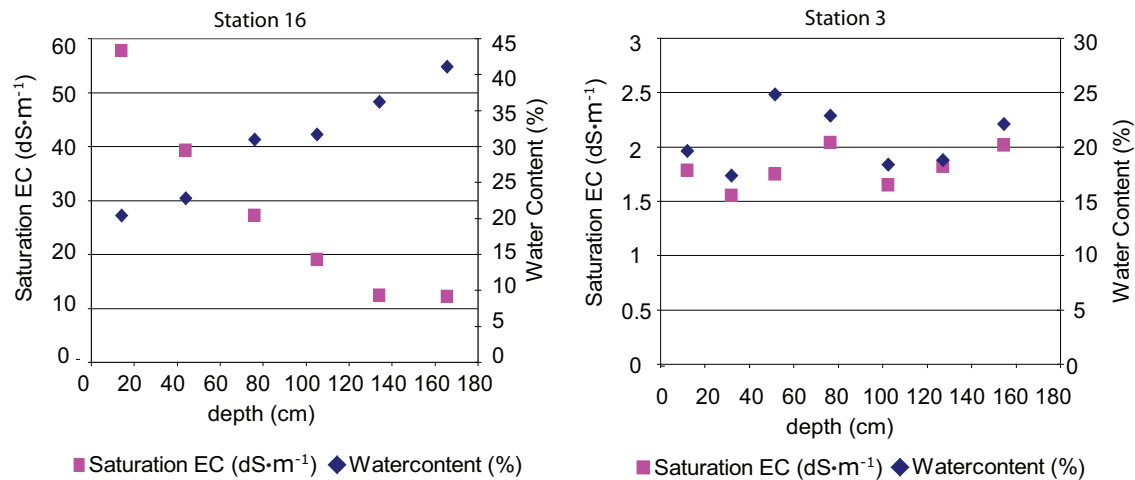


Figure 4.4: Soil moisture and electrical conductivity profiles for the non-irrigated station 16 and the irrigated station 3. The x-axis indicates the depth from which the samples were taken.

## EM38

51 locations were mapped with the EM38. If possible, the EM38 sites were chosen within large areas featuring similar conditions around the measurement layout, for example centers of large fields. A constraint reducing the number of ideal EM38-sites is the high sensitivity of the instrument. It is impossible to measure in areas with electrical noise present, be it from power poles, metal objects or atmospheric noise.

The EM38 can be operated both in a horizontal or a vertical mode, depending on the orientation of the coils to the soil surface plane. The effective measurement depths of the instrument in the standard configuration are about 1 m in the horizontal and 2 m in the vertical dipole mode (Rhoades *et al.*, 1999). These differences of relative response can be used to determine an electrical conductivity profile (McNeil, 1980).

If the soil water content falls below 10 %, the topsoil is too dry and essentially behaves as an insulating layer, strongly affecting the horizontal EM38 reading. In this case, the dry loose soil should be scraped away before positioning the EM38. In the Yanqi basin, the dried out topsoil of the non-irrigated sites were generally so thin that no significant differences of the EM38 reading could be observed when comparing a measurement with and without the dry layer. The two exceptions, stations 38 and 11, are discussed in section 4.1.2.

The interpretation of the EM38 raw data has been discussed extensively by several authors e.g. Geonics Limited (2001); Hendrickx *et al.* (2002); McKenzie *et al.* (1997); Rhoades *et al.* (1999). Following Rhoades *et al.* (1999), the raw data of the EM38 can be inverted and yield a three-layered electrical conductivity profile



(0-30 cm, 30-60 cm, 60-90 cm). In this approach, Rhoades distinguishes between regular, uniform and inverted profiles. If salinity increases with depth, the profile is called regular; the profiles in which salinity decreases with depth are called inverted. The structure of the equation to predict soil electrical conductivity is as follows:

$$\ln EC = a + b \cdot \ln EM_h + c \cdot \ln(EM_h - EM_v) \quad (4.1)$$

where  $EM_h$  is the EM38 reading in the horizontal and  $EM_v$  is the EM38 reading in the vertical mode.  $a$ ,  $b$  and  $c$  depend on the type of profile as well as the depth of the layer.

McKenzie *et al.* (1997) pointed out that the EM38 readings are not independent of the field conditions. Various potential influences such as soil temperature or clay content are not taken into account in the models described by Rhoades. If such factors are not explicitly considered, the assumption is made that factors other than salinity that influence the reading are homogeneous over the project area. However, the influence of soil moisture is small, although moisture is directly related to the electrical conductivity under field conditions. If soil moisture is increased while the amount of salt in the soil column is held constant, there will be a trade-off between the decreasing salt concentration and the increasing water content. This tradeoff keeps the EM38 reading constant over a large range of electrical conductivity.

### Resistivity measurements

39 Schlumberger soundings were performed. The locations where resistivity measurements were performed are plotted in figure 4.2. Micro-soundings were carried out at sites with a depth to groundwater smaller than 5 m. A typical sounding consists of several resistivity measurements with an increasing distance between the current electrodes. Basically, any kind of arrangement between potential and current electrodes can be interpreted. However, the interpretation of the results is simpler for some special geometries of the current and potential electrodes. The Schlumberger geometry was used in this project. In this geometry, the current and potential electrodes have a common midpoint but the distances between adjacent electrodes differ. The calculation of the apparent resistivity ( $\rho$ ) requires the knowledge of the "cell or geometric constant" ( $k$ ) and the geometric configuration. The derivation of these constants as well as the inversion of the data can be found in geophysical textbooks, e.g. Telford *et al.* (1990); Lowrie (1997). The increment of the distance between the current electrodes was varied in the same way on all measured sites. The distance between the potential electrodes was increased if the measured resistivity became unstable. The spacing between the potential electrodes does not affect the depth of the measurement, nor the calculated value of the apparent resistivity. However, a slight shift of the apparent resistivity is often observed after increasing the spacing of the potential electrodes. Data of such a Schlumberger sounding in the Yanqi basin are presented in figure 4.5.

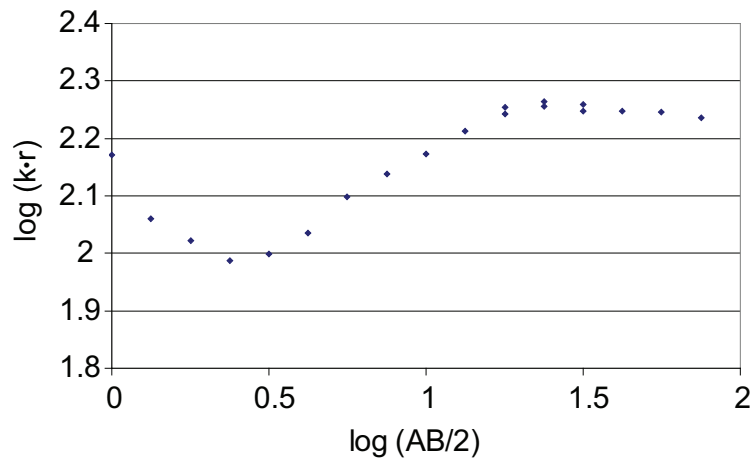


Figure 4.5: Schlumberger sounding at station 17 ( $42^{\circ} 16.016N$ ,  $86^{\circ} 49.261E$ ); after point 11 a different spacing between the potential electrodes was used, 11, 12 and 13 were measured in both configurations.  $AB$  is the distance between the current electrodes,  $r$  the measured apparent resistivity,  $k$  is the geometrical constant.

Commercial software and open source codes for the Schlumberger inversion are widely available on the internet. Every electrical conductivity profile has a corresponding (theoretical) relationship between the spacing of the current electrodes and the apparent resistivity. The interpretation of a Schlumberger sounding therefore consists of obtaining a resistivity profile with a corresponding relationship between the spacing of the electrodes and the apparent resistivity similar to the observed one. As in any model approach, the observations can be approximated to any desired goodness of fit by increasing the number of free parameters. In case of resistivity inversion, the number of parameters results from the number of layers used to describe the electrical conductivity profile. An over-parameterized model may be tempting, but leads to non-unique results. The goal is therefore to fit the measurements with a limited number of layers. The thicknesses of the model layers are, in contrast to the layers describing the EM38 readings, not equal. An example of an inversion (station 17) is presented in figure 4.6. The resulting apparent resistivities are inversely proportional to the electrical conductivity.

The Schlumberger soundings in the areas with a large depth to groundwater (found in the northern areas of the project region) yielded the smallest electrical conductivity values within the entire basin. In these areas, soil salinity is so small that it cannot be considered a problem.

### Comparison of the different methods

All three methods yield vertical, electrical conductivity profiles of different discretization. To be comparable, the electrical conductivity profiles of all methods

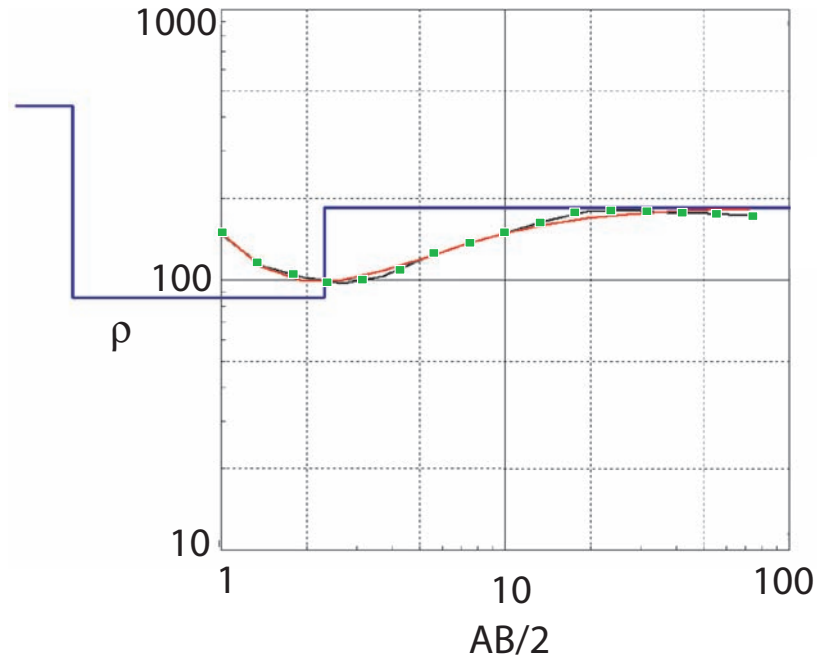


Figure 4.6: Inversion of a resistivity sounding. The x-axis [m] represents both the spacing between the source electrodes as well as the depth of modelled resistivity at Stn. 17. Logarithmic apparent resistivity is represented by the y-axis: the red curve indicates the relationship between apparent resistivity  $\rho$  and the spacing between the source electrodes for a soil having a resistivity profile as indicated with the blue curve. The green points are the measured, apparent resistivities at this station.

must be transformed to the same discretization. The profiles calculated on the basis of EM38 data feature 3 different layers with a vertical extent (depth) of 30 cm. The total depth of electrical conductivity profiles obtained from soil samples is not constant. Additionally, the depth of every subsample is not restricted to a constant value.

To compare data obtained with the EM38 to saturated paste conductivities, the saturated paste conductivities were depth weighted. For all three layers, the conductivities were plotted against each other, see figure 4.7. The linear regression functions and the corresponding correlation coefficients are plotted in table 4.1. The high correlation coefficients in all layers justify the assumption that factors other than salinity are not influencing the EM38 results significantly. The two stations 38 ( $41^{\circ} 45.379'N$ ,  $86^{\circ} 32.695'E$ ) and 11 ( $42^{\circ} 15.02'N$ ,  $86^{\circ} 40.963'E$ ) are outliers and are not included in the regression. At these stations, salt crusts were present with water contents far below 10%. In contrast to the soil samples, this layer had no influence on the electrical conductivity measured with the EM38. As expected, the saturated paste conductivities are higher than the predicted conductivities obtained with the EM38. The largest discrepancies of the two outliers in the relation found are in the first layer.



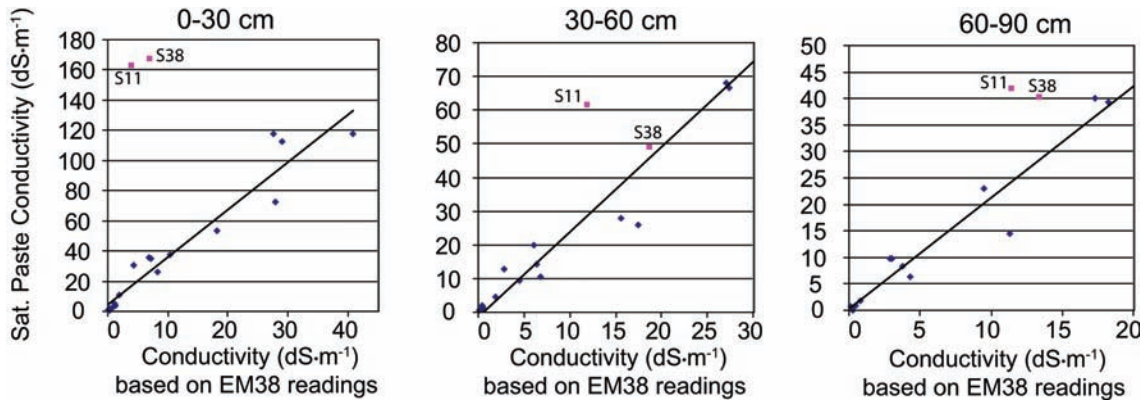


Figure 4.7: Relationship between saturated paste conductivities ( $y$ -axis, [ $dS \cdot m^{-1}$ ]) and the EM38 values ( $x$ -axis, [ $dS \cdot m^{-1}$ ]) for the three model layers (left: 0-30 cm, middle: 30-60 cm, right: 60-90 cm). The pink points are outliers.

Table 4.1: Linear relationships between EM-measurements ( $x$ ) and saturated paste conductivities of the soil samples ( $y$ ).

	0-30 cm	30-60 cm	60-90 cm
Function	$y = 3.15x + 4.5$	$y = 2.4x - 1.3$	$y = 2.25x + 0.1$
R <sup>2</sup>	0.93	0.96	0.92

Inverted resistivity data were compared in a similar way to the saturated paste conductivities. At every site, the saturated paste conductivities were averaged over a column of the same extent as the model-layers used to describe the resistivity measurements. The comparison between saturated paste conductivities and the reciprocal values of resistivity is plotted in figure 4.8. The crusts at the stations 38 and 11 do not contribute to the Schlumberger measurements, the two stations again are outliers. The difference is not as obvious as with the EM38. The correlation coefficient of the linear regression (obtained without taking the outliers into account) is high ( $R^2 = 0.96$ ).

Correlations between the methods have been found. Every single EM38 measurement was scaled to saturated paste conductivity. By averaging the 25 EM38 conductivity values at every station, 51 values (equal to number of EM38 measurement sites) on a pixel-scale were obtained (see figure 4.1). EM38 measurements at the two outlier stations had to be neglected. Additional soil samples were obtained in order to provide the same spatial information as at all other stations.

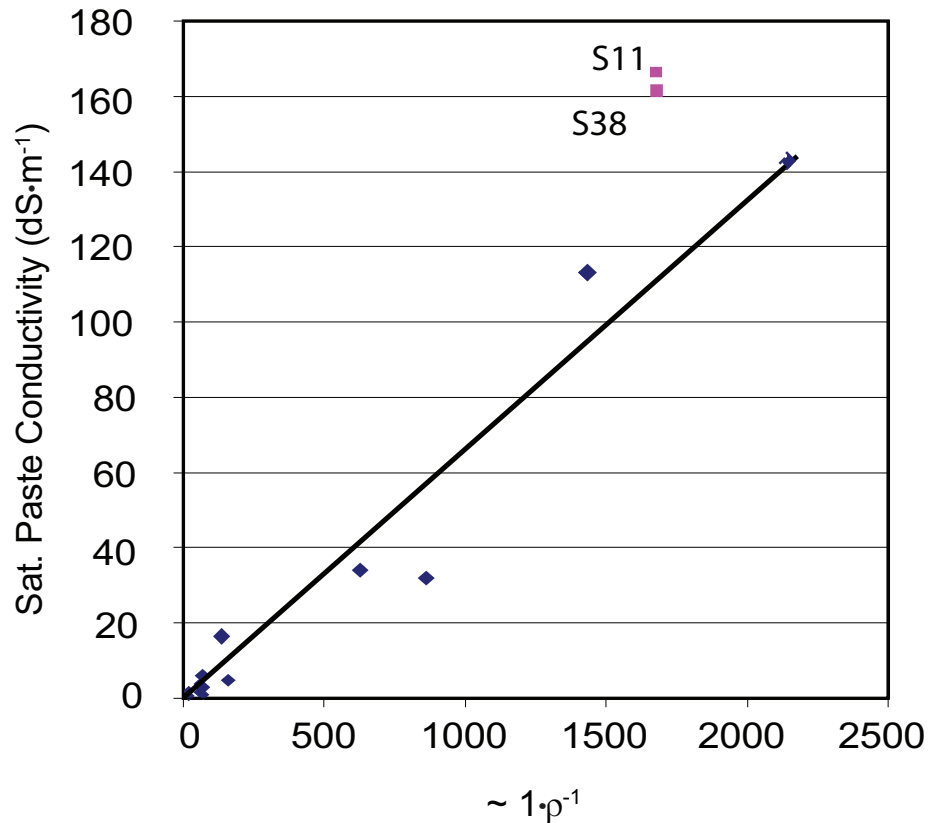


Figure 4.8: Relationship between saturated paste conductivities (y-axis, [dS·m<sup>-1</sup>]) and the reciprocal values of the apparent resistivities. The pink points are the outliers (stations 38 and 11).

### 4.1.3 Remote sensing

The Terra-Satellite, which carries the ASTER (Advanced Spaceborne Thermal Emission and Reflection Radiometer) instrument was launched in December 1999. ASTER images of the project region have been available since the year 2000. The spatial extent of an ASTER image on the ground is approximately 60 km by 60 km, not sufficient to map the entire basin with one image. The ASTER sensor features nine channels covering the spectra from the visible (VNIR, visible and near infrared) to short wave (SWIR, short wave infrared) infrared with a spatial resolution of 15 m and 30 m respectively. Uncalibrated salinity maps are calculated on the basis of an image derived reference spectrum. This spectrum consists of the reflectances of the nine channels over one pixel in an extremely saline area. This spectral signature was used to classify every image pixel in terms of spectral similarity. Several algorithms (e.g. Howari (2003a)) have been developed to calculate spectral similarity. In this approach a Spectral Correlation Mapper (SCM) was used (see section 4.1.3).

## Available remote sensing data and data preprocessing

Data are distributed by the Land Processes Distributed Active Archive Center (LP DAAC), located at the U.S. Geological Survey's EROS Data Center (<http://LPDAAC.usgs.gov>). The ASTER archive was searched for cloud free images over the Yanqi basin. Since the beginning of the mission until the end of 2003, 15 images covering the area have been available, but only 5 of them provide a sufficient area coverage as well as cloud free conditions. Figure 4.9 shows the temporal distribution of available images. The free level2b5 ASTER images were used. The

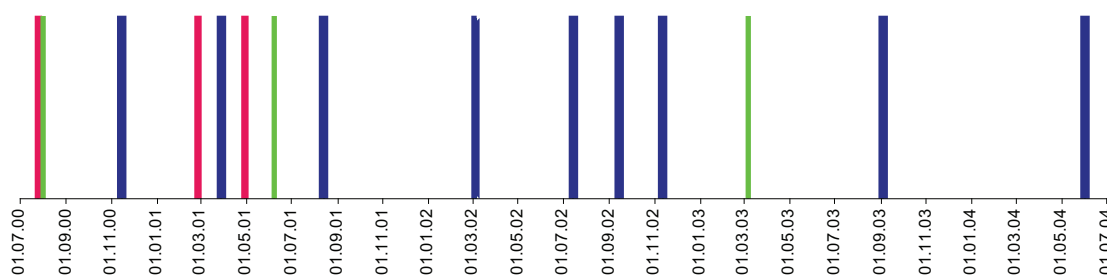


Figure 4.9: Temporal distribution of ASTER- images over the Yanqi basin- the green colour indicates an insufficient coverage of the area of interest, the red colour indicates a high cloud cover, the blue colour indicates both sufficient image quality and sufficient area coverage.

images are atmospherically corrected. The atmospheric correction of the images was processed by the EOS data center. The detailed description of the algorithms employed and the input data required can be found in Thome (1999). To process the images, the spatial resolution of all channels has to be the same. The spatial resolution applied to calculate salinity maps was 20 m, the same spatial scale as the measurement layout in the field.

Differential GPS data were available for 67 clearly visible surface features in the Yanqi basin. With this information, the quality of the georeference could be improved resulting in accuracies in the sub-pixel range.

## Image derived reference spectrum

Every material has characteristic spectral properties. These spectral properties in terms of reflectance can be analyzed in the laboratory using spectrometers. One could determine the spectral properties of a specific material and search a remotely sensed image for pixels with similar reflectance. One of the major limitations of this approach is the spatial and spectral resolution of space-borne sensors. The spectral properties of remotely sensed pixels are always the spectral mixture of the materials present at the soil surface, therefore the search for one specific material with known spectral properties often yields ambiguous results. Besides adsorption and scattering

of radiation in the atmosphere, parameters such as time of day, season or cloud cover directly affect the reflectance properties recorded by the sensor. It is therefore not straightforward to use information of the spectrally highly resolved laboratory data to its full potential.

In the approach described here, the reference spectrum was image derived (see figure 4.10). Although the images were corrected for atmospheric influences, factors such as changes of vegetation or the soil water content influence the spectrum. Differences between spectral responses at different dates are plotted in figure 4.11. To be consistent, the spectrum used to calculate an uncalibrated salinity map was always obtained from the image processed.

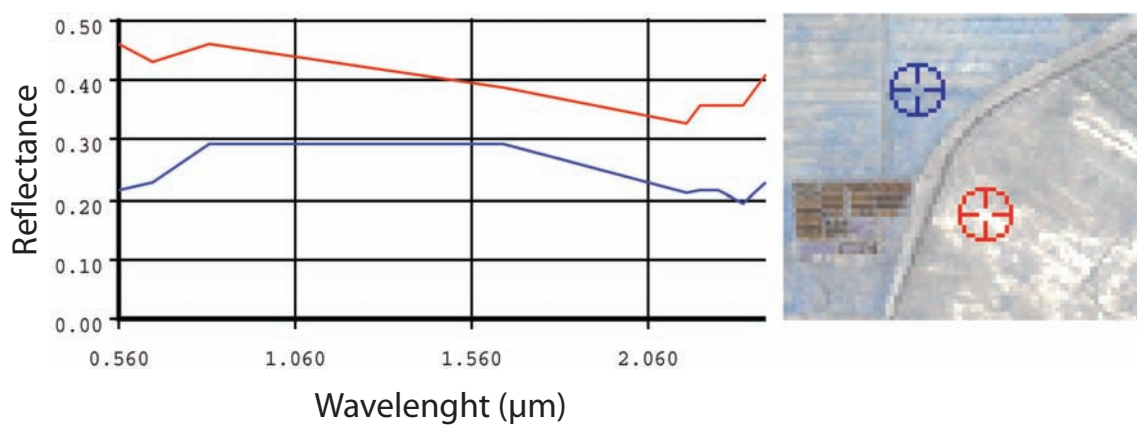


Figure 4.10: Two examples of an image-derived spectrum from an ASTER image over the project area on November 11<sup>th</sup>, 2002. The reflectance values in each channel of two pixels (see right image) are plotted as a function of wavelength (left). The station plotted in red (station 11) could be used as image derived reference spectrum, as electrical conductivity values observed at this location were very high.

Summer and winter images show a significant difference, not only over the overgrown areas: In wintertime, the spectral responses are much more pronounced. The more pronounced the spectral signatures in different channels are, the more clearly different materials can be distinguished. In summertime, the spectral responses over the agricultural area do not show the wide spectral range of the winter images.

The completely salinized station 11 (42° 15.02'N, 86° 40.963' E) was mostly used to derive the reference spectrum. Unfortunately, this station was not contained in all the images processed. If station 11 was not contained in the image processed, other completely salinized locations had to be used instead (e.g. station 38 (41° 45.379'N, 86° 32.695'E)). Just like station 11, station 38 features a thin salt crust. Both stations have been identified as outliers in figure 4.7. As the EM38 information could not be used at these specific locations, additional soil samples had to be taken in order to obtain a representative value over an area of the spatial dimension of a pixel.

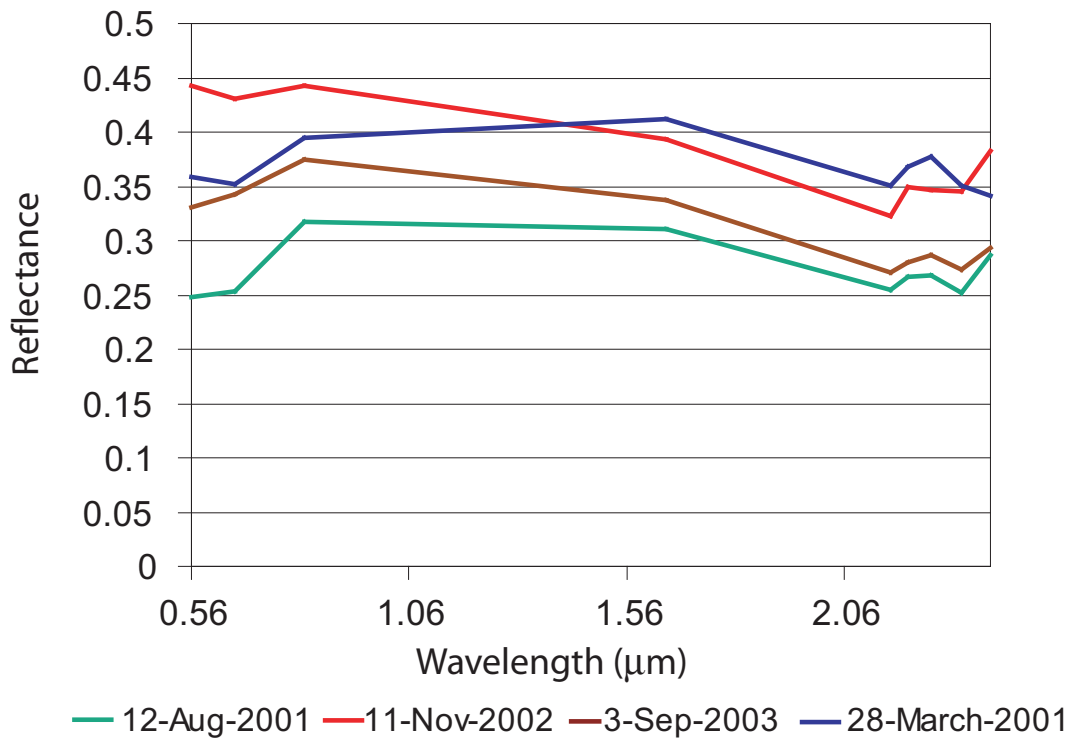


Figure 4.11: The plot shows the spectral responses of the same, salinized pixel on four different images.

It is important that the composition of salts at these locations does not differ from other sites. Chemical analysis of the salt crusts at the locations where reference spectra were obtained showed that the salts present and the ratios between their abundances is constant not only for these two stations, but also for other measurement sites (see section 4.1.2).

### Calculating uncalibrated salinity maps

With the image derived reference spectrum defined, the spectral similarity of every image pixel to this reference can be calculated. The Spectral Correlation Mapper (SCM) algorithm (de Carvalho & Meneses, 2000) was used to calculate the spectral similarity of every pixel to the image derived reference spectrum using the software package ERDAS-Imagine 8.7. SCM is a modification of the Spectral Angle Mapper (SAM). The Spectral Angle Mapper (Yuhas *et al.*, 1992) derives the angle formed in an n-dimensional space between the reference spectrum and the spectrum of every pixel. The dimensionality of space is equal to the number of channels. The mathematical formula for SAM is the basic vector geometric equation to determine

the angle between multidimensional vectors:

$$\alpha = \cos^{-1} \frac{\sum(X \cdot Y)}{\sqrt{\sum(X)^2 \cdot \sum(Y)^2}} \quad (4.2)$$

where  $\alpha$  = spectral angle,  $X$  = image spectrum,  $Y$  = reference spectrum.

This technique is more or less insensitive to changes in pixel illumination, because increasing or decreasing illumination does not change the direction of the vector, only its magnitude. The Spectral Correlation Mapper eliminates this inconsistency by normalizing every vector to the vector mean. For every image processed, the spectral angle of every image pixel to the reference is calculated. Spectral similarity is expressed with the cosine of this angle. Spectral similarity maps were calculated for several dates, both for summer and wintertime (see table 4.2).

An example of such an uncalibrated salinity map is shown in figure 4.12. This image was recorded on November 11<sup>th</sup>, 2002. Irrigated fields are clearly visible, all salt has been leached from the surface, resulting in a very low spectral similarity. Paths or earth walls around the fields are never irrigated, therefore salt can accumulate over time.

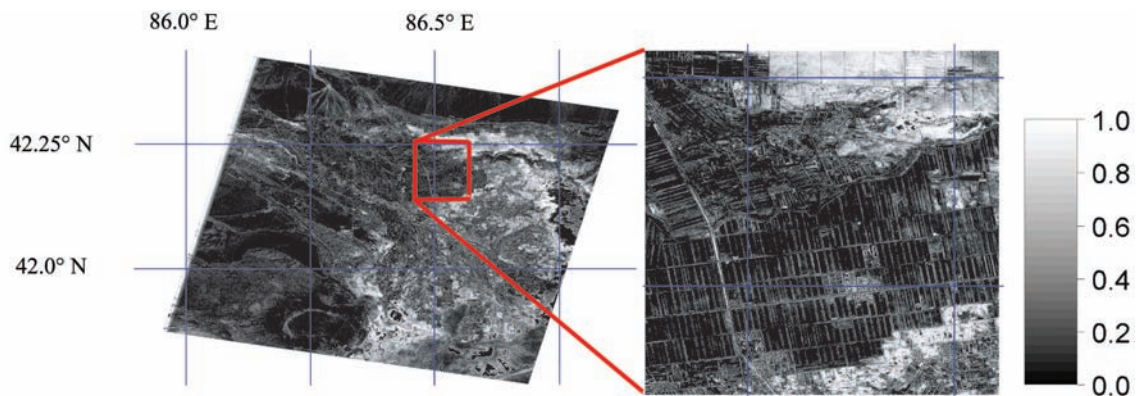


Figure 4.12: Map of spectral similarity calculated with the SCM (November 11<sup>th</sup>, 2002). White areas indicate a high spectral similarity to the reference spectrum.

The value range obtained from spectral similarity stretches from 0 to 1 in this winter image, even within the agricultural area.

Processed images from summertime had a more limited value range. A typical example of a spectral similarity map for summer time is plotted in figure 4.13. Although the non-saline areas in the north and single, recently irrigated, wet fields had a spectral similarity 0, the value range over the agricultural area (including irrigated and non-irrigated sites) was only from 0.5 to 1. Summer images do not show pronounced differences over the area of interest, it is difficult to directly distinguish between saline and non-saline areas. One can therefore try to obtain uncalibrated salinity maps using alternative image transformations. The NDVI can be used as such an alternative image transformation because plant growth is reduced by soil salinity.



One drawback of the NDVI in the context of salinity mapping is the fact that different plants grow on different levels of salinity and so the index is an ambiguous indicator for the extent of salinity. Moreover, if the absence of vegetation or its reduced vigor is not due to the presence of salt, the NDVI predicts wrong results. The diminished vitality could likewise be related to the absence of essential nutrients. In wintertime, practically no vegetation is present and, it is therefore not appropriate to use the NDVI instead of the Spectral Correlation Mapper.

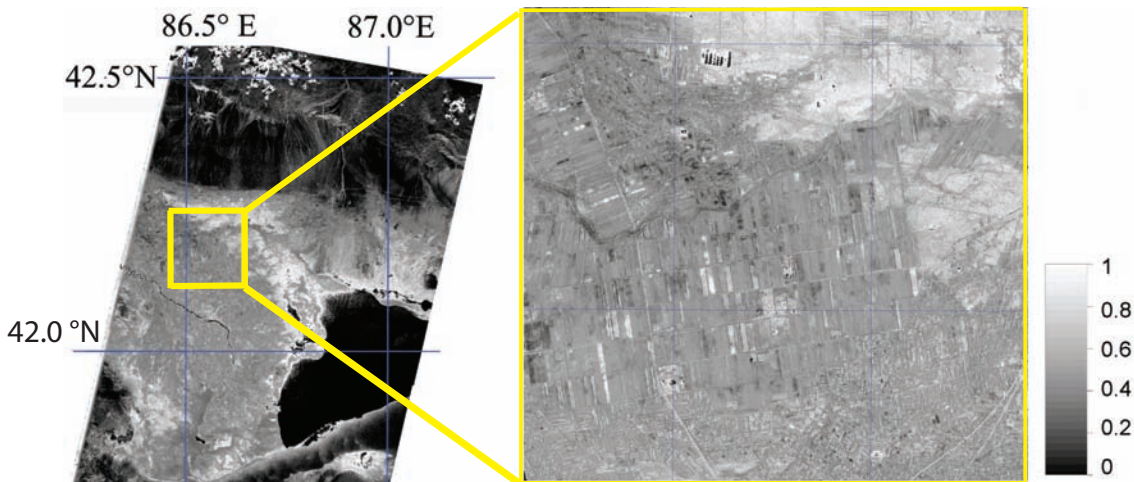


Figure 4.13: Uncalibrated salinity map calculated with the Spectral Correlation Mapper. The images (mosaic of two ASTER images) were recorded on September 3<sup>rd</sup>, 2003.

Several, areas which are completely saline are present in the Yanqi basin and could potentially be used to obtain an image derived reference spectrum. For the image of November 11<sup>th</sup>, 2002, two uncalibrated salinity maps were calculated based on two different image derived reference spectra. Although the reference spectra were not identical, the patterns of the uncalibrated salt maps were similar and therefore could be scaled to the same electrical conductivity values with slightly different relationships between the field data and the remote sensing data. A comparison between the two similarity maps is shown in figure 4.14. The correlation coefficient is very high but the offset shows that the different reference spectra do not yield identical results. The lowest values are around 0.8. These low values are exclusively found in the northern part of the basin.

## 4.2 Combining remote sensing and field data

Two types of uncalibrated salinity maps have been calculated: Spectral similarity for all the images and the NDVI for images obtained in summer. The next step is to combine the field data with the uncalibrated salinity maps. The field data are represented by the scaled EM38 measurements as described in section 4.1.2. Before one can plot the field data versus the uncalibrated salinity maps, two important

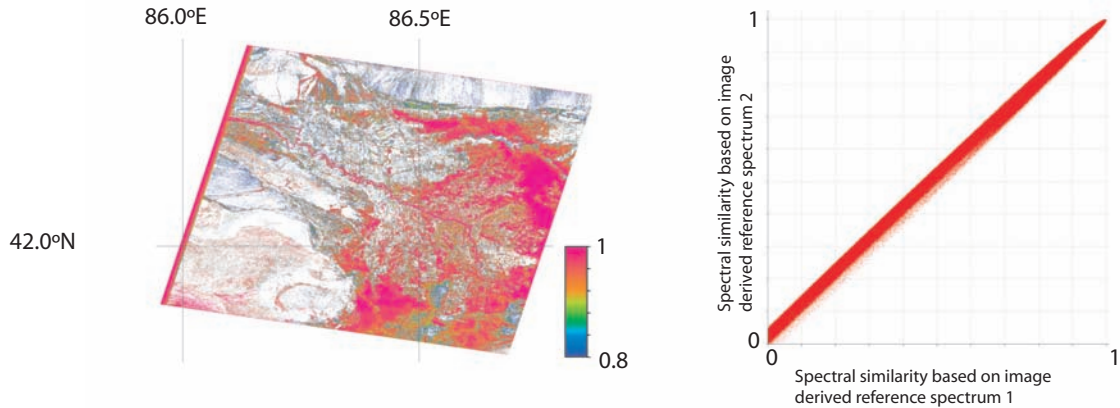


Figure 4.14: Ratio between two maps calculated with a different reference spectrum (left) and their pixelwise comparison (right). The image was recorded on November 11<sup>th</sup>, 2002. The white areas have a spectral similarity of zero.

points have to be taken into account: The time gap between measurements on the ground and the date the image was obtained. Moreover, inaccuracies of the coordinates of ground measurement sites have to be taken into account: The locations of the measurement site have been determined by using a hand held GPS, not reaching the precision of differential GPS.

#### 4.2.1 Comparing measurements on the ground with satellite images from different dates

It is very difficult to get satellite images of exactly the same date as field work is done, especially when field work is performed over a long time. Remote sensing data were not available for the dates when field data were obtained. The image from November 11, 2002 is with 1 month delay closest in time to fieldwork. If the parameter of interest, in this case electrical conductivity of the soil, is subject to quick changes, it should only be compared to a satellite image of the same date. Fortunately, the Yanqi basin features large areas where soil conductivity is not subject to quick changes. Measurements obtained at such locations can be compared with remotely sensed images, even if the dates are not identical.

To identify these areas, it is helpful to recall the factors influencing the total amount as well as the distribution of salt in a soil column. Capillary rise of saline groundwater will increase the amount of salt. On the other hand, a major rain event

or the irrigation of a field will remove the accumulated salts from the surface layer, changing within minutes the electrical conductivity profile of the soil as well as the surface properties recorded by the satellite. The annual precipitation of 20 mm is, however, by far not sufficient to flush down the salt accumulated by the continuous evaporation through the soil column. If a field is not irrigated, only capillary rise will change the amount and distribution of salt in the soil column.

This process is slow. In the Yanqi basin, salinization was triggered by irrigation. Across the non-irrigated areas salt accumulated for at least 50 years. If  $1.2 \text{ m}\cdot\text{a}^{-1}$  of groundwater (equal to the potential ET) evaporated with a solute concentration of  $2.1 \text{ g}\cdot\text{l}^{-1}$  (equal to the highest concentration of salt found in drainage water), the annual increase of salt would be around  $2.5 \text{ kg}\cdot\text{m}^{-2}\cdot\text{a}^{-1}$ . This value is unrealistically high as the soil column between groundwater and the atmosphere will reduce the potential ET significantly. Moreover, the concentration of salt in groundwater does not reach the high values of the drainage water. However, compared to the total amount of salt stored in the soil column, even an annual increase of  $2.5 \text{ kg}\cdot\text{m}^{-2}$  would still be small: station 16, an example of a moderately saline, non-irrigated station, contains about  $60 \text{ kg}\cdot\text{m}^{-2}$  salt within the soil column from the surface down to the groundwater table at 1.8 m.

Besides variations of the total amount of salt, the water content influences the electrical conductivity in the field, and may even change the spectral properties of the surface. In this approach, field data consist of an electrical conductivity measure independent of field conditions. The water content in the non-irrigated soil does not vary quickly, as the only source of water is groundwater. Still, the variation of the depth to groundwater could influence the spectral properties at the surface. Even though changes of the groundwater table up to 10 cm per irrigation cycle have been observed under irrigated fields, the annual changes of the groundwater table under non-irrigated sites are much smaller. Therefore, it is unlikely that variations of the groundwater table significantly influence the spectral properties, but the potential constraint is also addressed by deriving the used reference spectrum from the image processed.

#### 4.2.2 Inaccuracies of the location of measurement sites on the ground

Coordinates of the center of every EM38 site were obtained with a hand-held GPS. The accuracy of this hand-held GPS is around 10 m. On the assumption that the maximum error of position is no more than claimed by the manufacturer, the measurement layout could overlap with each of the eight surrounding pixels. Therefore, the minimum and maximum of these pixels define the upper and lower limit of the real spectral similarity, while the probable value is the area weighted value around the measured location. Additional information, e.g. the presence of a nearby road, is important when it comes to comparing raster data with field data. For example, pixels 1,2 and 4 in figure 4.15 could not be taken into account in the assessment of the min-max values around station 36. Pixels 2 and 4 are situated on a road. The

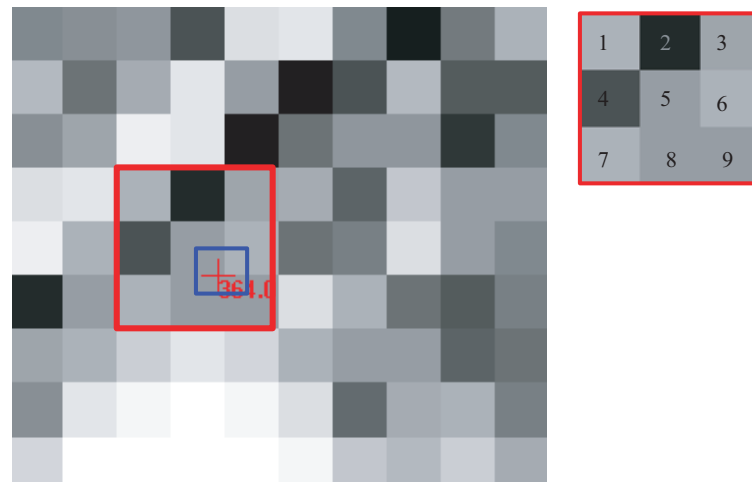


Figure 4.15: Detail of the pixels surrounding station 36 ( $41^{\circ} 52.028N$ ,  $86^{\circ} 38.517E$ ). The center of the measurement layout is very close to the center of the pixels 5,6,8,9. The contribution of each of these pixels is therefore around 25%.

measurement was done southeast of that road, therefore it is impossible that pixel 1 is within the measurement layout. Most probably, pixels 3,5 and 7 are influenced by the road as well, as it is unlikely that the raster exactly follows the road (in this case that is even impossible because the road runs in a southwest- northeast direction) and that the road features the same spatial extent as the pixel resolution. The best way to cope with this problem is to measure, whenever possible, far away from objects such as roads, houses or boundaries between fields. If this was not possible, as at station 36, pixels including objects that were of different nature from the area within the measurement layout were neglected. The pixels just next to these unfavorable features may still be influenced by them. This is unfortunate but inevitable due to the limited spatial resolution of the sensor.

## 4.3 Results

### 4.3.1 Combining field data with uncalibrated salinity maps

For 51 locations, the average electrical conductivity over an area equal in size to the pixel have been quantified as described in section 4.1.2. These electrical conductivity values represent the first 30 cm of the soil column. Aster images are not large enough to cover the entire region, therefore not all measurement sites are covered by every image. Nevertheless, at least 13 and at most 26 stations were within in the images processed. For the reasons discussed in 4.2.1, only non-irrigated sites are admissible for comparison. The measurements over the non-irrigated sites have been obtained during the field campaign from September to October 2002, see section 4.1.2. Table

*Table 4.2: Overview of processed images.* The number of measurements sites included in every image is given by the area coverage of the image.

Date of the ASTER image processed	Number of non-irrigated measurement sites included in the image	Method used to calculate uncalibrated salinity maps
28 March 2001 (Winter)	20	SCM
12 August 2001 (Summer)	26	SCM,NDVI
13 November 2001 (Winter)	13	SCM
11 November 2002 (Winter)	24	SCM
3 September 2003 (Summer)	21	SCM,NDVI

4.2 gives an overview of the images processed, the number of non-irrigated sites included in the image and the method how uncalibrated salinity maps have been calculated.

As described in 4.2.2, the positions of the EM38-layout centers were considered exact and the values at these locations were used to calculate a linear regression for every image processed. The minimum and maximum of the surrounding pixels, plotted as error bars, (see figure 4.16) indicate the largest and smallest possible value of spectral similarity. The sometimes wide error bars reflect the situation found in the Yanqi basin: homogeneous areas were present but their spatial extent was mostly small.

### 4.3.2 Field data vs. spectral similarity

All images were processed with the SCM. Figure 4.16 plots for the uncalibrated salinity maps of November 11<sup>th</sup>, 2002 and March 28<sup>th</sup>, 2001 the relation between remote sensing and field data. Only electrical conductivities obtained at non-irrigated sites correlate with the corresponding values from the uncalibrated salinity maps. The relations found and corresponding correlation coefficients are listed in table 4.3. Two non-irrigated sites, S19 and S20 do not fit into the correlation. The two stations are situated close to each other, in the southeastern part of the basin. The measured conductivities on the ground are far below the value expected from spectral similarity. Both outliers can be explained with the electrical conductivity profile found exclusively at these specific locations. Compared to all other non-irrigated sites, the electrical conductivity profiles at both stations clearly have a different shape. A typical electrical conductivity profile of a non-irrigated site was presented in figure 4.4: Electrical conductivity gradually decreases with depth. At the outlier stations S19 and S20, high conductivities were measured in the first 10 cm of the profiles. Below this layer, electrical conductivity dropped to only 10% of the first

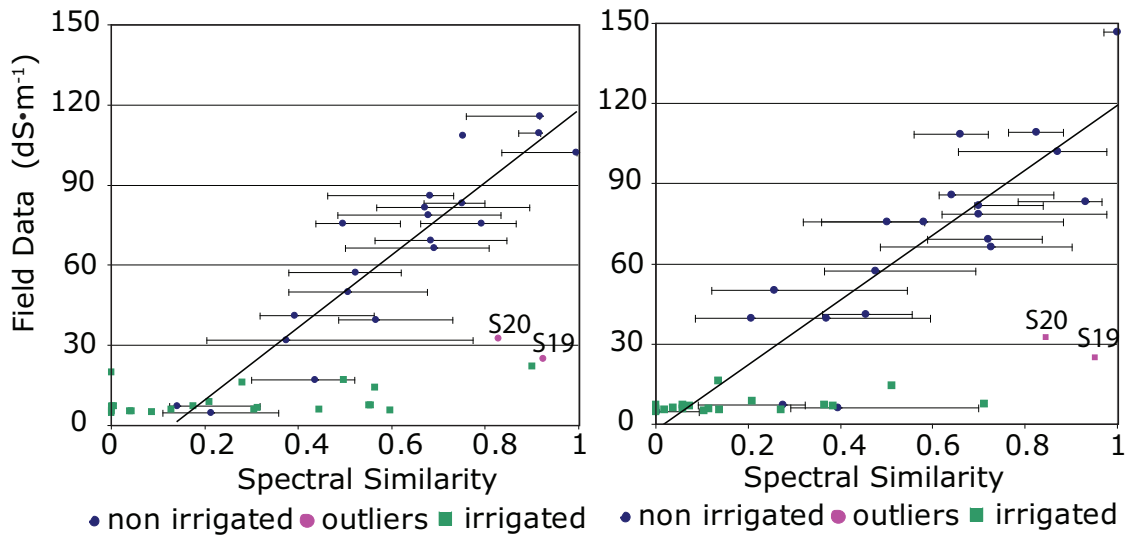


Figure 4.16: Field data (y-axis) vs. pixel similarity (x-axis) for November 11<sup>th</sup>, 2002 (left) and March 28<sup>th</sup>, 2001 (right). Green points are from irrigated areas, blue points from non-irrigated sites.

10 cm. At all other sites, such small values were observed at depths of at least 60 cm. The interpretation of EM38 data yields an average electrical conductivity of the first 30 cm. The uncalibrated salinity maps, which take into account the surface only, therefore overestimate electrical conductivity values. The shape of an electrical conductivity profile depends on the soil type. The clay content determines the relationship between depth and evaporation and therefore the distribution of salt in the soil column. If a soil map is available, different relations between field data and remotely sensed data could be developed for every soil type.

Besides stations S19 and S20, the image of March 28<sup>th</sup> 2001 has an additional outlier (not printed in the plot). This point fitted well into the correlations obtained for all other images. The reason why the surface composition was different on March 28<sup>th</sup> compared to all other dates cannot be explained with the available data. Images recorded in winter time and processed with SCM showed the best correlation between spectral similarity and field data. However, the spectral flatness of the summer images did not allow to distinguish satisfactorily between saline and non-saline pixels using the SCM.

### 4.3.3 Field data vs. NDVI

Compared to the SCM, the NDVI showed higher correlations between raster and field data for images obtained in summer. A comparison of the two methods for the same date (September 3<sup>rd</sup> 2003) is shown in figure 4.17.

The left hand side of this figure plots the relation between field data and spectral similarity. Even non-saline pixels still have a spectral similarity of 0.4. The



right hand side of figure 4.17 plots the relation between field data and the NDVI. As expected, the smallest NDVI values are found around the most saline stations. Despite all the implicit assumptions made by defining the NDVI as an uncalibrated salinity map (see section 4.1.3), a correlation could be established, see table 4.3. Another comparison between SCM and NDVI for a summer image is presented in figure 4.18. The spectral similarity of the pixels is too high to distinguish between saline and non-saline areas. However, a significant correlation between field data and the NDVI was found, see table 4.3.

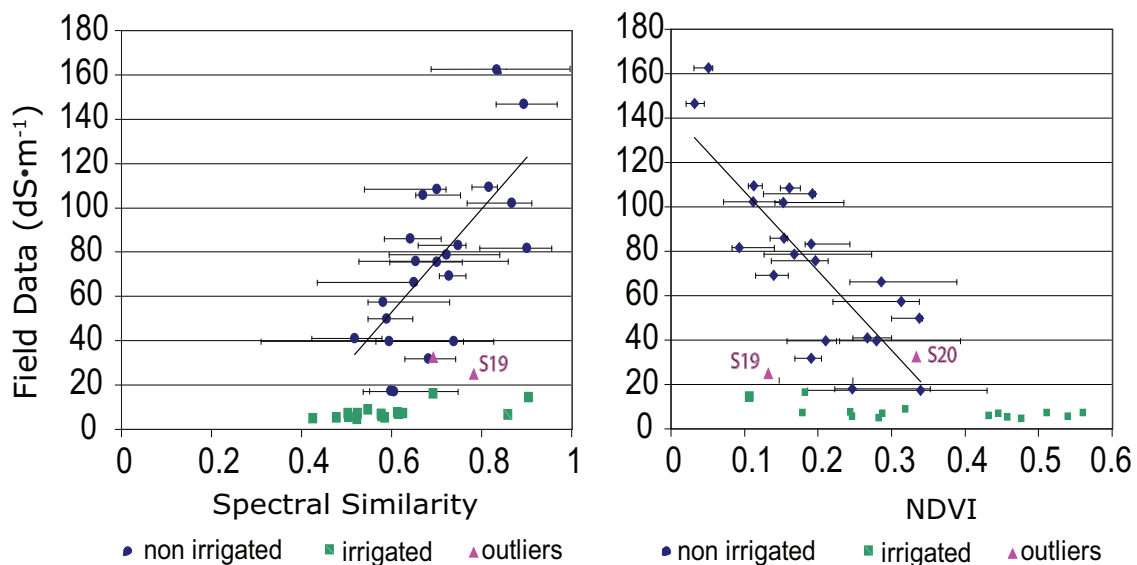


Figure 4.17: Field data vs. spectral similarity and NDVI (September 3<sup>rd</sup> 2003).

#### 4.3.4 Summary of obtained relations between field data and uncalibrated salinity maps

Compared to the NDVI-field data relations, correlation coefficients are remarkably higher if the uncalibrated salinity maps were obtained with the Spectral Correlation Mapper. The highest correlation coefficients were found with the image obtained on November 13<sup>th</sup>. This image was closest in time to the measurements over the non-irrigated sites in September 2002.

## 4.4 Conclusions

The aim of this study was to map the electrical conductivity of the soil. The correlations found between field data and raster data allowed to scale the 5 uncalibrated salinity maps to continuous electrical conductivity maps. The combination of methods on different scales was the key to the derivation of such maps. The combination

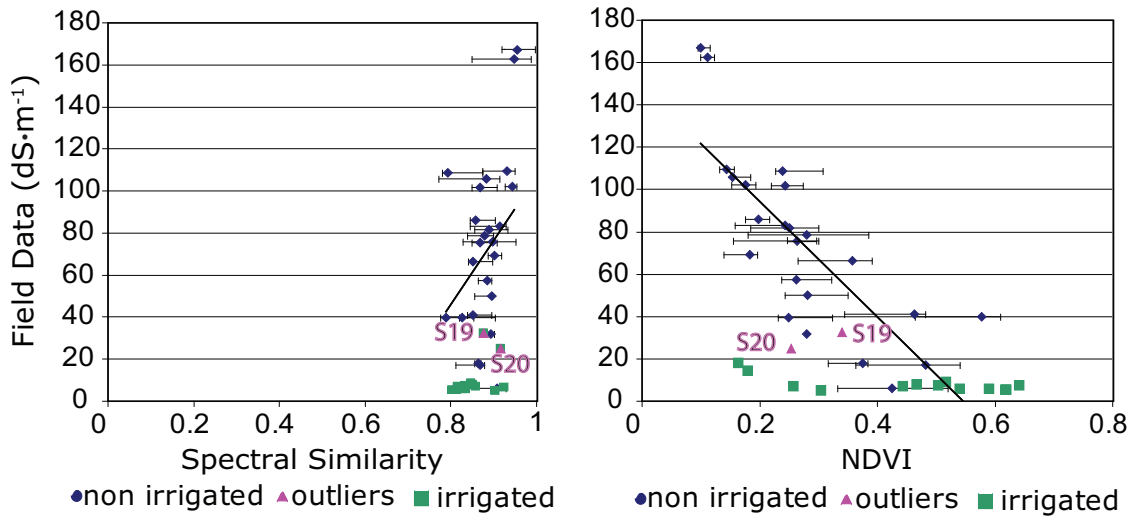


Figure 4.18: Field data vs. spectral similarity and NDVI (August 12<sup>th</sup>, 2001).

Table 4.3: **Linear relationships between uncalibrated salinity maps and field data.** The correlation coefficients between field measurements and spectral similarity for the images of August 12<sup>th</sup>, 2001 and September 3<sup>th</sup>, 2003 are below 0.5 and are not printed explicitly.

	Function	R <sup>2</sup>
28 March 2001	$y = 121.4x - 2.1$	0.74
3 September 2003 (NDVI)	$y = -357.9x + 142.7$	0.61
11 November 2002	$y = 135.5x - 17.4$	0.85
12 August 2001 (NDVI)	$y = -272.0x + 148.8$	0.63
13 November 2001	$y = 228.7x - 110.9$	0.75

of soil samples with the EM38 allowed to map large areas within a reasonable time period. By using saturated paste conductivities as a reference, the values obtained are independent of the field conditions. Even though quantifying salinity by using the EM38 is fast, no continuous map can be produced over a large area. Only the combination with remotely sensed data allows to produce a conductivity map over such a large area.

The accuracy of the electrical conductivity maps depends on the quality (and consistency) of the field data, and on the extent to which the string of assumptions made to combine these two methods is fulfilled. In the case of the Yanqi basin, the quality of the field data does not limit the reliability of the method, as data are consistent between the different methods and the outliers could be explained. Very high correlation coefficients between saturated paste conductivities, interpreted EM38 measurements as well as inverted resistivity soundings were found.

One assumption made when combining the two methods was that the electrical conductivity profiles at all stations are similar. The outlier stations 19 and 20 do not fulfill this condition. If the shape of the electrical conductivity profiles varies considerably, this method will yield wrong results. If there is a large variation of soil types within the area of interest, field data should be obtained on every soil type separately. Consequently, the relation between field data and remote sensing data should be examined for every single soil type.

This method can be applied to other regions, provided the same assumptions are fulfilled. The presence of sufficiently large and well distributed, non-irrigated areas (preferably several times the extent of a pixel) is required. This is often the case, as areas between fields are usually large enough to fulfill this constraint.



## Chapter 5

---

### Digital Terrain Modelling

The spatial distribution of salt at the soil surface is strongly determined by the evaporation flux from the aquifer to the atmosphere. This quantity is dependent on the depth to groundwater. A precise digital elevation model (DEM) as well as the distribution of its errors are therefore required. Preprocessed DEMs are provided for free through the internet but most of them have large errors. An alternative to the preprocessed DEMs is to calculate DEMs on the basis of stereo radar images. Highly resolved and precise digital elevation models can be obtained by using synthetic aperture radar (SAR) data and interferometry techniques. This standard method was described by Zebker & Goldstein (1986). The DEMs obtained do not provide absolute elevation above datum. Measurements on the ground are required to scale the relative DEM to the absolute height in a defined ellipsoid system.

The construction of a digital elevation model for the Yanqi basin consisted of several steps: First, the applicability of existing DEMs was checked. As these models could not be used for the Yanqi project, two relative DEMs covering most of the project area were calculated by using interferometry techniques. These relative DEMs were scaled to absolute values by using height measurements on the ground (ground control points or GCP). The areas not covered by the radar images were patched by using available data (but with a lower spatial resolution) from the radar topography mission, the best available DEM of the region. In a final step, the DEMs were scaled to absolute height quantities.

#### **5.1 Generation of the DEM by using radar images, measurements on the ground and SRTM data**

##### 5.1.1 Preprocessed DEMs

Several sources offer elevation models on a global scale. The USGS provides a hydrologically corrected elevation model on a 1 km to 1 km resolution basis ([http://edcdaac.usgs.gov/gtopo30/hydro/as\\_dem.asp](http://edcdaac.usgs.gov/gtopo30/hydro/as_dem.asp)). Both the insufficient accuracy (30 m) and the unsatisfactory spatial resolution do not allow to use this model in the context of this project. Spatially highly resolved DEMs (30 m resolution) based on multispectral ASTER data are calculated on demand and provided by the EOS data gateway (<http://edcimswww.cr.usgs.gov/pub/imswelcome/>). Several absolute DEMs over the Yanqi basin have been ordered and verified with ground control points. Unfortunately, the verification with ground truth could not confirm the accuracy claimed by the provider. The residuals between measured and calculated elevations were on average 18 m. The latest and best source for elevation data is based on records of the shuttle radar topography mission (SRTM), carried out

in 2002. The DEMs have been available since the year 2003. They feature a spatial resolution of 90 m to 90 m (<http://www2.jpl.nasa.gov/srtm/>). The verification with ground truth has shown that the SRTM-DEM is the only usable free source of topography data. These data were used to fill up the northern fringes of the Yanqi basin, which were not covered by the radar images.

### 5.1.2 A brief introduction to SAR interferometry

A detailed description of the fundamentals of Synthetic Aperture Radar (SAR) is beyond the scope of this dissertation, but a short introduction is helpful to understand how interferometry works. The information provided in this section is based on an introduction published by Curlander & McDonough (1991). SAR data can be transformed into two dimensional images. One dimension is called range and is a measure of the distance from the radar antenna to the target in the line of focus of the satellite. Like any other radar system, the range is determined by measuring precisely the time between the transmission of a signal to the receiving of the echo from the target. The second dimension is called azimuth and is perpendicular to the range. The main difference between SAR to other radar systems is its ability to produce a fine azimuth resolution. To obtain this high resolution, a physically large antenna would be required to focus the transmitted energy into a sharp beam. Fortunately, a fine resolution can be obtained without a large antenna: The spacecraft can fly the distance of the required length of the antenna, this distance is called synthetic aperture. The basic geometrical model for SAR interferometry is shown in figure 5.1.  $A_1, A_2$  are the antenna position,  $z_{ac}$  is the elevation of the satellite,  $B_i$  is the baseline,  $R_1, R_2$  the vectors from the antenna to the point of interest and  $\psi$  the angle between  $R_1$  and the baseline vectors. A target's position along the flight path determines the doppler frequency of its echoes. Targets ahead of the space- or aircraft produce a positive doppler offset, targets behind it a negative one. The position of the target can therefore be identified on the basis of the doppler shift. Based on the decoded doppler shift as well as the range and azimuth information a geo-coded raster map can be constructed.

The information of every pixel of this image consists of the magnitude of reflectivity and the phase. The phase of a pixel consists both of a deterministic and a stochastic part. With the proper selection of two images it is possible to eliminate the statistical part simply by subtracting the phase. Representing a corresponding pair of pixels  $P_1$  and  $P_2$  from two matching images, the complex quantities can be written as:

$$\begin{aligned} P_1 &= a_1 \cdot e^{i(\theta_1 + \Phi_1)}, \\ P_2 &= a_2 \cdot e^{i(\theta_2 + \Phi_2)} \end{aligned} \tag{5.1}$$

with  $a_1$  and  $a_2$  representing the magnitude of each pixel ("image intensity"),  $\Phi_1, \Phi_2$  the random, and  $\theta_1, \theta_2$  the deterministic components of the phase. The multiplica-



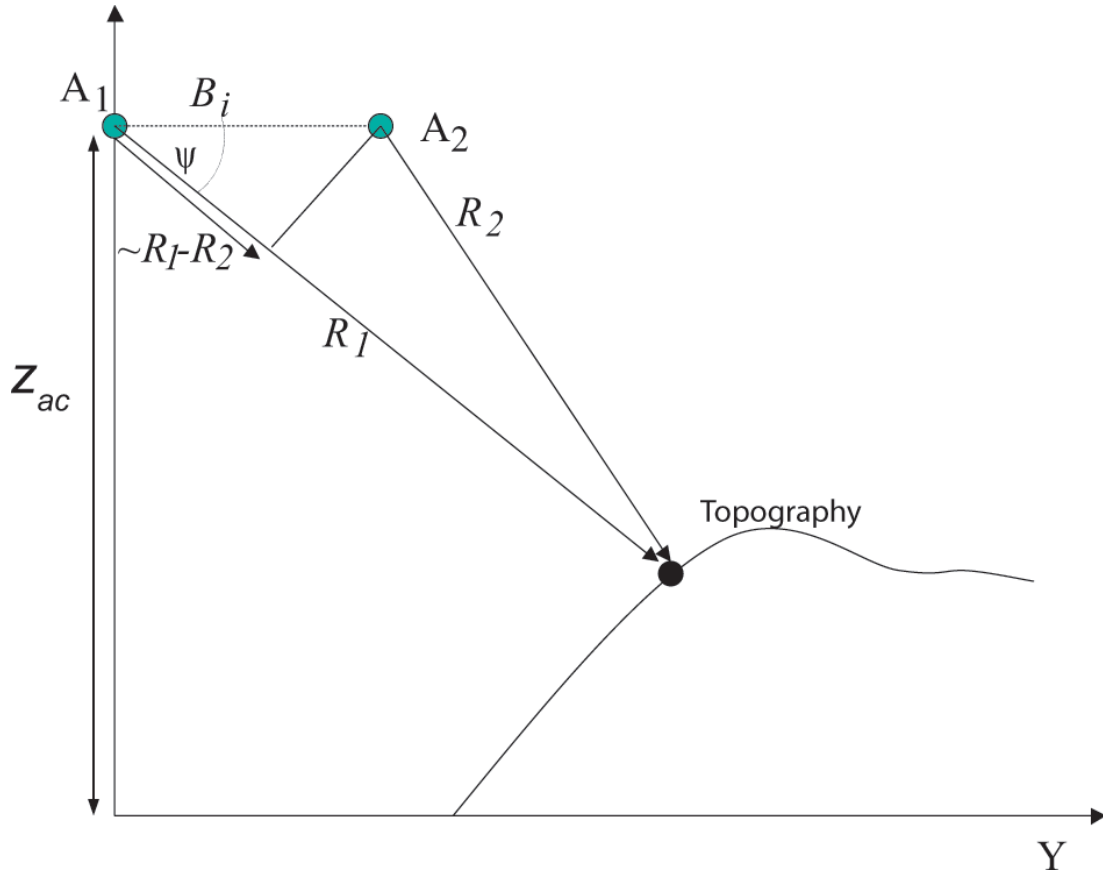


Figure 5.1: Schematic sketch of the geometric model used for SAR interferometry.

tion of one image with the complex conjugate of the second one on a pixel by pixel basis yields the phase difference, also called interferogram I:

$$I = P_1 \cdot P_2' \quad (5.2)$$

with  $P_2'$  being the complex conjugate of  $P_2$ . The phase value can be related to the wavelength  $\lambda$  and the distance  $R_i$  between the antenna and the point of interest i:

$$\Phi_i = \frac{4\pi \cdot R_i}{\lambda} \quad (5.3)$$

A pair of images selected must fulfill special geometric conditions to ensure that the random components are nearly identical. If this prerequisite is fulfilled,  $\theta_1$  and  $\theta_2$  as well as  $a_1$  and  $a_2$  are nearly equal. The interferogram I can therefore be written as:

$$I = a^2 \cdot e^{-i\left(\frac{4\pi}{\lambda}\right)(R_1 - R_2)} = a^2 \cdot e^{i\phi_{12}} \quad (5.4)$$

by using  $a_1 = a_2 = a$ , the phase  $\phi_{12}$  turns into

$$\Phi_{12} = \frac{4\pi \cdot (R_2 - R_1)}{\lambda} \quad (5.5)$$

With the following approximation the interferogram can be related to the depression angle  $\psi$  (compare figure 5.1):

$$R_2 - R_1 \approx B_i \cdot \cos(\psi) \quad (5.6)$$

Therefore equation 5.5 can be written as

$$\Phi_{12} \approx \frac{4\pi \cdot B_i \cdot \cos(\psi)}{\lambda} \quad (5.7)$$

The distance ( $R_2 - R_1$ ) includes many wavelengths, but the quantity calculated is only the phase difference ranging from 0 to  $2\pi$ . Height values are related to an unknown multiple of  $\pi$ . This ambiguity is called the wrapped phase problem, as illustrated in figure 5.2. However, relative height differences between targets can still be calculated. The differential of equation 5.7 provides this relative measure:

$$\frac{\Delta\phi}{\Delta\psi} = -\frac{4 \cdot \pi \cdot B_i}{\lambda} \sin(\psi) \quad (5.8)$$

or

$$\Delta\psi = -\frac{\lambda}{4 \cdot \pi \cdot B_i \cdot \sin(\psi)} \Delta\phi_{12} \quad (5.9)$$

Therefore two pixels in the interferogram that differ in phase by  $\phi_{12}$  represent scatter differing in depression angle by  $\Delta\psi$ . A change in phase is related to a change in height  $\Delta h$  (see figure 5.3):

$$Z_{AC} - \Delta h = \frac{Z_{AC} \cdot \sin(\psi - \Delta\psi)}{\sin(\psi)} \quad (5.10)$$

By using a small angle approximation and by substituting equation 5.9 into equation 5.10, the difference in height can be calculated:

$$\Delta h = -\frac{\lambda \cdot Z_{AC} \cdot \cot(\psi)}{4\pi \cdot B_i \cdot \sin(\psi)} \Delta\phi_{12} \quad (5.11)$$

The interferometric model has to be unwrapped to obtain a continuous function or, in other words, the correct multiple of  $2\pi$  has to be obtained. Advantage is taken of the fact that unwrapping is easy in flat regions. After successfully unwrapping flat areas, the steeper regions can be unwrapped step by step. An already existing DEM is very helpful in the process of unwrapping, even if its quality is low.

Best results for interferometry techniques are obtained with dual antenna systems or a pair of satellites following each other within a short distance. The ERS satellites were designed mainly for this purpose and allow to obtain high quality results. The data used to calculate a DEM for the Yanqi basin was collected by ERS1 and ERS2.

Interferometry techniques can only be applied over dry areas, not over open water surfaces or very moist areas. Such areas have to be interpolated.

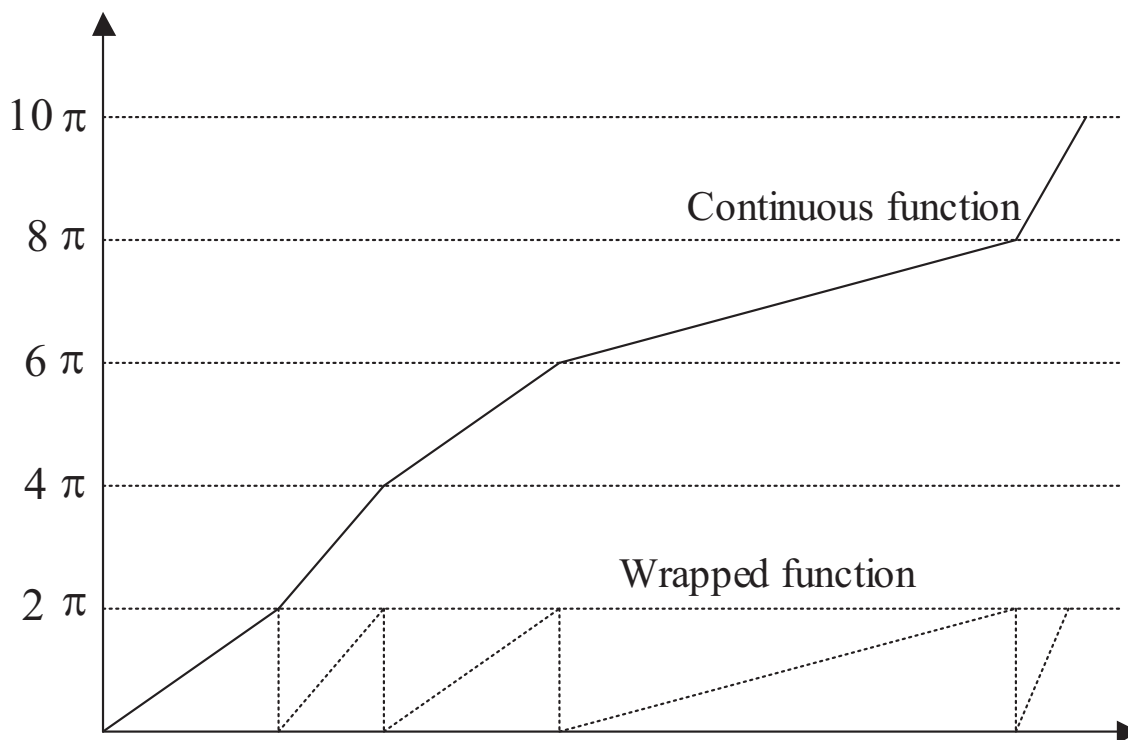


Figure 5.2: Continuous and wrapped phase function.

### 5.1.3 Calculating relative DEMs for the Yanqi basin by using SAR interferometry

The software package EV-INSAR (Atlantis Scientific, 2001) was used to generate the DEMs. No ERS-tandem pair covering the total area of interest existed. Therefore two tandem pairs were required. The coverage of these two images is shown in figure 5.4. The following ERS images were ordered: ERS1: 23.3.1999 and 17.3.1996 (track/frame: 119/2763), ERS2: 24.3.1999 and 18.3.1996 (track/frame: 119/4754).

The first step to calculate a DEM is the image to image co-registration. A detailed description of this procedure can be found in Zebker & Goldstein (1986). The critical input of this step is the position of the satellite at the time the raw image was produced. Orbit data are included in the image meta-data, but their accuracy is poor. The Delft Institute for Earth-Oriented Space Research (<http://www.deos.tudelft.nl/ers/precors/orbits/>) provides precise ERS1 and ERS2 orbits with much higher accuracy by using more sophisticated gravity models than the European Space Agency (Scharroo & Visser, 1998). Radar system noise as well as undesired speckle effects have to be filtered out before the generation of the interferogram. The algorithms used by EV-INSAR to correct speckle effects and to filter out radar system noise take antenna-specific effects of the ERS system into account (Atlantis Scientific, 2001).

After the image to image co-registration and the filtering of the images, the inter-

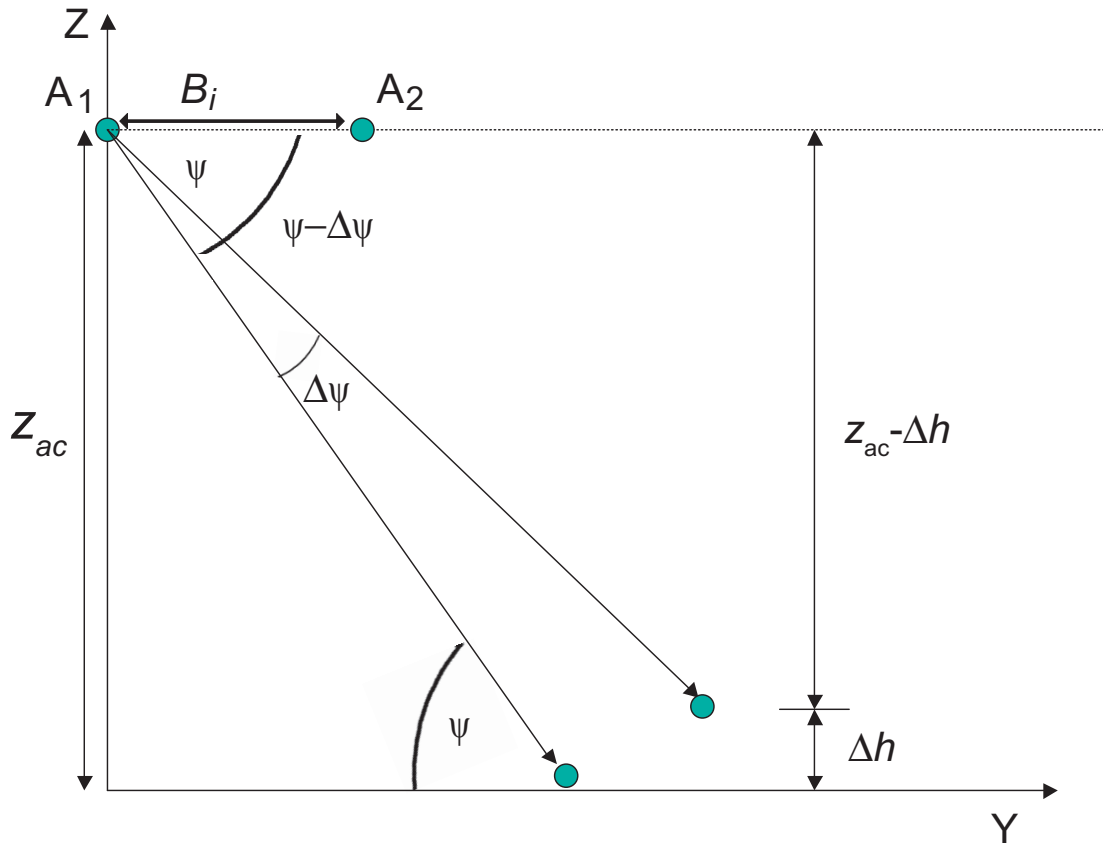


Figure 5.3: Collection geometry of the interferometric model. The parameters are explained in the text.

ferogram was calculated and the phase unwrapped. To reduce potential unwrapping errors, a crude DEM (GTOPO30) was used to ensure the smooth unwrapping of the phase. The result of the phase unwrapping is a relative DEM.

The spatial resolution of a DEM calculated by using interferometry techniques is the result of an optimization between the overall accuracy and the spatial resolution. It depends on the accuracy of the image to image co-registration as well as the signal quality and the spatial distribution of the GCP. For scaling elevation data and determining the optimal cell resolution, accurate ground control points (GCPs) are essential. Good ground control points are easily identifiable features on both the draft DEM and a multispectral image, see figure 5.5.

## 5.2 Postprocessing

### 5.2.1 Obtaining ground control points

GCPs were obtained by using differential GPS (d-GPS) during the fieldwork in 2002. With d-GPS, the elevation of a location can be measured within a range of

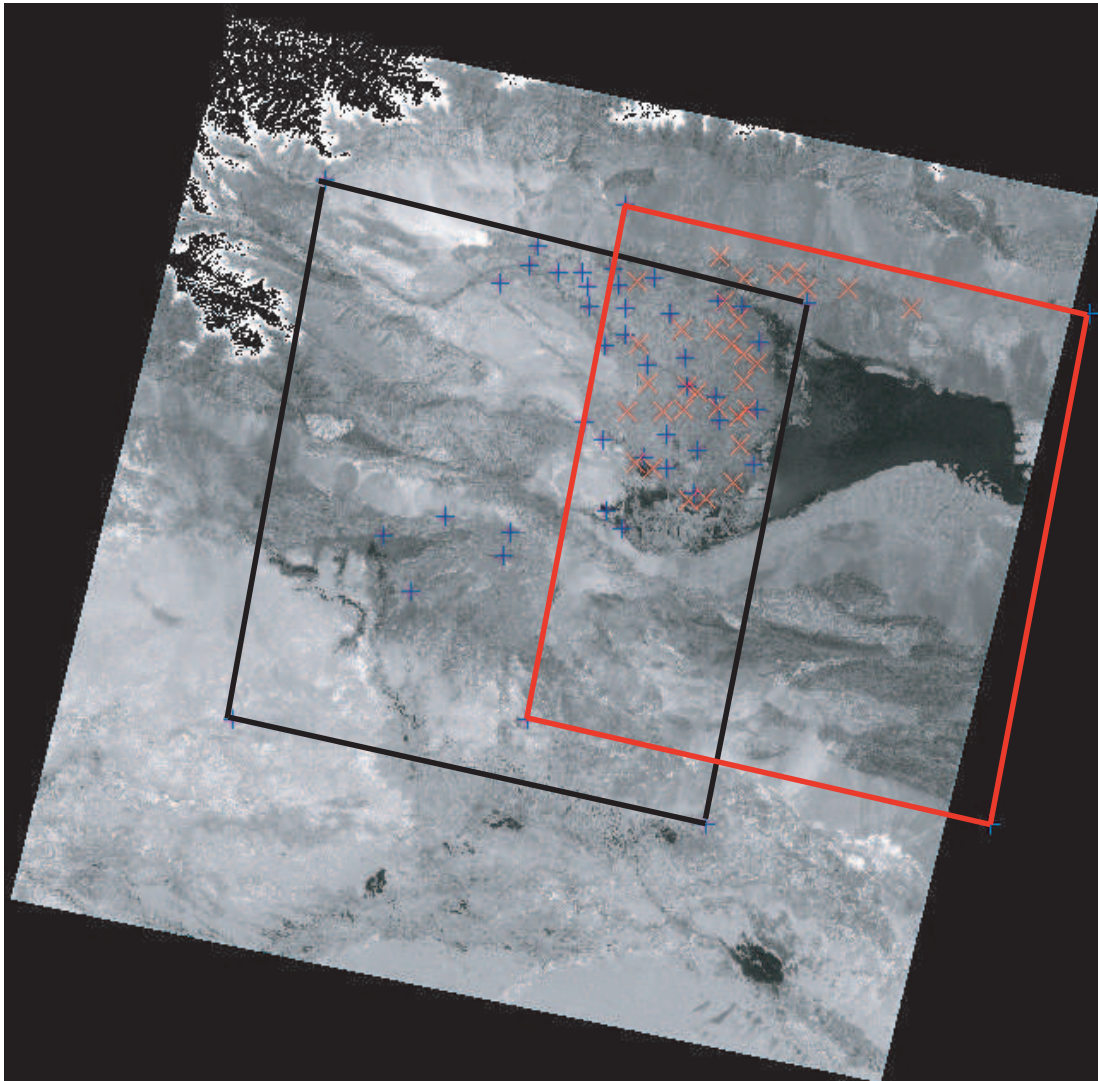


*Figure 5.4: The black and the red box show the coverage of the two tandem pairs. The crosses indicate the locations where ground truth was measured. The different colours of the crosses indicate in which DEM their location has been predefined.*

centimeters. Over 200 potential GCPs were preselected before the field campaign by using the panchromatic channel of a Landsat image and the draft DEM. In the field, 72 points have been documented. The limited amount of time made it impossible to measure all the preselected points. High buildings and trees cause a scatter of the GPS signals additionally reducing the amount of suitable ground control points. The most accurate results are obtained at locations with a clear view of the sky. Another factor reducing the number of GCPs was of a political nature. The Chinese army has a missile test site in the area of Bostan lake. All access to this region (even without sophisticated mapping equipment) is forbidden.

The locations of the documented GCPs are plotted in figure 5.4. The net of



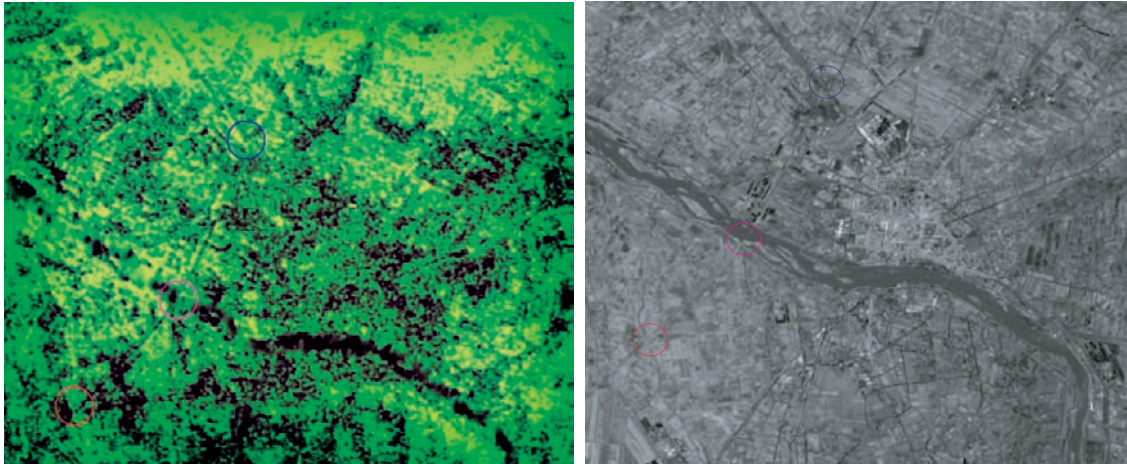


Figure 5.5: Examples of easily identifiable points in both the draft DEM and a panchromatic image (Landsat).

these GPS points covers an area of about 100 km in both the east-west and the north-south directions. Within this area, the selected points are evenly distributed. Measuring the height and location at a specific site takes over 1.5 hours. During this time, a huge amount of data is collected by two GPS receivers. The interpretation of data and their conversion to topographical elevation was carried out in a master thesis (Frick, 2002) at the Institute of Geodesy and Photogrammetry, ETH Zurich. The accuracy within the net of ground control points is very high: the measured coordinates have an average error within the range of 3 cm along the fringe of the net, in the central area the location is known with an accuracy as close as 1 cm. The accuracy of elevation data is independent of the location. Within the coordinate system applied, the WGS84 ellipsoid system, the accuracy is 2 cm.

These 72 ground control points were used to determine the optimal spatial resolution of the final DEM as well as to scale the relative draft DEM to heights in the WGS84 ellipsoid system. A comparison of the overall accuracy of several DEMs with a different spatial resolution showed that the accuracy significantly declined for resolutions finer than 20 m. The final resolution of the DEMs was therefore set to 20 m.

### 5.2.2 Coordinate systems and geoid correction

The relative DEMs were scaled by using the measured ground control points. All coordinates and heights obtained are in the WGS84 ellipsoid system. To directly compare these data with Chinese maps, a height and coordinate translation into this Chinese system had to be carried out. This step was far more difficult than expected. In the Yanqi basin, a local Chinese coordinate system is used and all height values on maps are within this projection. For unknown reasons, the required translation parameters of the Chinese coordinate system were not made available



by the responsible department. A d-GPS measurement at 3 Chinese fix points with known position and height (in the local system) could be used to calculate the translation parameters. Several fix points exist in the Yanqi basin, but only two could be located. Most of these fix points were set up 40 years ago and the best map available showing the location of these points was at a scale of 1:200'000, making it extremely difficult to locate them. Moreover, many of the fix points have been destroyed due to different land use or construction work. However, two points could still be located. A third point could not be located in the field and the data required for the transformation had to be read out of a map. This third point was chosen in a very flat area, so that a shift in position does not imply a large shift in altitude. Frick (2002) estimated that the largest error due to the uncertainty in location would result in 50 m error in the x-y direction, while the uncertainty in altitude is in the range of 3 m. Due to this uncertainty, all modelling approaches were carried out in the WGS84 coordinate system. Information compiled in the Chinese system such as the locations of boreholes was reprojected into the WGS84 system.

To transform the geodetic heights of the WGS84 system into orthometric heights, the geoid undulation (the difference between the geoid elevation and the ellipsoidal elevation) has to be subtracted from the heights in the WGS84 system. The US national geospatial intelligence agency provides a worldwide geoid model (<http://164.214.2.53/GandG/egm96/intpthel.htm>). For most of the Yanqi basin, the geoid undulation is around -61 m. In the northernmost parts of the project the undulation is around -62 m. The DEM was corrected for the geoid undulation. After this correction the lake shore is on average at 1047.2 m. This is very close to the heights reported on the Chinese maps (1047 m) and suggests that the (to us unknown) geoid used by the Chinese mapping agency must be nearly identical to the geoid presented by the geospatial intelligence agency.

### 5.2.3 Merging the single DEMs into one

The relative DEMs calculated with the methods described above have an overlapping area (see figure 5.4). To ensure continuous values along the cut-line, synthetic GCPs were introduced. Figure 5.4 indicates the area covered by the DEM obtained by using SAR. The northern areas of the Yanqi basin are not covered by the DEM. The quality of the SRTM-DEM was verified in comparison to GCPs. The average error between measured and observed heights was very similar compared to the error of the SAR-DEM. A 3-dimensional mosaic image of the final DEM is presented in figure 5.6.

### 5.2.4 Patching wet areas

Due to the high dissipation, interferometry techniques cannot be applied to open water surfaces. Open water surfaces and very moist areas have therefore to be

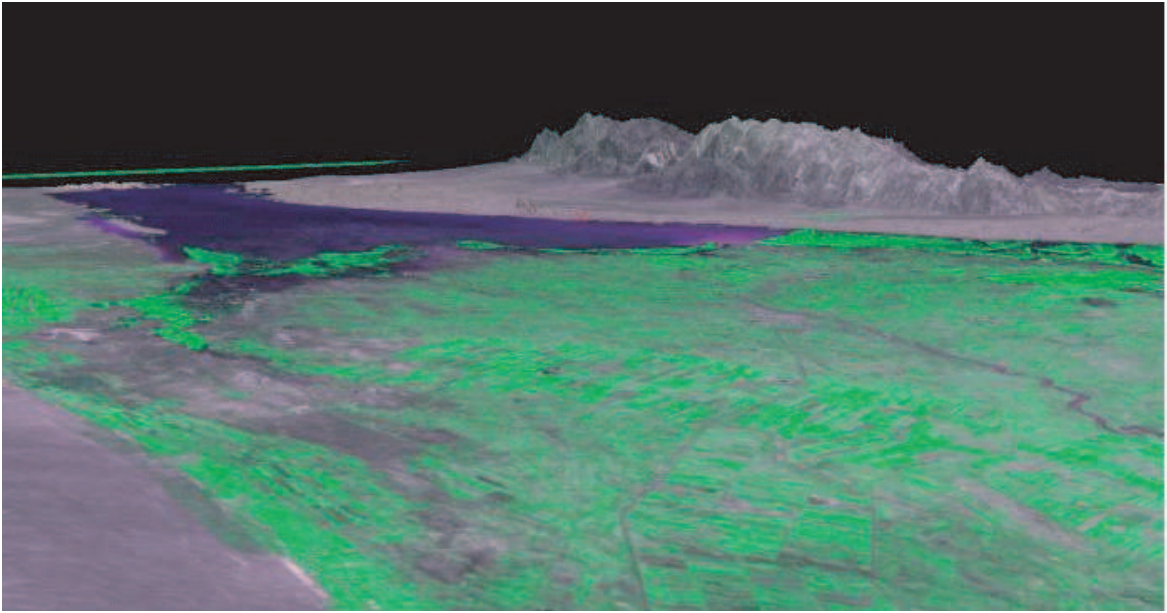


*Figure 5.6: 3-dimensional, vertically exaggerated view of the Yanqi basin (NW to SE), overlaid with a Landsat colour composition.*

interpolated. Various algorithms have been developed to cope with this problem. In the Yanqi basin, these areas consist of the entire Bostan lake area as well as the rivers and the recently irrigated fields. Methods have been developed to interpolate faulty terrain data. A multisurface technique to interpolate DEMs has been developed and successfully applied by Wang (1990). This method was used here.

The quality of this interpolation can be verified along the river reaches, as the slope along downstream river cells must be negative. After patching wet areas (except for the area of Bostan lake) by using the multisurface technique, the drainage net of the Yanqi basin was applied to check if the flow direction could be reproduced only on the basis of the DEM. In the very flat areas of the basin, over 5% of the river cells were higher than their upstream neighbors. However, in these areas the slope is so small that already a small error in elevation will change the slope. If necessary, the elevation data were corrected by using an algorithm developed by Hellweger & Maidment (1997). This algorithm requires the location of the drainage net and the height values around these cells. The interpolation is then performed with the constraint that the elevation must decline downstream. After the elevation has been corrected for the inconsistent river cells, the final DEM can be compared to the measured heights.

The bottom of Bostan lake was obtained by subtracting a series of depth measurements obtained by the local Water Resources Management Office in Korla (unpublished data) from the reference stage of the lake (1047 m).

### 5.2.5 Verification and resampling of the elevation model

The residuals between measured and calculated elevation are presented in figure 5.7. The largest errors are found outside the area of interest, along the steep slopes in

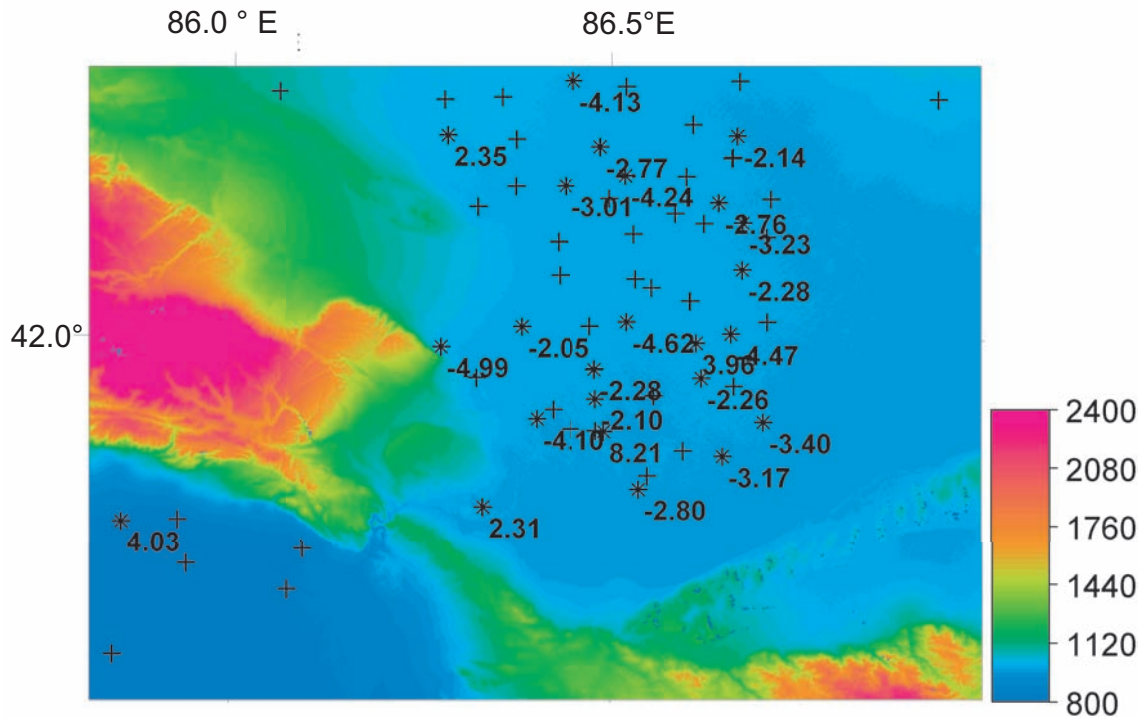


Figure 5.7: The raster map represents the digital elevation model [m.a.m.s.l.]. The crosses indicate measurement stations of DGPS, with an error smaller than 2 m. Only residuals larger than 2 m are plotted.

the northern areas of the basin. The average accuracy of this DEM is around 1.5 m. This is higher than what is generally expected from interferometry techniques. The relatively large amount of fix points as well as the integration of very accurate orbit data made higher accuracies possible. With the obtained ground control points, the SRTM DEM of the project area can also be verified. The average accuracy was around 2.5 m and therefore of a quality comparable to the DEM calculated on the basis of radar images. If the SRTM data had been available at the beginning of the project, this free data set could have been used instead. However, the most time consuming part in the construction of the DEM, obtaining ground truth, cannot be skipped. Even if the SRTM data is an absolute measure of elevation, a verification of the accuracy with independent ground control points still has to be carried out.

Even if the average error is only around 1.5 m, the local error is still large considering the high sensitivity of phreatic evaporation to the depth to groundwater.

The largest error within the area of interest is 4.24 m. For many reasons, the resolution of the groundwater model is not as fine as the resolution of the DEM (see chapter 7). The dependencies on the pixel resolution of the average error as well as the minimum and maximum elevations included in a coarse model pixel are presented in figure 5.8. The average error is insensitive to changes in the cell

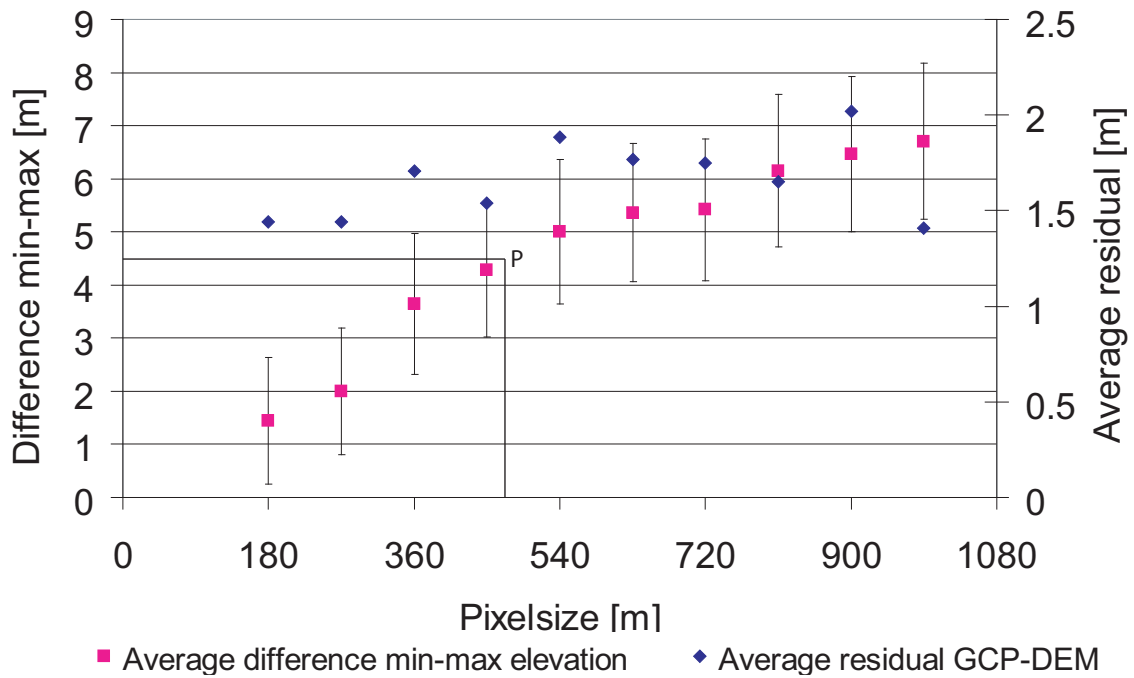


Figure 5.8: Difference between the minimum and the maximum value of the fine resolution DEM within a coarse pixel as a function of spatial resolution. Moreover, the average residuals are plotted.

resolution. This is not astonishing, as the terrain slope does not change significantly by resampling the cells. If the cell resolution is set to 500 m by 500 m, the average difference between the minimal and maximal elevation is around 4 m (see point P in figure 5.8). This difference is close to the highest residual between calculated and observed data in the area of interest. If a cell resolution of 500 m by 500 m is used, (this is the cell resolution in the groundwater model), the information lost by resampling the fine DEM to a coarse resolution is of the same magnitude as the highest residual in the area of interest.

Even though the slope along the rivers was corrected for the fine resolution, the constraint of a positive slope along the river and drains has to be verified in the coarse DEM. Elevation data in the upstream of all rivers fulfilled this criterion. In the very flat areas around Bostan lake, the slope of around 10% of the river and drain pixels and their upstream neighbors was negative or zero for a cell resolution of 500 m.

## Chapter 6

---

# Evapotranspiration and Infiltration

Evapotranspiration (ET) is the sum of the transpiration (T) from vegetation and the evaporation (E) from bare soil. The separation of these two quantities is important because they are related in different ways to the water and salt balance. Only if the groundwater table is high enough, a portion of the infiltrating water will evaporate from the groundwater through capillary rise. This flux is in the following called phreatic evaporation. It transports salts that have been stored in the unsaturated zone to the soil surface. Compared to the salt concentration of the irrigation water drawn from the Kaidu river, the salt concentration in the soil water is much higher. To model the water balance, three important factors related to evapotranspiration have to be quantified: The absolute value of ET, the ratio of transpiration to evaporation as well as the relation between the depth to groundwater and the resulting evaporation rate.

Various methods have been suggested to estimate the rate of evapotranspiration from vegetation and bare soil. These methods include energy budget calculations, the extrapolation of free surface water pans or empirical techniques which relate evaporation to average climatic factors. In this thesis, potential evapotranspiration and actual crop transpiration were calculated by using the standard methods suggested by the FAO (see section 6.1). The pattern of evapotranspiration was calculated by using NOAA-AVHRR satellite images, as described in section 6.2. Evaporation from bare soil was calculated on the basis of  $\delta^{18}O$  profiles in the unsaturated zone (see section 6.3). This method takes advantage of the fact that the heavier composites of water (such as  $\delta^{18}O$ ) are enriched during evaporation. The combination of NOAA-images and the analysis of isotope data made it possible to separate transpiration from evaporation in the NOAA-images (section 6.4).

In the previous chapters it was stated that the distribution of salt in the top soil layer results from the distribution of phreatic evaporation. Both distributions have been calculated and can therefore be compared (section 6.5). The combination of the amount of irrigation water applied with the derived, actual crop transpiration data allows to quantify the infiltration rates (section 6.6). Finally, an input map of potential phreatic evaporation is calculated. Both the infiltration rates as well as the map of potential phreatic evaporation are important input parameters for the hydrological model.

### 6.1 Potential evapotranspiration and crop transpiration

The standard approach to calculate potential evapotranspiration is based on the Penman-Monteith equation. It is the combination of an energy balance and a mass transfer method. A detailed discussion of the Penman method is presented by Allen

*et al.* (1998). The Penman-Monteith equation includes all parameters that govern energy exchange and the corresponding latent heat flux (such as aerodynamic resistance or the bulk surface resistance). To make potential ET rates comparable for different areas, a reference crop as well as a reference surface resistance were defined by the FAO. By using these definitions, the only input data required to calculate potential ET are average daily temperature, wind speed as well as humidity. Unfortunately, no continuous daily data were available for a location in the Yanqi basin. Data for Korla, close to the project area, are provided for free by GLOBALSOD (<ftp://ftp.ncdc.noaa.gov/pub/data/globalsod>). These data sets were used to calculate potential ET. The annual potential evaporation is around  $1400 \text{ mm}\cdot\text{a}^{-1}$  (average value for the period 1990-1999).

To relate the potential evapotranspiration to a specific crop, the concept of the crop coefficient was introduced. Crop transpiration  $T_{veg}$  can be written as the product of a potential reference evapotranspiration  $ET_{pot}$  and a crop specific coefficient  $K_c$ :

$$T_{veg}(x, y, t) = K_c(x, y, t) \cdot ET_{pot}(t) \quad (6.1)$$

The FAO provides crop coefficient data for commonly cultivated crops. Tumarbay *et al.* (2003) tested equation 6.1 for winter wheat in several regions in Xinjiang. They concluded that the combination of crop coefficients provided by the FAO as well as the potential ET rates obtained by using the Penman-Monteith equation are an accurate measure for estimating transpiration in this region.

The Yanqi basin is split up into four irrigation areas. The crop mix as well as the corresponding  $K_c$  values are known for each irrigation area, transpiration rates can be calculated by using the available data. The transpiration data as well as the crop mix of the Yanqi basin are presented in table 6.1.

*Table 6.1: Crop mix and transpiration for the year 2001.* Besides the crops explicitly mentioned in this table, cotton, trees, grass and rice are also cultivated. Transpiration rates for specific crops were calculated by using equation 6.1.

	Area [%]	Area [km <sup>2</sup> ]	Transpiration [m·a <sup>-1</sup> ]
Wheat	22	289	0.74
Sunflower	12	150	0.7
Fruit	16	200	0.7
Sugarbeet	7.5	95	0.98
Vegetables	7.5	95	0.67
Other	35	433	0.95 (area- average)



## 6.2 Calculating evapotranspiration by using remote sensing techniques

Bastiaanssen *et al.* (1998) calculated actual ET with a surface energy balance (SEBAL), by using multi spectral satellite images (NOAA-AVHRR, 1 km resolution at NADIR). This algorithm requires several input parameters (such as the temperature data of several stations), which were not available. Therefore, a simplified SEBAL algorithm, S-SEBI (Roerink *et al.*, 2000), which requires less input data, was used. In both approaches, the actual evapotranspiration  $ET_{NOAA}$  is written as the product of the average daily net radiation ( $R_n$ ) and the evaporative fraction  $\varepsilon$ . The daily net radiation can be calculated from satellite imagery and astronomical data by using standard algorithms.

$$ET_{NOAA}(x, y, t) = \varepsilon(x, y, t) \cdot \overline{R_n}^{day}(x, y, t) \quad (6.2)$$

$$\varepsilon = \frac{\lambda E}{\lambda E + H} = \frac{\lambda E}{R_n + G_0} \approx \frac{\lambda E}{R_n} \quad (6.3)$$

$\lambda E$  is the latent heat flux or the actual ET,  $H$  is the sensible heat flux and  $G_0$  is the soil heat flux (all in  $\text{W}\cdot\text{m}^{-2}$ ). According to Roerink, the evaporative fraction for each pixel of the satellite image can be extracted by plotting all pixels of the image in a coordinate system of the surface temperature  $t_{surf}$  versus the ground albedo  $r_{surf}$  (see figure 6.1). Roerink's method assumes that pixels close to the line AB are completely wet, their temperature is therefore equal to the blending height temperature and correspondingly, the sensible heat flux is zero. In contrast, pixels close to the line BC are completely dry and the latent heat flux from those pixels is assumed to be zero. By using a rough model for the atmospheric surface layer, assuming uniform aerodynamic resistance, the evaporative fraction for each pixel can be graphically extracted from the plot. In figure 6.1, the example of a pixel located at P is shown. The evaporative fraction at pixel P is:

$$\varepsilon = \frac{\overline{PC}}{\overline{AC}} \quad (6.4)$$

14 NOAA-14 images for the year 2000 have been processed with S-SEBI. An annual ET map over the project area for the year 2000 is presented in figure 6.2. The patterns of evapotranspiration are clearly visible: ET is significantly increased by irrigation. The only area where water availability does not limit ET, Bostan lake, has the highest evaporation rates in the project area. However, the evaporation rates over Bostan lake are only around  $1000 \text{ mm}\cdot\text{a}^{-1}$ . This is small compared to the  $1400 \text{ mm}\cdot\text{a}^{-1}$  of potential ET calculated with the Penman-Monteith equation. The large surface of Bostan lake reduces the evaporation rate, but even if a reduction of the moisture gradient over the water surface is taken into account, the absolute values remain too low. One reason for this underestimation of absolute values of ET could be the high temperature difference between the Yanqi basin and the Tianshan

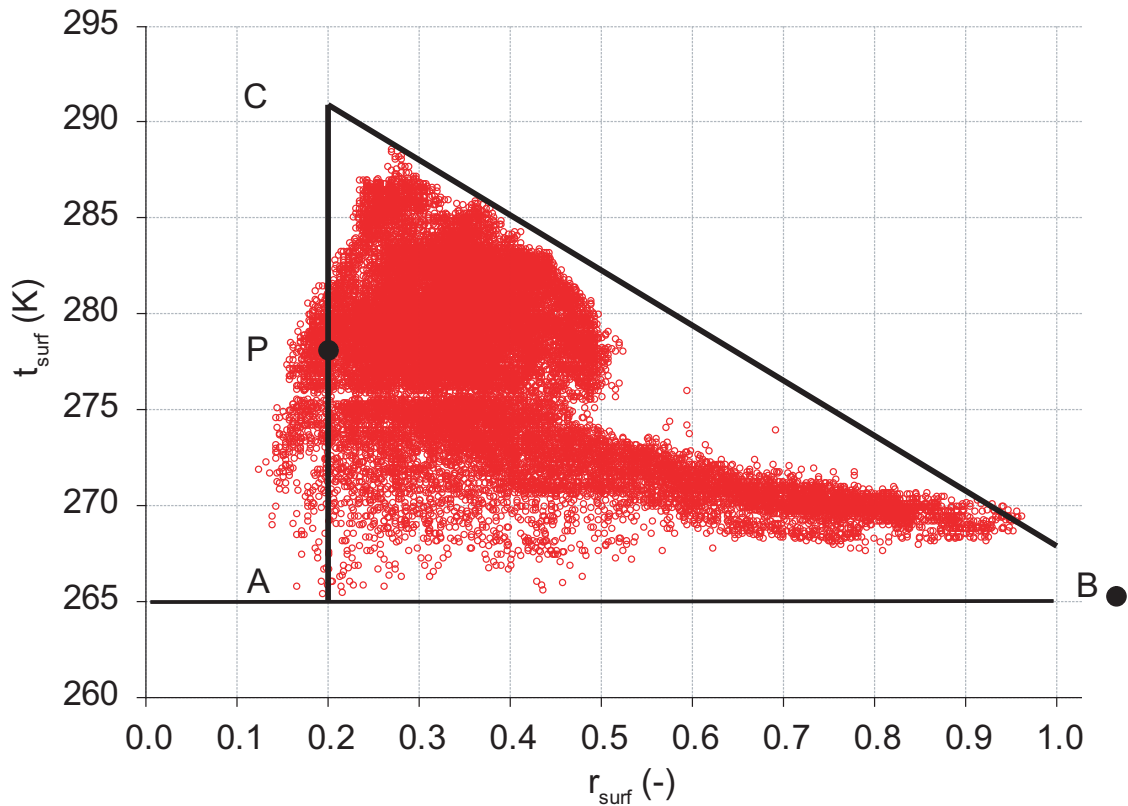


Figure 6.1: Example feature space plot for a NOAA-AVHRR image (27. Feb 2000). Pixels in the plot with surface temperatures below 275 °K and high reflectances are covered with snow. These pixels are located on the high peaks of the Tian Shan mountains.

mountains. SEBAL and S-SEBI relate different surface temperatures to changes in the energy balance (including the latent heat flux) and do not take into account temperature differences due to increased elevation. The minimal temperature in an image is reduced and therefore the evaporative fraction is underestimated. This effect also explains the relative high evaporation rates in area 1 indicated in figure 6.2. The elevation of this region is over 1 km above the Yanqi basin. The low temperatures are therefore not exclusively related to the cooling effect of water. Instead, the temperature difference is related to the increased terrain elevation. However, it is reasonable to assume that ET rates in areas with similar altitude are comparable.

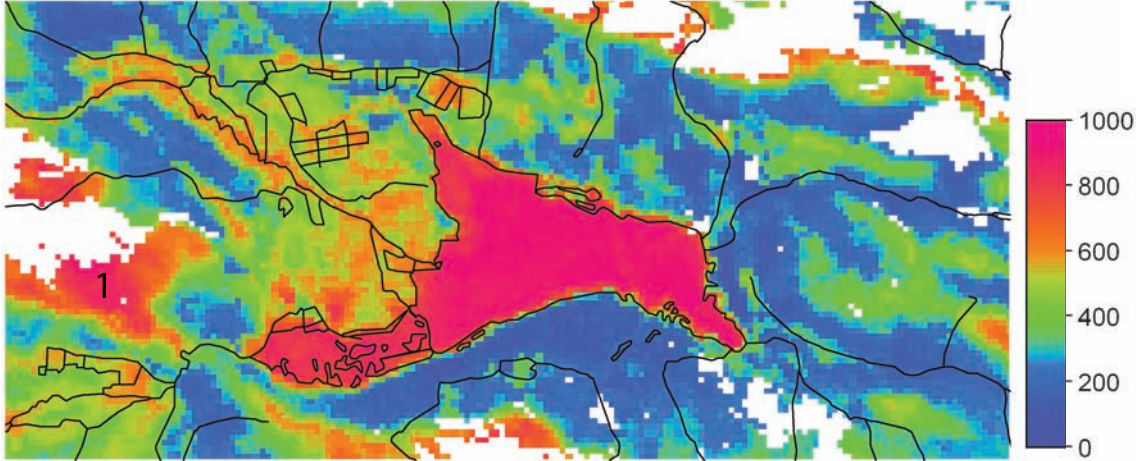


Figure 6.2: Evapotranspiration  $ET_{NOAA}$  [ $mm \cdot a^{-1}$ ] over the project area for the year 2000. The white pixels were covered with clouds in at least one image and therefore cannot be calculated.

### 6.3 Calculating phreatic evaporation on the basis of isotope profiles

Evaporation rates independent of vegetation can be calculated by using the distribution of stable isotopes in a non-irrigated soil column. If this distribution is measured at different sites with a different depth to groundwater, a relation between the evaporation rate and depth to groundwater can be established.

#### 6.3.1 Theoretical background

An analytical model describing the movement of isotopic components of water evaporating from a free water body into the atmosphere was developed by Craig & Gordon (1965). Zimmermann *et al.* (1967) demonstrated that the enrichment of deuterium in the soil water of a saturated soil column decreases with depth. The profile of deuterium could be approximated by an exponential function with a decay length approximately proportional to the evaporation rate. These findings were explained as the result of a superposition between diffusive and convective fluxes through the soil column. The isotopic profile in a saturated soil can be described by:

$$R(z) = R_{\infty} + (R_{eff} - R_{\infty}) \cdot e^{-\frac{z}{z_l}} \quad (6.5)$$

$R(z)$  is the isotopic signature as a function of the depth  $z$ ,  $R_{\infty}$  is the isotope ratio of the water entering the column from below.  $z_l$  is defined as:

$$z_l = \frac{\theta \cdot f \cdot D}{E_{P,ISO}} \quad (6.6)$$

where  $E_{P,ISO}$  is the phreatic evaporation rate [ $\text{m}\cdot\text{s}^{-1}$ ],  $\theta$  the volumetric water content,  $f$  the tortuosity factor and  $D$  the self-diffusion coefficient for liquid water.  $D$  is  $2.3\cdot 10^{-9} \text{ m}^2\cdot\text{s}^{-1}$  at  $25^\circ\text{C}$  (Mills, 1973) and the tortuosity factor for sandy soils is around 0.66. Barnes & Allison (1988) extended this concept to unsaturated soils. The isotopic profile in an unsaturated soil column can be expressed as a function of depth in analogy to equation 6.5:

$$R(z) = R_\infty + (R_{eff} - R_\infty) \cdot e^{-\frac{z-z_{ef}}{z_v+z_l}} \quad (6.7)$$

$z_{ef}$  is the depth of the evaporating front.  $z_v$  is defined as:

$$z_v = \frac{D_v \cdot N^{sat}}{\rho \cdot E_{P,ISO}} = \frac{(n - \theta) \cdot f \cdot D_v \cdot N^{sat}}{\rho \cdot E_{P,ISO}} \quad (6.8)$$

where  $D_v$  is the diffusion coefficient for water vapor in air ( $2.65\cdot 10^{-5} \text{ m}^2\cdot\text{s}^{-1}$ ),  $\theta$  is the density of water ( $1000 \text{ kg}\cdot\text{m}^{-3}$ ),  $N^{sat}$  is the density of saturated water vapor ( $=23 \text{ g}\cdot\text{m}^{-3}$  at  $25^\circ\text{C}$ ).

The decay length results from the fit of the exponential curve to the data. It is given by:

$$\lambda = z_v + z_l = \frac{1}{E_{P,ISO}} \left( \theta \cdot f \cdot D + f \cdot D_v (n - \theta) \frac{N^{sat}}{\rho} \right) \quad (6.9)$$

After fitting  $\lambda$ , equation 6.9 can be solved for  $E_{P,ISO}$ .

### 6.3.2 Soil sampling and extraction of soil water

Soil samples have been collected during the two field campaigns (see chapter 4). Any kind of evaporative loss will change the isotopic signature. All soil samples therefore were sealed in PET- containers and weighed. A change of weight can only be related to evaporation. Of the 142 samples taken, 130 had a weight loss below 0.5 %. The 12 remaining samples had a significant loss of water and no longer represented the isotopic signature of the field conditions. Even though soil samples have been taken at stations in the Yanqi basin with a depth to groundwater as small as 0.5 m, the station with the smallest depth to groundwater used to calculate phreatic evaporation was 0.7 m. It is very difficult to obtain a sufficient amount of soil samples at locations with a depth to groundwater smaller than 0.7 m. Special equipment is required to take soil samples with a vertical height smaller than 0.1 m.

A method described by Revesz & Woods (1990) allows extracting soil water from the samples without changing the isotopic signature. Water and toluene form an azeotropic mixture: The toluene- water mixture has a boiling point of  $84.1^\circ\text{C}$ , significantly below the boiling point of its constituents ( $100^\circ\text{C}$  for water,  $110^\circ\text{C}$  for toluene). By distilling this azeotropic mixture, the water in the soil can be extracted without leaving traces of water in the soil pores. The procedure is as follows: From a small amount of soil the water content is determined. The appropriate amount of soil required to collect at least 1 ml of water is added into a flask. Enough toluene

has to be added to completely cover the soil. The mixture is distilled and collected in a specially designed receiving funnel, described by Revesz & Woods (1990). The density difference between water and toluene makes it easy to separate the two liquids. As a last step, liquid wax is added to the water mixture in order to remove any traces of toluene.

The oxygen isotopic composition of the water was determined by equilibration with  $CO_2$  on an automated ISOPREP 18 equilibration device coupled to a FISIONS-OPTIMA mass spectrometer. The results are reported in the conventional per mil notation with respect to the Vienna standard mean ocean water (VSMOW). The analytical reproducibility is 0.01%.  $\delta^{18}O$  profiles for the station 11 and station 12 are plotted in figure 6.3.

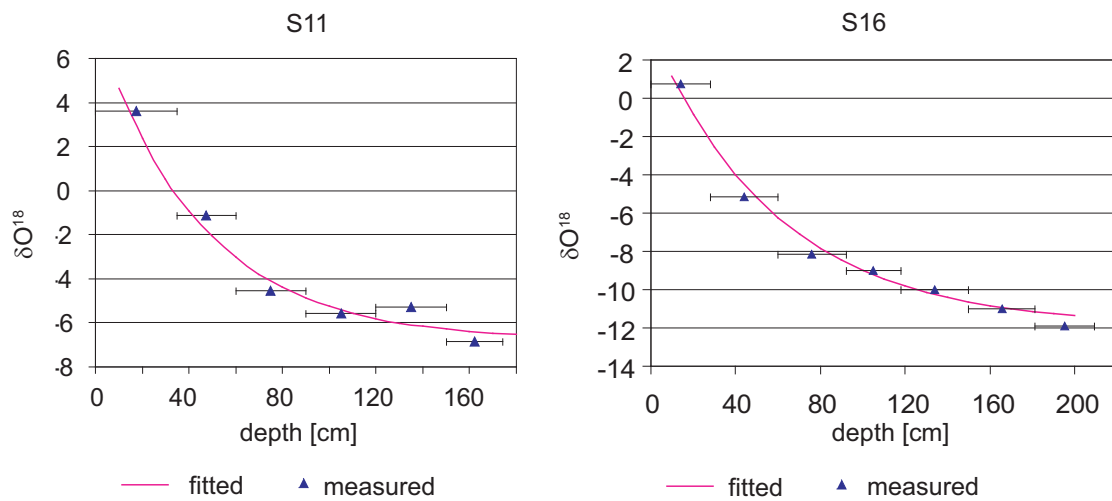


Figure 6.3: Two examples (station 11 and station 16) of  $\delta^{18}O$  profiles.

### 6.3.3 Results

The evaporation rate of 7 stations was calculated by fitting the decay length of the exponential function (section 6.3.1). A relation between the depth to groundwater and the evaporation rate can be established. Figure 6.4 plots the results of the analysis in the Yanqi basin as well as results presented by Hu *et al.* (2003). The shape of these relations is in agreement with Coudrain-Ribstein *et al.* (1998) who concluded that, independent of the soil type, the relation between the depth to groundwater and phreatic evaporation is concave.

Hu established a relation between phreatic evaporation and depth to groundwater for Aksu, close to the Tarim river. Hu reported a significant increase of phreatic evaporation up to the potential evaporation of  $1.2 \text{ m}\cdot\text{a}^{-1}$  as soon as the groundwater was closer than 0.53 m to the surface. This depth to groundwater is called  $d_{ext1}$ . In this approach, it was assumed that  $d_{ext1}$  is the same as observed by Hu. The

extinction depth  $d_{ext2}$  for the Yanqi basin is 2.66 m. It was obtained by extrapolating the relation between  $E_{P,ISO}$  and the depth to groundwater to a value of zero.

The relation between depth to groundwater and phreatic evaporation used in the model is the solid red line plotted figure 6.4. This relation is of great importance for the water balance of the Yanqi basin.

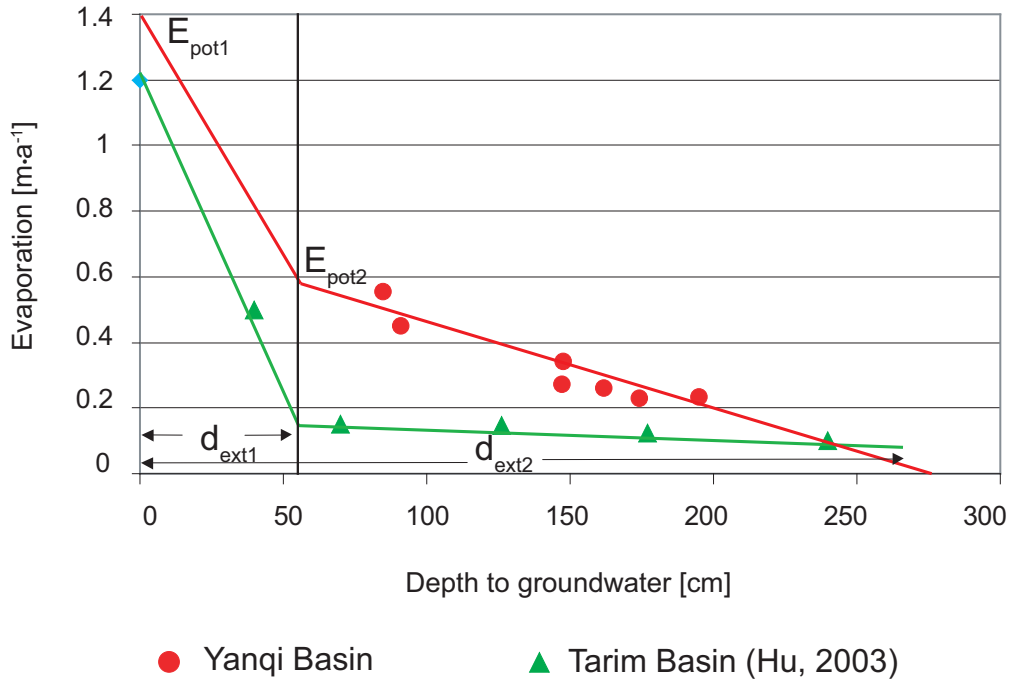


Figure 6.4: Phreatic water evaporation vs. depth to groundwater.

## 6.4 Splitting up NOAA-ET into evaporation and transpiration

The obvious dependency of evapotranspiration on vegetation can be used to separate evaporation from transpiration. Remotely sensed evapotranspiration  $ET_{NOAA}$  consists of the transpiration rate of the vegetation cover  $T_{VEG,NOAA}$  and phreatic evaporation  $E_{P,NOAA}$ :

$$ET_{NOAA} = T_{VEG,NOAA} + E_{P,NOAA} \quad (6.10)$$

For locations where the phreatic evaporation  $E_{P,ISO}$  was quantified by using stable isotopes, the difference to  $ET_{NOAA}$  can be calculated:

$$T_{VEG,NOAA} \approx ET_{NOAA} - E_{P,ISO} = f(NDVI) \quad (6.11)$$



Plant activity can be determined from remote sensing by using the Normalized Differential Vegetation Index (NDVI). If the NDVI can be related to the transpiration rate of the vegetation cover, the NOAA-ET can be split up into transpiration and evaporation by using the NDVI. In figure 6.5,  $T_{VEG,NOAA}$  and  $ET_{NOAA}$  are plotted vs. the average NDVI (year 2000). The comparison between the two quantities was

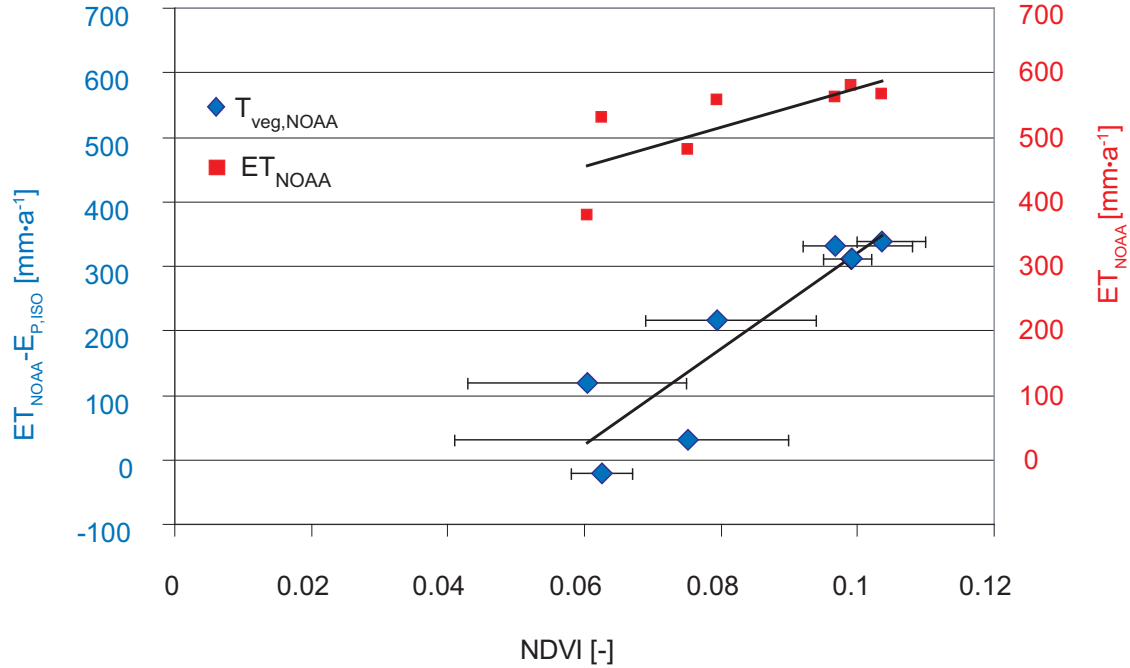


Figure 6.5:  $T_{VEG,NOAA}$  and  $ET_{NOAA}$  versus the NDVI.

carried out on a spatial resolution of 2 km by 2 km, the min-max values of the 4 pixels within one 2 km by 2 km pixel are plotted as error bars in figure 6.5. The linear regression analysis between  $T_{VEG,NOAA}$  and the NDVI yields:

$$T_{VEG,NOAA} = 7483 \cdot NDVI - 428, R^2 = 0.80 \quad (6.12)$$

Even though the correlation coefficient is high, the absolute quantities remain uncertain. A correlation between  $T_{VEG,NOAA}$  rates and the NDVI can also be found if the absolute quantities are systematically biased.

A map showing the distribution of phreatic evaporation is presented in the upper half of figure 6.6. Figure 6.6 indicates that the highest evaporation rates found are in the close vicinity of the little lake and along the rivers. These areas all have a small depth to groundwater. The irrigated areas also feature an increased evaporation rate. But even though the intensity of irrigation is similar in all irrigation areas (see chapter 7.3.3), the distribution of evaporation is not homogenous. This is the result of different depths to groundwater found in these specific areas. Outside the irrigation areas, the depth to groundwater is high and phreatic evaporation is low or zero.

## 6.5 Combining saltmaps with phreatic evaporation

The comparison of the saltmap and the map of phreatic evaporation is instructive. The soil salinity map represents a long-term integral over time of the phreatic evaporation. The phreatic evaporation rates in figure 6.6, however, were calculated considering only data of one year. The two quantities can therefore only be compared to each other where the depth to groundwater has been very shallow for a long time. The areas around Bostan lake have always had a very small depth to groundwater. Not surprisingly, both phreatic evaporation as well as the salinity values are high. If high values of phreatic evaporation are found in areas with low salinity, the groundwater table has only in recent years come close to the surface.

Such areas can easily be identified in figure 6.6, and the statement that soil salinity is driven by phreatic evaporation is confirmed. For example, irrigation in the areas north of the Kaidu river at location 1 (see phreatic evaporation in figure 6.6) was intensified from the year 1995 to 2000. As a consequence, the groundwater table has been rising and has already reached a critical level, which is above the extinction depth. However, the transport of the salt stored in the aquifer to the soil surface has only been going on during the period the groundwater table has been above the extinction depth. The amount of salt at the soil surface is therefore small compared to the amount of salt that accumulated in the topsoil around the lake. Area 2 in figure 6.6 is similar to area 1: Soil salinity will become more and more severe if the high evaporation rates will be maintained by ongoing irrigation. The effect of drainage is clearly visible at location 3. Even though this area has been irrigated for a very long time, the extent of soil salinity over the non-irrigated patches does not reach the high levels of soil salinity in the areas south of location 3. Interestingly, besides the fact that the relatively dense drainage net in this area keeps the groundwater table down, the irrigation efficiency in this area is among the highest in the Yanqi basin.

The effect of over-irrigation on the distribution of salt is clearly visible around area 4. The very high salinity values in this area are abruptly followed by an area with relatively low soil salinity in the north. In the seventies, attempts were made to use the entire area for crop production. The area was irrigated and it appeared that the salt was flushed down. However, the depth to groundwater was very shallow even before irrigation took place, and the applied irrigation water quickly evaporated. Instead of flushing down the salt, the effect of irrigation was the concentration of salt close to the surface. The depth to groundwater table slightly north of the area number 4 increases rapidly. In this area, over-irrigation has, at least for a certain time, the desired effect: flushing the salt stored in the root zone down into the aquifer.

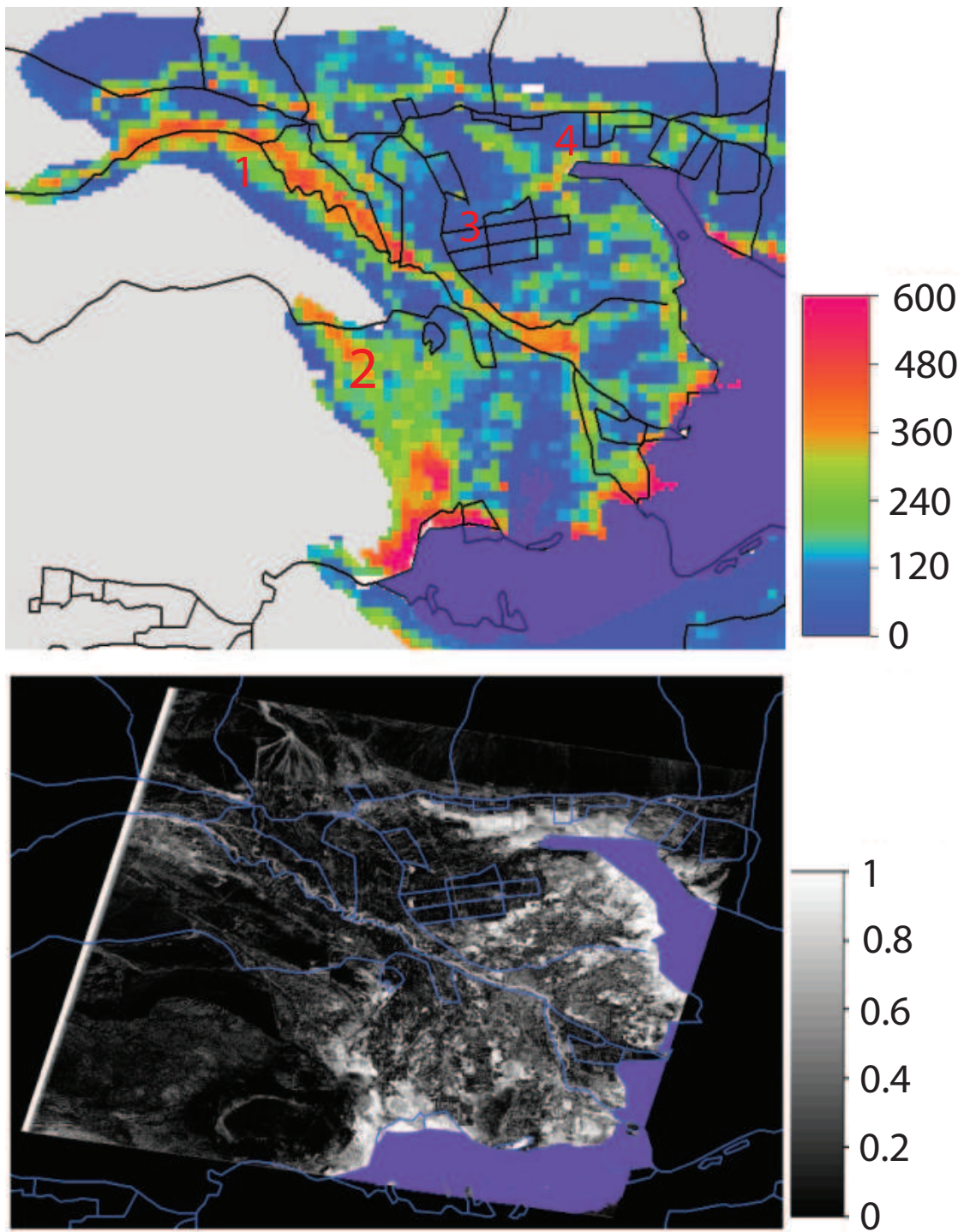


Figure 6.6: Phreatic evaporation for the year 2000 [ $\text{mm}\cdot\text{a}^{-1}$ ] and the soil salinity map, presented as spectral similarity. Both maps are overlaid by the drainage system of the basin.

## 6.6 Estimating infiltration rates

For monitoring purposes, the Yanqi basin was split up into four irrigation areas, see figure 6.7. The amount of water drawn from the main rivers, Kaidu He, Huangshui

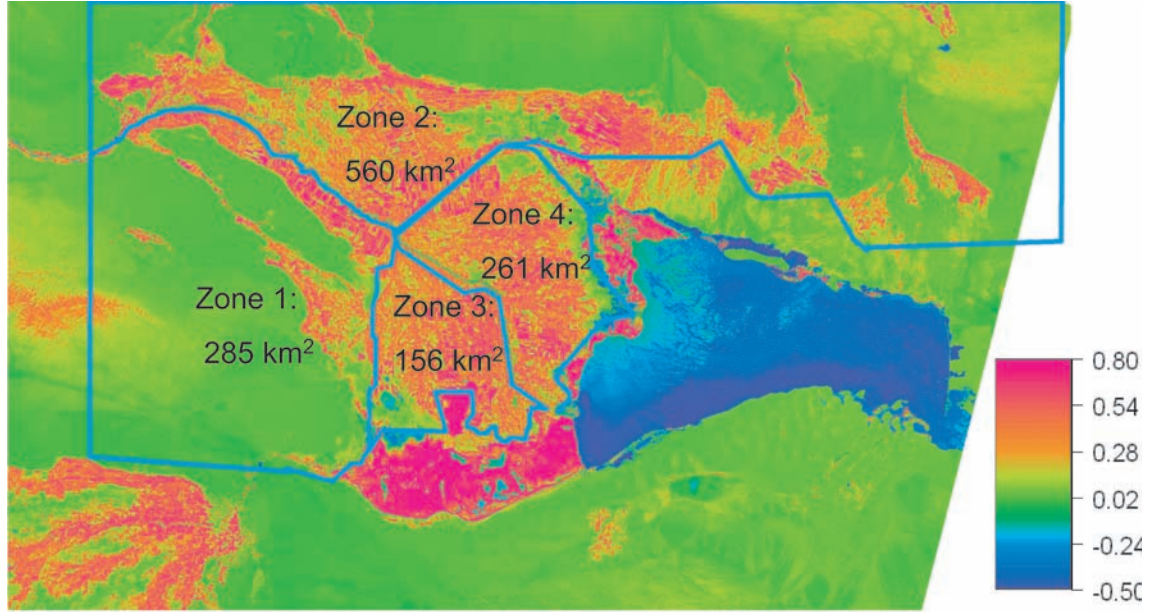


Figure 6.7: Irrigation zones and irrigated areas (2001) - the background of the map is the NDVI [-] distribution (2001).

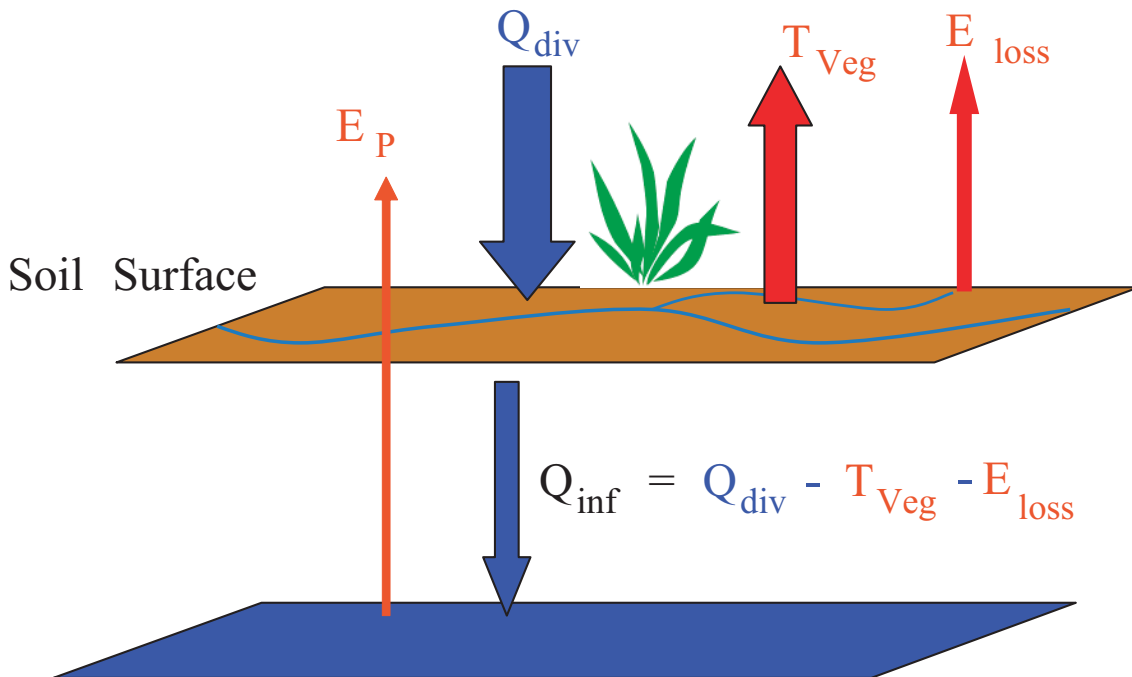
Gou, Qingshui He and Wulasitai is regularly recorded. Water drawn from these rivers is conducted to the specific irrigation areas. A portion of the water diverted is lost via infiltration along the irrigation channels. The total amount of water  $Q_{inf}$  infiltrating along the channels and on the fields can be written as:

$$Q_{inf} = Q_{div} - T_{veg} - E_{loss} \quad (6.13)$$

$Q_{div}$  is the amount of water diverted from the rivers,  $T_{veg}$  is the transpiration rate and  $E_{loss}$  is defined as the evaporative loss during irrigation. Equation 6.13 is illustrated in figure 6.8. The infiltration rate is equal to the groundwater recharge as long as no water evaporates from the aquifer, or, in other words, provided the depth to groundwater is lower than the extinction depth. As the groundwater table rises above the extinction depth, phreatic evaporation starts with a rate depending on the depth to groundwater (see section 6.3).

According to equation 6.13 the transpiration and the evaporative losses have to be estimated in order to calculate the infiltration rate. Transpiration rates could be estimated by using the concept of the crop coefficient:

$$T_{veg,max} = k_c \cdot ET_{pot} \quad (6.14)$$



## Groundwater

Figure 6.8: Relevant fluxes over an irrigated plot. Only the phreatic evaporation  $E_P$  is dependent on the depth to groundwater.

Due to the variation of both  $ET_{pot}$  and  $k_c$  in time, this equation has to be calculated on a monthly basis. If the transpiration rates of the crops are calculated by using the concept of the crop coefficient, it is implicitly assumed that sufficient water is available to cover the water requirement of the crop. If the amount of water available for the crops is not sufficient, transpiration rates are below  $T_{veg,max}$ . The amount of available water depends on the total amount of water diverted, on the channel efficiency of the irrigation network as well as and on the irrigation method applied. The amount of water available at the field and potentially available for the plants is given by:

$$Q_{field} = \eta_{channel} \cdot Q_{div} \quad (6.15)$$

The amount of water lost in the irrigation channels is a measurable quantity. According to an unpublished report by Dong Xinguang, the water loss in the irrigation channels is around 55%. If the irrigation method is highly efficient, a high portion of  $Q_{field}$  is available for crop growth. However, direct infiltration during the flooding of the fields as well direct evaporation from the soil during flood irrigation again reduces the amount of water available for the crop. Taking these additional losses into account, the available amount of water for plant transpiration within a specific



*Table 6.2: Overview of the infiltration rates in the four different irrigation zones.* The estimated irrigation efficiencies are below the efficiencies presented by the Water Management Authorities in Korla. Infiltration includes losses of the distribution system as well as the direct infiltration of water during irrigation.

	Irrigation intensity [mm·a <sup>-1</sup> ]	Crop transpiration [mm·a <sup>-1</sup> ]	Infiltration [mm·a <sup>-1</sup> ]	Efficiency [%]
Zone 1	1008	368	585	36.5
Zone 2	961	339	569	35.3
Zone 3	843	311	485	36.9
Zone 4	865	304	514	35.2

period of the irrigation cycle can be written as:

$$Q_{available} = Q_{field} - E_{direct} - I_{direct} \quad (6.16)$$

$I_{direct}$  is defined as the direct infiltration of water during the flooding of the field,  $E_{direct}$  as the direct evaporation during the flooding. According to another unpublished study carried out by Dong Xinguang, 15 % of the water reaching a field directly infiltrate into the ground and 10 % directly evaporate. Only if  $Q_{available}$  within a specific growth period is higher than or equal to the water requirements of the plants, is transpiration given by equation 6.14. If  $Q_{available}$  is smaller than  $T_{veg,max}$ , the growth of crop is limited by the lack of water and the highest possible transpiration equals  $Q_{available}$ . Taking all these considerations into account, the infiltration rates for all irrigation zones have been calculated on a monthly basis and are summarized in table 6.2. According to the Water Management Authorities in Korla, the official irrigation efficiency in the Yanqi basin is 60%. However, if the losses in the channels as well as the high infiltration rates during irrigation are taken into account, the irrigation efficiency in the Yanqi basin is smaller than 40 %. The largest portion of water lost (75%) infiltrates into the channels. Infiltration could potentially be reduced by 13 % if the temporal distribution of the water diverted were to match the crops water requirement. However, the leaching requirement of the soil before the crop's are planted has to be considered. In order to apply equation 6.13 in a spatially distributed manner, the irrigated areas have to be identified. The NDVI can be used to identify such areas because plant growth is more active in the irrigated areas. The irrigated fields were sorted out by using two NDVI maps (September 17<sup>th</sup> 2000 and March 25<sup>th</sup> 2000) calculated on the basis of Landsat images. The two NDVI maps were added up and a cutoff value was defined. If the sum of the NDVI is above this cutoff value, the pixel is defined as an irrigated field. The cutoff itself was defined in such a way that the irrigated areas identified by using the NDVI match the documented area of the four irrigation zones. This binary identification of irrigated fields was carried out by using the fine resolution Landsat



NDVI maps. Nevertheless, equation 6.13 must be applied by using a coarse spatial resolution, owing to the distribution of transpiration rates only being known on the basis of 1 km by 1 km resolution. For the distribution of  $Q_{div}$ , the portion of the irrigated areas within one coarse pixel was therefore calculated. It is assumed that the irrigation intensity is the same on every field. Over large areas this assumption is justified, because the crop mix is similar within all irrigation areas.

The spatial distribution of transpiration is the basis for distributing the transpiration values presented in table 6.2. The patterns are scaled in such a way that the average transpiration rates of the irrigated areas equal the transpiration rates presented in table 6.2. Figure 6.9 presents a binary map of recharge, the portion of irrigated areas within a coarse pixel as well as the final infiltration map.

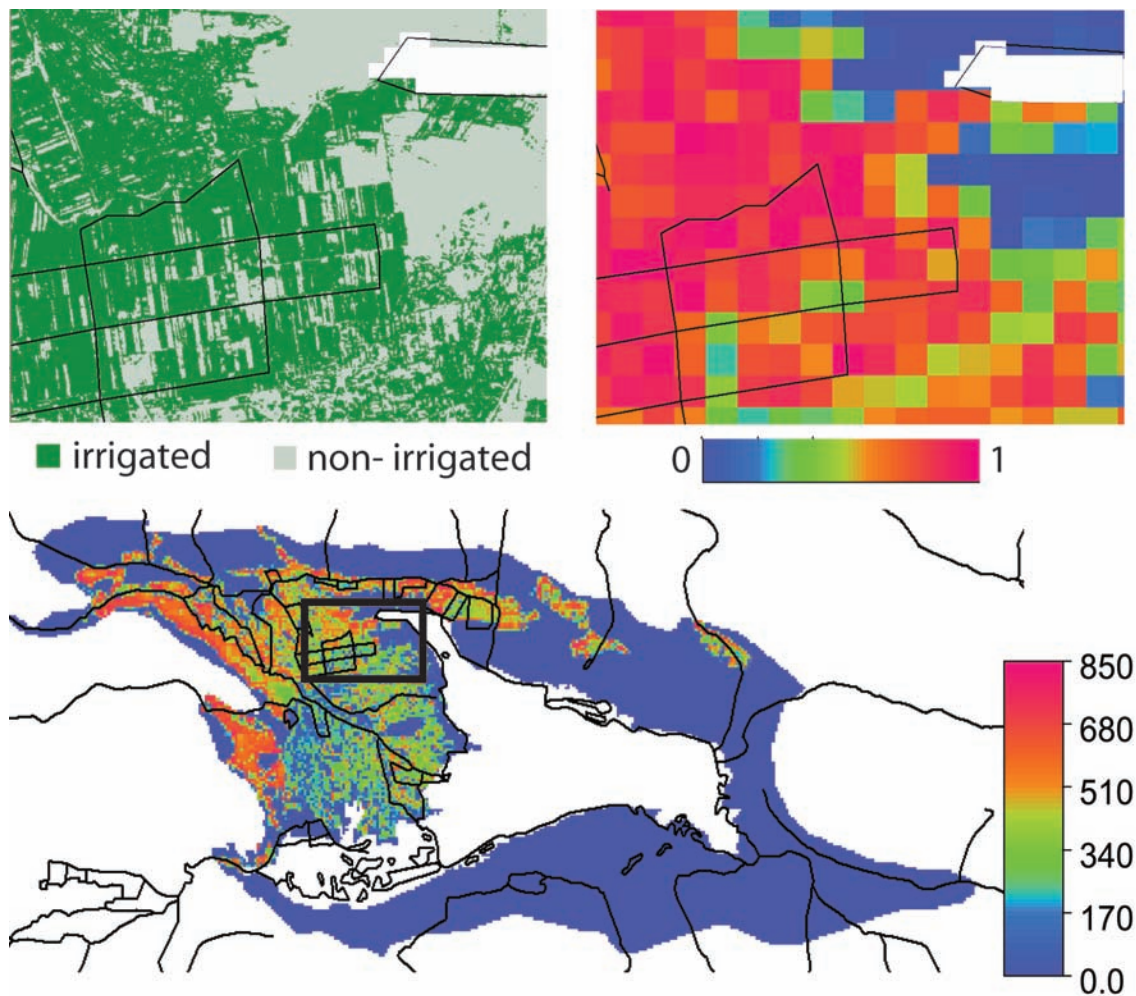


Figure 6.9: Detail of the binary irrigation map (upper left), portion of irrigated area within a low resolution map (upper right) and the final infiltration map [ $\text{mm}\cdot\text{a}^{-1}$ ].

## 6.7 Estimating potential, phreatic evaporation considering vegetation

The energy consumed by plants for transpiration and evaporation during irrigation reduces the available energy for phreatic evaporation. A model calculating phreatic evaporation only must take this into account, or else the sum of energy used for evaporation and transpiration (calculated by using the concept of the crop coefficient) could exceed the available energy provided by the sun. Nevertheless, it has been observed that the actual evapotranspiration can be up to 20% above the potential ET if the groundwater table is very high and vegetation is present (Allen *et al.*, 1998). The conditions required to observe actual ET rates above the potential ET do not exist in most of the Yanqi basin. It is therefore assumed that the highest ET rates do not exceed potential ET rates. The starting point for a map of potential evaporation rates for the model was the potential ET based on the Penman-Monteith equation. The potential evaporation rate for all non-irrigated areas was set at  $1.4 \text{ m}\cdot\text{a}^{-1}$ . Potential evaporation for all irrigated areas is reduced by the amount of water consumed by plants. Moreover, the amount of water evaporating during irrigation has to be taken into account.

Splitting up the area into irrigated and non-irrigated regions implies that non-irrigated areas are treated as if no vegetation was present. An error is made because ET over a non-irrigated area with vegetation present will be slightly larger compared to an area with the same depth to groundwater but without vegetation. However, even if the bias is unknown, its influence is small. The ET-rates over non-irrigated areas are significantly smaller compared to the irrigated areas. The high groundwater tables in the Yanqi basin allow plants with a small root depth to grow. Vegetation with very deep roots (e.g. trees) will still continue to consume water, even if the depth to ground water is below the extinction depth. As these trees are usually located close to the river, their effect will be drowned out by the high ET rates found along the river anyway.

To obtain a map of potential phreatic evaporation, the transpiration map and the direct evaporation during irrigation are subtracted on a pixel basis from the potential evaporation. The resulting map of potential evaporation is presented in figure 6.10.

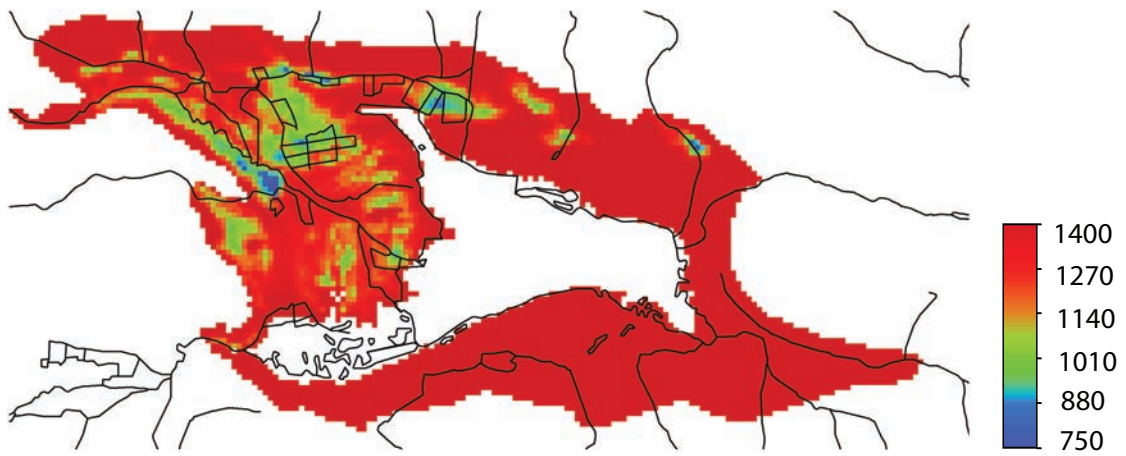


Figure 6.10: Map of potential evaporation [ $\text{mm}\cdot\text{a}^{-1}$ ] for the model area.



## Chapter 7

---

# Construction and Calibration of the Distributed Flow Model

The intention of the thesis was to develop a sustainable water management strategy for the Yanqi basin including the downstream requirements. The 1-box model (chapter 3) illustrates that sustainable agriculture in the Yanqi basin can be achieved by substituting a portion of the irrigation water drawn directly from the river by pumping river water indirectly from the aquifer. However, due to nonlinearities, the 1-box model is not a sufficiently accurate approach to predict the influence of such a measure on the water balance. A more sophisticated method to evaluate the maximum amounts of and the ideal ratio between river-water and groundwater applied to irrigation, must be based on a spatially distributed model which describes the flow of ground- and surface water and the coupling between them. Based on the Modflow code and recent additions, such a model has been constructed. This chapter contains a short introduction to Modflow as well as the additional flow models applied. Finally, the calibration strategy for the model is discussed.

### 7.1 Introduction

A considerable amount of input data is required to construct and verify a distributed model. Borehole data yield important information about the geological structure, the hydraulic conductivities as well as the elevation of the groundwater table. The digital terrain model has been calculated as described in chapter 5. Recharge has been quantified by using the transpiration rates calculated in chapter 6 as well as the documented amount of irrigation water applied. The relation between the groundwater table and phreatic evaporation has been quantified in section 6.3. The information required to model the surface hydrology comprises the structure of Bostan lake as well as the basic geometry of the rivers and drainage channels. Figure 7.1 presents an overview of the model in- and outputs. The calibration of the model is a crucial point. The main problem in all modelling approaches is non-uniqueness. In order to reproduce observed values, e.g. the elevation of the groundwater table at different locations, unknown parameters such as transmissivity or the leakance of the streambed have to be adjusted. Basically, all observed values can be reproduced with any desired accuracy if the number of calibration parameters are increased and adjusted. Accordingly, an over-parameterized model is unlikely to predict the impacts of a change in the system correctly, no matter how high the correlation between the calculations and the observations are. Just as crucial as the number of calibration parameters is their selection. Highly dependent parameters can produce identical results with different parameter combinations.

The constraints for the hydrological model are subject to the following considerations: (1) The discharge of the rivers, the amount of surface drainage water,

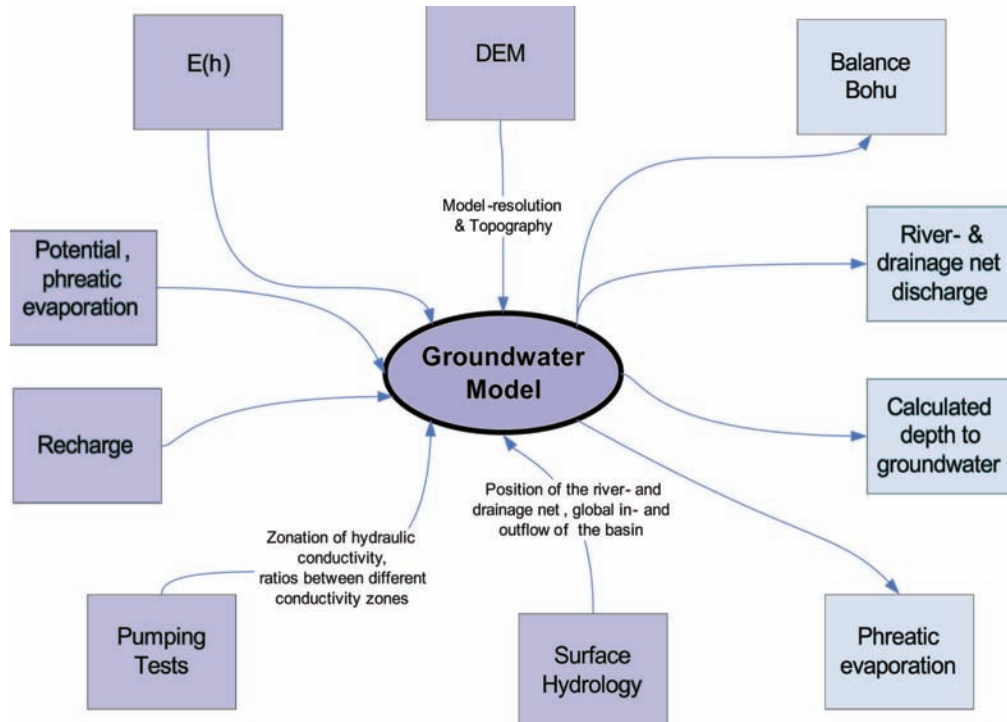


Figure 7.1: Schematic overview of the required input data sets for the model as well as the model outputs.  $E(h)$  is the relation between evaporation rate and the depth to groundwater.

the lake level and the groundwater tables should be reproduced correctly. (2) The patterns of spatially distributed verification data such as phreatic evaporation have to be reproduced by the model. This comparison between predicted and measured data is an important measure for the reliability of the final model. The verified model will then be used to demonstrate to which extent water can be saved and how the danger of soil salinization can be reduced. The calibration strategy was that all external fluxes of the aquifer are specified and only leakances and hydraulic conductivities are adjusted.

## 7.2 Modflow

A standard code for aquifer simulation, Modflow, was used to simulate the hydrological system in the Yanqi basin. The original Modflow code published by the USGS was developed by McDonald & Harbaugh (1988). Meanwhile, many additions and improvements have been made. For example, rivers can be modelled with a Streamflow Routing Package. The package is able to calculate the exchange between river and groundwater, as well as a water balance for every stream reach in every time step. If the stream stage is below the groundwater table, the river drains the aquifer. Another module, recently developed, is the Lake Package. This package calculates a water balance for a lake linked to an aquifer. Streams can be linked to the Lake



Package. Modflow also allows to account for evaporation by using the Evapotranspiration Segment Package (ETS). The evaporation rates are calculated according to a user-defined function which describes the relation between the depth to groundwater and the evaporation rate. A nonlinear relation between these two quantities can be defined. The latest version of Modflow (MF2k 1.15) is freely available at <http://water.usgs.gov/nrp/gwsoftware/modflow2000/modflow2000.html>.

Modflow is based on a finite difference approach. Finite differences use a regular discretization, whereby the aquifer is divided into a series of rectangular gridblocks. The gridblocks can follow the stratigraphy. This option was chosen here. It leads to a so called 2.5-D model which is a series of coupled, horizontally 2-D models for the layers. The flow of groundwater in every layer is described by the Darcy equation:

$$\nabla \cdot (mK\nabla(h(t)) + q(t)) = S \frac{\partial h(t)}{\partial t} \quad (7.1)$$

$m$  [L] is the saturated thickness and  $K$  is the permeability tensor,  $q$  [L/T] is a source-sink term including pumping from the layer and the head dependant exchange with other layers.  $S$  [-] is the storage coefficient. In the first layer a positive flux term  $q$  accounts for all the flow into the groundwater (such as recharge or infiltration from rivers) while a negative flux term represents the flow out of the groundwater (such as for example evaporation). At the midpoint in every model cell, called node, the hydraulic head is calculated. When equation 7.1 is combined with initial and boundary conditions, it describes the transient groundwater flow in an aquifer. This equation can be solved iteratively by using solvers provided with the Modflow code. Boundary conditions are defined through the IBOUND Package.

In Modflow 2000, the layer properties can be defined through the Basic Package (BAS) or the Layer Property Package (LPF). The LPF Package is an alternative to the BAS Package. In contrast to the BAS Package, the LPF Package only uses two types of layers: confined and convertible. A layer defined as convertible is treated as an unconfined layer, as long the groundwater table is below the layer top. The USGS recommends using the Layer Property Package if streams are simulated.

Additional flow packages are independent subroutines that perform specific simulation tasks, such as the calculation of evaporation or the interaction between a lake and the aquifer. The input data for the specific packages are defined through text files. The preprocessor PMWIN Pro version 5.3, developed by Chiang & Kinzelbach (2001), supports some of Modflow 2000 flow packages. No preprocessor for the recently developed packages such as the ETS Package simulating evaporation, the Lake Package, or the latest version of the Streamflow Routing Package exists yet. The input files for these packages have to be generated manually. The post processing of the data was carried out using the ILWIS 3.2 software (<http://www.itc.nl/ilwis/default.asp>) and a text editor with macro functionality (UltraEdit 32, <http://www.ultraedit.com/>) converting the numerous types of output data generated by Modflow.

## 7.3 Flow packages and input data

### 7.3.1 Layer properties, units and geometric set-up

In analogy to an existing model developed at Xinjiang Agricultural University, this model consists of 4 layers. The first model layer is defined as a convertible layer. All other layers are confined. In total, 96620 aquifer cells and 6562 lake cells are calculated. The cell resolution was set to 500 m by 500 m in the horizontal layers. This resolution is based on the findings described in section 5.2.5: If the cell resolution was above 500 m by 500 m, the average difference between the minimum and maximum elevation within one coarse model cell was above the largest error observed in the area of interest. The coordinate system applied is the Universal Transverse Mercator (UTM), projection zone 45N. The unit for length is set to meters. The time unit in the model is set to days. The boundary conditions are presented in figure 7.2. The closed shape of the Yanqi basin as well as the sharp borders between different geological compartments make the definition of the boundaries straightforward. The boundary conditions (except for Bostan lake) as well as the horizontal conductivities are set equal for all layers. The top of the first layer is the digital elevation model. The thickness of all layers was interpolated based on borehole

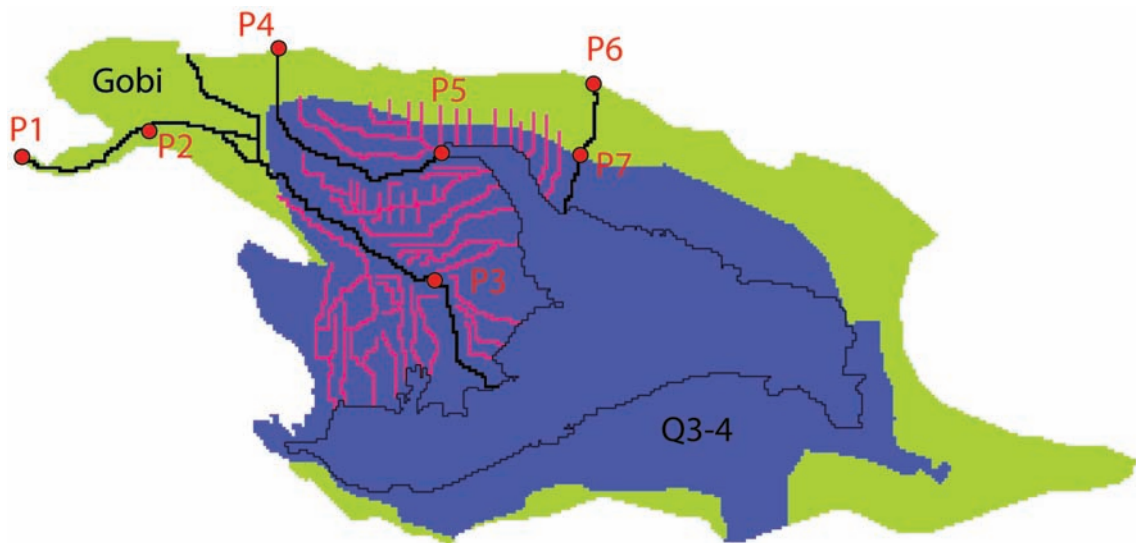


Figure 7.2: Boundary conditions, rivers, drains and rough conductivity zonation for the first model layer. The Gobi-formation is shown in green, the Q3-4 formation in blue. Rivers are plotted with a thick, black line. Drainage channels are plotted in red. The red circles indicate the presence of measurement stations.

data. The data for the first three layers are presented in figure 7.3. The vertical discretization and the boundary conditions of the aquifer layers are in agreement with the unpublished model developed at Xinjiang Agricultural University.

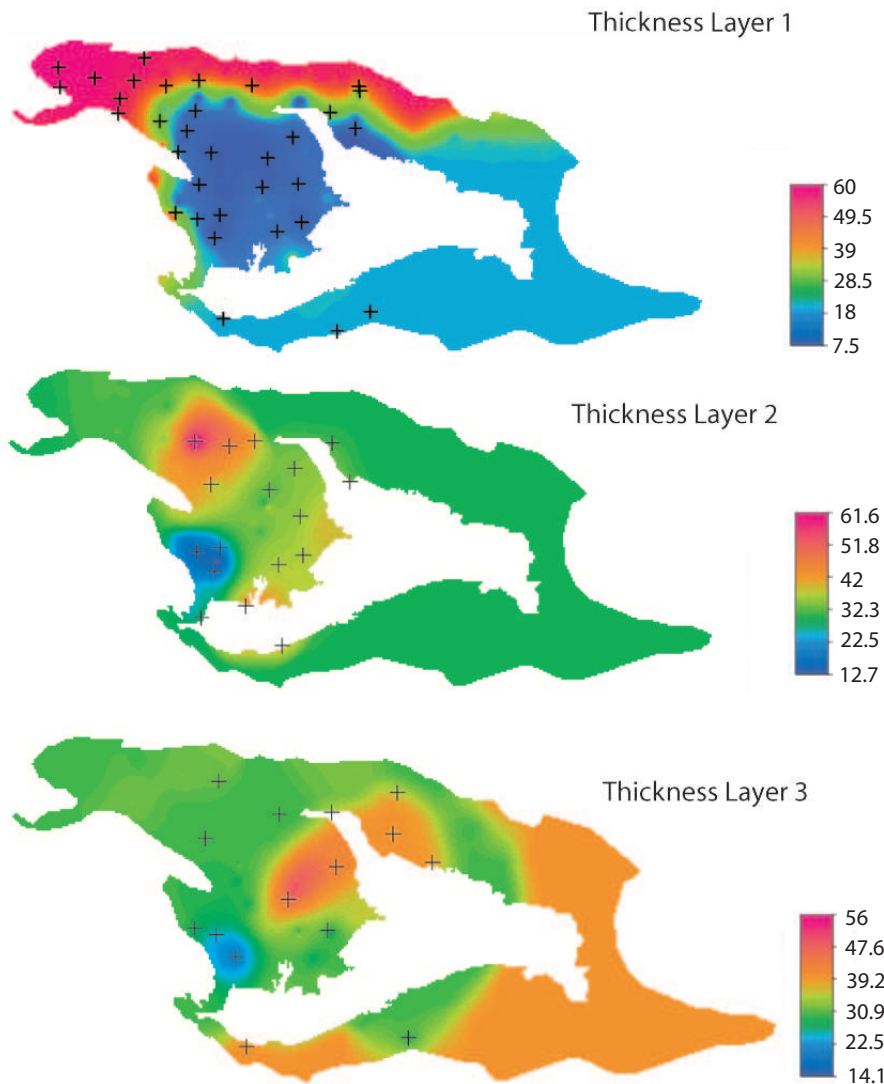


Figure 7.3: Layer thicknesses for the first three layers [m]. The crosses indicate where borehole data were available. These boreholes do not necessarily correspond to the observation boreholes presented in the flow model.

### 7.3.2 Hydraulic conductivities

The hydraulic conductivities of the aquifer have been measured at several locations for all layers. Pumping test data revealed that two significantly different zones of hydraulic conductivities can be distinguished. The extensions of these two zones are presented in figure 7.2. These two zones are the starting point for the model calibration. In every model layer, this zonation of hydraulic conductivity is the same. In the areas where the Gobi-formation is the predominant morphology, the aquifer is unconfined and hydraulic conductivities are high. Pumping tests in the Gobi-

zone revealed that the horizontal hydraulic conductivity values range from  $10 \text{ m}\cdot\text{d}^{-1}$  to  $60 \text{ m}\cdot\text{d}^{-1}$ . A different situation is found for the Q3-4 formations. Hydraulic conductivities throughout the Q3-4 formation are up to two magnitudes lower than in the Gobi-formation. Measured hydraulic conductivities in the first layer above the confined system range from  $0.1 \text{ m}\cdot\text{d}^{-1}$  to  $1.5 \text{ m}\cdot\text{d}^{-1}$ . However, the hydraulic conductivities of the second layer are around a factor of 15 higher than in the first, third and fourth layer.

The aquifer in the non-irrigated zones of the Gobi-formation is vertically continuous (see figure 2.1). In order to simulate these areas as one, non-interrupted aquifer, the leakage factors describing the exchange between the model layers were set to a high value, effectively merging the layers into one. The vertical hydraulic conductivities between the confined layers within the Q3-4 formation are unknown, but the pumping tests have shown that the vertical exchange rates between the layers are small.

### 7.3.3 Recharge and Pumps

The distribution and amount of infiltration has been quantified in chapter 6.6. This distributed recharge is assigned to the aquifer by using the Recharge Package. In this model, recharge is assigned exclusively to the top model layer. Borehole data have shown that the groundwater table stays in layer 1 throughout the irrigated area. The source of groundwater recharge is essentially excess irrigation water infiltrating from the irrigated areas. Infiltration rates from the rivers are calculated by the Streamflow Package (see section 7.3.4), and are not taken into account in this flow package. The infiltration rates of the lake are calculated by using the Lake Package (see section 7.3.5). Even though there is a small amount of precipitation, it is very unlikely that rainwater contributes to groundwater recharge.

A total amount of  $3 \text{ m}^3\cdot\text{s}^{-1}$  is abstracted from the second aquifer layer in the northeastern area of the Yanqi basin. The abstraction rate has been distributed to 23 pumps. These pumps are considered in the steady state model. Wells are defined in and assigned to the model's water balance by the Well Package.

### 7.3.4 Rivers and drains

Rivers or drainage channels can be modelled in Modflow by using the Streamflow Routing Package programmed by Prudic *et al.* (2004). The package is able to calculate the exchange between river and groundwater as well as a water balance for each stream reach in each time step. Likewise, surface drainage systems can also be modelled with this package. The stream network is defined by segments and reaches. A stream reach is a section of the river related to a particular grid cell in the model. A segment is a group of reaches that have uniform or linearly changing properties. Multiple segments can be joined to tributary streams. In the latest version of the Streamflow Package more than one reach can be associated with a model cell. The

Streamflow Routing Package can be coupled to a lake by defining the outflow of the last segment of a reach as inflow to a lake. The Streamflow Routing Package calculates the exchange between river and groundwater by Darcy's law. The flow is computed as:

$$Q_s = \frac{K \cdot L \cdot w}{m} \cdot (h_s - h_a) = k \cdot (h_s - h_a) \quad (7.2)$$

$Q_s$  [ $L^3/T$ ] is the volumetric flow between the river and the aquifer,  $K$  [ $L/T$ ] is the hydraulic conductivity of the streambed sediments,  $w$  is the width of the stream [ $L$ ],  $L$  is the length of the stream in the corresponding model cell [ $L$ ],  $m$  is the thickness of the streambed deposits [ $L$ ],  $h_s$  is the head in the stream, calculated by adding the stream depth to the elevation of the streambed,  $h_a$  is the head in the aquifer beneath the streambed and  $k$  is the streambed conductance [ $L^2/T$ ]. If the groundwater table is below the streambed, the leakage from the river into the aquifer is no longer dependent on the groundwater table. In this case, the flow is calculated by replacing the aquifer head in equation 7.2 with the streambed elevation.

Several sources of in- and outflow can be calculated and defined in the Streamflow Routing Package. The stream water budget for every cell as well as the leakage rate are computed at the end of each time step. The water budget for the first reach in every segment yields the flow out of the reach which is routed to the next downstream reach. The water balance for a specific river cell is given by the following set of equations:

$$\begin{aligned} \sum Q_{in} &= Q_{sri} + Q_{trb} + Q_{ro} + Q_{ppt} - Q_{li} \\ \sum Q_{out} &= Q_{sro} + Q_{div} + Q_{et} + Q_{Lo} \end{aligned} \quad (7.3)$$

$Q_{sri}$  is a specified inflow at the beginning of the first reach in a segment,  $Q_{trb}$  is the sum of the tributary rivers from the upstream segments to the first reach of a segment,  $Q_{ro}$  is the direct overland discharge to a reach,  $Q_{ppt}$  is the precipitation and  $Q_{li}$  is the groundwater leakage to a reach. It is subtracted from the other terms because discharge from the aquifer is a negative value in Modflow. Losses are the streamflow out of a reach  $Q_{sro}$ , the diversion from the stream  $Q_{div}$ , the evaporation  $Q_{et}$  and the leakage to the underlying aquifer  $Q_{Lo}$ . This leakage is only added if water is infiltrating from the river into the aquifer. For each reach, the sum of flows into the reach is equal to the sum of flows out of the reach. The water depth can either be calculated by Manning's equation or set to a constant value in every reach. In this modelling approach, the water depth in the streams and drainage channels were predefined. Calculating the stream depth would have required additional, unknown input data. Moreover, no verification data of the stream depth in the drainage channels and the rivers are available at present.

The geometry and depth of the rivers and drains is not constant. The available data describing the geometry of the drainage channels suggest that two different types of drainage channels are predominant, see table 7.1. The rivers can also be classified into two different types. All rivers flow across the Gobi-formation as well

## Construction and Calibration of the Distributed Flow Model

---

*Table 7.1: Relevant parameters that describe the different types of rivers and drains.* The different types are characterized by the elevation of the streambed bottom (with the soil surface as reference) and the water depth of the rivers or the drains.

	Depth of streambed [m]	Water depth [m]
Drain Type (1)	3.5	0.2
Drain Type (2)	2.5	0.2
River Type (1)	1	1
River Type (2)	3	2

as the Q3-4 formation. In the Gobi formation, the rivers are shallow and wide, and they all infiltrate into the aquifer (see chapter 2.2.1). In the irrigated areas (Q3-4), the streambed has been lowered. In these areas the rivers are narrow and deep and sequentially infiltrating and draining the aquifer system. It is therefore reasonable to apply two different types of river geometry, one for the rivers over the Gobi formation and one for the rivers over the Q3-4 area. The relevant parameters of the two types of rivers are summarized in table 7.1. According to equation 7.2, the flow of water between the aquifer and the river is proportional to the streambed conductance. The streambed conductance consists of the product of 4 unknown parameters, the hydraulic conductivity, the length of the river within one cell, the width of the river as well as the thickness of the streambed. No classification of the streambed conductance could be sorted out, as the length of the river within one cell, the width of the stream and the thickness of the streambed vary to a much higher extent than for example the depth of the river. The hydraulic conductances were therefore used as a calibration parameter.

The depth of the water in the rivers and drainage is an additional, unknown parameter. Moreover, this parameter is time dependent. The water levels in the rivers and drains result from the balance between inflow, diversion, infiltration and drainage. However, the water flux between ground- and surface water is related to the product between the head difference and the conductance of the river or drain bed material. Whether the river is infiltrating or draining the system is determined only by the gradient between surface and groundwater. An error in the streambed elevation could therefore result in a wrong direction of the water flow. Over the Gobi formation, river heads are significantly above the aquifer. Errors in the stream stage will therefore not cause any inconsistencies. The fact that the rivers over the Q3-4 formation both drain and infiltrate the aquifer makes it impossible to verify the flow directions on a cell by cell basis. The only way to assess whether, on average, the river stages above the Q3-4 area are correct, is by comparing the overall river water balance between the entry into the Q3-4 area and Bostan lake. Two different river depths have been assigned to the two types of rivers, according to the two types of rivers defined in table 7.1.



The position of the drainage net was taken from the model developed at Xinjiang Agricultural University. The position of the rivers is based on the panchromatic channel of Landsat satellite image data. The rivers were split up into different segments. A new segment was defined if either the diversion rates changed or if the river was flowing into a different formation. The Kaidu river was split up into 5 segments. The first two segments are defined as river type 1. Segment 1 reaches from Dashan Kou to the first diversion point (Points 1 and 2 in figure 7.2). From the first diversion point to the boundary between the Gobi-formation and the Q3-4 formation irrigation water is drawn from the Kaidu river and a new segment is defined. The remaining segments, separated by their different diversion rates, are defined as river type 2. From the Gobi-formation up to the Q3-4 formation, the reaches of Qingshui He and Huangshui Gou are defined as type 1 (see figure 7.2). The segments above the Q3-4 formation are all defined as type 2.

The Kongque river is not modelled explicitly, as it flows out of the model domain without further influencing the water balance of the Yanqi basin. However, in the calculation of the lake water balance, the discharge of the Kongque river is taken into account.

### 7.3.5 Bostan lake

Different approaches to model lake-aquifer interactions are feasible in Modflow. The straightforward approach is to define a layer with very high hydraulic conductivities and a storage coefficient of 1. The lake stage is then calculated with the same equations that are used for the aquifer. However, numerical problems limit this approach to very simple systems. The Lake Package by Merrit & Konikow (2000), provided with Modflow 2000, is connected to the inflowing streams and the aquifer. Modflow requires that lake cells are defined inactive in the I-BOUND Package.

The specific exchange rate with groundwater is calculated by means of Darcy's law:

$$q = K \cdot \frac{h_l - h_a}{\Delta l} \quad (7.4)$$

where  $q$  is the specific discharge rate [L/T],  $K$  the hydraulic conductivity [L/T] in the sediment zone between the lake and the aquifer,  $h_l$  the lake stage [L],  $h_a$  the aquifer head [L], and  $\Delta l$  [L] the thickness of the lake sediments above the aquifer. The volumetric flux  $Q$  [L<sup>3</sup>/T] can be expressed as:

$$Q = q \cdot A = \frac{K \cdot A}{\Delta l} (h_l - h_a) = c(h_l - h_a) \quad (7.5)$$

with the lake bed conductance  $c=K \cdot A/\Delta l$  [L<sup>2</sup>/T], and  $A$  [L<sup>2</sup>] the area of the grid cell.

The hydraulic conductivity of the lake bed was set to a very small value. The exchange rate between the aquifer and the lake is unknown, but the lake bottom is covered with a thick layer of sediment. Apart from the lake conductivity, the amount

of water pumped from the lake to the Kongque He has to be quantified. This amount has been documented since the construction of the dam. No discharge data for the Kongque river were recorded before this construction. The most critical parameter, however, is the lake's evaporation rate. Already a small error in the evaporation rate has a far more significant influence on the lake's water balance than for example inaccuracies of the river inflow into the lake. Unfortunately, calculating evaporation by using the Penman equation is not a good approach. The average evaporation rate over the open water surface is lower than the potential evaporation over land, as the large evaporating surface changes both the temperature as well as the relative humidity. The evaporation rate of the lake has been calibrated against the lake stage. The calculated lake stage can therefore not be used as a verification of the input fluxes.

The small and the large lake are considered as one fully connected system. This simplification is reasonable as the water level of the small lake is essentially the same as the water level of the large one. Evapotranspiration over the reed covered little lake is smaller than pure evaporation over the open water surface. The calibrated evaporation rate therefore represents an area weighted average.

### 7.3.6 Evaporation

The relation between transpiration rates of vegetation and the irrigation water used has been described in chapter 6.6. The rates calculated by the groundwater model only concern evaporation. The transpiration rate of vegetation has been considered in the calculation of the recharge map. The ETS Package developed by Banta (2000) allows to calculate evaporation with user defined functions. This relation is conceptualized as piecewise linear function between the extinction depth and the evaporation surface. This is a great advantage compared to the original Evapotranspiration Package provided with Modflow, in which the relation between evaporation and the depth to groundwater is one single linear function between the extinction depth and the evaporating surface.

Based on the results discussed in chapter 6.3, the relation between the depth to groundwater and the evaporation rates was split into two segments. The first segment describes the evaporation for a groundwater table between 0 to 0.53 m below the surface. The second relation is used if the groundwater table is between 0.53 m and the extinction depth at 2.66 m. The evaporation rate for a groundwater table reaching the soil surface was set to the potential ET calculated in section 6.7.

$$ET_{12} = (ET_{Pot1} - ET_{Pot2}) \cdot \frac{d_{ext1} - d_{GW}}{d_{ext2}} + ET_{Pot2}, \quad 0 \text{ cm} < d_{GW} < 56 \text{ cm}$$

$$ET_{23} = \frac{ET_{Pot2}}{d_{ext2} - d_{ext1}} \cdot (d_{ext2} - d_{GW}), \quad 56 \text{ cm} < d_{GW} < 266 \text{ cm} \quad (7.6)$$

The elevation of the evaporating surface is the same as the elevation of the top of the first model layer.

## 7.4 Steady state calibration and results

The goal of calibration is to obtain an optimal fit between the calculated data and the verification data. In this approach, verification data consist of borehole observations, the pattern of phreatic evaporation and all available data describing the surface hydrology (except the inflow of the rivers into the basin, the discharge of the Kongque He and the stage of the lake). Data such as recharge, all parameters required to calculate phreatic evaporation and the position of the drainage channels and rivers have been predefined and have not been used for calibration. The remaining calibration parameters are the hydraulic conductivities (vertical and horizontal, in total 4 calibration parameters), the streambed conductances (3 parameters in total: the conductance of the rivers over the Gobi formation and the Q3-4 formation as well as the conductance of the drainage cells), the streambed type (binary parameter, only used for drainage cells- the river cells have been predefined in section 7.3.4) and the evaporation rate of the lake system (1 parameter) as well as the lakebed conductance (2 parameters).

A steady state calibration was carried out. The steady state model represents the average conditions for the years 1990 to 1999. Likewise, the steady state model could have been set up with data for one specific year. However, the pattern of phreatic evaporation is not related to one specific year. It is the result of a long term water balance. Moreover, the inflow of surface water varies considerably over time. For example, compared to the average discharge for the years 1990-1999, the discharge of the Kaidu river for the year 2000 is nearly 40% higher. The surface water balance for the year 2000 does therefore not represent the usual hydrological conditions of the Yanqi basin and the lake system, even though the water diverted for irrigation purposes in the year 2000 is very close to the average diversion from 1990 to 1999.

As a starting point, the horizontal hydraulic conductivities (according to the initial zonation presented in figure 7.2) as well as all other free parameters (the evaporation rate of the lake, vertical hydraulic conductivity, the conductance of both drainage and river cells) were set to an initial value. The initial values of the hydraulic conductivities (horizontal and vertical as well as the conductances of the river and drainage cells) are based on the groundwater model developed at Xinjiang Agricultural University. The initial evaporation rate of the lake is based on the 1-box model. The calibration of the model is an iterative process and can schematically be split up into three steps corresponding to the parameter adjusted (see figure 7.4). The sequential structure was chosen because of the hierarchy of the sensitivity of the parameters calibrated.

In a first step, the horizontal hydraulic conductivities of the two conductivity zones were adjusted in order to obtain a first fit between calculated and observed groundwater tables. For the elevation of the groundwater table, the horizontal hydraulic conductivity is the most sensitive parameter. The two zones were adjusted with the constraint that hydraulic conductivities for the Gobi-formation are at least

one order of magnitude higher than in the Q3-4 formations. Moreover, the hydraulic conductivity of the second, confined layer is significantly higher than the hydraulic conductivities of the first, third and fourth layer. The ratio between these conductivities is given by the analysis of the available pumping test data (unpublished data collected by Xinjiang Agricultural University). These tests revealed that the hydraulic conductivity of the second layer is around 15 times larger compared to that of the less permeable layers within the Q3-4 formations. All these constraints have been taken into account during the calibration process: the hydraulic conductivity of the second layer was tied to the hydraulic conductivity of the less permeable layer. The vertical conductivity for the Gobi-formation was set to a high value to ensure that the calculated groundwater tables in these areas are the same for every model layer.

The second step consisted of adjusting the conductance of all drainage and river cells. The river bed conductance of the drain cells and river cells were modified until the observed infiltration and drainage rates were reproduced. All measurements of discharge along the rivers (see figure 7.2), the water level of Bostan lake as well as the total amount of drainage water flowing into it were considered. Due to the high depth to groundwater in the Gobi area, the infiltration rate in this area can significantly influence the steady state groundwater table. If required, the horizontal hydraulic conductivity of the Gobi- formation had to be readjusted and both the first and second step repeated. In the area of interest, the depth to groundwater and no longer the absolute height of the calculated and observed groundwater water tables were optimized.

The third step of calibration consisted of the adjustment of the vertical hydraulic conductivities in order to get an optimal fit between calculated and observed patterns of phreatic evaporation. A variation of the vertical conductivity affects the pattern of evaporation, the effectiveness of the drainage net as well as the infiltration rates of the rivers within the Q3-4 formations. Therefore, step 2 or even step 1 have to be repeated. By using only one hydraulic conductivity within the Gobi area, the phreatic evaporation along the Kaidu river in the Gobi-formation could not be reproduced. An additional conductivity zone in the Gobi-formation had therefore to be introduced as presented in figure 7.5.

Figure 7.6 illustrates two examples of phreatic evaporation calculated by applying different vertical hydraulic conductivities. If vertical hydraulic conductivity is set to a small value (around  $0.01 \text{ m}\cdot\text{d}^{-1}$ ), the patterns of phreatic evaporation cannot be reproduced satisfactorily- phreatic evaporation is too high. On the other hand, by applying a high vertical hydraulic conductivity (around  $0.5 \text{ m}\cdot\text{d}^{-1}$ ), the calculated hydraulic heads are systematically smaller than the observed ones and phreatic evaporation cannot be reproduced to the extent observed. Moreover, the drainage net cannot remove the observed amount of water from the system, even if the conductance of the drainage cells is set to a very high value. The lake level is kept constant in both simulations. However, the evaporation rate along the lake shore is not the same. The evaporation zone along the lake is important as it strongly

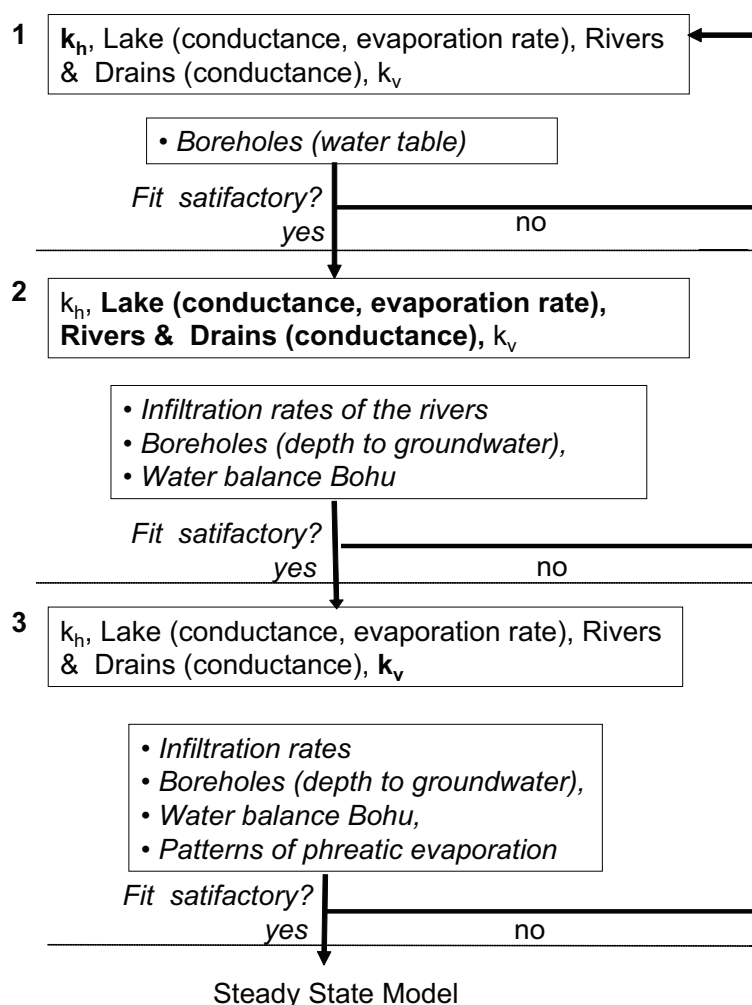


Figure 7.4: Schematic plot of the calibration process. Verification data are printed in italics, the most important parameters for every calibration step are printed bold.

influences the water balance of the second layer- the water evaporated along the lake's shore is originating from the second layer (see section 8.1.5).

The results of the calibrated model parameters are presented in table 7.2. Compared to the model developed at Xinjiang Agricultural University, one difference (besides including the surface water balance, non-linear phreatic evaporation as well as a better DEM) is the reduced amount of free parameters. Only four different types of hydraulic conductivities have been used in this approach. The hydraulic conductivity of the second layer has been tied to the conductivities of the first layer, so that there are only three effective calibration parameters for the hydraulic conductivities. The sharp difference between the Gobi and the Q3 formation is essentially the same in both models. The values of hydraulic conductivities in the previously existing model constructed at Xinjiang Agricultural University vary between  $3.6 \cdot 10^{-4} \text{ m} \cdot \text{d}^{-1}$  and  $1.3 \text{ m} \cdot \text{d}^{-1}$  in the Q3-4 formation and from  $0.3 \text{ m} \cdot \text{d}^{-1}$  to  $40 \text{ m} \cdot \text{d}^{-1}$  in the Gobi

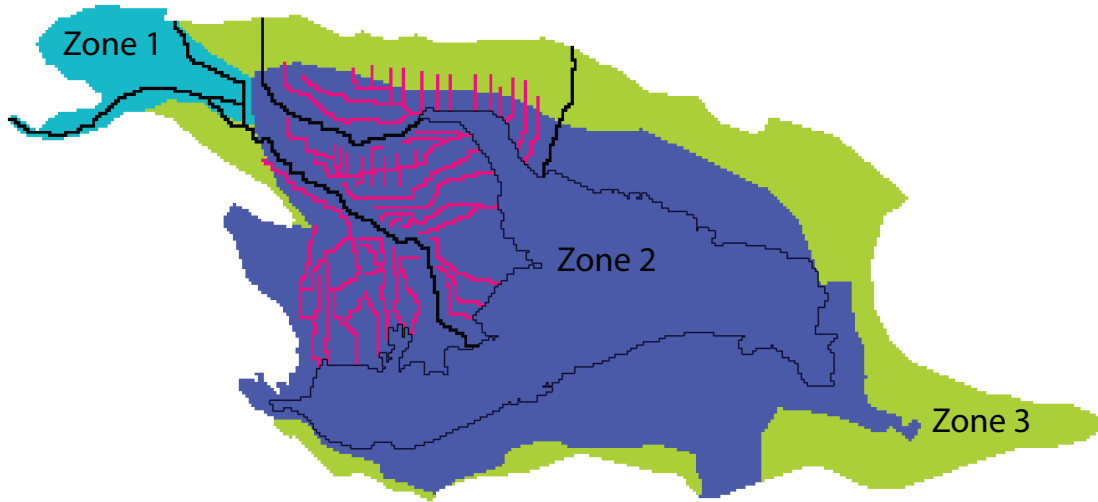


Figure 7.5: Overview of the zonation of hydraulic conductivities used for the steady state model.

Table 7.2: Overview of the horizontal and vertical hydraulic conductivities for all layers as well as the lakebed conductance and the evaporation rate over Bostan lake.

Aquifer	Layer 1	Layer 2	Layer 3	Layer 4
Horizontal k Zone 1 [m·d <sup>-1</sup> ]	25	25	25	25
Horizontal k Zone 2 [m·d <sup>-1</sup> ]	0.9	15	0.9	0.9
Horizontal k Zone 3 [m·d <sup>-1</sup> ]	50	50	50	50
Vertical k Zone 1 [m·d <sup>-1</sup> ]	5	5	5	5
Vertical k Zone 2 [m·d <sup>-1</sup> ]	0.09	0.09	0.09	0.09
Vertical Zone 3 [m·d <sup>-1</sup> ]	5	5	5	5
Lake				
Evaporation rate [m·d <sup>-1</sup> ]	0.0028	-	-	-
Lakebed conductance Layer 1 [m·d <sup>-1</sup> ]	0.001	-	-	-
Lakebed conductance Layer 2 [m·d <sup>-1</sup> ]	0.0005	0.005	-	-

formation. The geometric average of these hydraulic conductivities in the two zones are of the same magnitude as the hydraulic conductivities obtained through the calibration.

The calibrated evaporation rate of the lake is 1.03 m·a<sup>-1</sup>. One could argue the evaporation rate should be the same as calculated with the Penman equation (1.4 m·a<sup>-1</sup>), as water is not limiting the evaporation process. For several reasons, this evaporation rate cannot be directly compared with potential evaporation. The



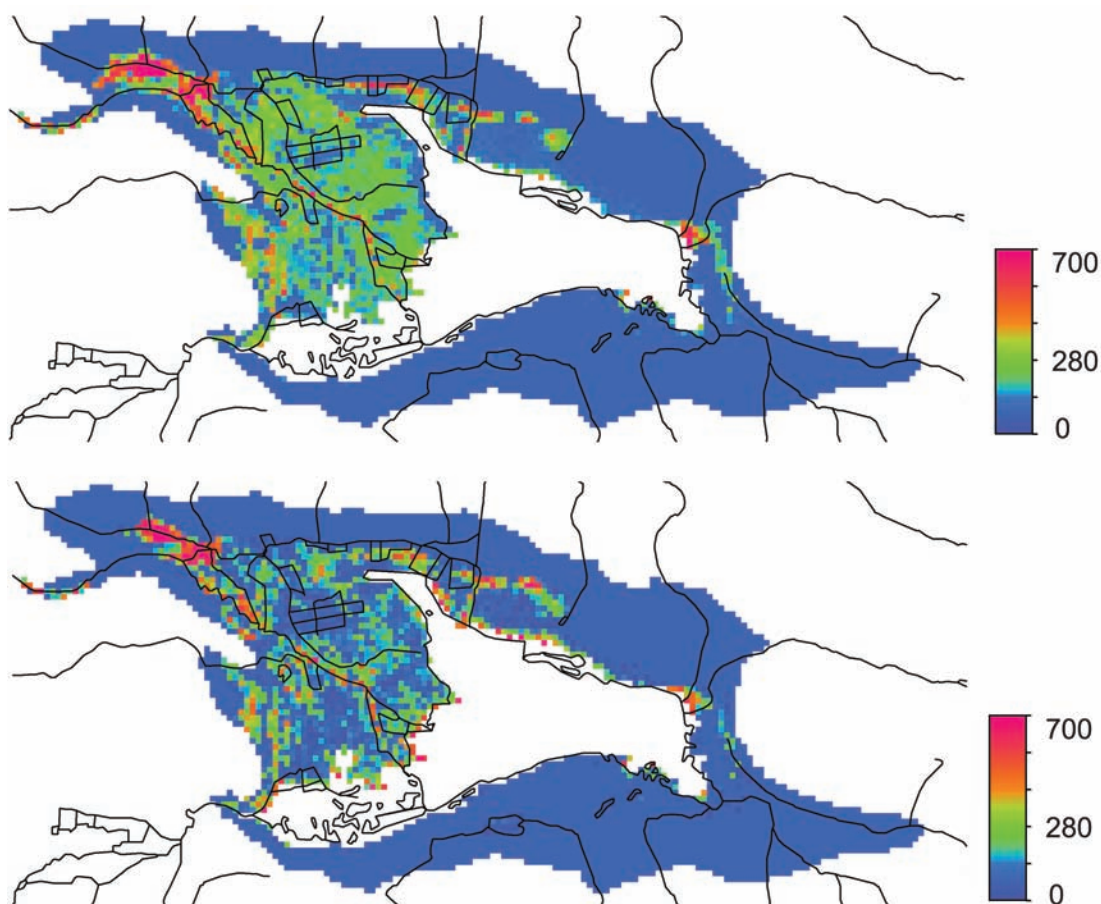


Figure 7.6: Two examples of calculated phreatic evaporation maps [ $m^3 \cdot d^{-1}$ ] obtained during the calibration. The first map was calculated by using a vertical hydraulic conductivity of  $0.01 m \cdot d^{-1}$ , the map below a value of  $0.5 m \cdot d^{-1}$ . If a small value of vertical hydraulic conductivity is applied, phreatic evaporation in the irrigation area is significantly increased. Along the lake shore, however, phreatic evaporation is reduced.

evaporation rates obtained by using NOAA-AVHRR images showed that evaporation rates over the little lake are 10% below the evaporation rates of the open water surface. The little lake and the large lake have been considered as one system in the model with uniform potential evaporation. If the reduction of evaporation over the little lake is taken into account, the evaporation rate over the open water surface is  $1.1 m \cdot a^{-1}$ . However, the most important reason why the Penman equation overestimates the potential evaporation over a large, open water surface is the reduced moisture gradient. These considerations again show the difficulties of accurately estimating evaporation rates over the lake. However, the calibrated value is consistent with estimates from other Chinese sources (oral communication 2002, Dong Xinguang).

The streambed conductance of the rivers over the Gobi formation is high. In

these areas, the rivers virtually flow over the aquifer, and the streambeds consist of coarse material. In the Q3-4 area, fine particles form the streambeds of the drainage channels or the rivers. The streambed conductance in the Gobi formation had to be set to a value of  $6000 \text{ m}^2 \cdot \text{d}^{-1}$ . In the Q3-4 formation, the river conductance was set to a value of  $1500 \text{ m}^2 \cdot \text{d}^{-1}$ . The conductance of the drainage cells was set to  $3000 \text{ m}^2 \cdot \text{d}^{-1}$ .

The lakebed conductance in the first and second layer was also adjusted. It is impossible to obtain reliable verification data for the exchange of water between the lake and the aquifer. However, compared to the uncertainties of the evaporation rate, this parameter is not of great importance. The infiltration through the dam into the first aquifer layer is small, according to the Water Management Department in Korla. The Kongque river is not used for verification. The discharge of the Kongque river has been defined in the Lake Package.

### 7.5 Numerical considerations

The numerical accuracy of the model is given by the convergence criterion of the solver. The convergence criterion is defined as the maximum absolute value of head change for all cells during an iteration. The solver used for this model was the strongly implicit procedure (SIP). The maximum head change was set to  $10^{-4} \text{ m}$ . Finer convergence criteria produced identical results. The Lake Package requires an additional convergence criterion, as the water balance of the lake is calculated independently of the main Modflow routine. The convergence criterion for the lake was set to  $0.01 \text{ mm}$ . A so-called acceleration parameter can be defined in the SIP Package. The acceleration parameter is a multiplier for head changes to compute the head in the new iteration step. This value is between 0 and 1. The segmented function of evaporation is nonlinear and is prone to cause numerical instabilities. However, it turned out that by using an acceleration parameter smaller than 0.5, the convergence criterion could always be fulfilled.

### 7.6 Additional data required for transient simulations

In order to simulate the influence of irrigation over time, a dynamic model was constructed. The basic geometric set-up of this model is analogous to the set-up used for the steady state simulations. Additional input data required for transient simulations are the initial conditions, the specific yield as well as specific storage. Moreover, the discretization of the variable time has to be defined. The period length in the transient model was set to one year. Every period is calculated in 182 time steps. Specific yield as well as effective porosity are based on the values applied in the model developed at Xinjiang Agriculture University. In this model, several zones for both effective porosity and specific yield have been defined. However, in analogy to the distribution of hydraulic conductivities, two major zones can be

sorted out. Compared to the Q3-4 area, both specific yield and effective porosity are significantly larger in the Gobi formation. The average value of the zones applied in the model developed at Xinjiang University have been calculated and used in this approach. In the Gobi formation, specific yield is 0.28. In the Q3-4 formation, the specific yield amounts to 0.15. Specific storage is set to  $0.0001 \text{ m}\cdot\text{d}^{-1}$  for all confined layers.



# Chapter 8

---

## Modelling Results

In this chapter, the results of the calibrated steady state model based on average data from the period 1990 to 1999 are presented. The results of this calibrated model are compared to all the available observation data. Moreover, a zero-irrigation scenario and a scenario where a portion of irrigation water drawn from the river is substituted by water pumped from the aquifer are simulated both in transient and steady state. Finally, the results obtained through the transient simulations are described and the long term sustainability of groundwater abstraction is evaluated.

### 8.1 Calibrated steady state model

#### 8.1.1 Water balance of the aquifer

The global water balance of the steady state model is presented in table 8.1. The discrepancy between the in- and outgoing fluxes is smaller than 0.01%. Irrigation induced recharge is nearly a factor of 1.4 higher than the natural infiltration of river water. Considering the large area covered by the lake, the exchange rate between the lake and the aquifer is very small. Phreatic evaporation is, according to this water balance, nearly twice as high as the amount of water removed through stream leakage. The stream leakage presented in table 8.1 consists both of water removed by the drainage net as well as water re-infiltrating into the river system. In the lower reaches of the Kaidu river, the water re-infiltrates from the aquifer into the river, while in the Gobi formation water infiltrates from the river into the unconfined aquifer system. This water balance is in agreement with the rough water balance presented in figure 2.2.

*Table 8.1: Aquifer water balance.*

In fluxes [ $\text{m}^3 \cdot \text{s}^{-1}$ ]		Out fluxes [ $\text{m}^3 \cdot \text{s}^{-1}$ ]	
Recharge	20.4	Stream leakage	12
Stream leakage	14.1	Phreatic evaporation	22.5
Wells	0	Wells	3.0
Lake seepage	3.1	Lake seepage	0.1
Total	37.6	Total	37.6

The water balance presented in this figure has been calculated with the box model. The comparison of the distributed and the box model is discussed in section 8.1.6.

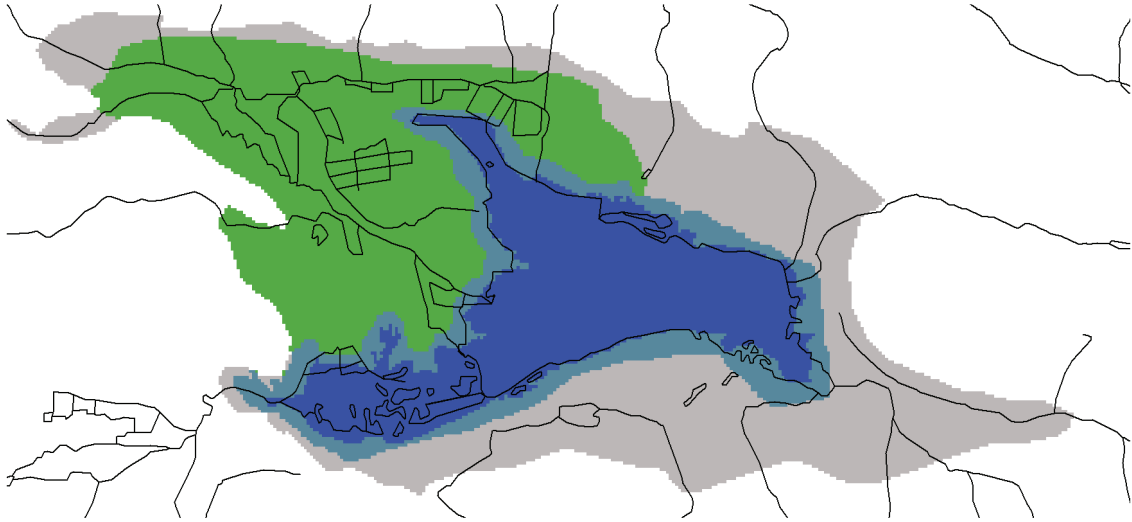


Figure 8.1: The irrigated area (shown in light green colour, also called area of interest) is of interest as phreatic evaporation and soil salinization occur mainly in this region. The lake is plotted in dark blue, the lake shore in light blue.

Table 8.2: *Exchange rates between the aquifer layers in the area of interest.*

Layer 1 in fluxes [ $\text{m}^3 \cdot \text{s}^{-1}$ ]		Layer 1 out fluxes [ $\text{m}^3 \cdot \text{s}^{-1}$ ]	
GW from layer 2:	10.8	GW to layer 2:	6.2
Layer 2 in fluxes		Layer 2 out fluxes	
GW from Layer 1:	6.2	GW to layer 1:	10.8
GW from layer 3:	1.1	GW to layer 3:	0.6
Layer 3 in fluxes		Layer 3 out fluxes	
GW from layer 2:	0.6	GW to layer 2:	1.1
GW from layer 4:	0.6	GW to layer 4:	0.4

The irrigated area is of particular interest. This area of interest is presented in figure 8.1. The exchange rates between the aquifer layers in the area of interest are presented in table 8.2. The water balance of the rivers and the lake are presented in section 8.1.4.

### 8.1.2 Hydraulic heads

The calculated hydraulic heads for the areas in the Gobi formation are the same for all layers. Around Bostan lake, the hydraulic heads of the second, third and fourth layer are slightly above the terrain surface. This is in agreement with the



*Table 8.3: Comparison between observed and calculated depth to groundwater.* The number of observation boreholes, the largest residual as well as the average absolute error are printed.

	#Obs	largest error [m]	average absolute error [m]
Layer 1	28	8.5	2.1
Layer 2	17	-4.3	1.8
Layer 3	12	-4.9	2.5

borehole data: the aquifer system in this area is artesian. Borehole data have been documented for the first three layers. The comparison between the calculated and observed groundwater tables is presented in figure 8.2, table 8.3 presents an overview. In terms of absolute values, the fit is satisfactory. The best fit is found for the data of the first layer. The comparison between the calculated and observed depths to groundwater is presented in figure 8.3. Considering the high dependency of phreatic evaporation on the depth to groundwater, the comparison between calculated and observed depth to groundwater is disappointing. In figure 8.4, the distribution of residuals between calculated and observed groundwater tables is plotted. In the Q3-4 formation (the largest part of the area of interest), the fit between the two quantities is the best.

The calculated depth to groundwater is negative for 9 boreholes of the first layer (see figure 8.4). This does not necessarily mean that the calculated groundwater table is above the surface elevation of the top layer. The depth to groundwater was obtained by subtracting the calculated groundwater table from the high resolution DEM. The surface elevation of a coarse model pixel is not equal to the surface elevation at the borehole. If the depth to groundwater at these specific boreholes is calculated on the basis of the surface elevation applied in the model, the depth to groundwater is, as it should be, positive. The largest errors occur along the mountain range of the basin. This is not surprising, as the topography around the area of interest is steep and already a small error in the location of the borehole leads to a considerable error. The error in the surface elevation of the measurement height is of the same magnitude as the residuals between observed and calculated values. This already indicates that the accuracy of the DEM is the limiting factor for the accurate determination of depth to groundwater. Therefore the assessment of the quality of the calculated water tables has to use a different method. In the following, the distributed quantity of phreatic evaporation is used for this purpose.

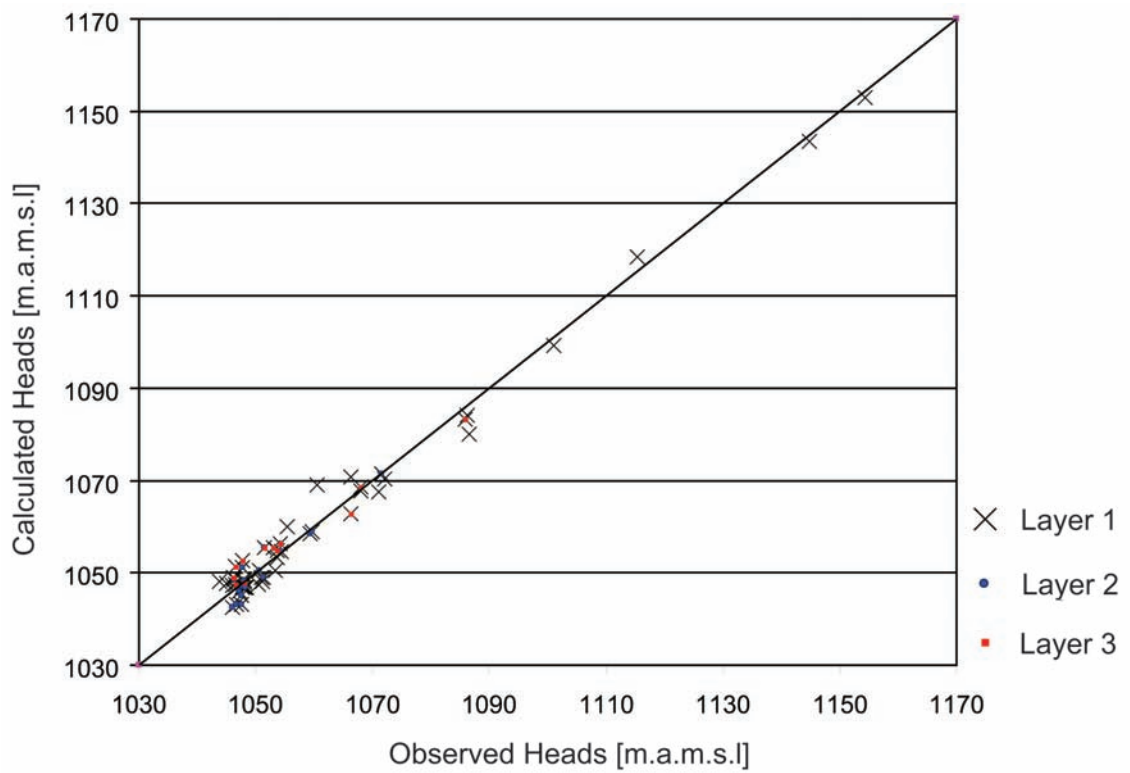


Figure 8.2: Comparison between observed and calculated groundwater tables for 3 layers. Data for the first layer are plotted in black (crosses), the second layer in blue and the third layer in red.

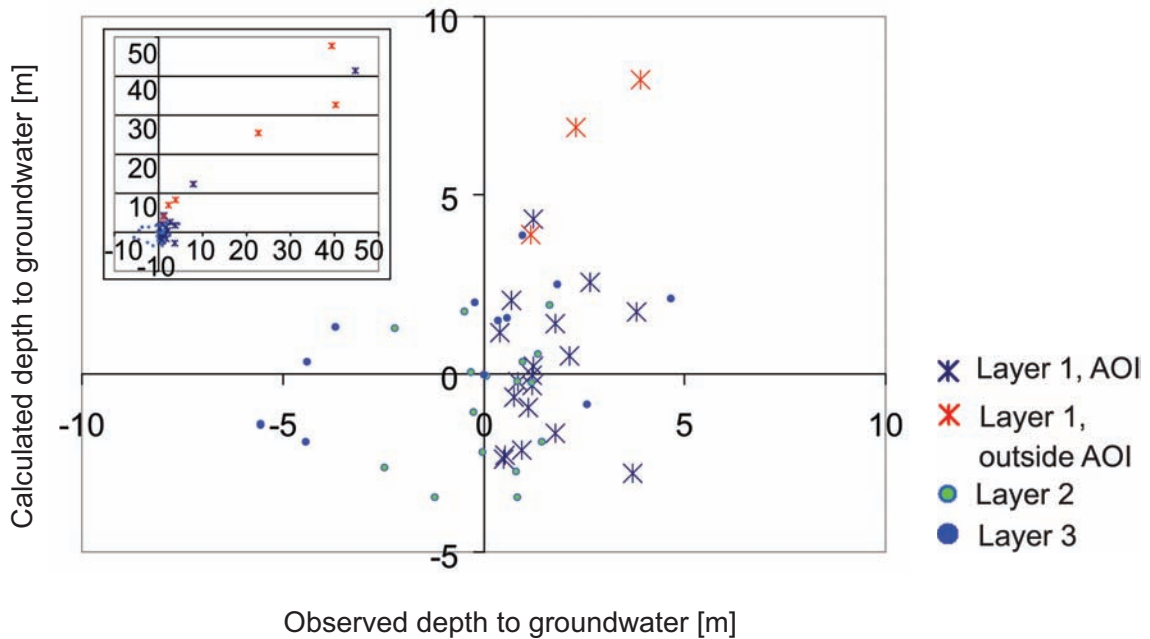


Figure 8.3: Comparison between observed (*x*-axis) and calculated depth to groundwater. The calculated heads in the lower left quadrant are above the soil surface.

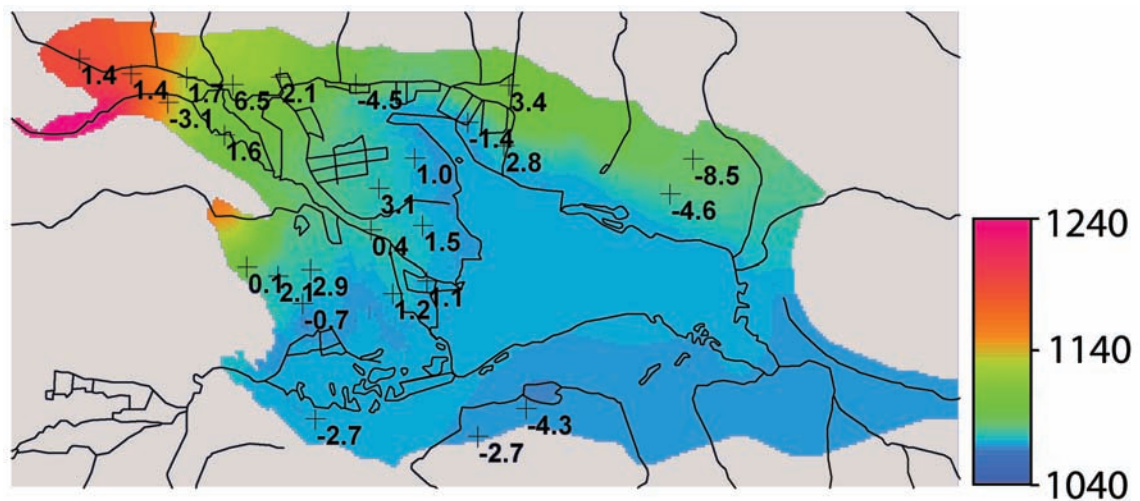


Figure 8.4: Calculated groundwater tables [m] of the first layer- the numbers are the residuals between the measured and the observed groundwater tables.

### 8.1.3 Phreatic evaporation

Figure 8.5 presents phreatic evaporation calculated with the model and phreatic evaporation based on remote sensing data. The numerical agreement of the two quantities is too low to plot a correlation on a pixel basis. By using only a limited amount of calibration parameters for the model, only the structure of the patterns can be reproduced. However, an alternative to comparing the maps on a pixel-wise basis is splitting them into classes and comparing the agreement within the classes. The most simple alternative is to carry out this comparison on a binary level. If the model predicts phreatic evaporation for a specific pixel, the error of the calculated groundwater head is between zero and the extinction depth (as long as the calculated water table is not above the elevation of the terrain). Here, phreatic evaporation is split up into three different classes. This amounts to filtering noisy data. All pixels with phreatic evaporation smaller than  $80 \text{ m}^3 \cdot \text{d}^{-1}$  are assigned to class 1, pixels between  $80 \text{ m}^3 \cdot \text{d}^{-1}$  and  $300 \text{ m}^3 \cdot \text{d}^{-1}$  to class 2, all pixels above to class 3. The class ranges are the same for both the model output and the phreatic evaporation based on the NOAA-images. By applying 3 different classes, 9 different combinations of agreement are possible. In order to visualize this agreement of the classes within one single map, the two maps can simply be divided. If a pixel belongs to the same class in every map, the division of the two class-maps yields 1. Such a division has been carried out, see figure 8.6.

Table 8.4 shows the quality of agreement for the entire model domain (not including the area of Bostan lake) between the two class maps. For the entire model domain, 79.5% of the pixels-classes are in agreement. Along the border of the irrigated area in the north, the NOAA-AVHRR images indicate phreatic evaporation. The model does not reproduce this. However, the observed absolute quantities in this area are small compared to phreatic evaporation along the rivers. In the north-eastern fringes of the model domain, the NOAA-AVHRR images show phreatic evaporation not reproduced by the model. This is an indication that the model has calculated the groundwater tables in these areas too low. Unfortunately, no borehole data are available in these areas to verify this statement. Most probably, these areas situated right at foot of the mountains receive a small portion of recharge originating in the Tianshan mountains. Such possible boundary fluxes have not been taken into consideration in the model set-up.

### 8.1.4 Surface water fluxes

The riverbed conductance over the Gobi-formation has been calibrated in order to reproduce the observed infiltration rate for every river. All discharge data are based on unpublished measurements documented by the Water Management Office in Korla and made available through Xinjiang Agricultural University in Urumqi. Table 8.5 presents the comparison between calculated and observed quantities. Station P1 of the Kaidu river is located at Dashan Kou. Station P2 is located at the first

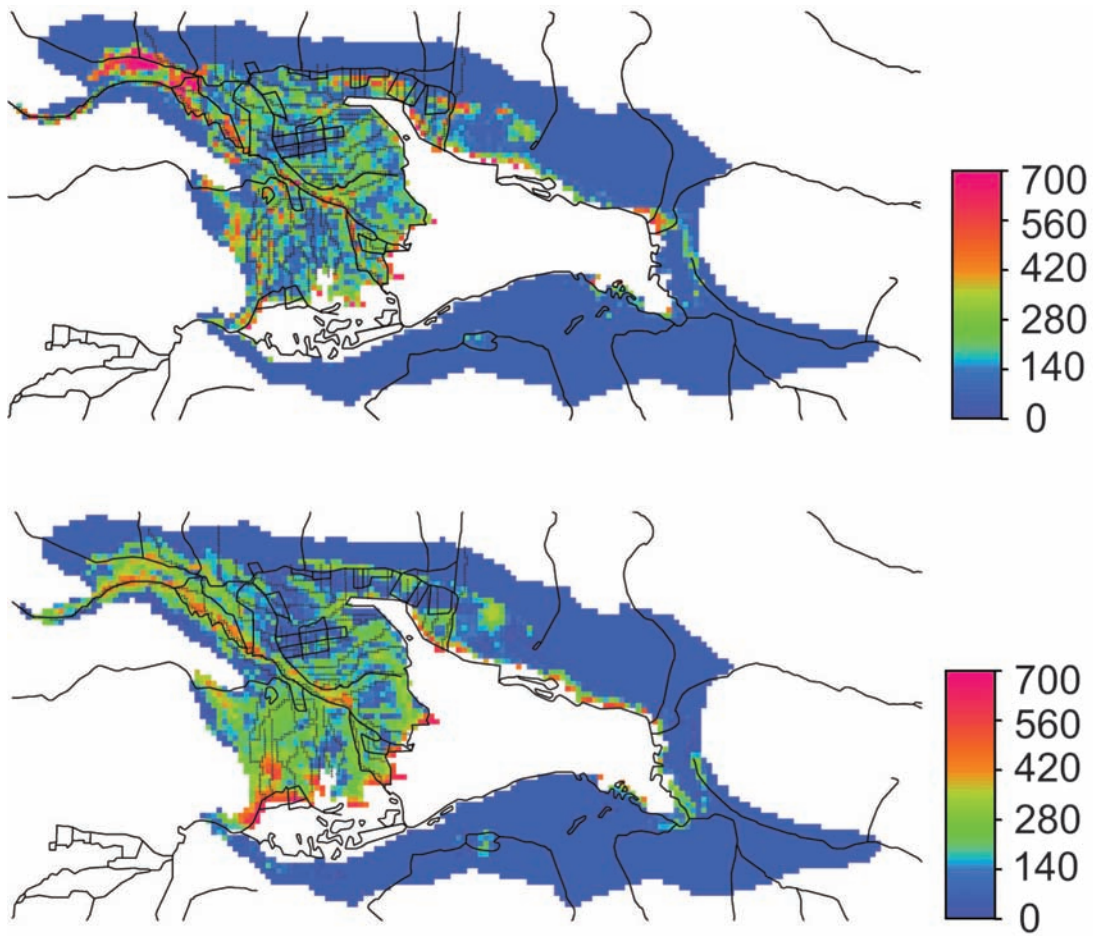


Figure 8.5: Phreatic evaporation [ $\text{m}^3 \cdot \text{d}^{-1}$ ] from NOAA-AVHRR images and phreatic evaporation calculated by the calibrated model.

Table 8.4: *Comparison between the classification of the NOAA- images and the model output.* The ratio is calculated by simply dividing the two classes- the distribution of the data summarized in this table is presented in figure 8.6.

Model- Class	NOAA-Class	Ratio	#pix	%
1	1	1	2790	59.8
1	2	0.5	430	9.2
1	3	0.3	8	0.2
2	1	2	292	6.3
2	2	1	716	15.3
2	3	0.7	114	2.4
3	1	3	18	0.4
3	2	1.5	95	2
3	3	1	205	4.4

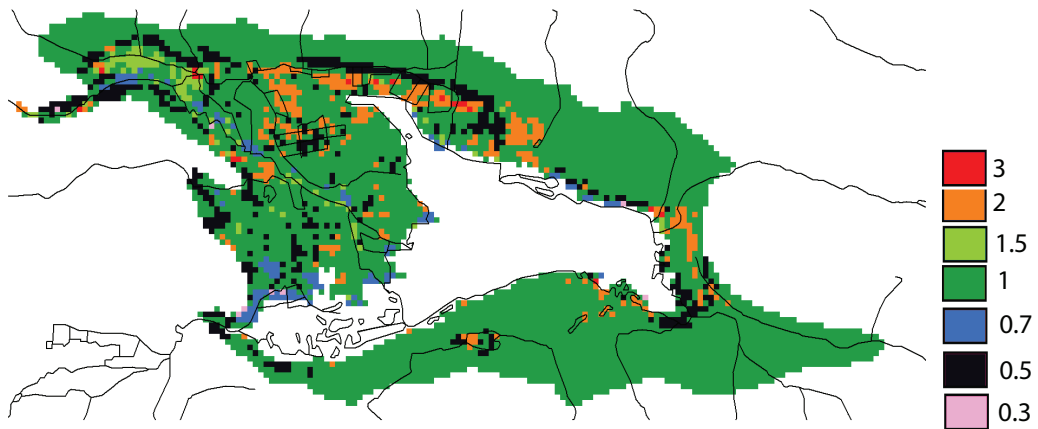


Figure 8.6: *Quotient of the class map from the model output and the class map from remote sensing.* 1 indicates an agreement, while 0.3 and 3 indicate the poorest agreement between the classifications.



*Table 8.5: Comparison between measured and calculated surface water discharge.* Measurement data of three gaging stations along the Kaidu river are available, as well as data from two stations for the Huangshui Guo and one station for the Qingshui He. The locations of the points are presented in figure 7.2.

	Measured discharge [ $\text{m}^3 \cdot \text{s}^{-1}$ ]	Calculated discharge [ $\text{m}^3 \cdot \text{s}^{-1}$ ]
Kaidu: P1	119	-
Kaidu: P2	117	118
Kaidu: P3	92	93
Qingshui He: P4	3.6	-
Qingshui He: P5	1.4	2
Huangshui Gou: P6	8.3	-
Huangshui Gou: P7	-	8
Drainage	4	4.2

diversion point, and station P3 is the measurement station of Yanqi city. The first measurement stations of Qingshui He P4 and Huangshui Gou P6 are located close to the mountains. Stations P5 and P7 are located close to the inflow to Bostan lake. Discharge data from the first measurement station at every river have been used as an input parameter.

### 8.1.5 Bostan lake

The only directly accessible parameters of Bostan lake are the lake level as well as the amount of water pumped into the Kongque river. Table 8.6 presents the calculated water balance for Bostan lake. The resulting lake level is 1047.1 m. The exchange rates between the aquifer and the lake have been calculated (see figure 8.7). The inflow from the lake to the aquifer system is  $3.1 \text{ m}^3 \cdot \text{s}^{-1}$ . Around the direct boundary of the lake (the width of this boundary is 500 m, corresponding to one model pixel)  $3.8 \text{ m}^3 \cdot \text{s}^{-1}$  are evaporated. Phreatic evaporation in the wider vicinity of the lake is therefore not only related to the infiltration of lake water into the system. The water balance of the wider vicinity of the lake shows that water from the second layer is infiltrating into the first layer where it is evaporated.

### 8.1.6 Comparison between the box model and the distributed steady state model

Several fluxes have been considered in the box approach including phreatic evaporation and drainage. Drainage consists both of water removed from the system by the drainage channel network as well as the direct infiltration of water into Bostan

Table 8.6: *Water balance for Bostan lake.* All fluxes except the discharge of the Kongque He are calculated.

Input fluxes [ $\text{m}^3 \cdot \text{s}^{-1}$ ]		Output fluxes [ $\text{m}^3 \cdot \text{s}^{-1}$ ]	
Kaidu	86.1	Evaporation	52.4
Qingshui He	0.02	Kongque He	38.9
Huangshui Gou	4.0	Groundwater	3.1
Drainage water	4.2		
Groundwater	0.1		
Total	94.4		94.4

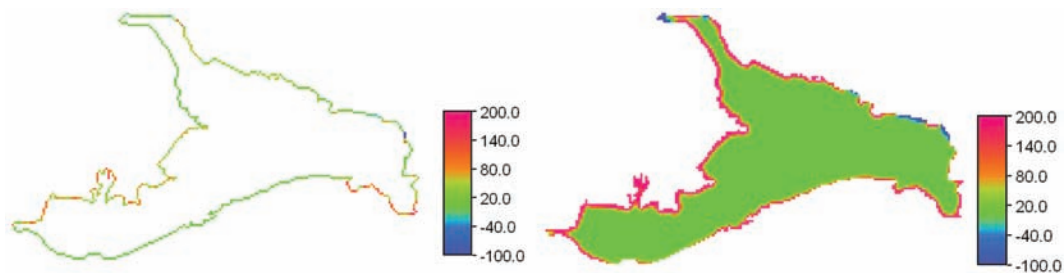


Figure 8.7: Infiltration [ $\text{m}^3 \cdot \text{d}^{-1}$ ] into aquifer layer 1 (left) and layer 2 (right).

lake. The infiltration rates of the rivers are included in the irrigation water flux, as the distribution of infiltration is not important. The water fluxes through the basin shown in figure 2.2 have been calculated by using the box model and represent the average conditions between 1990 and 1999.

In the box model, the total amount of drainage water leaving the system is  $12 \text{ m}^3 \cdot \text{s}^{-1}$  and phreatic evaporation amounts to  $21 \text{ m}^3 \cdot \text{s}^{-1}$ . These quantities are close to the phreatic evaporation rates calculated with the distributed model. Even though the box model allows to estimate the water balance of the Yanqi basin satisfactorily, it does not allow to determine in which specific regions the groundwater table is close to the surface and where the risk of triggering the salinity problem is high.

## 8.2 Scenarios

### 8.2.1 Zero-irrigation scenario

In order to simulate the conditions in the Yanqi basin before irrigation was introduced, a model was set up without any diversion from the rivers and without any recharge. Consequently, the drainage net was deactivated by setting the streambed conductance to zero. The outflow of the Kongque river was increased to maintain

the level of Bostan lake at 1047 m.

Table 8.7 presents the surface water fluxes for this scenario. The flow through Bostan lake is, not surprisingly, significantly higher if no irrigation water is drawn from the rivers. Compared to the calibrated steady state model, phreatic evaporation in the zero-irrigation scenario is around 50% lower. The highest values of phreatic evaporation mainly occur along the Kaidu river (see figure 8.8). The distribution of phreatic evaporation shows where the groundwater table is high even without irrigation. In the area embraced by Wulasitai and the Kaidu river (see figure 8.8), the groundwater table is above the extinction depth. This is an independent verification of the model, as indeed a swamp system is found in this area. Phreatic evaporation is also observed in area 4 (see figure 6.6). This is in agreement with the observations in the salinity map. The salinity map indicates a very high degree of salinization in this area.

The model predicts that over the entire model domain, phreatic evaporation occurs in 3386 pixels (around 850 km<sup>2</sup>). Compared to the irrigation case, this is 49 % lower.

Table 8.7: *Aquifer water balance for the zero-irrigation scenario.*

Input fluxes [m <sup>3</sup> ·s <sup>-1</sup> ]		Output fluxes [m <sup>3</sup> ·s <sup>-1</sup> ]	
Recharge	0.0	Stream leakage	6.2
Stream leakage	14.4	Phreatic evaporation	10.3
Lake seepage	2.1	Lake seepage	0.01
Total	16.5	Total	16.5

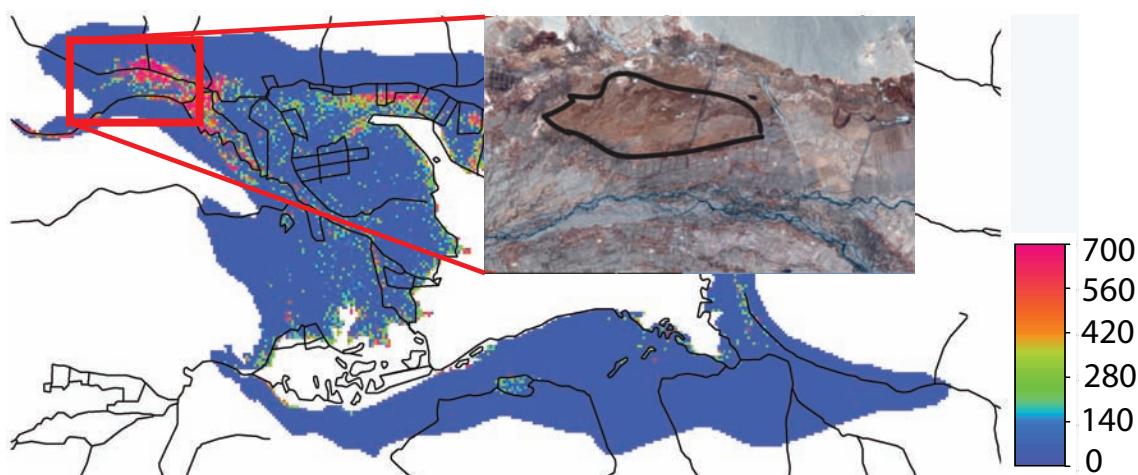


Figure 8.8: *Phreatic evaporation [m<sup>3</sup>·d<sup>-1</sup>] without irrigation. The area embraced between Wulasitai and the Kaidu river is a swamp and is periodically flooded.*

Table 8.8: *Lake water balance for the zero-irrigation scenario.*

Input fluxes [ $\text{m}^3 \cdot \text{s}^{-1}$ ]		Output fluxes [ $\text{m}^3 \cdot \text{s}^{-1}$ ]	
Kaidu	115.6	Evaporation	52.4
Qingshui He	1.4	Kongque He	69.1
Huangshui Gou	6.7	Groundwater	2.2
Groundwater	0.0		
Total	123.7		123.7

Because the drainage net has been deactivated, stream leakage is only related to the rivers. Compared to the river infiltration calculated with the model representing the average conditions for the period 1990-1999, infiltration in the zero-irrigation scenario is slightly higher. This was to be expected, since the depth to groundwater in the zero-irrigation scenario is larger.

Phreatic evaporation around the lake shore also occurs in the zero-irrigation scenario. The second layer is drained by the first layer close to the lake, independently of agricultural practices in the upstream. Even though the evaporation rates are small (compared to the rates of phreatic evaporation triggered by agriculture) the continuous evaporation of water originating from the second layer along the lake shore must result in a long term accumulation of salt. Indeed, the highest values of soil salinization are found along the lake's shore.

### 8.2.2 Pumping groundwater scenario

As stated in the introduction, the substitution of a portion of the irrigation water by pumped groundwater is a promising alternative to the present water management practice. Compared to the first layer, the hydraulic conductivity in the second layer is high. Moreover, the depression cone around the pumps is flatter if groundwater is pumped from the second layer. Finally, the water quality of the second layer is superior to the one of the first layer. For all these reasons, it is obvious that pumps should abstract groundwater from the second aquifer layer.

In this scenario, the extent to which the phreatic evaporation caused by irrigation can be reduced by pumping groundwater from the second layer is examined and the resulting increase of downstream water resources is calculated. The distribution and intensity of recharge are the same as in the model used for calibration. The very low hydraulic conductivities in the Yanqi basin do not allow the installation of a few, big pumps. Instead, many small wells have been distributed throughout the second layer. The pumping rates were adjusted through trial and error in such a way that the cells in the first layer do not fall dry. The pumps have been installed in the areas where irrigation has significantly increased phreatic evaporation. These regions can easily be identified by subtracting phreatic evaporation calculated in the

zero-irrigation scenario from one calculated in the steady state scenario. In areas where an efficient drainage net is present, the difference between the two quantities is small. Therefore, the reduction of phreatic evaporation by the drainage net is implicitly considered.

The abstraction rates range from only  $1700 \text{ m}^3 \cdot \text{d}^{-1}$  in the area south of Yanqi city to  $10000 \text{ m}^3 \cdot \text{d}^{-1}$  in the Gobi formation. The distribution of the pumps is shown in figure 8.9. In total, 300 pumps have been installed. The diversion of irrigation water drawn from the rivers has been reduced by the amount of groundwater pumped. The aquifer water balance of this scenario is shown in table 8.9. By pumping an

*Table 8.9: Aquifer water balance with groundwater pumping.*

Input fluxes [ $\text{m}^3 \cdot \text{s}^{-1}$ ]		Output fluxes [ $\text{m}^3 \cdot \text{s}^{-1}$ ]	
Recharge	20.3	Stream leakage	10.5
Stream leakage	15.1	Phreatic evaporation	15.3
Lake seepage	3.1	Wells	12.6
		Lake seepage	0.1
Total	38.5	Total	38.5

additional amount (compared to the steady state model) of  $9.6 \text{ m}^3 \cdot \text{s}^{-1}$ , the total phreatic evaporation is reduced by  $7.2 \text{ m}^3 \cdot \text{s}^{-1}$ . Phreatic evaporation in the zero-irrigation scenario was around  $10.3 \text{ m}^3 \cdot \text{s}^{-1}$ . Taking this into account, irrigation induced phreatic evaporation is reduced by around 50%. The total amount of cells where the model predicts phreatic evaporation is reduced from 6881 cells (without any pumping) to 4931 in the pumping scenario. If only the areas where phreatic evaporation does not occur naturally are compared, the reduction is 66%.

Figure 8.9 presents phreatic evaporation for this scenario. The exchange rates for the aquifer layers in the area of interest are shown in table 8.10. By pumping the additional amount of  $9.6 \text{ m}^3 \cdot \text{s}^{-1}$  of water from the second aquifer layer, the amount of water infiltrating from the first layer is increased by nearly a factor of 3 (compare with table 8.2). Considering the huge volume of the second layer, this flux remains small. Nevertheless, the saline water infiltrating into the second layer will lead to a salinization of the second aquifer layer. Phreatic evaporation of water originating from the second layer along the lake's vicinity is not reduced by pumping groundwater from the second layer. The water balance of Bostan lake is influenced by both the reduced amount of water drawn from the river, the increased infiltration rates of the rivers, and the reduced drainage rates. The water balance of Bostan lake is presented in table 8.11. The increased amount of water available for the Kongque river can be compared with the total amount of water pumped from the aquifer. The comparison of these two measures shows that for  $1 \text{ m}^3 \cdot \text{s}^{-1}$  of water pumped from the aquifer, the available water resources for the Kongque river are increased by  $0.75 \text{ m}^3 \cdot \text{s}^{-1}$ . However, this estimation does not take into account that

*Table 8.10: Calculated exchange rate between the different layers in the area of interest for the pumping scenario.* The area of interest consists of the confined area (covering the first, saline aquifer layer) as well as the area where the Kaidu river infiltrates into the unconfined aquifer system.

Layer 1 input fluxes [ $\text{m}^3 \cdot \text{s}^{-1}$ ]		Layer 1 output fluxes [ $\text{m}^3 \cdot \text{s}^{-1}$ ]	
GW from layer 2	9.3	GW to layer 2	17.5
Layer 2 in fluxes		Layer 2 out fluxes	
GW from Layer 3	3.7	GW to layer 3	3.3
GW from layer 1	17.5	GW to layer 1	9.3
Layer 3 in fluxes		Layer 3 out fluxes	
GW from layer 4	1.8	GW to layer 4	1.5
GW from layer 2	3.3	GW to layer 2	3.7

*Table 8.11: Lake water balance with groundwater pumping.*

Input fluxes [ $\text{m}^3 \cdot \text{s}^{-1}$ ]		Output fluxes [ $\text{m}^3 \cdot \text{s}^{-1}$ ]	
Kaidu	93.3	Evaporation	52.4
Qingshui He	0.4	Kongque He	46.1
Huangshui Gou	4.7	Groundwater	3.0
Groundwater	<0.1		
Drainage Water	3.0		
Total	101.5		101.5

the average transport way of water from a pumping station to the field is smaller than the average transport way from the river to the field. The water saved by reducing infiltration is potentially available for the downstream and could be taken into account in the input data of the model.

Stream leakage from river water into the aquifer is, compared to the calibrated steady state model increased by  $1 \text{ m}^3 \cdot \text{s}^{-1}$ . Pumping groundwater therefore does not significantly increase the infiltration of the Kaidu river. The drainage water entering Bostan lake is only reduced by  $1.2 \text{ m}^3 \cdot \text{s}^{-1}$  (compared to the steady state model). This is expected, as no pumps have been installed in the areas where the drainage net is efficient. However, even though pumping groundwater can potentially increase the available water resources downstream, abstraction from the second layer does include a risk. If the groundwater table in the first layer is lowered due to the abstraction of water in the second layer, there must be a water flux infiltrating from the (saline) first layer to the second layer. The saline water of the first layer



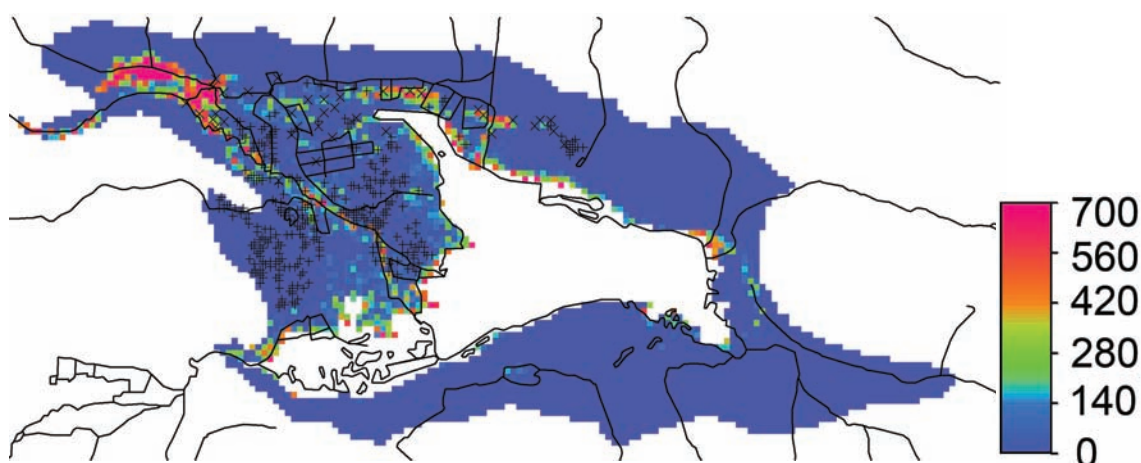


Figure 8.9: Distribution of phreatic evaporation [ $\text{m}^3 \cdot \text{d}^{-1}$ ] for the pumping scenario. Crosses indicate that a pump is abstracting water from the second layer.

will increase the salt concentration in the second layer. Lowering the groundwater table in the first aquifer layer could also deactivate the drainage net as the groundwater table falls below the bottom of the drainage channels. As shown with the 1-box model, the efficiency of the drainage net is important: not in terms of water quantity, but to guarantee an output flux for salt. Moreover, by using the pumped groundwater for the irrigation of the fields, salt removed from the second layer by pumps is recycled. The water pumped from the second layer will become saline and consequently the quality of irrigation water applied decreases. The long-term sustainability of abstracting groundwater can therefore not only be judged by the changes of the water balance. As stated in chapter 3, the resulting steady state concentration of salt within the system also has to be considered. The calculation of the steady state concentration of the first and second aquifer layer as well as the changes of the irrigation water quality are discussed in chapter 8.4.

### 8.3 Transient model

The dynamic model simulates the influence of irrigation in the Yanqi basin in two different steps. First, a steady state model representing the average conditions between 1954 and 1976 was constructed. The main difference between this steady state model and the model used for calibration is the modified recharge map. The exact locations of the irrigated areas have not been documented for this period. The recharge map is based on the assumption that no irrigation has been carried out in the areas where irrigation channels have been constructed after 1976. The results of this steady state simulation were used as initial conditions for the dynamic model. Alternatively, a dynamic model simulating the entire irrigation history could have been set up. The initial conditions of such an approach are unknown. However, according to the box model the time required to reach steady state conditions



(by using the average amount of irrigation water applied between 1954 and 1976) is around 10 years if the initial groundwater table is set to 7 m below the surface. In the area of interest, the average thickness of the first aquifer layer is 7 m. During the period between 1965 and 1976 the irrigated area remained essentially the same, see figure 2.12. It is therefore reasonable to assume that steady state conditions were reached during this period. The rising groundwater table in the northwestern part of the Yanqi basin after 1976 is related to the construction of the large irrigation channels in this area.

### 8.3.1 Initial conditions

No hydrological data are available before 1954. Borehole data are available from a few measurement campaigns between 1980 and 2000. However, some information is available. From 1954 to 1976, the irrigated area consisted mainly of the irrigation districts between Yanqi city and the eastern lake shore. After 1976, the development of agriculture in the Yanqi basin was continuously intensified, see figure 2.12. According to the Water Management Authorities in Korla (oral communication 2005), the increase of farmland was achieved by irrigating additional areas surrounded by the large irrigation channels built after 1976. These channels have been constructed to supply the developing irrigation channel net with water.

In order to simulate the average conditions between 1954 and 1976, model input data such as the distribution of recharge had to be constructed according to the sparse information available. The drainage system was deactivated and diversion from the rivers was only calculated for the Kaidu river downstream of Yanqi city. Based on the considerations mentioned above, it is assumed that no irrigation existed along the main irrigation channels constructed after 1976. The remaining agricultural area consists of the area between Yanqi city and Bostan lake. The amount of irrigation water applied before 1976 was distributed over this remaining irrigated area. The construction of the dam has not been taken into account even though before this construction, the lake periodically covered a larger area than today. This is a justified simplification considering the lack of verification data. For a more realistic simulation more data would be needed.

### 8.3.2 Transient simulation for the period from 1976 to 2000

The total amount of irrigated farmland between 1976 as well as the amount of irrigation water applied have been documented for the four irrigation zones. However, the documented data only represent the total area of the irrigated fields. The exact locations of the irrigated fields are not further specified. It is therefore assumed that the boundaries of the irrigated areas did not change significantly between 1976 and 2000. This implies that the increase of farmland observed after 1976 was within the irrigated areas of today. This is a reasonable assumption because this increase was mainly achieved by irrigating additional areas embraced by the large irrigation

channels. Two different recharge maps have been constructed for the period between 1976 and 2000. The first recharge map represents the conditions between 1976 and 1985. It was calculated on the basis of the average amount of irrigation water applied, as well as the average irrigated area for this period. The resulting infiltration rates have been distributed within the irrigated area used for the calibrated model. For the second period, the recharge map constructed for the calibrated steady state model was used (see section 7.3.3). It is a crude simplification to represent the irrigation history between 1976 and 2000 with only two recharge maps. However, more data would be required to construct a series of reliable recharge maps on an annual basis.

Based on the initial conditions and the 2 recharge maps constructed, the influence of irrigation on the water balance of the Yanqi basin was simulated. The transient simulations reveal that after 1996 the system is close to a steady state. The calculated heads as well as the overall water balance for the year 1996 are very close to the steady state conditions calculated with the model representing the average conditions for the years 1990-1999. This is not astonishing, because the distribution of recharge as well as the infiltration rates in the steady state model are, from the year 1985 to 1999, the same as in the transient simulation.

The calculated phreatic evaporation rates can be summed up over all stress periods. This measure represents an integral over time of water that has evaporated directly from the groundwater table and can be compared with the saltmap. One could argue that the import of salt through irrigation water also has to be considered. The amount of salt at the soil surface is not only increased by the capillary rise of the saline groundwater. The irrigation water itself contains salt. Most of this salt remains in the root zone of the crop until it is flushed down in the following pre-irrigation period. This additional saltflux increases the total amount of salt stored in the aquifer. However, the initial amount of salt stored in the aquifer is unknown. Taking into account the salt flux imported by irrigation does not reduce this uncertainty. It is therefore assumed that, if the groundwater table is above the extinction depth, the additional amount of salt imported by irrigation is small compared to the absolute quantities stored in the soil and transported to the soil surface. Figure 8.10 presents the sum of phreatic evaporation for the years 1980, 2000 and 2020. The most obvious discrepancy between the total of phreatic evaporation and the saltmap are found in the direct vicinity of the lake. As the salinity map indicates a very high level of salinization along the lake's eastern shore for a strip as wide as 500 m, the model predicts high phreatic evaporation only for the pixels very close to the lake. This discrepancy is related to the unknown initial conditions. The zero-irrigation scenario has shown that phreatic evaporation in the areas around Bostan lake has always occurred, but at very small rates. For the calculation of figure 8.10 only 50 years of phreatic evaporation have been accumulated. The salt accumulation before 1980 has not been taken into account, the total stock of salt is therefore underestimated.

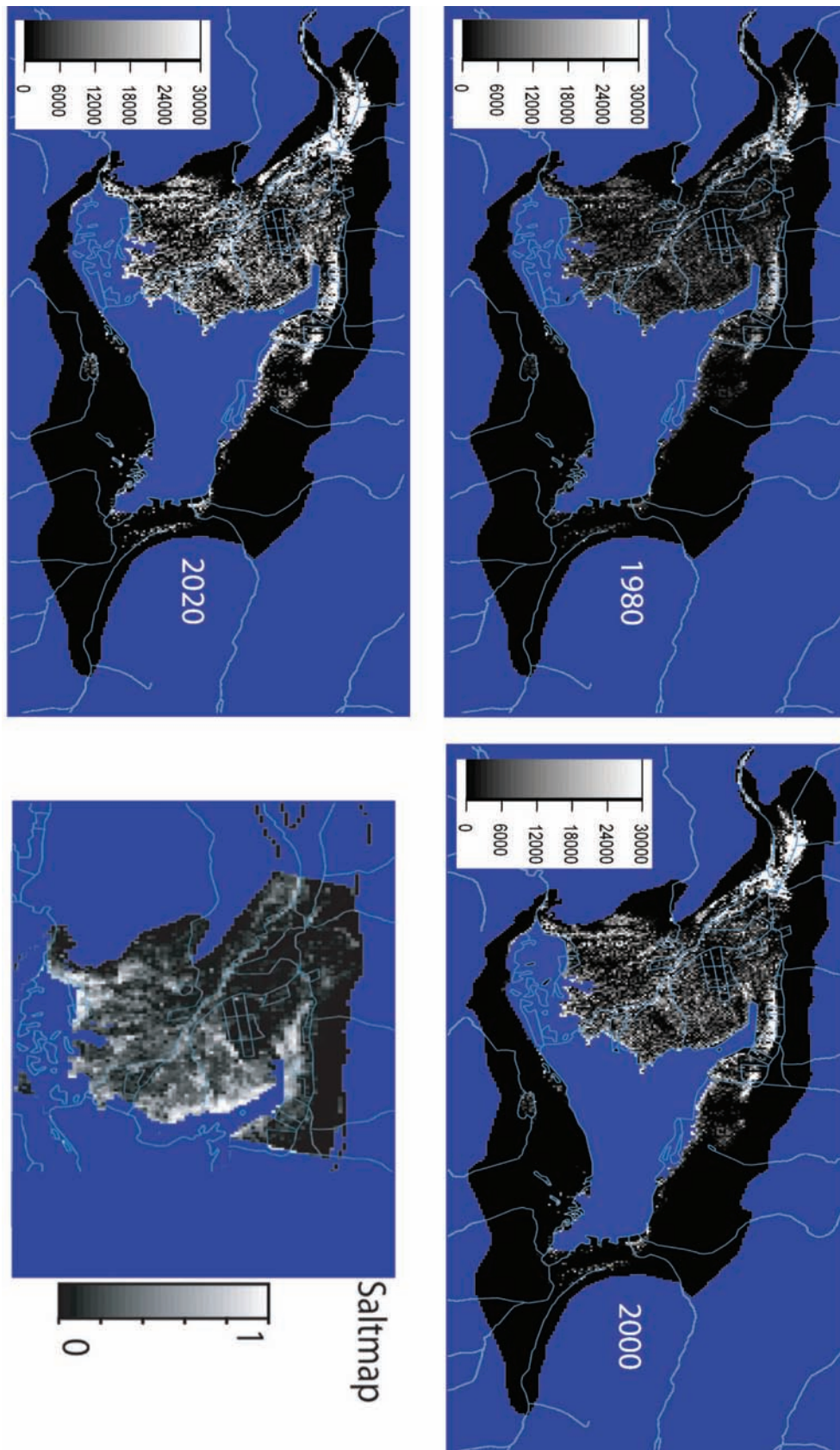


Figure 8.10: Integral of phreatic evaporation in time (years). The saltmap (plotted as spectral similarity) is representing the conditions for the year 2002.

### 8.3.3 Transient simulation of groundwater abstraction

The transient model described in the previous chapter is the basis to simulate the influence of pumping in time. This model is run unchanged until the year 2000, abstraction is started in the year 2001. The diversion of the rivers was adjusted according to the pumping rates. The steady state calculations have shown that the highest abstraction rates in the Q3-4 area can only be around  $1700 \text{ m}^3 \cdot \text{d}^{-1}$ . If more water is pumped, the corresponding model cells fall dry in steady state. Three different pumping scenarios have been tested. Scenario 1 uses the distribution and abstraction rates from the model described in section 8.2.2. In scenario 2, only 250 pumps are installed: the 50 smallest pumps from scenario 1 have been deactivated. The total abstraction rate is set to the same value as in scenario 1 ( $12.6 \text{ m}^3 \cdot \text{s}^{-1}$ ). In scenario 3, the locations of pumps are the same as in scenario 2, but the total abstraction rate is increased to  $15.2 \text{ m}^3 \cdot \text{s}^{-1}$ . Figure 8.11 plots the development of phreatic evaporation in time for all three scenarios. Within only 5 years, phreatic evaporation drops rapidly for all three scenarios. Phreatic evaporation continuously decreases, but no steady state is reached, even after 30 years of pumping. The water flux between the second and first layer for both scenario 1 and scenario 2 are very close to the infiltration rates of the steady state model. The highest infiltration from the first to the second layer is of course observed in scenario 3. In any case, the steady state for these infiltration rates is reached within only 5 years.

## 8.4 Evaluation of the long-term sustainability of groundwater abstraction

As shown with the 1-box model, the steady state salt concentration of a system is given by the ratio of the (non-evaporative) in- and out going water fluxes. Therefore these fluxes have to be quantified in order to evaluate the long term sustainability of groundwater abstraction in the second layer.

The area of interest presented in figure 8.1 also includes areas of the first aquifer layer where the salt concentration is low. However, for the salt balance of the second layer, only the vertical fluxes between the first and second layer in the confined (saline) area are important. The system boundaries to calculate these fluxes are therefore given by the confined, irrigated area. Even though the confined area south of Bostan lake is saline, it has not been taken into account: The horizontal and vertical exchange rates between the layers in this area are close to zero. Table 8.12 presents the water fluxes for the second layer for all three scenarios.

Compared to the steady state model, pumping groundwater from the second aquifer layer increases the water flux from the first to the second aquifer layer by  $5.3 \text{ m}^3 \cdot \text{s}^{-1}$  (84 %), see table 8.12. Figure 8.12 presents the distribution of the exchange between the first and second layer for the confined area (pumping scenario). Even though water is pumped from the second layer, there is a water flux from the second to the first layer in the close vicinity of the lake. Salt transported to this

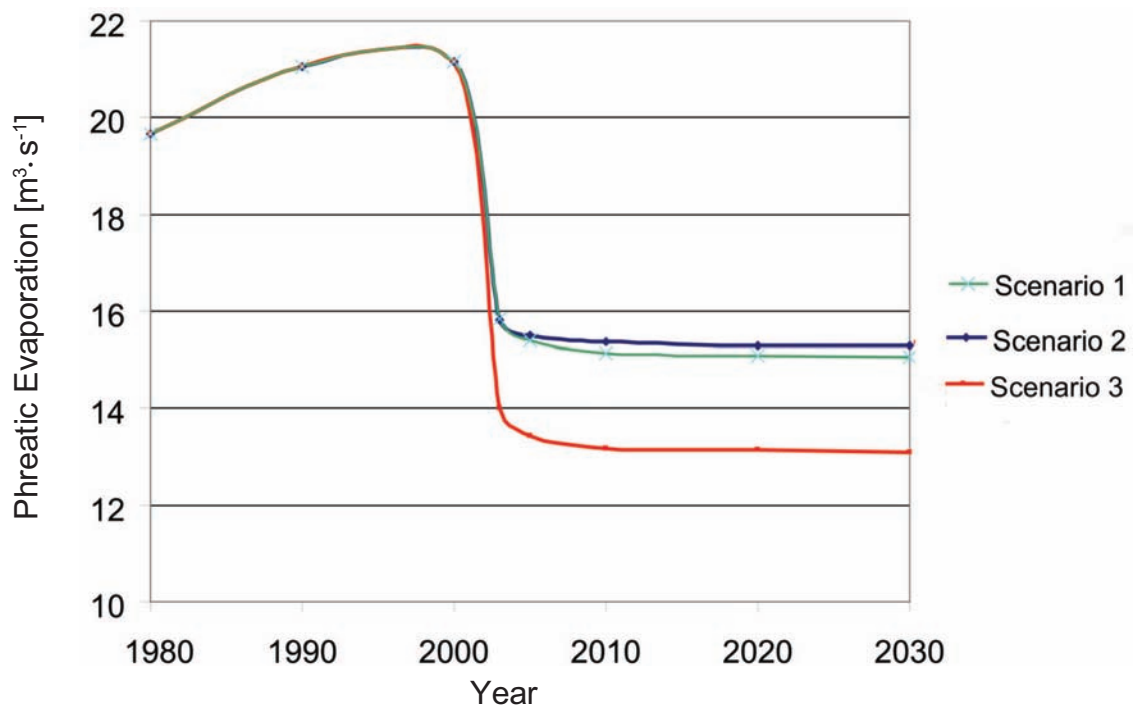


Figure 8.11: Phreatic evaporation flux as a function of time for the three scenarios described. In scenario 1 and 2 the total abstraction rate is  $12.6 \text{ m}^3 \cdot \text{s}^{-1}$ . In scenario 3,  $15.2 \text{ m}^3 \cdot \text{s}^{-1}$  are abstracted.

*Table 8.12: Comparison of the water balance of the second aquifer layer (only confined area, not including the lake) for the calibrated steady state model, the steady state pumping scenario and the steady state zero-irrigation scenario. All units are in  $\text{m}^3 \cdot \text{s}^{-1}$ . The pumping rates are slightly below the pumping rates discussed in the other scenarios, as in this water balance only pumps located in the confined area are considered.*

In Fluxes: Pumping Scenario		Out Fluxes: Pumping Scenario	
Horizontal Exchange	5.1	Horizontal Exchange	0.3
Exchange Upper Layer	11.6	Exchange Upper Layer	7.0
Exchange Lower Layer	1.5	Exchange Lower Layer	1.0
Wells	0.0	Wells	9.9
Total	18.2	Total	18.2

In Fluxes: Steady State		Out Fluxes: Steady State	
Horizontal Exchange	5.1	Horizontal Exchange	0.3
Exchange Upper Layer	6.3	Exchange Upper Layer	10.7
Exchange Lower Layer	1.1	Exchange Lower Layer	0.7
Wells	0.0	Wells	0.8
Total	12.5	Total	12.5

In Fluxes: Zero-Irrigation		Out Fluxes: Zero-Irrigation	
Horizontal Exchange	4.2	Horizontal Exchange	0.2
Exchange Upper Layer	1.1	Exchange Upper Layer	5.6
Exchange Lower Layer	0.6	Exchange Lower Layer	0.1
Wells	0.0	Wells	0.0
Total	5.9	Total	5.9

area is effectively removed from the system because the only major output flux of water in this area is evaporation. The salts accumulating therefore cannot easily be re-mobilized- in contrast to salt removed by the drainage network which will contribute to the salt freight of the downstream systems.

To calculate the steady state salt concentration of the aquifer layers and of the irrigation water, a box model consisting of the confined area of the first and second aquifer layer has been set up. The system boundaries as well as the main salt fluxes are presented in figure 8.13. The following considerations and assumptions have been made: In the salt balance for the first aquifer layer, only a portion ( $\eta$ ) of the salt flux from the second to the first aquifer layer is considered. This assumption is based on the fact that salt deposited along the lake's vicinity is not easily re-mobilized. This area is the final sink of the second aquifer layer. However, upward salt fluxes from the second to the first layer within the irrigated area (for example in the areas



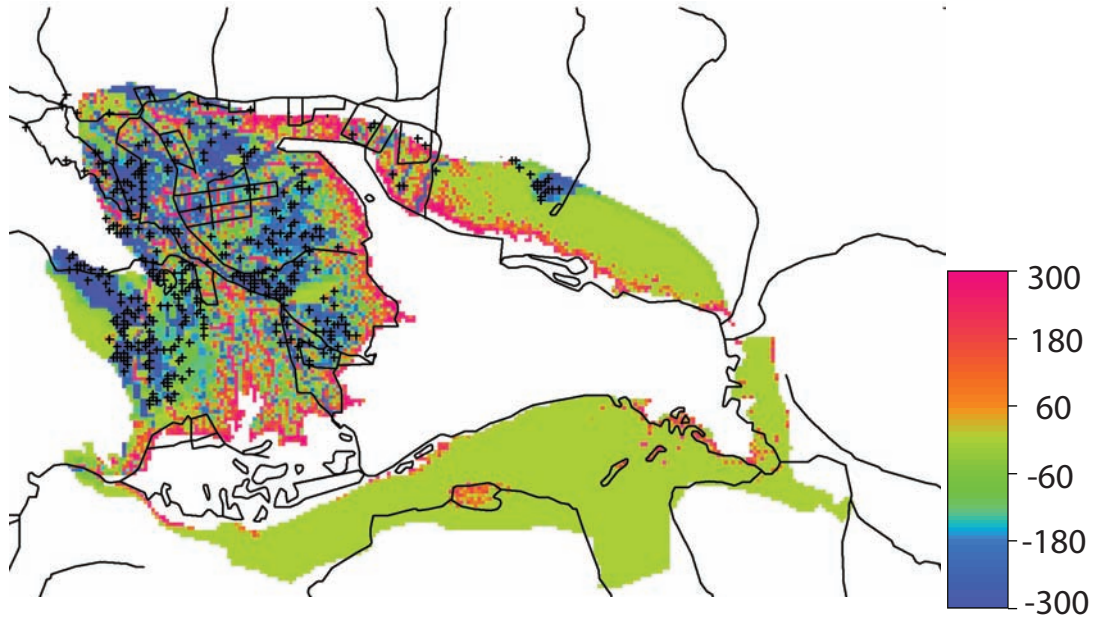


Figure 8.12: Vertical exchange [ $m^3 \cdot d^{-1}$ ] between the second and the first aquifer layer for the confined area in the steady state pumping scenario. Positive numbers indicate a water flux from the second to the first layer. Crosses indicate that a pump is abstracting water. In the areas where no pumps have been installed, the drainage net is still active and an upward flux into the first layer is observed.

where the drainage net remains active) are not necessarily removed from the system and therefore are considered in the salt balance. For the pumping scenario  $\eta$  is 0.48 (for the steady state scenario  $\eta$  is 0.6). It is also assumed that the concentration of the drainage water equals the salt concentration of the first layer. Horizontal fluxes in the first aquifer layer are neglected. The horizontal hydraulic conductivity of the first layer is so small these fluxes amount to less than 1% of the infiltration rate in the pumping scenario. Moreover, the exchange with the third layer is neglected. The net- exchange rate of water between the second and third layer is less than 3% of the incoming water fluxes (in all scenarios). Moreover, the output fluxes from the second layer inside to the second layer outside of the system boundary are very small (less than 2% of the outgoing water fluxes in all scenarios) and are therefore not taken into account. The last assumption is that the salt concentration of water flowing from the unconfined area of the second layer to the confined area of the second layer equals the concentration of the river water. This is to be expected as the only source of water in the unconfined area of the second layer is the Kaidu river. The analysis of water samples of the second layer has shown that this assumption is justified. Based on these assumptions, the salt balance for layer 1 can be expressed by:

$$c_2 \cdot (Q_{GW} + \eta \cdot Q_{21}) - c_1 \cdot (Q_{sd} + Q_{12}) + Q_{inf} \cdot c_{riv} = V_1 \cdot \frac{dc_1}{dt} \quad (8.1)$$



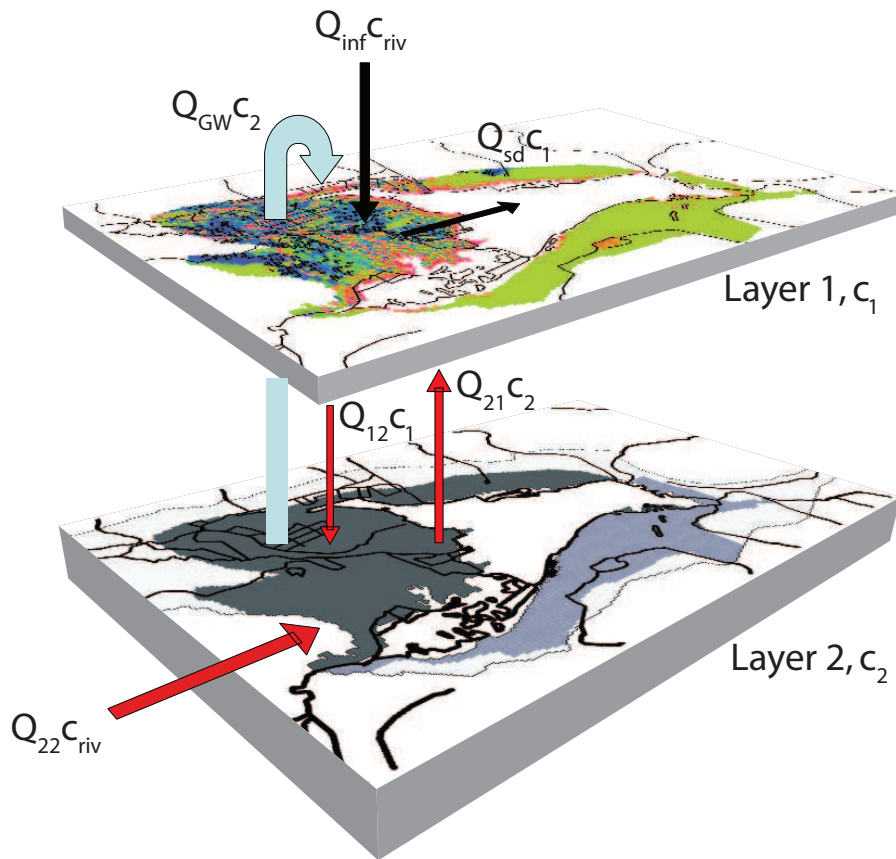


Figure 8.13: Salt fluxes for the confined area between first and second model layer. The system boundary to calculate the salt balance is plotted dark gray (see second layer).

$Q_{GW}$  is the amount of water pumped from the second layer,  $Q_{inf}$  is the sum of water diverted for irrigation and infiltrating directly from the rivers into the system.  $Q_{sd}$  is the amount of water removed by surface drainage.  $c_1$  is the salt concentration in the first layer and  $c_2$  the salt concentration of the second layer, as  $c_{riv}$  is the concentration of the river water.  $Q_{12}$  is defined as the water flux from the first to the second layer,  $Q_{21}$  the water flux of the second to the first layer.  $V_1$  is the aquifer volume (taking the porosity into account). For layer 2, the salt balance is given by:

$$c_1 \cdot Q_{12} + Q_{22} \cdot c_{riv} - c_2 \cdot (Q_{GW} + Q_{21}) = V_2 \cdot \frac{dc_2}{dt} \quad (8.2)$$

$Q_{22}$  is the flux of water from the unconfined area of the second layer to the confined area of the second layer. The concentration of the irrigation water consisting of a mix between ground- and surface water can be calculated by the following equation:

$$c_{mix} = \frac{(Q_{GW} \cdot c_2 + Q_{div} \cdot c_{riv})}{(Q_{GW} + Q_{div})} \quad (8.3)$$

Table 8.13: *Parameters required to solve equations 8.4 and 8.5.*  $Q_{inf}$  is the sum of water diverted in the pumping scenario as well as the infiltration of river water into the aquifer. The volumes of the layers are based on the geometrical setup and the porosities of the model. The pumping rates are slightly below the pumping rates discussed in the steady state model as some of the pumps are located outside this system boundary.

$Q_{inf}$	$[\text{m}^3 \cdot \text{s}^{-1}]$	20	$Q_{GW}$	$[\text{m}^3 \cdot \text{s}^{-1}]$	9.9
$Q_{21}$	$[\text{m}^3 \cdot \text{s}^{-1}]$	7.0	$Q_{12}$	$[\text{m}^3 \cdot \text{s}^{-1}]$	11.6
$Q_{SD}$	$[\text{m}^3 \cdot \text{s}^{-1}]$	8	$Q_{22}$	$[\text{m}^3 \cdot \text{s}^{-1}]$	5.1
$V_1$	$[\text{m}^3]$	$5.84 \cdot 10^9$	$V_2$	$[\text{m}^3]$	$1.74 \cdot 10^{10}$
$c_{1,0}$	$[\text{g} \cdot \text{l}^{-1}]$	10	$c_{2,0}$	$[\text{g} \cdot \text{l}^{-1}]$	1.0
$c_{riv}$	$[\text{g} \cdot \text{l}^{-1}]$	0.4	$\eta$	$[-]$	0.48

with  $Q_{div}$  being the amount of river water applied to irrigation. The steady state concentration in the first layer is given by:

$$c_1 = -\frac{c_{riv}(Q_{22} \cdot Q_{GW} + Q_{GW} \cdot Q_{div} + Q_{21} \cdot Q_{div} + Q_{22} \cdot \eta \cdot Q_{21})}{(Q_{12} \cdot \eta \cdot Q_{21} - Q_{sd} \cdot Q_{GW} - Q_{sd} \cdot Q_{21} - Q_{12} \cdot Q_{21})} \quad (8.4)$$

and  $c_2$  by :

$$c_2 = -\frac{c_{riv}(Q_{12} \cdot Q_{22} + Q_{sd} \cdot Q_{22} + Q_{12} \cdot Q_{div})}{(Q_{12} \cdot \eta \cdot Q_{21} - Q_{sd} \cdot Q_{GW} - Q_{sd} \cdot Q_{21} - Q_{12} \cdot Q_{21})} \quad (8.5)$$

The water fluxes required to evaluate  $c_1$  and  $c_2$  have been determined with the model (steady state pumping scenario). All parameters are presented in table 8.13. The initial concentration of the first layer is set to  $10 \text{ g} \cdot \text{l}^{-1}$ . This is of the same magnitude as the salt concentration in the drainage water.  $\eta$  equals the portion of the  $Q_{21}$  flux evaporated in the close vicinity of the lake (see figure 8.13). The water fluxes of the pumping scenario between these two compartments were used to calculate the changes of the salt concentration within the two layers as well as the resulting steady state salt concentrations.

The development of the concentrations of salt within the confined area of the first and second aquifer layer and the concentration of the irrigation water is presented in figure 8.14. The resulting steady- state concentration for the irrigation water is  $0.57 \text{ g} \cdot \text{l}^{-1}$ , for the first layer  $0.91 \text{ g} \cdot \text{l}^{-1}$  and for the second one  $0.76 \text{ g} \cdot \text{l}^{-1}$  respectively. The concentration of the irrigation water ( $c_{mix}$ ) increases to a maximum of  $0.81 \text{ g} \cdot \text{l}^{-1}$ . This maximum is reached after 20 years. Even though the maximum concentration is a factor of 2 higher than the concentration of the river water, the quality is still sufficient to irrigate crops. In the long run concentrations decrease. This is due to the fact that the amount of salt stored in the first layer is gradually removed from the system, either to the downstream or to the salt crust along the lake.

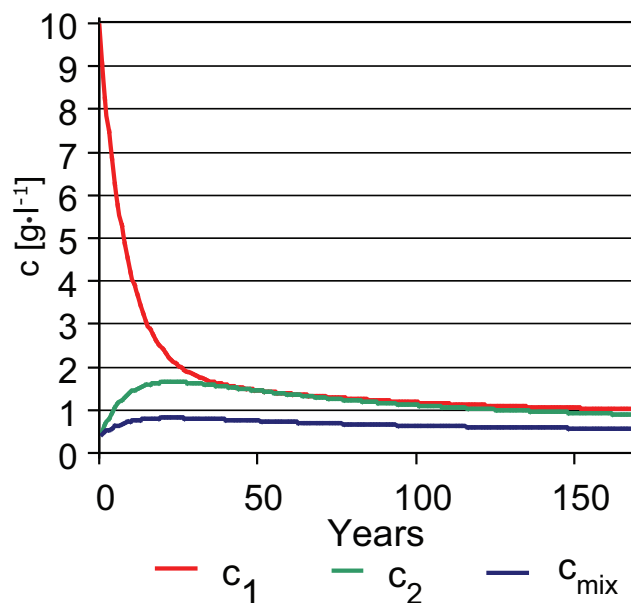


Figure 8.14: Development in time of the salt concentration of the irrigation water and of the first and second aquifer layer.

Besides the evaporation and storage of salt along the lake, the drainage net is very important for the salt balance of the system. The amount of salt removed through the drainage system is of the same magnitude as the salt stored around the lake. Deactivating the drainage net would therefore lead to a significant increase of the steady state salt concentration.

## 8.5 Conclusions

### 8.5.1 Model development and verification

Satellite images proved to be the most important source of distributed data. However, the key to the use of such data is still ground truth. Several conclusions without using the groundwater model could be made directly by using remote sensing data. The separation of evapotranspiration into transpiration and phreatic evaporation allowed to identify areas with different irrigation efficiencies. The soil salinity map confirmed the short term positive effect of over-irrigation: The irrigated fields can clearly be identified by a reduced surface salinity. The comparison of the saltmap and the phreatic evaporation map indicates where salinity will become a problem if the present water management policies are continued. Moreover, the comparison between phreatic evaporation and the salinity map confirmed that soil salinity is mainly driven by phreatic evaporation.

Even though a DEM of high quality was produced, elevation data are not of

sufficient accuracy. The combination of a model using a finer cell resolution and a more accurate digital elevation model would allow to calculate the depth to groundwater on a finer, more reliable basis. However, the accuracy of the input data was sufficient to construct a plausible and consistent model.

In order to simulate rivers, drainage channels and the lake, additional calibration parameters have been introduced. The hydraulic conductance of the river- and lake bed are unknown parameters. The verification data for the rivers consisted of the infiltration rates from the rivers as well as the pattern of phreatic evaporation. The observed quantities could be reproduced satisfactorily by defining two types of rivers and two types of drains. Even though the lake level has been documented for a long period of time, the calculated lake stage cannot be considered as a verification of the calibrated model. The evaporation rate of the lake is not known to the required accuracy. In fact, the lake is over-parameterized, as two parameters are calibrated (evaporation as well as the conductance of the lakebed), but only the lake level can be used as verification. It has been assumed that the exchange rates between the lake and the groundwater are small. Considering the thick layer of fine sediment covering the bottom of the lake, this assumption is plausible. However, this statement has never been verified.

The map of phreatic evaporation was the most important data set used for verification. The use of the soil salinity map for the verification is difficult because of the unknown initial conditions for the groundwater table as well as the distribution of salt in the basin before irrigation took place. Moreover, the distribution of irrigated areas in the course of time as well as the irrigation rates must be known and included in the model. It is unlikely that such data can be found. However, high phreatic evaporation rates in areas where the soil salinity map indicates a low degree of salinization indicate problem areas.

### 8.5.2 Model results

Three different types of steady state models have been set up: a steady state model representing the average conditions for the period of 1990-1999, a zero irrigation scenario analyzing the water fluxes if no irrigation takes place, as well as a model simulating the effect of groundwater use in irrigation. Table 8.14 summarizes all key parameters of the three different model types.

The zero-irrigation scenario clarified where phreatic evaporation is caused by irrigation and where it occurs naturally. High groundwater tables are found in many areas even without irrigation. Two large areas of natural, phreatic evaporation can be identified: The swamp in the north eastern ranges of the Yanqi basin as well as the band of salt along the lake. The examination of the exchange rates between the first and second aquifer layer along the lake showed that only a small portion of water evaporating in this area is from the lake while the major portion comes from the second aquifer layer. This mechanism demonstrates how nature evaporates water in the upstream without increasing the salt concentration in the downstream:

by transporting the salt accumulated by evaporation to a zone where it is deposited in the long term. Even though phreatic evaporation along the lake shore is not very high, it constantly removes salt from the system.

The steady state simulations revealed that around 50% of phreatic evaporation is related to irrigation. In the pumping scenario, an additional amount of  $9.6 \text{ m}^3 \cdot \text{s}^{-1}$  was pumped (compared to the steady state model). As a consequence, phreatic evaporation was reduced by  $7.2 \text{ m}^3 \cdot \text{s}^{-1}$ . In other words, every  $\text{m}^3$  of river water substituted by groundwater increases the available downstream resources by at least  $0.75 \text{ m}^3$  and reduces the salinized area by  $50 \text{ km}^2$ . The reduction of phreatic evaporation is exactly the amount of water that is additionally available for the downstream systems. The transient simulations showed the dynamics of the water balance of the entire system, especially how phreatic evaporation is reduced in time. These simulations have shown that the reduction of phreatic evaporation is reached within only a few years. Besides the changes on the overall water balance, the simulations could show that the flow of water from the second to the first layer along the lake is still maintained, even if groundwater is pumped from the second layer. As demonstrated in the previous chapter, this flux is an important sink of salt.

Table 8.14: *Final comparison between the zero-irrigation, the calibrated steady state model and the steady state pumping scenario.*

		Zero- irrigation	SS- model	Pumping Scenario
- Total salinized pixels	#	3386	6881	4931
- Irrigation induced, salinized pixels	#	-	3495	1545
- Phreatic evaporation	$\text{m}^3 \cdot \text{s}^{-1}$	10.3	22.5	15.3
- Irrigation induced, phreatic evaporation	$\text{m}^3 \cdot \text{s}^{-1}$	-	12.2	5
- Water diverted for irrigation	$\text{m}^3 \cdot \text{s}^{-1}$	-	36.2	26.6
- Groundwater Pumped	$\text{m}^3 \cdot \text{s}^{-1}$	-	3	12.6
- Water removed through drainage (including drainage into the rivers)	$\text{m}^3 \cdot \text{s}^{-1}$	6.2	12	10.5
- Water flowing into the aquifer	$\text{m}^3 \cdot \text{s}^{-1}$	14.4	14.1	15.10
- River water flowing into the lake	$\text{m}^3 \cdot \text{s}^{-1}$	123.7	90.1	98.5
- Water from the drainage channels flowing into the lake	$\text{m}^3 \cdot \text{s}^{-1}$	-	4.2	3
- Kongque He discharge	$\text{m}^3 \cdot \text{s}^{-1}$	69.1	38.9	46.1
- Kongque He salt concentration	$\text{g} \cdot \text{l}^{-1}$	0.8	1.4	1.2



## Chapter 9

---

### Conclusions, recommendations and open questions

The question throughout this thesis is whether sustainable agriculture in the Yanqi basin is possible. Owing to the abundant amount of fresh water resources, agricultural production in the Yanqi basin can be kept at a high level in the long run even if no changes in the water management are made. This is however only possible at a cost paid by the downstream i.e. the reduction of flow and an increased degree of mineralization. The Yanqi basin can be managed in a more effective way without reducing the present intensity of agriculture. The partial substitution of irrigation water drawn from the rivers by pumped groundwater helps to reduce the phreatic evaporation and prevents further (or even reverses) soil salinization. It augments the downstream fluxes up to around 20 % and keeps their mineralization low. However, this comes with the cost of installing and maintaining pumping infrastructure.

#### 9.1 Conclusions and recommendations

The overall conclusion of this project is that the productivity of agriculture can be maintained in the Yanqi basin and that the available resources for the downstream systems can be increased by substituting a part of the irrigation water drawn from the river by pumped groundwater. Besides the creation of the new infrastructure for groundwater abstraction, the old infrastructure of the drainage network must be maintained. Owing to the output fluxes through the drainage network, the steady state salt concentration of the system remains below a critical level. The drainage network accounts for up to 50 % of the output salt fluxes and therefore significantly reduces the steady state salt concentration of the first and second aquifer layers as well as the quality of the irrigation water. The drainage net as well as the deposition of salt along the lake shore are both important for the long term sustainability of the system. However, only the deposition of salt along the lake's shore effectively reduces the salt freight to the downstream system. Nevertheless, it is recommended to install pumps where no drainage network is present.

The highest reduction of phreatic evaporation in the first layer can be achieved by pumping groundwater in areas where the vertical hydraulic conductivity between the first and second layer is high. In the model, a uniform vertical conductivity has been assumed. Additional pumping tests to sort out ideal locations are therefore recommended.

Besides pumping groundwater, an increase of the irrigation channel efficiency is highly recommended. Even though only  $13 \text{ m}^3 \cdot \text{s}^{-1}$  of water are consumed by plants, the available water resources for the downstream systems are reduced by  $23 \text{ m}^3 \cdot \text{s}^{-1}$ . This loss contributes to phreatic evaporation. Installing pumps close to the fields where the water is applied for irrigation will reduce the channel losses and again will

contribute to the downstream resources.

Considering the large amount of salt stored in the soil column as well as the high groundwater tables in some areas of the basin, it becomes clear that sustainable irrigation in the Yanqi basin is indeed a difficult undertaking. It is therefore recommended to not increase the irrigated area. This recommendation can be relaxed only if the total amount of water applied for irrigation is kept at the present level by increasing the efficiency of the irrigation system. If new fields are claimed for irrigation, they should not be located in areas where the groundwater table is already high.

The crop mix should be adjusted to the saline environment of the Yanqi basin. Compared to crops such as grapes or wheat, salt tolerant plants require only a fraction of excess irrigation water. As a consequence, infiltration is reduced and the salinization process is slowed down. The cultivation of salt tolerant crops is highly recommended, especially in areas where the groundwater table is high.

### 9.2 Open questions and recommended further studies

The financial costs and benefits of a potential implementation have not been considered in this study. The costs for both installation and maintenance of the wells have to be evaluated. The low hydraulic conductivities in the Yanqi basin will cause relatively high installation costs. The management of the groundwater resources will have to be judged according to cost efficiency (minimal costs) and operational effectiveness (maximal reduction of phreatic evaporation). The optimal groundwater pumping policies can be determined by using state of the art multi-objective optimization (Siegfried, 2004).

Using the saltmap for verification purpose was difficult, as the initial conditions are unknown. If saltmaps of former years could be calculated, the increase of salt concentration would be known. This quantity could be compared with the changes calculated by the model. However, the saltmaps have been calculated on the basis of ASTER images. Unfortunately, this sensor has only been in use for a few years. One way to tackle this problem would be using Landsat images- for which long time series are available. However, the spectral resolution of the Landsat images is far below ASTER. If a cross correlation between the ASTER- and the Landsat channels can be found, saltmaps could be calculated by using Landsat images.

The calibration of the model was carried out manually. However, this process is very time consuming. In order to carry out the comparison between calculated and observed patterns automatically, algorithms calculating the spatial match between calculated and observed patterns have to be developed. Based on the spatial match of these patterns, calibration parameters such as the vertical hydraulic conductivities have to be adjusted in order to minimize the residuals.

In the current form, the model is not easy to operate. Changes to the model have to be carried out by modifying the input files for Modflow in a text editor. Moreover, even though post processing has been automated, two software packages

as well as several macros have to be operated. A user friendly pre- and postprocessor on the basis of a GIS database is being developed by Dr. Fang Chunsheng.



# Bibliography

---

- ALLEN, R., PEREIRA, L., RAES, D. & SMITH, M. 1998 *Crop evapotranspiration-Guidelines for computing crop water requirements*. Rome: Food and Agriculture Organization of the United Nations.
- ATLANTIS SCIENTIFIC 2001 *Ev-InSar Version 2.0 User's guide*. Nepean, Ontario, Canada.
- BANTA, E. 2000 *Modflow-2000, the U.S. Geological Survey modular ground-water model- Documentation of packages for simulating evapotranspiration with a segmented function (ETS1) and drains with return flow (DRT1)*. Denver, Colorado: U.S. Geological Survey Open-File Report 00-466.
- BARNES, C. J. & ALLISON, G. B. 1988 Tracing of water-movement in the unsaturated zone using stable isotopes of hydrogen and oxygen. *Journal of Hydrology* **100** (1-3), 143–176.
- BASTIAANSEN, W., MENENTI, M., FEDDES, R. & HOLTSLAG, A. 1998 A remote sensing surface energy balance algorithm for land (SEBAL) - 1. formulation. *Journal of Hydrology* **213** (1-4), 198–212.
- BEN-DOR, E., PATKIN, K., BANIN, A. & KARNIELI, A. 2002 Mapping of several soil properties using DAIS-7915 hyperspectral scanner data - a case study over clayey soils in Israel. *International Journal of Remote Sensing* **23** (6), 1043–1062.
- BROWN, L. 1995 *Who will feed China? Wake-up call for a small planet*. New York; London: Norton.
- DE CARVALHO, O. & MENESES, P. R. 2000 Spectral Correlation Mapper- an Improvement on the Spectral Angle Mapper (SAM). In *Paper read at the 9th Airborne Earth Science Workshop*. Pasadena, California 91109: Jet Propulsion Laboratory.
- CHEN, H. 1994 *Explanation of Quarternary Geological Map (1:500000) of Xinjiang Uygur Autonomous Region, China*. Beijing: Geological Publishing House.
- CHIANG, W.-H. & KINZELBACH, W. 2001 *3D-groundwater modeling with PMWIN: A simulation system for modeling groundwater flow and pollution*. Berlin: Springer.
- COUDRAIN-RIBSTEIN, A., PRACT, B., TALBI, A. & JUSSERAND, C. 1998 Is evaporation from phreatic aquifers in arid zones independent of the soil characteristics? In *Comptes rendus de l'Academie de Sciences*, pp. 326:159–165. Paris, France.

- CRAIG, H. & GORDON, L. 1965 Deuterium and oxygen-18 variations in the ocean and marine atmosphere. In *Stable Isotopes in Oceanographic Studies and Paleotemperatures* (ed. E. Tongiorgi), pp. 9–130. Pisa.
- CSILLAG, F., PASZTOR, L. & BIEHL, L. L. 1993 Spectral Band Selection for the Characterization of Salinity Status of Soils. *Remote Sensing of Environment* **43** (3), 231–242.
- CURLANDER, J. C. & MCDONOUGH, R. N. 1991 *Synthetic aperture radar systems and signal processing*. New York: Wiley.
- DONG, X., JIANG, T. & JIANG, H. 2001 Study on the pattern of water resources utilisation and environmental conservation of Yanqi basin. In *Development, Planning and Management of Surface and Groundwater Resources* (ed. G. Li), *IAHR congress proceedings*, vol. A, pp. 333–340. Beijing, China: Tsinghua University Press.
- DWIVEDI, R. S. & RAO, B. R. M. 1992 The Selection of the Best Possible Landsat TM Band Combination for Delineating Salt-Affected Soils. *International Journal of Remote Sensing* **13** (11), 2051–2058.
- EL BASSAM, N. 1998 Sustainable development in agriculture - Global key issues. *Landbauforschung Volkenrode* **48** (1), 1–11.
- EVANS, R. & NOLAN, J. 1989 A groundwater management strategy for salinity mitigation in Victorian river plain. In *Proceedings of the Benidorm Symposium, IAHS publication 188*, pp. 487–49. Valencia.
- FAO 2004 Irrigation Land Data Base- FAO Statistics, [http://www.fao.org/waicent/portal/statistics\\_en.asp](http://www.fao.org/waicent/portal/statistics_en.asp).
- FRICK, M. 2002 Auswertung von GPS-Messungen in der Chinesischen Provinz Xinjiang. Master thesis, ETH Zurich.
- GEONICS LIMITED 2001 *EM38- Ground Conductivity Meter Operating Manual*. Geonics Limited, Mississauga, Ontario, Canada.
- HALVORSON, A. D. & RHOADES, J. D. 1976 Field mapping of soil conductivity to delineate dryland saline seeps with 4-electrode technique. *Soil Science Society of America Journal* **40** (4), 571–575.
- HELLWEGER, F. & MAIDMENT, D. 1997 AGREE - DEM surface reconditioning system, <http://www.ce.utexas.edu/prof/maidment/gishyd97/terrain/agree/agree.htm>.

- HENDRICKX, J. M. H., BORCHERS, B., CORWIN, D. L., LESCH, S. M., HILGENDORF, A. C. & SCHLUE, J. 2002 Inversion of soil conductivity profiles from electromagnetic induction measurements: Theory and experimental verification. *Soil Science Society of America Journal* **66** (3), 673–685.
- HILLEL, D. 1987 *The efficient use of water in irrigation: Principles and practices for improving irrigation in arid and semi-arid regions*. Washington D.C.: World Bank.
- HILLEL, D. 1990 *Out of the Earth: Civilization and the Life of the Soil*. New York: Free Press.
- HILLEL, D. 2000 *Salinity management for sustainable irrigation: Integrating Science, Environment and Economics*. Washington D.C.: World Bank.
- HILLEL, D. & WARRICK, A. W. 1998 *Environmental Soil Physics*. San Diego, CA: Academic Press.
- HOWARI, F. M. 2003a A comparison of spectral matching algorithms for identifying natural salt crusts. *Journal of Applied Spectroscopy* **70** (5), 782–787.
- HOWARI, F. M. 2003b The use of remote sensing data to extract information from agricultural land with emphasis on soil salinity. *Australian Journal of Soil Research* **41** (7), 1243–1253.
- HOWARI, F. M., GOODELL, P. C. & MIYAMOTO, S. 2002 Spectral properties of salt crusts formed on saline soils. *Journal of Environmental Quality* **31** (5), 1453–1461.
- HU, S., KANG, S., SONG, Y. & CENG, X. 2003 Calculating phreatic water evaporation from bare soil for the Tarim River Basin, Xinjiang. In *International Conference on Water-Saving Agriculture and Sustainable Use of Water and Land Resources in Arid and Semiarid Areas* (ed. Kang, S. and Davis, B. and Shan, L. and Cai, H.), pp. 727–733. Yanglin, China: Shaanxi Science and Technology Press.
- JAKEMAN, A. J., NIX, H. A. & GHASSEMI, F. 1995 *Salinisation of Land and Water Resources: Human Causes, Extent and Management*. Wallingford Oxon: CAB International.
- KALRA, N. K. & JOSHI, D. C. 1996 Potentiality of Landsat, SPOT and IRS satellite imagery for recognition of salt affected soils in Indian arid zone. *International Journal of Remote Sensing* **17** (15), 3001–3014.
- LIN, A., FU, B., KANO, K., MARUYAMA, T. & GUO, J. 2002 Late quaternary right-lateral displacement along active faults in the Yanqi basin, southeastern Tian Shan, northwest China. *Tectonophysics* **354** (3-4), 157–178.



- LOWRIE, W. 1997 *Fundamentals of Geophysics*. Cambridge: Cambridge University Press.
- MAAS, E. 1990 Crop salt tolerance. In *Agricultural salinity assessment and management* (ed. K. Tanji), pp. 262–304. New York: American Society of Civil Engineers.
- MCDONALD, M. & HARBAUGH, A. 1988 *A modular, three-dimensional finite-difference ground-water flow model*. Tallahassee, Florida.
- MCKENZIE, R., GEORGE, R., WOODS, S., CANNON, M. & BENNETT, D. 1997 Use of the electromagnetic-induction meter (EM38) as a tool in managing salinisation. *Hydrogeology Journal* **5** (1), 37–50.
- MCNEIL, J. 1980 *Electromagnetic terrain conductivity measurement at low induction numbers, Geonics Technical Note TN6*. Mississauga, Ontario, Canada.
- MCNEILL, J. 1992 Rapid, accurate mapping of soil salinity by electromagnetic ground conductivity meters. In *Advances in measurement of soil physical properties: Bringing theory into practice* (ed. G. C. Topp, R. J. Luxmoore, S. H. Mickelson & N. H. Rhodehamel). Soil Science Society of America.
- MERRIT, M. L. & KONIKOW, L. 2000 *Documentation of a computer program to simulate lake-aquifer interaction using the Modflow groundwater flow model and MOC3D solute transport model*. Tallahassee, Florida: USGS.
- METTERNICHT, G. & ZINCK, J. A. 1997 Spatial discrimination of salt- and sodium-affected soil surfaces. *International Journal of Remote Sensing* **18** (12), 2571–2586.
- METTERNICHT, G. I. & ZINCK, J. A. 2003 Remote sensing of soil salinity: Potentials and constraints. *Remote Sensing of Environment* **85** (1), 1–20.
- MILLS, R. 1973 Self-diffusion in normal and heavy-water in range 1-45 degrees. *Journal of Physical Chemistry* **77** (5), 685–688.
- MULDERS, M. A. 1987 *Remote Sensing in Soil Science*. Amsterdam: Elsevier.
- OLDEMAN, L. R., HAKKELING, R. T. A. & SOMBROEK, W. G. 1991 *World map of the status of human-induced soil degradation- an explanatory note*, second revised edn. Wageningen: International Soil Reference and Information Centre.
- PRUDIC, D., KONIKOW, L. & BANTA, E. 2004 *A new stream- flow routing (SFR1) package to simulate stream-aquifer interaction with MODFLOW-2000*. Carson City, Nevada: U.S. Geological Survey Open-File Report 2004-1042.
- RAO, B. R. M., SANKAR, T. R., DWIVEDI, R. S., THAMMAPPA, S. S., VENKATARATNAM, L., SHARMA, R. C. & DAS, S. N. 1995 Spectral Behavior of Salt-Affected Soils. *International Journal of Remote Sensing* **16** (12), 2125–2136.

- 
- REVESZ, K. & WOODS, P. H. 1990 A method to extract soil-water for stable isotope analysis. *Journal of Hydrology* **115** (1-4), 397–406.
- RHOADES, J. 1996 Salinity: Electrical conductivity and total dissolved solids. In *Methods of Soil Analysis: Part 3 - Chemical Methods* (ed. D. Sparks), pp. 417–435. Madison, Wisconsin: Soil Science Society of America.
- RHOADES, J. D., KANDIAH, A. & MASHALI, A. M. 1992 *The use of saline waters for crop production*. Rome: Food and Agriculture Organization of the United Nations.
- RHOADES, J. D., LESCH, S. M. & CHANDUVI, F. 1999 *Soil salinity assessment: Methods and Interpretation*. Rome: Food and Agriculture Organization of the United Nations.
- RHOADES, R. & MIYAMOTO, S. 1990 Testing soils for salinity and sodicity. In *Soil testing and plant analysis*, 3rd edn. (ed. R. L. Westerman), pp. 299–336. Madison, Wisconsin: Soil Science Society of America.
- RICHARDS, L. 1954 *Diagnosis and Improvement of Saline and Alkali Soils*. Washington DC: US-SalinityLab.
- ROERINK, G. J., SU, Z. & MENENTI, M. 2000 S-SEBI: A simple remote sensing algorithm to estimate the surface energy balance. *Physics and Chemistry of the Earth Part B- Hydrology Oceans and Atmosphere* **25** (2), 147–157.
- SCHARROO, R. & VISSER, P. 1998 Precise orbit determination and gravity field improvement for the ERS satellites. *Journal of Geophysical Research-Oceans* **103** (C4), 8113–8127.
- SCHULLA, J. 1997 *Hydrologische Modellierung von Flussgebieten zur Abschätzung der Folgen von Klimaänderungen*. PHD-Thesis ETH Zurich- XXVI, 161 S, ISBN 3-906148-17-3.
- SIEGFRIED, T. 2004 Optimal utilization of a non-renewable transboundary groundwater resource - methodology, case study and policy implications. PhD Thesis ETH Zurich No.15635, <http://e-collection.ethbib.ethz.ch/show?type=diss&nr=15635>.
- SIMUNEK, J., SEJNA, M. & VAN GENUCHTEN, M. 2000 Hydrus2d, <http://www.ussl.ars.usda.gov/models/hydrus2d.htm>.
- SINGH, R. P., KUMAR, V. & SRIVASTAV, S. K. 1990 Use of Microwave Remote-Sensing in Salinity Estimation. *International Journal of Remote Sensing* **11** (2), 321–330.

- TAYLOR, G. & DEHAAN, R. 2000 Salinity mapping with hyperspectral imagery <http://www.bees.unsw.edu.au/research/remotesensing/salinity1.html>.
- TAYLOR, G. R., MAH, A. H., KRUSE, F. A., KIERYOUNG, K. S., HEWSON, R. D. & BENNETT, B. A. 1996 Characterization of saline soils using airborne radar imagery. *Remote Sensing of Environment* **57** (3), 127–142.
- TELFORD, W. M., GELDART, L. P. & SHERIFF, R. E. 1990 *Applied Geophysics*, 2nd edn. Cambridge University Press.
- THOME, K. 1999 *Algorithm Theoretical Basis Document for ASTER Level2B1 Surface Radiance and ASTER Level2B5 Reflectance*. Tucson, Arizona: University of Arizona.
- TUMARBAY, H., MA, D., GUO, L. & MA, Y. 2003 Testing Penman-Monteith for spring wheat in Xinjiang. In *Shaanxi Science and Technology Press* (ed. S. Kang, B. Davis, L. Shan & H. Cai), pp. 437–442. Yanglin: Shaanxi Science and Technology Press.
- UN 2003 *World Population Prospects: The 2002 Revision*. New York: United Nations, Department of Economic and Social Affairs.
- WANG, Z. 1990 *Principles of Photogrammetry*. Beijing, China: Press of Wuhan Techn. Univ. of Surveying and Mapping.
- WIEGAND, C. L., RHOADES, J. D., ESCOBAR, D. E. & EVERITT, J. H. 1994 Photographic and Videographic Observations for Determining and Mapping the Response of Cotton to Soil-Salinity. *Remote Sensing of Environment* **49** (3), 212–223.
- WORLD COMMISSION ON ENVIRONMENT AND DEVELOPMENT 1987 *Our Common Future*. Oxford: Oxford University Press.
- YUHAS, R., GOETZ, A. & BOARDMAN, J. 1992 Discriminating among semi-arid landscape endmembers using spectral angle mapper (SAM) algorithm. In *Third annual JPL Airborne Geoscience Workshop*, pp. 147–149. Pasadena, California 91109: Jet Propulsion Laboratory.
- ZEBKER, H. A. & GOLDSTEIN, R. M. 1986 Topographic mapping from interferometric synthetic aperture radar observations. *Journal of Geophysical Research-Solid Earth and Planets* **91** (B5), 4993–4999.
- ZIMMERMANN, U., EHALT, D. & MÜNNICH, K. 1967 Soil water movement and evapotranspiration: changes in the isotope composition of water. In *Isotopes in Hydrology*, pp. 567–84. Vienna: Int. At. Energy Agency.

## Curriculum vitae

<b>Name</b>	Philip Andreas Brunner
<b>Date of Birth</b>	24.07.1975
<b>Place of Birth</b>	Schaffhausen
<b>Nationality</b>	Swiss

### Education

- 2002 until present: PhD project on "Modelling the water and salt balance in the semi-arid Yanqi Basin, China", at the Institute of Hydromechanics and Water Resources Management, ETH Zurich
- 2001: Master Degree as an environmental engineer
- 2000: Diploma thesis "Modelling the Kavimba Wellfield"
- 1995-1999: Undergraduate studies at the ETH as an environmental engineer
- 1990-1995: Preparation to university entrance qualification emphasizing natural sciences (Swiss Matura examination), Kantonsschule Schaffhausen
- 1980 -1990: Primary and secondary level education in Schaffhausen

### Awards

- 2004: Young scientist outstanding poster presentation award, EGU
- 2002: "Willy Studer"- Award for best graduation at the department in 2002
- 2002: ETH medal for outstanding diploma thesis
- 2002 "Price Waterhouse Cooper Sustainability Award" for outstanding student work

### Work Experience

- 2002-2004: Three fieldwork campaigns in the Yanqi basin in co-operation with several Chinese institutes; Intensive language courses in Chinese
- 2002-2004: Supervision of four master thesis projects at the Institute of Hydromechanics and Water Resources Management
- 2000: Extensive fieldwork in Kavimba, Botswana

- 1998-1999: Trainee at the soil recycling company "Eberhard Recycling AG" in Rümlang, Switzerland; Participation in a whale research programme in Eastern Canada

### Publications

#### Reviewed Journal Papers

- Brunner, P., Bauer, P., Eugster, M., Kinzelbach, W. 2004 *Using remote sensing to regionalize local precipitation recharge rates obtained from the Chloride Method*, Journal of Hydrology, Vol. 294, No.4 (241-250).
- Brunner, P., Khan, S., Kinzelbach, W. *Comparing different arid basins with secondary salinization: towards a unified definition of sustainability*, Journal of Experimental Botany, Volume 54,(58-59), 2004.
- Bauer, P., Brunner, P., Alberich, C.M., Kinzelbach, W. 2004 *The use of remote sensing data in water resources management: some examples from Africa and China*, Géo-Observateur No.13, (13,24).
- Kinzelbach, W., Bauer, P., Siegfried, T., Brunner, P. 2003 *Sustainable Groundwater Management Problems and Scientific Tools*, Episodes, Vol. 26, No. 4.

#### Congress Papers and Talks

- Röser, I., Brunner, P., Kinzelbach, W. 2005 *Sustainable Agriculture in the Lower Murrumbidgee Catchment*, Australia, General Assembly of the European Geosciences Union 2005. European Geosciences Union, Vienna, Austria.
- Bauer, P., Brunner, P., Kinzelbach, W. 2002 *Quantifying the next exchange of water between land and atmosphere in the Okavango-Delta, Botswana*. In: K. Kovar (Editor), Model Care 2002. Acta Universitatis Carolinae-Geologica, Prag, pp. 581-584.
- Brunner, P., Kinzelbach, W., Li, H.T., Li, W.P. 2005 *Groundwater modelling in a remote Chinese Basin - How can models be improved in areas where data are scarce?* General Assembly of the European Geosciences Union 2005. European Geosciences Union, Vienna, Austria.
- Brunner, P., Kinzelbach, W. and Li, H.T. 2004 *Generating large scale soil salinity maps with geophysics and remote sensing*, General Assembly of the European Geosciences Union 2004. European Geosciences Union, Nizza, France.
- Brunner, P., Kgotlhang, L., Kinzelbach, W. 2004 *Remote Sensing as a Data Source for Surface- and Groundwater Modelling in Botswana*, Pretoria (South Africa), European Space Agency Tiger meeting 2004.
- Brunner, P., Khan, S., Kinzelbach, W., 2003 *Comparing different arid basins with secondary salination: Towards a unified definition of sustainability*. In: S. Kang, B. Davis, L. Shan and H. Cai (Editors), International Conference on Water- Saving Agriculture and Sustainable Use of Water and Land Resources in Arid and Semiarid Areas. Shaanxi Science and Technology Press, Yanglin, China, pp. 866-877.
- Brunner, P., Eugster, M., Bauer, P., Kinzelbach, W., Makobo, P., Carlsson, L. 2002 *Assessing the Groundwater Budget for Watersupply in an Area of Low Groundwater Recharge in Northern Botswana*, Proceedings of the International Conference on Balancing the Groundwater Budget, Darwin, Australia.

- Brunner, P., Bauer, P., Kinzelbach, W. 2002 *Determination of recharge patterns by combining remote sensing and the chloride method*. In: K. Kovar (Editor), Model Care 2002: Calibration and Reliability in Groundwater Modelling. IAHS Redbook. IAHS Publications, Prag, pp. 389-395.
- Hendricks Franssen, H.J., Brunner, P., Kgotlhang, L., Kinzelbach, W. 2005 *Use of a digital elevation model, satellite images and geophysical data to improve the groundwater modelling in Kavimba, Botswana*, General Assembly of the European Geosciences Union 2005. European Geosciences Union, Vienna, Austria.
- Hendricks Franssen, H.J., Brunner, P., Kgotlhang, L., Kinzelbach, W. 2002 *Inclusion of remote sensing information to improve groundwater flow modelling in the Chobe region (Botswana)*, Model Care 2002, Scheveningen (The Netherlands).
- Kinzelbach, W., P. Bauer, T. Siegfried, Brunner, P. 2004 *Sustainable water management in arid environments*, In: Research Basins and Hydrological Planning. Proceedings of an international conference. Hefei, China, X.,Gu. and P. Seiler, (eds), Taylor&Francis Group, London, p. 27-34.

## Reports

- Alberich C., Brunner P., Kinzelbach, W., 2003 *Groundwater modeling and environmental tracer information*. In: El agua y la ciudad sostenible: Hidrogeología urbana. Barcelona 23-25 October 2003. Publicaciones del Instituto Geológico y Minero de Espana. Serie: Hidrogeología y aguas subterráneas, No. 11.
- Brunner, P. 2004 *Folgen einer intensiven Bewässerungslandwirtschaft am Beispiel des Yanqi-Beckens, China*, Warnsignal Klima: Genug Wasser für alle? Wissenschaftliche Auswertungen, J. L. Lozán et al. (Hrsg.), Hamburg, p. 255-259.
- Brunner, P. 2003 *Wasserhaushalt im Yanqi Becken*, ETH Bulletin, p. 14-17.
- Kinzelbach, W., P. Bauer, T. Siegfried, P. Brunner 2003 *Nachhaltige Grundwasserwirtschaft - Probleme und wissenschaftliche Werkzeuge* Österreichische Wasserwirtschaft, 55(3-4).

## Varia

- Brunner, P., Kinzelbach, W. 2002. *Use of spreadsheet for soil water balance method* In: A survey of methods for analysing groundwater recharge in arid and semi-arid regions. Early Warning and Assessment Report Series. United Nations Environment Programme, UNESCO, UNEP, DEWA, RS.02-2. UNEP, Nairobi, Kenya, p. 20-21.